Ion Specificity at Non-Aqueous Solvent Surfaces: Concentration Depth Profiles of Monovalent Inorganic Ions

By

Anand Kumar

Thesis

Submitted to Flinders University

for the degree of

Doctor of Philosophy

College of Science and Engineering

20th February 2023

TABLE OF CONTENTS

ABSTRACT

Against the continuum electrostatic description of the image charge interaction, it is known that inorganic ions are present at the vapour-water interface and show ion specificity in their presence/absence at the interface. Ion specificity for the presence/absence of inorganic ions at the vapour-water interfaces has been investigated using various advanced surface-sensitive techniques as discussed in this thesis. However, it is still largely unexplored at other vapour-solvent interfaces. Here, the specific ion effects (SIE) for the distribution of monovalent inorganic ions along the depth scale at the vapour-solvent interfaces of 4 non-aqueous solvents are investigated. Neutral impact collision ion scattering spectroscopy (NICISS) is employed to elucidate the ion specificity within the distribution of ions at these vapour-solvent interfaces. NICISS provides individual ion concentration depth profiles (CDPs) formed from the inorganic electrolytes dissolved in the solvents. This information is obtained from the energy loss of helium projectiles during their trajectory into the sample and then backscattering from the samples' constituent elements. Employing NICISS, in this thesis, the complexity of ion specificity due to separate ion contributions and solvent perturbations at the vapour-solvent interface is presented.

Thirteen different glycerol solutions are studied to compare CDPs of inorganic monovalent ions. Results show that smaller chloride ions (Cl^-) are comparatively more abundant at the vapour-glycerol interface than larger bromide ions (Br^-) and show equal enhancement to larger iodide ions (I^-). This is in contrast with aqueous electrolyte solutions but consistent with the expected influence of the change in the solvent. NICISS measurements reported here reveal the anions' strong influence towards the CDPs of the cations, but cations only influence the CDP of Br^-, whereas Cl^- and I^- distribution are mostly independent of the counterion. Following, a reverse Hofmeister series for monoatomic inorganic ions at the vapour-formamide interface in comparison to the vapour-water interface is reported. The CDPs of ions are found to be independent of the counterion at the vapour-formamide interface. The latter observation suggests that the ions in formamide follow a "Hofmeister paradigm" where the counterion has no impact on the order of the series. This is also observed in the various electrolyte solutions through X-ray absorption near-edge structure (XANES) measurements. Even though a negligible counter-ion effect is observed, cations seem to drive the overall depletion of electrolytes which is measured using NICISS and suggested through surface tension measurements.

In the last experimental chapter, ionic CDPs of selected monovalent inorganic electrolytes were investigated at the vapour-solvent interfaces of propylene carbonate (aprotic) and benzyl alcohol (protic). Here, the SIE at both solvent interfaces is alike suggesting that the interfacial hydrogen bonding does not influence the ion-specific CDPs at these vapour-solvent interfaces. The dominant role of cations in overall electrolyte depletion is also observed. This work further emphasizes the importance of anion-cation interactions towards ion specificity at the vapour-solvent interface. These

overall findings display the variation in ionic behaviour at various vapour-solvent interfaces thus displaying the role of solvent perturbation towards the ion specificity. These findings were then tested against various existing concepts and hypotheses for the adsorption/desorption of ions at the vapour-water interface to elucidate the underlying mechanism of ion specificity at the vapour-solvent interfaces.

DECLARATION

I certify that this thesis:

1. does not incorporate without acknowledgment any material previously submitted for a degree or diploma in any university

2. and the research within will not be submitted for any other future degree or diploma without the permission of Flinders University; and

3. to the best of my knowledge and belief, does not contain any material previously published or written by another person except where due reference is made in the text.

Signed.....

Date: 23/02/2023

ACKNOWLEDGEMENTS

I would like to acknowledge the Australian Research Council for funding this project (DP190100788) and Flinders University for providing me with the Tuition fee sponsorship and HDR scholarship through the grant. Flinders University is further acknowledged for the international travelling fellowship, Bank SA travelling award, Amy Forwood fellowship, and HDR conferences support. I am also very grateful for the financial support from AINSE Ltd. through Postgraduate Research Award (PGRA). Part of the PhD research work was conducted at the Australian Synchrotron XAS beamline (M18495 and M18608), and their financial support is greatly acknowledged.

I am deeply indebted to my supervisor Prof. Gunther Andersson; you had taken me under your wing since my undergraduate and helped me grow as a researcher ever since. You have provided me with immense support over the past 5 years during my undergraduate and throughout my PhD and helped me tackle any problems that arose. I admire your enthusiasm for research and the calmness needed to face the challenges of research, I aspire to have that calmness someday. I am extremely grateful to my co-supervisor Prof. Vince Craig, for providing important feedback and advice related to my research work and about being a researcher; and for pointing out my mistakes and how to fix those mistakes. I am also thankful to Prof. David Lewis for providing access to his labs and for his honest feedbacks. I would like to thank Prof. Erica Wanless, Prof. Grant Webber, and Prof. Alister Page for providing important feedback related to the research and the support and encouragements throughout my PhD and especially during the weekly meetings. I would also like to thank everyone in the unravelling ions group over the past three and half years. It has been a great pleasure to work with all of you and learn so much from you. I would especially like to thank Hayden for bringing me along to ANSTO and coming and helping me with synchrotron experiments. I thank Dr Valerie Mitchell for the training and guidance during the synchrotron experiments and for agreeing to supervise me as an ANSTO supervisor so late into my PhD. I am also grateful to Prof. Mark Schlossman for letting me visit his lab to conduct synchrotron experiments at the APS and for being patient when the plan got rescheduled and cancelled so many times over the past 2 years due to COVID and to Bikash for helping me with APS experiments.

I would like to thank everyone of my Flinders group members for providing support throughout my PhD, it's been great listening to your ideas and research works. I would like to especially thank Abdul for listening to all of my frustrating stories and giving me important advice. I am grateful of Dr. Ben Chambers and Dr. Liam Howard’s technical assistance with the NICISS instrument and general advice. I would also like to thank Chris, Darren, Anthony, and everyone else at the Physical Sciences workshop for helping me with all the machining stuffs needed for NICISS. A special thanks to all my friends, Ashwin, Rhea, Sitansu, Ha, Mitra, PK, Prakhar, Karle, Bhavani, Tanay, Matt, and Ketan for putting up with my conversations, giving me advice, and sending memes. Finally, I am grateful for the never-ending support of my parents, my brother, and everyone in my family back home.

CONTEXTUAL STATEMENT

Most of the results included in this thesis were from the experimental measurements performed in Prof. Andersson's lab at Flinders University, Australia. Further complimentary experiments were also performed at the X-ray absorption spectroscopy (XAS) beamline at the Australian Synchrotron (M18495 and M18608). For these experiments, all measurements, data analysis, and manuscript preparations, and revision were performed by the author of this thesis.

In chapter 1, a reformatted version of a section published in a peer-reviewed perspective article *(Phys. Chem. Chem. Phys., 2022, 24, 12682)* and a section published in a book chapter *(Elsevier Encyclopedia Entry - Book Chapter, In press)* is included. For the perspective article, as a co-author, I provided section 1.5.3 of the drafted literature review to the collaborators which is included as the *"SIEs at the liquid-vapour interface"* in the publication. Only the original draft provided by the author of this thesis is included in Chapter 1 with additional reformatting. For the book chapter, I drafted, edited, and finalised the accepted manuscript with small contribution from Thomas Ceme and Prof. Gunther Andersson. Further, Prof. Andersson validated all the derivations included in this book chapter and provided feedbacks on the draft. Chapter 2 contains a reformatted version of part of the sections published in a peer-reviewed journal article *(Journal of Colloid and Interface Science, 2022, 626, 687–699)* while the rest of the section of this peer-review journal is included as whole in Chapter 3. The remaining part of chapter 2 was written by the author of this thesis. For this peer-reviewed journal article included in Chapters 2 and 3, the author of the thesis made a major contribution. For this peer-reviewed journal article, Prof. Andersson had written the deconvolution code used for the NICISS data evaluation and guided the author of this thesis in applying the deconvolution procedure to the measured experimental results. Prof. Andersson together with Profs. Craig, Page, Webber, and Wanless made intellectual contributions, provided access to their labs, and provided feedback on the manuscript draft. Prof. Page provided the solvation-free energy data used in the publication.

For chapter 4, all the experimental plan was designed by the author of this thesis with guidance from Prof. Andersson and Prof. Craig. In this chapter, synchrotron XAS measurements data are included, the synchrotron experiments were designed by the author of this thesis, and the synchrotrons proposals were written by the author of this thesis with contributions from Prof. Andersson. Hayden Robertson and Alex Griesser joined the author of this thesis during the XAS beamtime at the Australian Synchrotron where all the sample preparation were done by the author of this thesis. Dr Valerie Mitchell supervised the experiments during the beamtime, measured the reference samples, and trained the author of this thesis on the XAS beamline. Prof. Page provided the solvation-free energy data used in this chapter. Prof. Andersson and Prof. Craig further made intellectual contributions and provided feedback on the manuscript draft (in preparation) that was revised and included in chapter 4 as a reformatted version. All the experimental plans for chapter 5 were designed by the author of this thesis with guidance from Prof. Andersson and Prof. Craig who also

provided feedback on the chapter draft. The solvation-free energy data used in this chapter was provided by Dr Kasimir Gregory. No professional editing services were sought out for the writings included in this thesis.

PUBLICATION AND CONFERENCES

Published/prepared contributions related to this thesis:

1. **Kumar, A**., Craig, V.S., Page, A.J., Webber, G.B., Wanless, E.J. and Andersson, G., 2022. Ion specificity in the measured concentration depth profile of ions at the Vapour-Glycerol interface. Journal of Colloid and Interface Science, 626, pp.687-699.
2. Gregory, K.P., Elliott, G.R., Robertson, H., **Kumar, A**., Wanless, E.J., Webber, G.B., Craig, V.S., Andersson, G.G. and Page, A.J., 2022. Understanding specific ion effects and the Hofmeister series. Physical Chemistry Chemical Physics, 24(21), pp.12682-12718.
3. **Kumar, A**., Ceme, T., Andersson, G., Interfacial excess, interfacial tension, interfacial entropy, and tools to measure thermodynamic quantity at the solid-liquid interface, 2022, Book Chapter, Encyclopedia of Solid-Liquid Interface, Elsevier, accepted, In press
4. **Kumar, A**., Craig, V.S., Robertson, H., Page, A.J., Webber, G.B., Wanless, E.J., Mitchell, V.D., and Andersson, G, Specific ion effects at formamide surfaces: a reverse Hofmeister series in ion concentration depth profiles, Submitted
5. **Kumar, A**., Craig, V.S., Gregory, K.P., and Andersson, G., Weak specific anion trends in measured concentration depth profiles at propylene carbonate and benzyl alcohol surfaces, In preparation

Published collaborative work:

1. Duong, T., Pham, H., Yin, Y., Peng, J., Mahmud, M.A., Wu, Y., Shen, H., Zheng, J., Tran-Phu, T., Lu, T., Li, L., **Kumar, A.,** Andersson, G., Ho-Baille, A., White, T. P., Weber, K. J., Catchpole, K. R., 2021. Efficient and stable wide-bandgap perovskite solar cells through surface passivation with long alkyl chain organic cations. Journal of Materials Chemistry A, 9(34), pp.18454-18465.
2. Mahmud, M.A., Pham, H.T., Duong, T., Yin, Y., Peng, J., Wu, Y., Liang, W., Li, L., **Kumar, A.,** Shen, H., Nguyen, H. T., Mozaffari, N., Tabi, G. D., Andersson, G., Catchpole, K. R., Weber, K. J., White, T. P.,2021. Combined Bulk and Surface Passivation in Dimensionally Engineered 2D-3D Perovskite Films via Chlorine Diffusion. Advanced Functional Materials, 31(46), p.2104251.

Conference presentations related to this thesis:

1. 10th International Workshop on High-Resolution Depth profiling, **Invited Oral talk**, 6th – 10th November 2022, Flinders University, Adelaide, South Australia
2. 17th Conference of International association of Colloid and Interface scientist, **Oral talk**, 26th – 30th June 2022, Brisbane.
3. 11th Annual Conference Flinders Institute for Nanoscale Science & Technology, **Poster Presentation**, 15th June 2021, Flinders University, Adelaide, South Australia
4. 33rd Australian Colloid and Surface Science Student Conference, **Oral talk**, 31st January – 2nd February 2022, Virtual.
5. Molecular Science and Technology HDR Student Conference, **Oral talk**, 17th November 2021, Flinders University, Adelaide, South Australia
6. 10th High Resolution Depth Profiling Online Meeting, **Oral talk**, 9th & 10th November 2021, Virtual.
7. Sydney Surfaces and Soft Matter Meeting, **Oral talk**, 9th July 2021, Virtual.
8. 10th Annual Conference Flinders Institute for Nanoscale Science & Technology, **Poster Presentation**, 16th June 2021, Flinders University, Adelaide, South Australia.
9. 10th Australian Colloid and Interface Symposium, **Oral talk**, 8th – 11th February 2021, Hybrid mode, University of South Australia, Mawson lakes, South Australia.
10. 17th Australia Japan Colloids Symposium, **Poster Presentation**, 17th September 2020, Virtual.
11. 32nd Australian Colloid and Surface Science Student Conference, **Poster presentation**, 28th – 31st January 2020, Gippsland, Victoria, Australia.
12. 3rd Annual CSE HDR Conference, **Poster presentation**, 26th & 27th November 2019, Flinders University, Adelaide, South Australia
13. 9th Annual Conference Flinders Institute for Nanoscale Science & Technology, **Poster Presentation**, 18th June 2019, Flinders University, Adelaide, South Australia

LIST OF FIGURES

LIST OF TABLES

LIST OF ABBREVIATIONS

AN	Acceptor Number
ASM	Amorphous solid methanol
ASW	Amorphous solid water
ATR – FTIR	Attenuated total reflection – Fourier transformed infrared
BA	Benzyl Alcohol
CDFT	Conceptual density function theory
CDP	Concentration depth profile
CTTS	Charge transfer to the solvent
DCL	Deuterated hydrochloric acid
DFT	Density functional theory
DFT-D	Density functional theory – dispersion corrected
DMSO	Dimethyl sulfoxide
DN	Donor Number
EDA	Energy decomposition analysis
EC	Ethylene carbonate
EXAFS	Extended X-ray absorption fine structure
FA	Formamide
FWHM	Full width at half maximum
HOMO	Higher occupied molecular orbitals
HSAB	Hard and soft acids and bases
IEP	Isoelectric point
ISS	Ion scattering spectroscopy

LCST	Lower Critical solution temperature
LEISS	Low energy ion scattering spectroscopy
LUMO	Lower unoccupied molecular orbitals
LWMA	Law of matching water affinity
MCP	Multi-channel plate
MD	Molecular dynamics
MEIS	Matching effective ion size
MIES	Metastable impact electron spectroscopy
MIR	Mid infrared region
NICISS	Neutral impact collision ion scattering spectroscopy
NIPAM	N-Isopropylacrylamide
NLO	Non-linear optical methods
NMR	Nuclear magnetic resonance
NR	Neutron reflectivity
PEMTAC	Poly-(2-methacryloyloxyethyl-trimethylammonium chloride)
PPG	Poly propylene glycol
PPO	Poly propylene oxide
PC	Propylene carbonate
PS-SFG	Phase sensitive- Sum frequency generation
QCM -D	Quartz crystal microbalance – dissipation mode
RBS	Rutherford backscattering spectroscopy
SEC	Size exclusion chromatography
SFG	Sum frequency generation

SHG	Sum harmonic generation
SIE	Specific ion effects
STI	Surface tension increment
SWAB	Soft and weak acids and bases
TGA	Thermal gravimetric analysis
TOF	Time of flight
UHV	Ultra-high vacuum
VSFG	Vibration sum frequency generation
XANES	X-ray absorption near edge structure
XAS	X-ray absorption spectroscopy
XPS	X-ray photoelectron spectroscopy
XR	X-ray reflectivity

CHAPTER 1 : INTRODUCTION AND LITERATURE REVIEW

Section 1.5.1. is reformatted and edited version of a section of an accepted book chapter. This book chapter is part of the Elsevier's Encyclopedia of the solid-liquid interface which currently is in press. See the Contextual Statement section for details on the contribution of the author of this thesis to the accepted version of the book chapter.

Section 1.5.3. is reformatted and edited version of a section for a perspective article published in a peer-reviewed journal. See the Contextual Statement section for details on the contribution of the author of this thesis to the published version of the manuscript.

Reference for the published version:

Gregory, K.P., Elliott, G.R., Robertson, H., Kumar, A., Wanless, E.J., Webber, G.B., Craig, V.S., Andersson, G.G. and Page, A.J., 2022. Understanding specific ion effects and the Hofmeister series. Physical Chemistry Chemical Physics, 24(21), pp.12682-12718.

1.1. Overview

Search for understanding ionic behaviours is going on for centuries. For instance Aristotle's explanation for the desalination process for water purification is based on the ion exchange process [1, 2]. Now in the 21st century the term for explaining ionic interaction is various occurrence is "Specific ion effects". The term 'Specific ion effects (SIE)' covers instances where physical, chemical and biological properties of a system depend on the type of ions present in it and not just by its charge or ionic strength in the system [3]. SIE is a convolution of a plethora of studies on electrolyte solutions [4], protein precipitation [5-7], bubble coalescence [8-10], polymer brushes [11, 12], self-assembled monolayers [13-15], and biological ion pumps [16].

The first systematic investigation on electrolytes (or salts) were carried out by Poiseuille [17] who found that some electrolytes increase the viscosity of water more compared to the other electrolytes. Later this change in the viscosity of water due to electrolyte presence was investigated by Jones & Dole [18]. They reviewed previous studies [19-23] on viscosity change by electrolytes and described this change as the stiffening of lattice due to interionic forces exerted by these electrolytes. Following this explanation, they derived the infamous Jones-Dole coefficient [18]. Developing from Jones & Dole's explanation, Frank & Evans [24] classified ions as 'Water makers structure' and 'Water Breaker Structure' and later "close to the synonym" of these terms were coined as Kosmotropes & Chaotropes. 'Kosmotropes' was termed by Washabaugh and Collins [25] while 'Chaotropes' was named by Hamaguchi and

Geiduschek [26] based on the chromatographic behaviour of ions on ordering or disordering of water molecules. Kosmotropic & Chaotropic ions do not have long-range effects on water molecules and hence are considered "close to the synonym" to water structure maker and breaker terms.

Most referred/discussed work on electrolytes (or salts) in the interest of this thesis was presented by Lewith and Hofmeister in the late 19th century. Through a series of investigation, they described the salting-in (dissolving) and salting-out (precipitating) effects of various electrolytes on egg white globulin (or protein). They described this occurrence as salt's ability to destabilize the egg white globulin and cause globulin to precipitate or salts' ability to enhance the egg white globulin stability in the solution [27]. They further added that "one can use this physiochemical behaviour of salts to form an order based on its water-absorbing effects, but we don't know much about this water-absorbing activity of salt". Following these series of investigations, the Hofmeister series for ions was coined [28]. The Hofmeister series is a combination of various orders developed by researchers like Voet [29], Freundlich [30] & Pearson [29, 31, 32]. Freundlich [30, 33] discovered the Lyotropic effect while providing an explanation for increment in molar surface tension in electrolyte solutions with Hofmeister salts and Voet [29] employed this theory to obtain an ionic series and quantitatively explained the surface tension increment by calculating the lyotropic number of salts in agar and gelatin lyophilic colloids. Later, Pearson [31] classified ions according to their softness and hardness (not the same as Kosmotropic and Chaotropic nature of ions) by measuring the heat of formation of halides in the gas phase and other thermodynamic properties which were not specific to Hofmeister or lyotropic ions but to all alkali metals ions. Most of these terminologies of ionic behaviour and trends within were compiled by Mazzini and Craig [34] as shown in Figure 1-1.

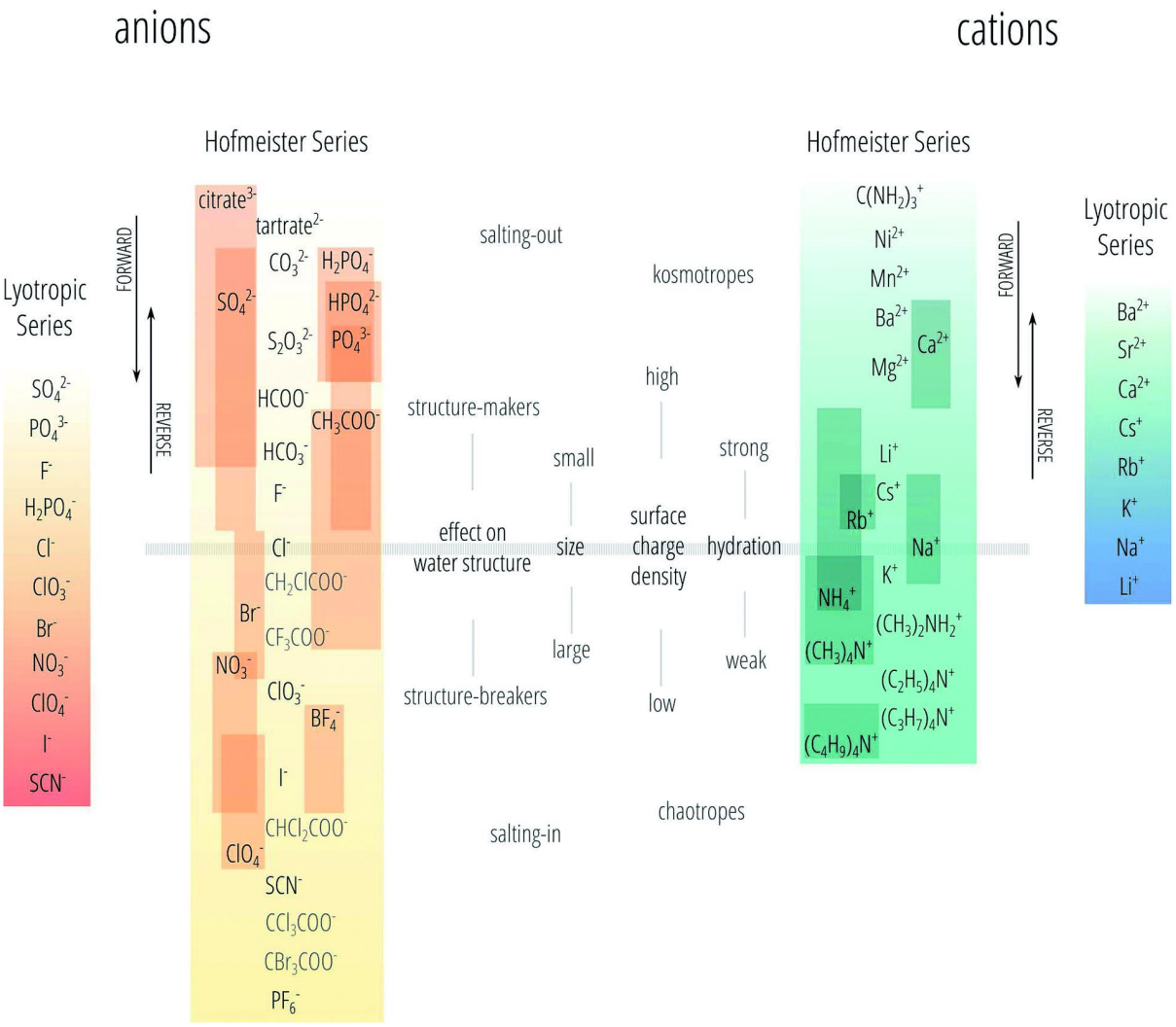

Figure 1-1: The Hofmeister and Lyotropic series of ions in water. The order of ions is represented with the strong protein precipitating ability on the top and with weak ability in the bottom. The variation in each series for an ion is indicated by the individual boxes. Reproduced from [34] with permission from the Royal Society of Chemistry.

1.1.1. Omnipresence/Significance of Specific Ion effects

In an ideal electrolyte solution, SIE emerges from ions itself which is predominant in nature. For example, it is hard to find water that does not contain any ions in it. There are over 4000 bottled water companies that package mineral water with different types of minerals as ingredients. SIE occurs in complex systems and controls the functioning of biological molecules i.e., bacteria growth [35], enzymatic activity [36, 37], water retention process of wool [38] and even controls the colour of salts we sprinkle on our food. Himalayan salt is pink in colour and contains trace mineral ions such as potassium, magnesium, and calcium but common table salt is white being essentially pure sodium chloride. So, understanding SIE is essential to untangle these conceptions of complex systems.

SIE is important in understanding atmospheric chemistry as seawater aerosols contains a range of ionic species and their presence can alter N_2O_5 reaction by forming $ClNO_2$ and $BrNO_2$ in presence of Cl^- and Br^- respectively [39, 40]. Salt solution rejection occurring in the arctic regions is one of the reasons for the melting of ice as an aftermath of climate change [41]. When the sea water or ocean wave crashes near beaches we can see the foam formation, but a similar effect does not result with waves in lakes. This is an action of inhibition in bubble coalescence caused by electrolytes' presence in seawater [8, 42]. The solubility of a gas in water changes according to the ionic presence hence SIE governs marine life sustenance as the amount of oxygen or other important gas solubility changes with the electrolytes present in the water bodies [43].

Recently researchers have utilized a salt-based method to increase the stiffness and biodegradability of collagen scaffolds [44]. Versteegden et al. patented a diseased seed amplification process that is influenced by SIE [45]. Hofmeister effect has been found to influence chemotaxis [46, 47] which refers to an organism's ability to move. Chemotaxis commands the food collection process in bacteria & algae, wound healing [48], and tumour metastasis [49]. SIE influences ion's kinetic ability towards corrosion as anion-specific hydration property has an influence on the corrosion phenomenon in tin [50]. There are experimental proofs of ionic influence in drug delivery [51], wastewater treatment [52], oil recovery [53], solvent extraction [54], and surface coatings because supramolecular self-assembly of surfactants are also ion dependent [55, 56]. Na^+ and Ca^{2+} have been shown to influence ordering in lipid films [57]. In the model solvent extraction and cell membrane processes [58] heavier lanthanide ions are shown to form an inverted bilayer (a thermodynamically unfavourable system) at air-liquid [59] and oil-water [60, 61] interfaces. Polymeric 3D-Chain arrangements (conformations) are rich in ion specificity and have applications in the development of next-generation lithium polymer batteries [5, 62].

1.2. Debye- Hückel Theory

Much of our thinking for electrolyte solutions is underpinned by the Debye- Hückel theory. Based on the observation from the freezing point depression of electrolyte solutions, Peter Debye and Erich Hückel explained that the organized distribution of oppositely charged ions is related to their activity in electrolytesolutions. This activity is related to the activity coefficient given as activity over concentration of the solute (electrolyte) in electrolyte solutions [4].
Further using the linearized Poisson-Boltzmann equation they introduced the Debye length (k_D^{-1}) that explains the organized separation of opposite charges in the electrolyte solution. This separation of opposite charge in electrolyte solution is dependent upon the concentration of electrolyte and dielectric permittivity (ε_r) of the medium given as:

$$k_D^{-1} = \left(\frac{\varepsilon_0 \varepsilon_r \, k_B T}{q^2 n_j z_j}\right)^{1/2} \quad (1)$$

Where, q is the charge of the ion, n_j and z_j are the number density and valance of ion j. The Debye-Hückel theory of electrolytes has acceptable predictability for ionic interactions in dilute electrolyte solution but failed at electrolyte concentration higher than 0.1 Molar (M) [a]. Assumptions made here were that in an electrolyte solution, all charges are considered spherical point charges and not affected by the polarizability of solvent molecules. However, Washabaugh and Collins [25] showed that ionic hydration depends on the charge density of ions proving that ions do not act as a point charge and that the assumption of point charge ignores the ion specificity.

1.3. Laws of Matching Water Affinity

One of the most important theories for SIE investigation is the Collins "Law of matching water Affinity (LMWA)". Collins [65] argued that the degree of ion pairing is determined by the relative water affinity (charge density) of the ions and their counter-ion. Ions with matching water affinity form closely associated 'contact' ion pairs, which lowers the solubility of their composite electrolyte whereas if ions have a mismatch in affinity, then they will have stronger interaction with water and higher solubility (Figure 1-2 (a)). Collins made this argument from a collection of experimental evidence (viscosity B coefficient, Nuclear magnetic resonance (NMR) spectroscopy, size exclusion chromatography, and Neutron and X-ray diffraction) and thermodynamical observation [25, 66, 67]. The thermodynamic foundation was based on the volcano plot with axes of constitute electrolytes' standard heat of solution vs differences in absolute heat of hydration for anion and cation in the gas phase at infinite dilution (kcal mol^{-1}). The volcano plot (Figure 1-2 (b)) trend showed that the two composite electrolytes with two Chaotropic or Kosmotropic ions will take off heat (unfavourable solvation) thus locate on the maxima of the volcano plot whereas constitute electrolytes of Kosmotropic – Chaotropic or Chaotropic – Kosmotropic ions will give off heat (favorable solvation) and locate at the bottom ends of a volcano plot.

[a] For defining the electrostatic separation between charges (called screening), the Debye length works up to 1 M but at higher concentrations (< 1 M), underscreening of the Debye length is observed. 63.Liu, G., D. Parsons, and V.S.J. Craig, *Re-entrant swelling and redissolution of polyelectrolytes arises from an increased electrostatic decay length at high salt concentrations.* Journal of Colloid and Interface Science, 2020. **579**: p. 369-378, 64. Perez-Martinez, C.S., A.M. Smith, and S.J.F.d. Perkin, *Underscreening in concentrated electrolytes.* 2017. **199**: p. 239-259..

There have been successful attempts to extend this seminal theory to other solvents as the Law of matching solvent affinity, and the Law of matching effective ion size which is presented in the next section. Further, LWMA is well accepted to define the interaction of macromolecules with the anions at aqueous interfaces [67]. Thus, this framework can be extended to vapour-water interfaces where the relative affinity of ions for water determines the comparative strength of their interactions with surfaces - ions of higher water affinities are more strongly depleted from the surface since they prefer to reside in the bulk solution.

One irregularity in LWMA is that it assumes that the large ions will interact weakly with water during which the water-water interaction will be more favourable. However, the Gibbs free energy of solvation for large ions like Cs^+ or I^- is still negative i.e., favourable, hence this justification is unsustainable [68]. These favourable interactions of large ions result from dispersion interactions as quantitatively shown by Salis and Ninham [69].

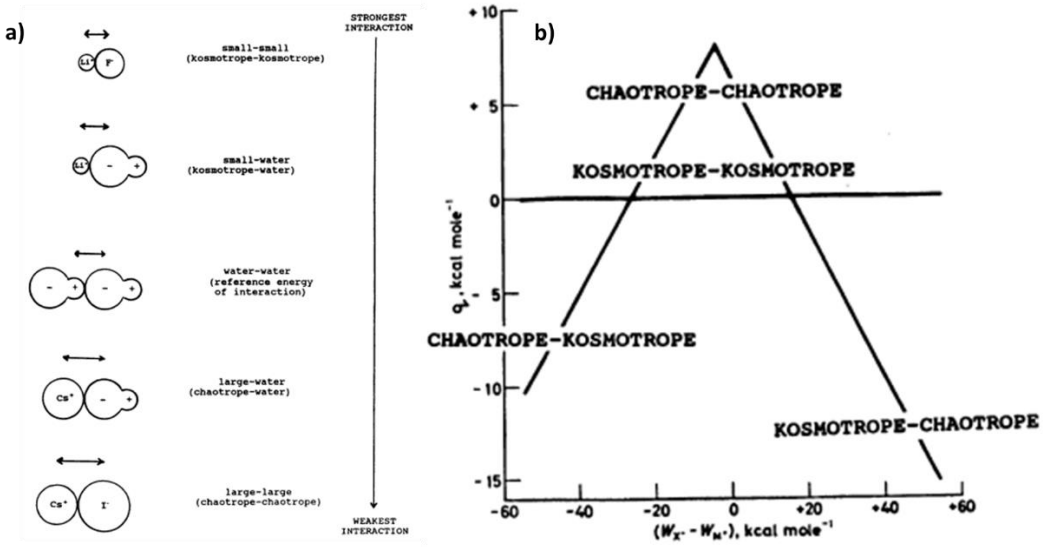

Figure 1-2: Collins rank ordering for ion interaction in water and (b) the volcano plot of ions in water depending on the choice of ion interactions. Reproduced with permissions from ref[65]

1.4. Briefing of Specific Ion Effects Investigation for Non-aqueous Solvents

There are plenty of research done for Hofmeister series in water, but this series often changes in solvents other than water and no proper explanation was found for this behaviour. Werner Kunz in his review of trends in SIE brought up an interesting topic that there is not any systemized research done with SIE in nonaqueous solvents [28]. Since then, advances have been made in the field to a considerable extent, this section will present an overview of existing research with ions in nonaqueous solvents and a summary of Mazzini & Craig's work [34, 68, 70-73] which has inspired this thesis.

The very first work with ions and non-aqueous solvents in relevance with SIE was done by A.J parker [74] in the early 60s through a review of anions solvation effect in aprotic solvents and its conductance analysis. Following a similar analysis, Symons & Butler [75] studied the ion-solvent interaction in methanol employing NMR spectroscopy. While Melendres [76] investigated and obtained NMR experimental data of cations' magnetic relaxation time in the water together with methanol and found a similar trend for both solvents. Most vital work was done by Marcus & co-workers [77, 78] [79] [80] by the compilation of data for ions in various solvents. Marcus and Hefter [79] calculated ionic partial molar volumes for electrolytes in various solutions. In a later publication, Marcus & Jenkins [80] revised ionic B coefficient data in water and non-aqueous electrolyte solutions by splitting electrolytes B coefficient into cations and anions by selecting a reference ion. Further, Marcus & Hefter [81] collected the data available in literature for ion-solvent interactions at infinite dilution and separated the cation and anion contributions to discuss various ion-solvent interactions. Later, Marcus [82] published a book with a combined review of all these works and provided extensive information for ionization potentials, electron affinity, ion solvation, Gibbs free energy, enthalpy calculations, etc. which made finding information on ionic properties and their interaction with various solvents easily accessible. Peruzzi et al. investigated potassium electrolytes solubility in ethylene carbonate (EC), aprotic solvents with no hydrogen-bonded species present. They found that the electrolytes in EC followed the Hofmeister series hence disproving the old belief that ion specificity emerges from the effects of water hydrogen-bonded nature [83]. They explained this as an effect of ion-electrostatic interactions with the dipole of solvent and the contribution of dispersion interactions. Succeeding this work authors made a comparison with similar experiments in propylene carbonate (PC), a solvent with a similar structure to EC with the attachment of the methyl group on the ring structure. Results from this comparison also followed the Hofmeister series with few exceptions due to the limited solubilities of electrolytes in PC [84].

Recently Mazzini & Craig in a series of publications investigated SIEs based on various phenomena i.e., electrostriction [34], partial molar volumes [34], Volcano plot [68], solvadymaic radius, and polyelectrolyte brush conformational change [71] in non-aqueous solvents. In their first extensive article, Mazzini and Craig [70] collected an arranged existing data for NMR molecular reorientations time, the molar heat capacity of ions at infinite dilution, Viscosity B coefficient of ions and relative dielectric decrement due to ion concentrations in various non-aqueous solvents whilst looking for a common pattern. They found that the Hofmeister series is not consistently present throughout the experiments for cations and anions. However, the overall collection showed a qualitatively consistent Hofmeister series for anions and reverse lyotropic series for cations in non-aqueous solvents. This review was

notable as it showed the depth of complexity involved with SIE while proving that Hofmeister or lyotropic series does not necessarily limit to protic solvents [70].

In the second publication [34], Mazzini and Craig investigated the SIE at infinite dilution for electrostriction and molar partial volume of electrolytes in 12 aqueous and non-aqueous solvents. Electrostriction is defined as the ionic movement in solvent based on its electric field and molar partial volumes are defined as the change in volume of a solution by the addition of one mole of solute at constant pressure, temperature, and other relevant solvent components. Within electrostriction and partial molar volume change at infinite dilution, they found a Hofmeister and reverse Hofmeister (lyotropic) series with few exceptions present in ethanol, acetone, and N-methyl formamide. The authors also normalized electrostriction data to evaluate the degree to which ionic size affects electrostriction hence making this investigation truly ion specific. Overall this investigation showed that ion specificity is independent of solvents and the belief of Hofmeister series discrepancies at infinite dilution [85] was disproven. These collections of datasets were explained based on the hypothesis that SIE will be found in any solutions at infinite dilutions when electrostatic effects and dispersion forces effects are considered equal [86].

Furthermore, Mazzini & Craig explored the volcano plot for ions in non-aqueous solvents to find if LMWA extends to solvents other than water [68]. Their results showed that the LMWA and volcano plot holds for ions in protic and aprotic solvents in all investigated thermodynamic cases (with few exceptions). This eminent investigation also showed that the maxima of a volcano plot shifts with the solvents due to solvent perturbation [68]. This solvent perturbation primarily arises from the fact that the effective ionic radii, hence the solvation of ions in each solvent is different [87]. Moreover, moving from one side arm of the volcano plot to the other side arm, a counter-ion-induced SIE reversal can be observed.

Finally, Mazzini et al. [71] investigated anions effects with sodium electrolytes in 5 solvents: water, dimethyl sulfoxide (DMSO), formamide, PC and methanol employing size exclusion chromatography (SEC) (motivated by Washabaugh and Collins study [25]). From SEC measurements, authors found that the sodium electrolytes in water and methanol follow a Hofmeister series while ions in DMSO and PC followed a revered Hofmeister series. While ions in formamide showed an inconsistent trend. Extending their efforts Mazzini and co-workers studied SIE towards swelling and collapsing of PMETAC brushes in the same list of non-aqueous solvents and electrolytes. For this investigation quartz crystal microbalance in dissipation mode (QCM-D) was used to measure rheological changes in polyelectrolyte brushes. Authors observed a similar trend to the SEC experiments for the conformation changes caused by ions with the exception that ions in formamide followed the Hofmeister

series at the weaker degree [71]. These behaviours were interpreted as an interplay between ion and solvent polarizability where less polarizable solvents i.e., water and methanol showed the Hofmeister series and highly polarizable solvents i.e., DMSO and PC showed a reversal. Consequently, formamide being a solvent with intermediate polarizability showed an inconsistent trend when accounting for both experimental situations.

Following Mazzini and Craig's imminent work, various other research groups studied the SIE in non-aqueous solvents. Gregory and co-workers [88] investigated the Lewis Strength correlation for SIE in water and non-aqueous solvents using energy decomposition analysis (EDA) for ion-NIPAM polymer model systems. Authors discussed their observations based on the available dipoles for ions within the NIPAM polymer structure i.e., carbonyl moiety of NIPAM for cation and hydrogen bonded amine group for anion favourable interaction. Their calculations followed the Hofmeister series in non-aqueous solvents (methanol and DMSO) as F^- binds to the NIPAM model strongest and SCN^- weakest. To further understand the reasoning behind this phenomenon, continued work was done in vacuum conditions without any solvent and a Hofmeister series was still observed. This meant that solvents were not affecting the Lewis strength of the ion-NIPAM polymer model. From this investigation, Gregory and co-workers concluded that the Lewis strength index can be used as a fitting parameter for further works and that the ion specificity originates from ions themselves. However, solvent parameters need to be included in calculations to account for polarizability and dispersion interactions. Gregory and co-workers also observed that the inclusion of anion-cation interaction (when ion pairs were forced computationally) within ion-NIPAM interaction in water results in a series reversal compared to when only single ion interaction is included. This observation showed the significance of anion-cation interactions for ion specificity [88]. Further investigating this matter, Gregory and co-workers [89] found that the Lewis strength of a solvent quantified through the Gutmann acceptor number (AN) provides a quantitative correlation with the Gibbs energy required to transfer ions from water to non-aqueous solvents. This quantitative correlation was associated with anions' radial charge density parameter "Sho" and following this correlation, SIE reversal can be predicted. This ideology of Lewis acidity/basic nature ions comes from Pearson's hard and soft acids and bases (HSAB) law [31]. Following HSAB, Pearson defined that the combination of hard acids (cations), and hard bases (anions) are non-polarizable whereas combination of soft acids and bases are polarizable and both combinations form a strong ion pair. LMWA shows a strong resemblance with the HSAB theory. Albeit Pearson categorized ions including transition metals and non-ionic molecules which were not considered in LMWA.

Following onto a similar path of LMWA and HASB theory, Smiatek and co-workers [90-92] provided a detailed description of SIE and defined the Soft and weak acids and bases (SWAB) law [93]. Employing conceptual density functional theory (DFT) calculations, Smiatek and Miranda-Quintana [93] showed that the chemical reactivity index like chemical hardness (η) and electronegativity (χ), of ions and solvents are important to understand SIE in aqueous and non-aqueous solvents. Where η is the representative term of the inverse ion polarizability which can be calculated by taking the energetic difference between ionic Higher occupied molecular orbital (HOMO) and Lowest unoccupied molecular orbital (LUMO) states. Following SWAB law, Smiatek and co-workers [90, 92-95] suggested that if the electronegativity of cation (χ_C) is large compared to the solvent's electronegativity (χ_S), and the solvent's electronegativity is large compared to anion's electronegativity (χ_A) then anion and cations will have higher solvation energy in a respective solvent. In this case, the cations and anions will be strong acids and bases respectively and form the strongest ion pairs in the solvent of intermediate electronegativity index. This law is similar to the HSAB law [31] but considers the solvent perturbation towards SIE and provides a detailed rationale for the law of matching solvent affinity (an extension to the Law of Matching Water Affinity [65]).

Interest for SIE in the non-aqueous solvent is growing [72, 96-98]. From this overview, we can see that important work has been done with SIE that proves that water is not a special solvent. This overview also shows that SIE changes between the solvent thus we need to understand the solvent perturbation towards ion specificity. Considerable development has been made to gain a fundamental understanding of SIE in non-aqueous solvents. Even the Hofmeister effect of anions has been quantified in the bulk of various solvents [89]. However, SIE at the vapour-solvent interface is still not well understood.

1.5. Inorganic Ions at Solvent surfaces

1.5.1. Gibbs Adsorption Equation

The *Gibbs adsorption equation* is the most critical equation involving surface (or interfacial) thermodynamics. At constant temperature this equation is called *Gibbs adsorption isotherm* and is given as:

$$-d\gamma = \sum_{i=1}^{j} \Gamma_i \, d\mu_i \qquad (2)$$

This equation is derived from the comparison of the Gibbs energy for two bulk phases α and β separated by an interfacial region (σ) as shown in Figure 1-3. These two bulk phases can be vapour, liquid or solid and the Gibbs adsorption isotherm holds for any such combination.

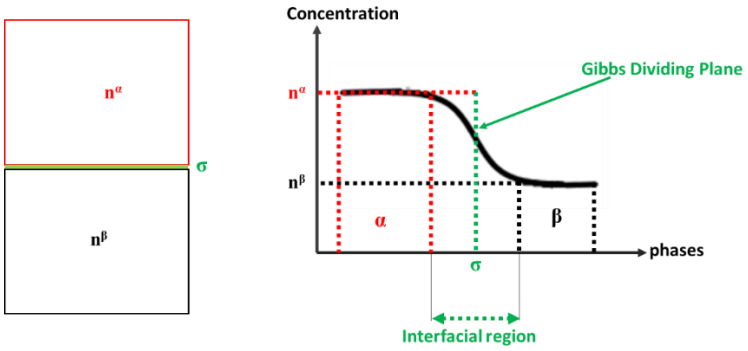

Figure 1-3: Schematic representing the Gibbs model for surface thermodynamics between two bulk phases α and β with an interfacial region (σ) between these phases. Based on Adamson[99] description, the Gibbs dividing plane would be situated where the excess of both α and β phases will be zero (shown as a green dashed line). n^{α} and n^{β} are the number of moles of a component in bulk phases α and β.

As can be seen from Figure 1-3, the Gibbs adsorption isotherm is dependent upon an arbitrary choice of the position of the Gibbs diving plane which defines the interface between two bulk phases. For a binary system with a solute (1) in the liquid phase (α) against the vapour phase (β) equation (2) can be written as [100]:

$$-d\gamma = \Gamma_{\alpha}\, d\mu_{\alpha} + \Gamma_1\, d\mu_1 \qquad (3)$$

Because the position of the Gibbs dividing plane can be chosen arbitrarily, its position (Z_0) at a vapour-liquid interface can be chosen such that the surface excess of the liquid phase is zero, e.g., $\Gamma_{\alpha} = 0$.

For this choice the overall surface excess of both phases is only related to the excess of the solute (1) as $\Gamma_i = \Gamma_1^{excess}$ (4)

By measuring the surface tension of the solution (liquid phase with solute) and availability of the chemical potential of the solute, its surface excess (or depletion) information can be obtained from equation (3).

For a solution of 1:1 dissociating electrolyte, the chemical potential of the solute is defined with the activity of anion and cation. Then the Gibbs adsorption isotherm equation (3) for 1:1 electrolyte is written with mean activity coefficient (a) of anion and cations as:

$$\frac{d\gamma}{d\ ln\ A} = -\ 2\ RT\ \Gamma_1 \quad \text{whereas } A = {C_1}^{bulk}/a \qquad (5)$$

1.5.2. Theories and Driving Parameters for Ionic Presence at Vapour-Solvent Interfaces

In 1910, Heydweiller [101] observed that inorganic electrolytes increase the surface tension of aqueous electrolyte solution compared to the pure water which thermodynamically indicated

a deficiency of inorganic electrolytes at the interface. To explain this, Wagner [102], Onsager and Samaras [103] developed a theory for the surface tension increment (STI) of aqueous electrolyte solution using the Debye-Hückel theory. They explained that the inorganic ions are repelled from the air-water interface due to the large difference in the dielectric permittivity of the air and water. This difference in dielectric permittivity leads to an opposing electrostatic self-energy (image charge) which inhibits inorganic ion adsorption. This theory showed qualitative consistency with inorganic electrolytes' surface tension increments. However, it failed to account for STI above 0.1 M electrolyte concentration due to its calculation by linearization of a part of adsorption excess in the Gibbs adsorption equation. Linearization of Gibbs adsorption equation resulted in the disappearance of the self-consistent potential present in the adsorption excess derivations [104]. In these derivations, the Self-consistent potential is an ionic size dependent parameter set as a boundary condition for ion's closest distance of approach at the interface. Since their explanation was based on the Debye Hückel theory, the consideration of ions as point charges further ignored the ion specificity.

As the surface tension value of a solvent increases due to the presence of inorganic electrolyte in the solution (with exceptions of inorganic acids [105]), calculated surface excess from equation (3) will produce a negative surface excess meaning ions are depleted (or devoid) at the interface. Thus, it can be concluded that simple inorganic halides i.e., I^-, Br^-, and Cl^- are depleted (or devoid) from the solvent surfaces since these ions increase the surface tension value of a solvent. This interpretation was also contradicted by improved surface computational calculations, advanced surface-sensitive techniques [106], and from the observation of certain interfacial chemical reactions [107]. Perera & Bercovitz [108-110] in a series of publications contradicted the conventional STI interpretation by performing MD simulation. In this simulation, the authors performed experiments with clusters of water molecules and I^-, Br^-, and Cl^- while including the electronic polarization force field for the ions and observed that these ions are present in the outermost layer of water clusters. These calculations were later found to agree with Hu and co-workers [111] observation where an increased uptake coefficient for gas-phase bromine and chlorine was found. Hu and co-workers finding could only be explained if the halide anions were present at the electrolyte solution surface and not when ions are depleted from the surface [111].

Applying the electronic polarization force fields, Jungwirth and Tobias [112, 113] showed that the bigger ions (I^- and Br^-) are present in enhanced concentration nearby the air-water interface and smaller ions (Cl^- and F^-) are devoid at the interface which followed the Hofmeister series for decreasing surface ion presence for sodium salts as $I^- > Br^- > Cl^- > F^-$ (Figure 1-4). Analogous to Dang and co-workers' explanation [114, 115], Jungwirth and Tobias explained

that the large polarizable ions are stabilized at the surfaces by the induced dipole of solvent. This induced dipole polarizes the ion which leads to an energy gain that compensates for the energy penalty for ionic adsorption at the interface. Based on this notable investigation, ionic size and polarizability were defined as the driving parameter for ions at water interfaces. However, Jungwirth and Tobias's calculation consistently produced larger surface tension increments for electrolyte solutions compared to the experimental observation. This was later explained by Levin [116] as an effect of overestimation of the pure water's surface potential employing polarizable forces fields.

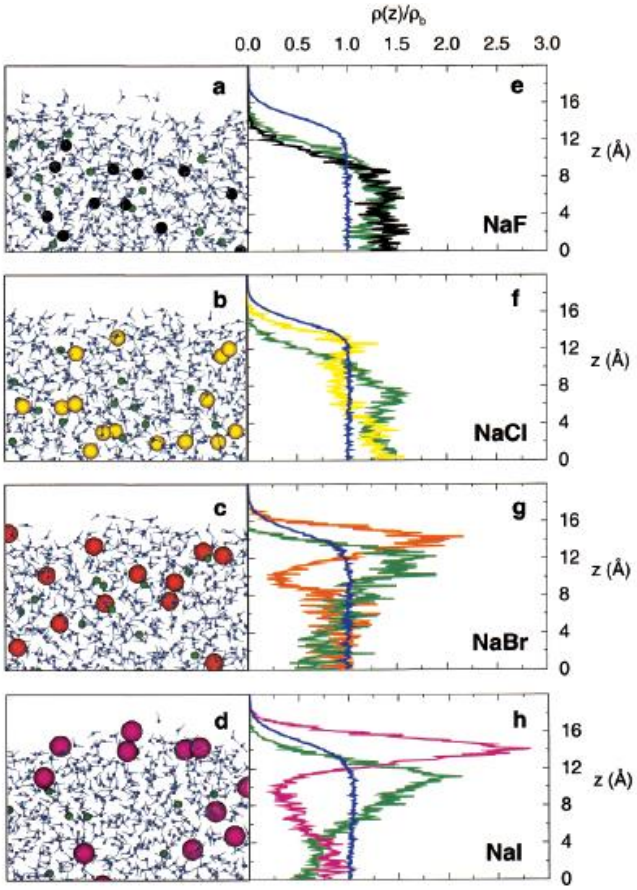

Figure 1-4: MD simulation of anion and cation (Na^+) distribution of sodium halides at Vapour-water interfaces. Figures (a), (b), (c), and (d) show the snapshot of F^-, Cl^-, Br^- and I^- organisation respectively with Na^+ at Vapour-water interface. Figures (e), (f), (g), and (h) showing the density depth profiles of F^-, Cl^-, Br^- and I^- with Na^+ at Vapour-water interface. The Gibbs dividing plane lies at 15 Å in these density profiles. Reproduced with permission from ref [113]

Including the refined polarizable ions theory, Levin and et al. [116, 117] showed an excellent correlation with the experimental STI. Authors explained that ions moving to the interface is caused by a void formation in the solvent. This void results in cavitation energy formations in the solvent (related to the hydrated size of ions) which pushes ions into a low dielectric medium

(air-water interface) in competing effects with the opposing electrostatic forces. To facilitate their presence at the interface (against the electrostatic forces), ions redistribute their charges towards the water bulk and balance the energetic penalty which can only happen for polarizable ions since non-polarizable ions do not have the energetic support required to redistribute these charges. Based on this explanation, they calculated the STI for anions by varying the cations' hydrated radius. However, a fundamental explanation for using cation as a variable parameter was not provided. Further, the correlation of ionic polarizability with ionic surface presence has been refuted by many researchers computationally and experimentally [118, 119].

Noah and Glisseler [118] simulated a model solvent system (called Stockmayer fluid) with ions and found that even smaller and less polarizable ions can adsorb at the solvent interface based on their charge fluctuations closer to the outermost layer of the solvent. Colussi et al. [119] investigated anion affinity towards the air-water interface by studying electrolyte solutions droplets using electrospray ionization mass spectrometry and found weak relationship between anion affinity for the interfaces and its polarizability. From this investigation, the authors concluded that polarizability is not the factor driving the ions to the air-water interface and that it was just another missing force field component essential to perform any simulation for ions at water surfaces.

Stairs [120] calculated the surface tension of electrolyte solutions by adding ion-induced dipole terms in Onsager-Samaras equation and inferred the need for additional force presence while observing the change in the surface tension of electrolyte. A few years later Ninham and Yaminsky [104] calculated this additional missing term as the dispersion forces (or interaction). However, they also stated that it will be crude to assume that the dispersion interaction describes the whole story of electrolytes at the air-water interface and other parameters still need to be considered. Later, Ninham and coworkers [121, 122] performed further calculations by including dispersion interactions and various physical parameters to mimic the surface tension results and found that the solvation energy of ions are one of the important parameter for determining the ion specificity. In a systematic computational study, Horinek and Netz [123-125] optimized different ionic parameters to gain a close to accepted experimental bulk solvation energy values of ions and used the hydrophobic solvation of ions as the theory to explain ionic affinity at the water surface. This theory defines that the solvation-free energy of a hard-charged cavity of radius ‘R’ is proportional to the formation of a void of similar cavity volume. They were able to correctly predict the STI trend of inorganic electrolytes at the air-water interface following this theory and by applying a rigorous parametrization using various bulk parameters of ions [126]. This theory shows a resemblance to the cavitation energy

theory for ionic adsorption at the air-water interface and has similarity to Ninham and co-workers' observations with the solvation energy of ions.

Another interaction to consider for adsorption of ions at the vapour-solvent interfaces is the solvent molecular orientations. This consideration results from the understanding that the surface potential of electrolyte solutions also shows SIE [127] and has been reported as one of the important driving parameters for ionic adsorption at the air-water interface [128]. Since the surface potential of a solvent is a measure of its average molecular orientation at the interface [129], it is expected that the unique electrical properties of a solvent interface will have a strong manifestation on ionic organization through the change in dipole moment of ions and solvent. Further, surface potential is also suggested to control the mechanism of bubble coalescence inhibition (a naturally occurring interfacial phenomenon) [130]. Bubble coalescence is influenced by the electrolytes and follows the specific anion and cation combining rules developed by Craig and co-workers [8-10, 42]. Various other parameters that are suggested to play important roles for presence of ions at the vapour-water interface are dehydration energy [131], capillary waves [118], enthalpic contributions through change in solvation of ions at the interface [132], and asymmetric solvation of ions [114]. Overall, this list shows that considerable developments have been made to understand the fundaments of ion specificity at the vapour-solvent interface but the correct driving parameter(s) for specific ionic adsorption at the vapour-solvent interfaces is not yet determined.

1.5.3. Surface Sensitive Techniques to Measure SIE and their Investigations

Few techniques that can determine quantitatively the presence of ions at electrolyte solution surfaces and their interaction with solvent molecules: electron spectroscopy (X-ray photoelectron spectroscopy (XPS) and metastable induced electron spectroscopy (MIES)), X-ray & Neutron reflectivity (XR and NR), Neutral impact collision ion scattering spectroscopy (NICISS), Molecular beam scattering experiments, non-linear optical (NLO) techniques, surface tension, and surface potentials measurements. XPS provides quantitative depth information within a range of a few nanometers (nm) that depends on the change in the inelastic electron mean free path of an x-ray beam in a solvent which leads to varying electron emission [133]. NR and XR can be used to determine concentration depth profile by measuring refractive index change respective of probing depth in a solution, but simple inorganic ions do not produce high enough contrast in electron density in a solution. Hence, the lack of studies for simple inorganic electrolyte solutions using these techniques. MIES determines the composition of the outermost layer through the de-excitation of metastable helium atoms (He*) at the surface. The technique applied in the current thesis is called neutral impact collision ion scattering spectroscopy (NICISS) which measures the direct concentration depth profile

of solutions by converting energy loss experienced by a neutral ion beam while passing and getting backscattered through a matter. NICISS can measure concentration depth profile with a depth resolution of ~ 2Å and only a small uncertainty is present with NICISS measurement which is associated with the depth scale calibration. Further description of the NICISS technique is included in Chapter 2.

At the surface of an electrolyte solution, the Gibbs isotherm relates to increasing surface tension values of an electrolyte solution as a depletion of the ions from the interface (if electrolytes are treated as a binary system) [134]. However, separate ion contributions are essential to understand ion-specific adsorption, and it is impossible to directly infer these from surface tension measurements (which reflect the influence of both cation and anion). Pegram and Record [135-137] have utilized surface tension data to determine single ionic partition coefficients (Kp) at the water-vapour interface (relative to Na_2SO_4 at 0). These coefficients show similarity to the reported Hofmeister series (Figure 1-5). This similarity meant that presence of ions at the air-water interface and their binding with the surface of protein follow a similar thermodynamic mechanism. Dehydration (desolvation) of an ion was proposed as the thermodynamic mechanism where an ion has to lose water molecules out of its shell to partition to the air-water interface or protein interface. However, the SPM assumes that the anion-cation interactions are absent by considering that the anion and cation effect on STI is additive. This assumption further requires that the contribution of an arbitrary ion is assumed constant and assigned a reference value.

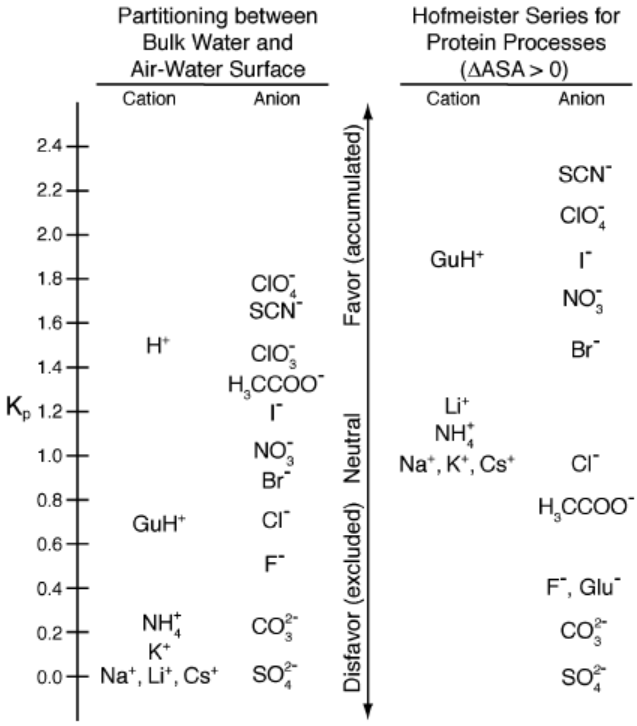

Figure 1-5: Ordering of ionic partition coefficient at air-water interfaces from bulk water obtained from solute partition model. The original Hofmeister series for protein processes is shown for reference which show similarity to the series of ionic partition at the air-water interface. Reproduced with permission from ref[136].

XPS investigations performed by Hemminger and co-workers have contributed largely to this topic and evidenced the enhanced concentration of I^-, Br^- [138], and depleted concentration of F^- at the surfaces of aqueous solutions hence finding a specific ion order for a surface propensity for anions as $I^- > Br^- > F^-$ [139]. From another investigation with LiI & KI salts [140] in water. Hemminger and co-workers measured a higher cation/oxygen concentration ratio at the surface of LiI solutions than for KI solutions suggesting a specific cation effect for the surface propensity of cation in the order of $Li^+ > K^{+\cdot}$ Sloutskin et al. XRR studies [141] with RbBr in water showed depletion of bromide ions from water's interface in contrast with Hemminger and co-workers [142] XPS results. This conflict was addressed by Hemminger and co-workers as an incompatibility of fitting model selection during the conversion of XRR data which can be challenging for simple inorganic ions due to their small electron density yield in an electrolyte solution. Kempter & co-workers [143, 144] investigated CsF, CsI & NaI salts on amorphous solid water (ASW) and amorphous solid methanol (ASM) surfaces using MIES. Their results displayed the presence of iodide ions at the surface of ASW for CsI and NaI salts while for ASM surface segregation of iodide ions was absent. Cs^+ was found to be depleted from the surfaces of ASW & ASM for CsI salt and F^- of CsF salt was depleted together with Cs^+ at the surface of ASW.

Molecular beam scattering experiments [145-147] investigate the varying effect of ions towards reaction pathways of deuterated hydrochloric acid (DCL) molecules at salty glycerol surfaces. From these experiments, one can indirectly make conclusions regarding the presence of ions in the surface region of a solvent since the reaction pathways of DCL molecules are influenced depending on the presence of ions nearby solution surfaces. Nathanson and co-workers [146, 148] have performed molecular beam experiments to study the influence of electrolytes on the reaction pathways of DCL at the surface of glycerol. They found that the presence of LiI, NaI, KI and NaBr in glycerol solutions had a similar effect on reaction pathways of DCL and suggested that these observations arise from ion-counterion and ion-solvent interactions.

Non-linear optical methods focus on measuring the change in vibrational intensities of species like -OH, CH_2 and CH_3 in the non-centrosymmetric region of any solvent which allows gaining interaction of the ions with the solvent molecules at the interface [149]. The techniques used are sum frequency generation (SFG) and second harmonic generation (SHG). Allen & co-workers have employed SFG spectroscopy extensively for studies related to the propensity of ions to adsorb at surfaces by interpreting the effect ions have towards the surface hydrogen-bonded network of an aqueous solution. They suggested an order of $I^- > Br^- > Cl^- > F^-$ for anions with common cation [150] and $Li^+ = Na^+ > NH_4^+ > K^+$ for cations with common anion [151] in an aqueous solution. Furthermore, Allen & co-workers also investigated the propensity of iodide and bromide ions in salty glycerol solutions and concluded that I^- has a larger degree of disturbance than Br^- towards the surface glycerol molecules due to their differences in ionic sizes & polarizabilities [152]. Employing SFG, Richmond & Raymond [153] showed that halide ions perturbation towards surface hydrogen-bonded network is consistent with structure making the effect of F^- and structure breaking effect of I, Br^- & Cl^-. Hong-Fei Wang & coworkers [154] [155] observed specific cation effects between NaF and KF aqueous solutions suggesting that Na^+ cations act as a structure breaker while K^+ cations possess structure-making properties depending on the direction these salts orient the surface -OH molecules of aqueous solutions (i.e. towards surface normal or away from the surface normal). Peterson et al.[156] also found specific ion trends within sodium and potassium electrolyte solutions using SHG spectroscopy from the change in nonresonant water background intensity at surfaces of electrolyte solution. The specific ion series observed in the SHG investigation was $I^- > Br^- > Cl^-$ between sodium salts and $I^- > Br^- > Cl^- > F^-$ for potassium salts.

There have been reports of direct concentration measurements of ions at the shallow depths (average probing depth being 4-6 Å [157]) of electrolyte solution surfaces using variants of SHG and SFG spectroscopy. Peterson et al. measured and confirmed the enhanced concentration of azide, thiocyanate, iodide and ferrocyanide anions at the surface of the water

from (charge transfer to solvent) CTTS transition of anions in the UV region by employing femtosecond SHG spectroscopy [158-161]. However, separating an anion's resonant signal from the water background signal was difficult for Br^-, Cl^- & F^- in UV-SHG spectroscopy due to weaker resonant responses produced by these anions [156], therefore no direct conclusions for specific ion effects between simple inorganic ions were made in the mentioned investigation. Recently, Piatkowski et al [162] employed time-resolved SFG spectroscopy to quantify I^- and Cl^- anions concentration by measuring the resonant vibrational energy transfer rate between D_2O molecules and anions. From this investigation, they quantified that I^- and Cl^- concentration is 3.5 and 1.8 times higher respectively at the surface compared to the bulk of the D_2O solution (averaged over the SFG probing depth of ~6 Å estimated using MD simulation [157]). This result reveals a high surface propensity for large polarizable iodide anion compared to the smaller less polarizable chloride anion.

Surface potential measurements provide indirect information for the organization and average orientation of water molecule (or solvent molecule) dipoles at the interface. In terms of electrolyte solutions, Frumkin [163] made the first notable observation that electrolytes cause a change in the relative surface potential of water which was further supported by Randles measurements [164]. At that time, investigated electrolyte solutions only showed a negative increase in the relative surface potential which was interpreted as a higher presence of anions at water surfaces leading to negative surface potential. Randles [164] provided a correlation between the magnitude of surface potential and differences between anion and cation's "real" hydration energy which later showed poor quantitative correlation with experimental results. So far collected dataset for surface potential change in aqueous electrolyte solutions suggests an agreeable SIE trend compared to the Hofmeister series as [127, 164]:

$$SO_4^{2-} > CO_3^{2-} > Cl^- > Br^- > NO_3^- > I^- > SCN^- > ClO_4^-$$

$$K^+ = NH_4^+ > Na^+ > Li^+$$

Here, the “>” implies more positive surface potential. However, surface potential measurements often lead to different results for the same investigated system. Jarvis and Schemin [165] reported differences in Na_2SO_4 electrolyte solution surface potential value of +30 mv compared to Frumkin. Their observation meant that the surface potential was not primarily related to anion’s presence at water surfaces because a positive relative surface potential means cations were more abundant at water surfaces. Due to these debated results and interpretation surface potential measurements have not been largely investigated for electrolytes in non-aqueous solvent.

Table 1-1: Advanced surface-sensitive experimental techniques available to investigate ionic presence at vapour-liquid interfaces.

Experimental Techniques	Probing depth	Information obtained
X-ray Photoelectron spectroscopy (XPS)	Dependent upon Inelastic mean free path of electrons (IMFP) [166]. 20 – 80 Å for the primary kinetic energy of 200 - 1000 KeV	Measures surface concentration of elements present in the system through emitted photoelectron signal. Requires high-energy X-ray sources and measurements can only be performed in UHV conditions hence requires special setup. The concentration depth profile can be obtained from angle-resolved XPS measurements[167].
Metastable Induced Electron Spectroscopy (MIES)[168]	Few angstroms (topmost layer)	Measure the surface composition through deexcitation of metastable Helium atoms (He^*) at the surface. Only probes elements are present in the outermost layers and require special setup as MIES measurements are done under UHV conditions
Neutral Impact Collision Ion Scattering Spectroscopy (NICISS)[169]	2 – 300 Å (depends on primary energy 1- 10 KeV) with a resolution of ~2 Å [170]	Measures Concentration depth profiles of elements through energy loss experienced by He neutrals backscattering through the matter. The high-Vacuum conditions requirement is a limitation. Water as a solvent can be measured but requires a special setup. Harder to measure lighter elements present in lower concentrations.
Non- Linear Optical (NLO) techniques (Sum frequency generation (SFG) and Second harmonic generation (SHG) spectroscopies)[171]	MD simulations suggest a probing depth of 4- 6 Å [157]. However, probing depth for NLO techniques depends on the non-centrosymmetric region nearby the vapour-liquid interface which differs between systems.	Measures the change in non-centrosymmetric signals present at the vapour-liquid interface formed due to the interfacial asymmetry. Provides important specific ion interactions present at the vapour-liquid interface. Indirectly measures the presence of ions at the vapour-liquid interface. Provides information on net ion contribution.
Charge transfer to the solvent- UV-SHG (CTTS-UV-SHG)[158]	Expected to be 4- 6 Å [157].	Measures ion's charge transfer to the solvent which exhibits a large non-linear cross-section that can be separated from the solvent's non-resonant contribution [129]. This separated contribution is fitted to an adsorption model to obtain Gibb's surface free energy of adsorption [159]. Separating the contribution of ions from the solvent's non-resonant contribution is harder for simple halides, especially in an intermediate concentration regime (0.1 M to 2 moles/litres) [156].

1.6. Significance of Non-aqueous Solvents – Interfacial Point of View

Non-aqueous solvents have broad significance that warrants a detailed understanding of electrolyte behaviour, especially at the interface. Solvents like glycerol and dimethyl sulfoxide (DMSO) are used for cryopreservation, the process of storing (or preserving) biological samples like cells and blood at low temperature [172]. Cryopreservation is performed by adding solvents (commonly DMSO and glycerol) to the biological media to limit ice formation which is lethal for cells and tissues. Such addition depicts the interfacial interactions hence gaining information on interfacial phenomena is of strong interest [173]. Glycerol is also used as a proxy solvent for water in vacuum-based techniques to investigate various interfacial atmospheric chemical reactions [40]. Alcohol-based spirits are a popular beverage, especially during this pandemic. The taste of these spirits is known to be enhanced upon dilution of water and guaiacol, where such behaviour of guaiacol is related to its interfacial propensity [174]. Non-aqueous solvents like propylene carbonate (PC) and ethylene carbonate (EC) are used in the batteries industry for the development of alkali -ion batteries [92, 175, 176]. The interaction of these application-relevant electrolyte solutions with an electrode is an interfacial phenomenon. Hence, fundamentals of ionic adsorption at PC and EC surfaces are of significant interest.

Formamide (FA) is considered one of the important prebiotic compounds over water as it is known that water is hazardous towards the cornerstone molecules of life i.e., DNA, RNA, and nucleic acids [177]. For instance, the synthesis of biomolecules requires the release of water, meaning the presence of water within the biomolecules is not thermodynamically favourable. Whereas in formamide with ionic compositions of clays and metal oxides in a heated environment (through wet and dry cycle present during prebiotic earth) single-step synthesis of building blocks of RNA, DNA, nucleic acids, and carboxylic acids is possible [178-182]. Although at one-point, prebiotic molecules must have evolved to tolerate water, considering in the current period, life cannot sustain without water. The transfer of prebiotic molecules (taking protein as a test case) from FA to water must have been an interfacial phenomenon where ionic presence seems sensible. Therefore, the understanding of ionic behaviour at non-aqueous solvents surfaces are of great applicability and of fundamental interest.

1.7. Aim and Outline of this Thesis

SIE is ubiquitous and the strength of the SIE of different anions and cations often follow the same order or series, such as the Hofmeister series and the lyotropic series (Figure 1-1). However, it is known that the ubiquity of SIE changes with the solvent (section 1.4) [72], counter-ion [68], temperature [183], concentration [184], surface wettability [184], and even the surface charge can reverse its order [185]. In addition, involvement of many different surface and solution properties also influence the relative strengths that different ions exhibit [71]. Understanding of this variation in relative strengths of ions is still lacking with reasons that surface involvement increases the

complexity of ion specificity. A further complication in SIE investigation at the vapour-solvent interface is that most experiments probing the interface give a net result of all the ions, where it is desirable to understand the contribution of the individual ions. A good example of the importance of this is the surface tension of aqueous electrolytes and observation made by Pegram and Record [135, 136] as mentioned in Section 1.5.3. Thus, employing techniques that identify the individual ions and map their concentration as a function of distance from the interface is advantageous. Hence, this thesis aims to employ NICISS to systematically investigate the ion specificity in ionic distribution at one of the simplest interfaces i.e., vapour-solvent interface and gain understanding of the following questions:

Q1 Where do ions remain in electrolyte solutions i.e., partitioned in the bulk or accumulated at the interface and does it change for every ionic combination (anion and cation), protic solvents, and aprotic solvents?

Q2 Does this depletion or accumulation follows a specific ion series and how does counter-ion, anion-cation interaction influence this ionic presence/absence?

Q3 What influences this ionic specificity at various solvent surfaces?

NICISS technique which is used to answer these research questions is discussed in the Chapter 2 with other complementary techniques employed throughout this thesis. In Chapters 3 and 4, a large set of electrolytes at glycerol and formamide surfaces are investigated and varying specific ion series is observed. In these chapters, the direct experimental result of anion and cation organization at the vapor-solvent interfaces are also reported. Further, with the large collection of electrolytes investigated, the complexity of ion specificity at the non-aqueous solvent surfaces due to the counter-ion effect and anion-cation interactions is presented. In Chapter 5 with the limited electrolyte set investigated, the role of the solvent nature (protic or aprotic nature) towards ion specificity at solvent surfaces is investigated. Finally, in Chapter 6, all the observations of this thesis are summarized and discussed against the existing theories/hypotheses and the hypothesis discussed in this thesis to understand the ion specificity at solvent surfaces

CHAPTER 2 : EXPERIMENTAL TECHNIQUES AND SAMPLE PREPARATION

Sections 2.1.2, 2.1.4, 2.1.5, 2.1.6 of this chapter are reformatted and edited versions of a manuscript for a journal article published in a peer-reviewed journal. See the Contextual Statement section for details on the contribution of the co-author to the published version of the manuscript.

Reference for the published version:

Kumar, A., Craig, V.S., Page, A.J., Webber, G.B., Wanless, E.J. and Andersson, G., 2022. Ion specificity in the measured concentration depth profile of ions at the Vapour-Glycerol interface. Journal of Colloid and Interface Science, 626, pp.687-699.

2.1. Neutral Impact Collision Ion Scattering Spectroscopy (NICISS):

2.1.1. Introduction:

Ion scattering spectroscopy (ISS) is a surface-sensitive technique to obtain structural and compositional information about the sample. This information results from the interaction of projectiles with the target through charge transfer processes, elastic, and inelastic kinetic energy transfer, backscattering from target atoms, sputtering of atoms, blocking, and shadowing of the projectiles [186]. Since the development of ISS by Smith in 1967, numerous ion scattering techniques were developed with advantages and disadvantages relevant to the choice of investigation [187]. A few of these ion scattering techniques currently in use to explore crystalline and non-crystalline matter are low energy ion scattering spectroscopy (LEISS), impact collision ion scattering spectroscopy (ICISS), Rutherford backscattering spectroscopy (RBS) & neutral impact collision ion scattering spectroscopy (NICISS).

LEISS provides information for outermost layer composition exclusively of a solid sample but is not widely used for liquid samples. ICISS investigates the elemental composition of the outermost layer and ordering of crystalline structure by utilizing the shadowing and blocking effect of any rare gas ion beam but limits to investigating only the outermost layer of a sample. RBS is a versatile ion scattering technique introduced to study crystalline & non-crystalline matter, but the employment of high kinetic energy (few MeV range) ionic projectiles to obtain concentration depth profile information creates the limitation of not being able to probe lighter elements like carbon and oxygen. Based on a similar principle of RBS, Niehus and Comsa [188] developed NICISS, and later Andersson and Morgner modified it to study soft matters [169] which is the interest of this thesis. NICISS obtains concentration depth profile information for soft matters (liquid surfaces, polymers, foam films) & crystalline surfaces while being able to characterize lighter elements.

2.1.2. NICISS as Method

In a NICISS experiment, a sample is bombarded with a pulsed inert gas ion beam (usually He^+) with a kinetic energy of a few keV. The time-of-flight (TOF) of the neutral projectiles backscattered from the atoms forming the sample is measured. During the backscattering process, the He projectiles undergo energy losses which are converted into concentration depth profile (CDP). There are two types of energy loss processes during the backscattering of projectiles in a NICISS measurement:

1) Backscattering of neutral projectiles resulting from a single head-on collision with the atoms forming the sample. From this energy loss, the identity of the atom from which the projectile was backscattered is determined.

2) Many small-angle collisions and electronic excitations of the projectile during its trajectory through the sample, can be treated as a continuous energy loss (stopping power). This energy loss allows the determination of the depth from which a projectile is backscattered.

The combination of both types of energy loss yields a direct measurement of the CDP of a sample with a depth resolution of ~ 2 Å in the near-surface region and with a probing depth range of ~ 100 - 300 Å depending on the kinetic energy of the He projectile. The first type of energy loss includes an inelastic energy loss during backscattering [189] which requires gas phase calibration. Regarding the second type of energy loss, the stopping power at low kinetic energies in the organic matter has been measured by Andersson and Morgner previously [189].

The charge transfer process between noble gas ions (especially for noble gas ions with kinetic energy <10 KeV) and target atoms happens within a distance of a few Å between the target atom and the projectile [190, 191]. The overall process is described as a sequence of several charge transfer processes [190, 191]. Due to the high excitation energy of noble gas ions, the projectile is mostly in a neutral state and is independent of the initial charge state of the projectile [190, 191]. This continuous charge transfer process is part of the inelastic energy loss. It should also be noted that the finite gradient of the onset of the concentration depth profiles is not due to the density gradient at the liquid surface but due to the energy resolution of the method. NICISS as such is not sensitive to density gradients because the stopping power is proportional to the density.

The intensity of the count rate related to a specific element is determined by its cross-section for the backscattering of the projectile. The cross-section depends on the atomic mass of the atom from which the He^0 projectile is backscattered and increases with the mass of the target atom. NICISS is usually applied to non-crystalline samples because samples showing a degree of ordering require separate consideration of the influence of the order in the sample on the measurement [189].

Helium is the selected rare gas for experiments in this thesis since the leading interest is to unravel elemental concentration depth profiles of lighter elements like carbon, nitrogen, oxygen, chlorine, etc. present in the sample. Ion beam generated with heavier rare gases creates limitation of sputtering lighter elements. Such limitation occurs as the backscattering of ions only results from

elements heavier than the gas used to generate the ion beam. This becomes a limitation in the case of ion beams of neon and argon gases. Also, heavier gases produce large-sputtered hydrogen background which diminishes the peaks for elements of interest. However, heavier rare gases ion beam can differentiate peaks for two elements very close of similar atomic masses like chlorine and phosphorous whose TOF spectrum overlaps when investigated with the He ion beam [192].

2.1.3. NICISS Setup:

A custom-made NICISS setup constitutes of vacuum chambers, a Wien filter controller, and two manipulator units purchased from Specs prodigy, Germany; and a model 1403-10 ion gun purchased from Nonsequitar technologies, USA. Commercially available Chevron multi-channel plate detectors are used for neutral detection. The deflection units and their controller were constructed in the workshops at Flinders University following the schematic used by Andersson [193]. The main components present in the ion gun are two thorium-coated tungsten filaments, a leak valve, an extractor lens, a condenser lens, a bend lens, a focus lens, two deflection plates as a part of an electrostatic deflection unit and Wien filter components. Helium gas is introduced into the ionization chamber where gas molecules pass through the grid cylinder (anode) and get ionized by the electron collision resulting from the potential applied to the filaments. A single-lens electrode called an extractor collects these ionized gas molecules and focuses them into an ion beam using the electromagnetic extractor lens. The extractor lens pushes the ions beam towards a condenser lens. Both lenses together work as a double lens system that forces this focused ion beam towards its defined trajectory. A focused ion beam passes through the Wien mass filter and assembly of 3 electrostatic lenses which filter out ionic impurities, i.e., charged ions, ions of unwanted isotopes, and astigmatism of ions beam to produce a well-purified and defined ion beam.

Before the ion beam reaches the sample, it is chopped into the small, pulsed beam of 4 ns width using x and y electrostatic deflector plates set to cause a time delay for the arrival of the beam onto the sample. The essential operation of these plates can be explained as a rectangular box consisting of one aperture (or hole) at one of the sides to let the ion beam pass through it. When the ion beam passes through the aperture, it is chopped off after a few ns while x and y deflector plates follow a rectangular path of time delay until reaching the aperture again and letting the ion beam passing through. This process keeps repeating and creates a pulsed focused ion beam for NICISS measurements. A commercially available powdered fluorescent sample (composition unknown) is used to observe and optimize the focus and centring of the beam spot for NICISS measurement. An ion beam is observed by introducing a prepared fluorescent sample spread over copper tape attached to the solid or liquid sample holders. To observe the ion beam, the electrostatic deflection unit is switched off as time delays and deflection setting makes it impossible to observe the ion beam. The beam is optimized for NICISS measurement by adjusting the voltages of each lens in a trial-and-error fashion to produce the best beam spot possible with a reasonable ion beam current.

2.1.4. NICISS Measurements:

NICISS measurements of solid, liquid, and gaseous samples are performed using different targets. For solid sample measurements, an 18x15 mm metal plate with a small metal tip is used (for handling using the solid sample loading arm). This target is introduced onto a solid manipulator that has filaments, a temperature sensor and copper wires attached to allow heating, temperature, and ion beam current observations during measurement. Solid samples on a substrate (or directly to the sample holder) can be attached using screws or copper tape depending on the nature of the solid sample.

The sample holder for the liquid surface measurement is the same as used in previous NICISS investigations [194, 195]. This sample holder setup "Rotating disk method" as shown in Figure 2-1 is commonly used for preparing the liquid-vapour interface inside the vacuum chamber for extended reaction time (> seconds) [167]. Solutions were added to the stainless-steel reservoir of the sample holder and introduced into the vacuum chamber of the NICISS equipment. In a general operation, a metal disc is half immersed into the reservoir filled with the liquid and rotated at a set speed to continuously form a fresh liquid layer on the disc. A metal scraper is fixed a few hundred microns from the disc to assist in the formation of a continuously refreshed liquid layer over the rotating disc. A small aperture is present in front of the rotating metal disc where the ion beam is focused to probe the liquid samples. An enclosed container is used to create a saturation of vapour pressure inside the cell compared to the analysis chamber, hence achieving minimal liquid loss due to evaporation. The liquid sample target also contains a PT100 temperature sensor and a level sensor to monitor the amount of liquid inside the reservoir. A metallic wire can also be attached slightly grazing the top of the metal disc for ion beam current measurements.

The gas-phase sample outlet is a metal tubing attached inside the liquid manipulator stage with a gate valve connected at the top of the liquid manipulator (outside the vacuum chamber) to control the gas flow. At the end of the gas-phase outlet (inside liquid load lock), a metal nozzle (Figure 2-1) is attached with a ~1 mm outer diameter tip to restrict the continuous gas flow to form a gaseous cone angle for the gas phase measurements. The ion beam is focused at the end of the nozzle tip while grazing a small part of the metal so that the measurement proceeds at the point of the smallest cone angled formed by the gas ejection. The tip is positioned at the end of the gas phase outlet such that the gas phase flow is above the liquid phase, as close as possible.

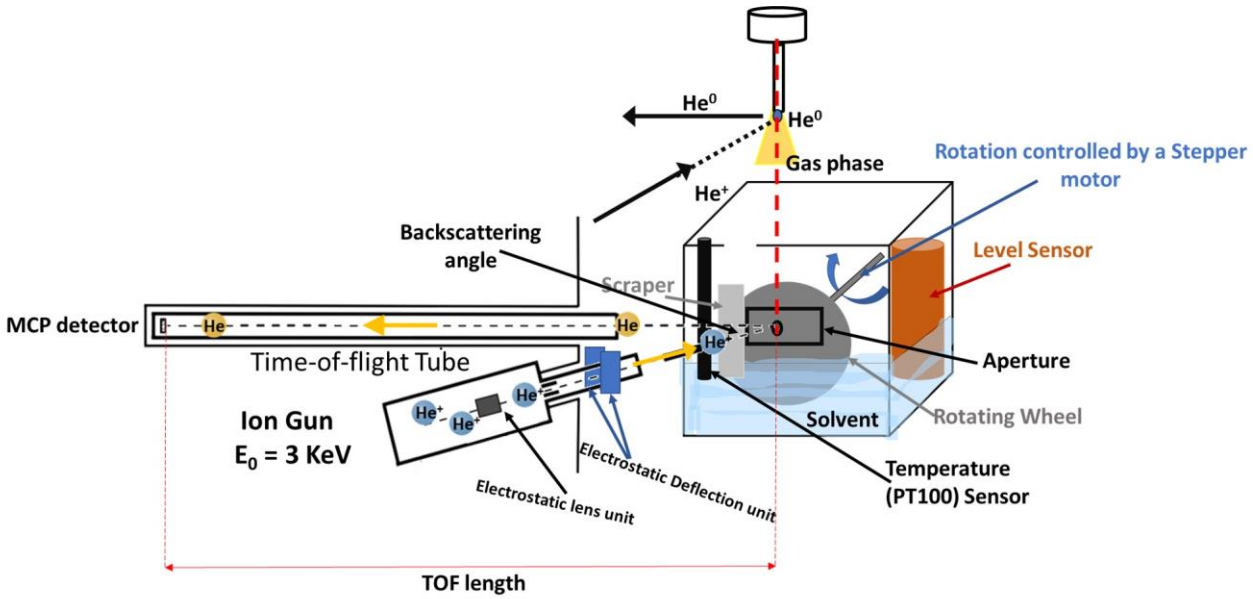

Figure 2-1: Schematics for NICISS sample holder setup for gas phase (top figure) and liquid phase measurement (bottom figure). The gas phase tip is placed such that the position of the gas phase cone lies over the similar position of the liquid sample on the rotating metal wheel. The size of the sample holders and NICISS ion gun set up is not up to scale and presented for illustrative purpose.

The location of the gas phase tip (sample holder) is determined by moving the manipulator arm horizontally and/or vertically towards the ion beam. When a projectile is backscattered from the metal part, the count rate on the detector will be high relative to a normal liquid, gaseous or organic sample. If the beam is too far from the gaseous phase, no counts will be observed. Hence, by moving the manipulator arm and monitoring the counts received on the detector, position of the gas phase tip is calibrated. The width of a cone made by the gas flow can be measured similarly by monitoring the count rate while moving the liquid manipulator stage horizontally and plotting a count rate vs position plot. If the gas phase of an element is not dilute enough (represents a monolayer of the element), the full-width half at maximum (FWHM) of the Gaussian curve will be broad and the centre of the gaussian curve will be shifted. Hence, a dilute gas phase suitable for calibration is selected by performing the gas phase measurements at various NICISS analysis chamber pressure until the FWHM and centre of the gas phase Gaussian curve become constant.

2.1.5. TOF Spectrum and Depth Profile Interpretation

The TOF spectrum of 3 keV He atoms backscattered from 1 m KI glycerol solution is shown in Figure 2-2 and shows the usual features found in a NICISS spectrum. The TOF length for projectiles backscattering to the MCP detector is 1.34 m. The feature at the lowest TOF is a photon peak which results from the first interaction of the He^+ with the sample surface in the outermost layer. It is worth noting that the photon generation and the event of a backscattered neutral projectile are not statistically correlated because both the probability for the formation of a photon and the

backscattering of a projectile are small [190]. Next, we observe an iodine step at 3.78 µs. The TOF of elements is determined by the kinematics of collision described in equation 1 [191].

$$E_b = E_i \left\{ \frac{\cos\emptyset + \sqrt{M^2 - \sin^2\emptyset}}{1+M} \right\}^2 - Q_{in} \qquad (6)$$

where E_b is the kinetic energy of backscattered He projectiles, $E_i = 3\,\mathrm{keV}$ is the initial kinetic energy of the He ion beam, $\emptyset = 165.0°$ is the backscattering angle of the focused beam from the target and $M = m_{He} / m_t$ is the ratio between the mass of helium atoms (m_{He}) and the mass of the target atoms[b] (m_t). Q_{in} is the inelastic energy loss during the head-on collision leading to the excitation of electrons of the projectile or the target atom when the He projectile is backscattered from the target atom. It should also be noted that in a NICISS experiment Q_{in} usually is not measured directly. Q_{in} has to be calibrated because it depends on the energy of the projectile and the mass of the target atom. Thus, the depth scale is calibrated using an elemental gas-phase spectrum as described below. Following the I step, steps for K, O and C can be identified at 4.32 µs, 5.82 µs and 6.96 µs, respectively, calculated using equation 6.

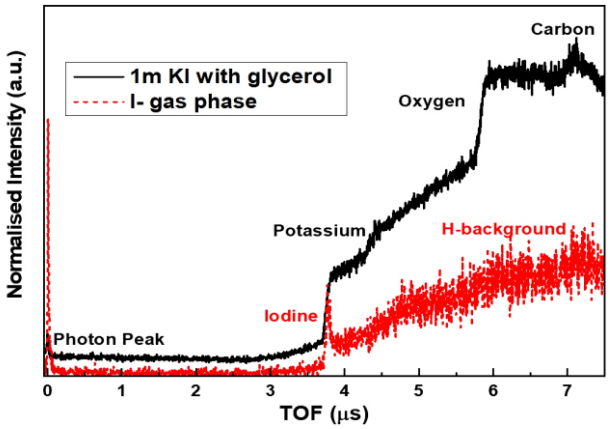

Figure 2-2: NICISS TOF spectrum of a 1 m KI glycerol solution (black) and diiodomethane gas phase (red) with 3 keV He projectiles. A vertical offset has been added to the KI glycerol solution spectrum for clarity. The I, K, O and C elemental TOF steps are labelled.

The second NICISS spectrum (red) shown in Figure 2-2 is from the gas phase of diiodomethane (CH_2I_2). This sharp peak results from He projectiles backscattered without any additional energy loss beyond the collision with iodine atoms. Therefore, the centre of this peak serves as a zero-depth calibration (or offset) for the iodine CDP. Similarly, bromoform ($CHBr_3$) and dichloromethane (CH_2Cl_2) gas-phase measurements are used to calibrate bromine and chlorine CDPs. The next feature in the TOF spectrum of KI glycerol solutions in Figure 2-2 is the potassium step. Unlike iodine, the zero-depth scale for potassium is not determined by measuring gas phase spectra due to the

[b] The TOF length and backscattering angle for formamide, propylene carbonate, and benzyl alcohol sets of measurement was 1.30 m and $\emptyset = 165.5°$ respectively.
This change was applied to install and align two TOF tubes to achieve higher backscattering signals.
This change does not influence the comparisons as all the compared profiles are calibrated with new gas phase measurements.

unavailability of gaseous compounds containing potassium atoms [195]. Here we have followed the procedure developed by Zhao et al. [195] who found that the energy for backscattering from a specific element in the outermost layer can be extrapolated from those of other elements provided that a range of gas phase measurements of other elements are available. Based on this procedure the uncertainty of backscattering energy for the projectiles from the outermost layer is larger than those determined from the gas phase spectra.

An elemental step in NICISS measurement is evaluated as a step function and the hydrogen background is removed by fitting a smooth linear polynomial curve to this step function as shown in Figure 2-3. Then the elemental step is converted into an energy loss scale as:

$$I(E) = I(t)\,\frac{dt}{dE}\,\frac{1}{(d\sigma/d\Omega)(E)}\,\frac{1}{\det(E)} \qquad (7)$$

Here I represents the spectrum counts, t is the TOF, E is the energy loss, $d\sigma/d\Omega$ is a differential cross-section factor of an element, and $\det(E)$ is the detector sensitivity. The energy loss is converted into the depth scale by calculating the events of energy loss of He neutrals for:

1) the incoming trajectory towards the sample, as (E_n^{in}) = E_{n-1}^{in} - D ×S
2) and the outgoing trajectory while leaving the sample, as (E_n^{out}) = E_{n-1}^{out} - D ×S. Here, E_n^{out} = $E_n^{in} \times E_b$.

Energy loss to depth scale conversion represents the recursive energy loss of He neutrals passing and backscattering through the parallel layers n of layer thickness D. Thus, the liquid layer is treated as parallel layers of $n, n-1, n-2, \ldots$ to calculate the projectiles energy loss. S is the average stopping power of He projectiles given as the energy loss per depth (eV Å^{-1}). The stopping power and the nonlinear empirical relationship of the stopping power with the increasing depth are taken as determined by Andersson and Morgner [189].

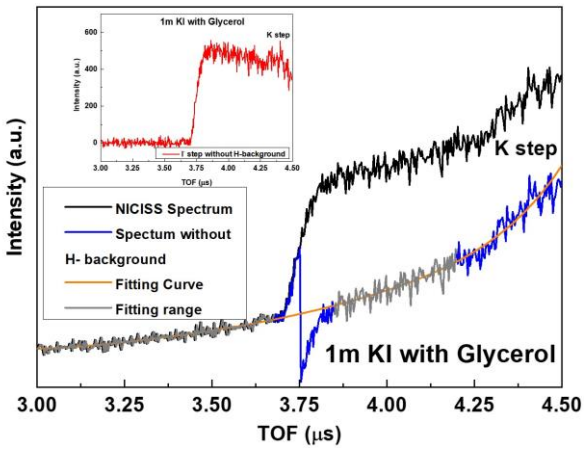

Figure 2-3: Background fitting of iodine step of 1m KI with glycerol solution. The inset shows the I$^-$ step after the removal of the hydrogen background using a step function.

For the CDP displayed in Figure 2-4, the uncertainty in the depth scale (horizontal error bars) arises from the determination of the timing/energy loss of the gas-phase peak and amounts to ± 1.7 Å. A comparison made between depth profiles calibrated using the same gas-phase spectrum will have the same offset due to the depth error for all profiles and therefore, for the sake of clarity, depth error bars are not included in the respective figures. Where the comparison has been made between the deconvoluted CDPs calibrated using different gas-phase spectra, error bars are included. These horizontal error bars are calculated based on each gas phase spectrum and averaged using an error propagation analysis procedure described in 2.1.8. Comparisons between the O and C profiles between measurements have been used to confirm that the experimental conditions are unchanged. A comparison of the O and C depth profiles of pure glycerol and a 1 m NaI glycerol solution demonstrates that the presence of the ions does not change the CDP of the solvent, see section 2.1.6.

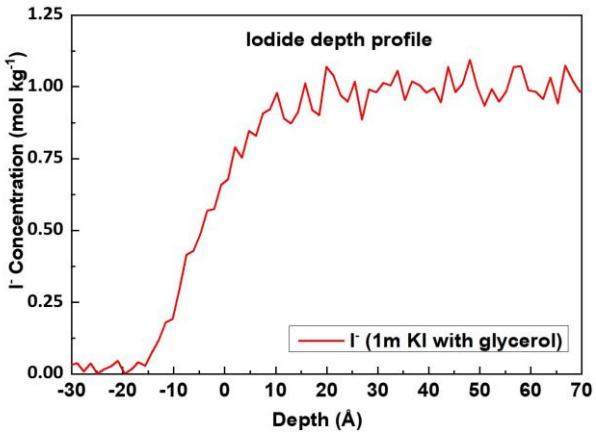

Figure 2-4: The raw I^- CDP (red) obtained after NICISS TOF to depth profile conversion of the iodine step of the 1 m KI with glycerol spectrum. The zero depth of the I^- depth profile is calibrated using the iodine gas phase measurement shown in Figure 2-2.

In NICISS measurements, the interface of a liquid appears as a sharp interface with a density profile that changes as a step function. With the scattering geometry detailed here, the interface is considered “laterally homogenous” [170, 196]. Moreover, the depth is derived from the energy loss that occurs at the first encounter of the projectile with the liquid surface. As such, NICISS measurement is not sensitive to capillary waves and the density profile of the sample (e.g., the solvent) is not a contributing factor to the measured NICISS profile. The reason is that the stopping power scales with the density of a sample which means that the density profile cannot be measured with NICISS [169]. This feature in the NICISS data does not affect the interpretation of the CDPs because the relative position along the depth scale is not affected by this effect.

2.1.6. NICISS Spectrum Feasibility Testing:

Comparison of the O, C and N (in the case of the formamide solutions) step between measurements of various solutions is used as a criterion for checking the spectra against any change in experimental conditions between measurements. In case the O steps of two measurements are the same, the

condition of the NICISS apparatus is considered the same within experimental uncertainties and the steps of other elements of the respective NICIS spectra can be compared directly. In case, the experimental conditions like the energy of the ion beam have changed by ± 5 eV (for 3 KeV primary energy) i.e., during the filament replacement process, then the shift in O, C and N of a set of measurements can be used to make the relative corrections.

Furthermore, while converting the TOF step into a depth profile the hydrogen background is removed by fitting the TOF step of an element with a polynomial curve (Figure 2-3). Hence to make a comparison between two different depth profiles, the background fitting constraints are also kept the same to avoid any artifacts arising during the background removal process. As shown in Figure 2-5 (a) and (b) the oxygen and carbon depth profile respectively of salty solutions overlap. Figure 2-5 shows that the experimental condition is the same hence comparison made between the concentration depth profiles of these solutions will be feasible.

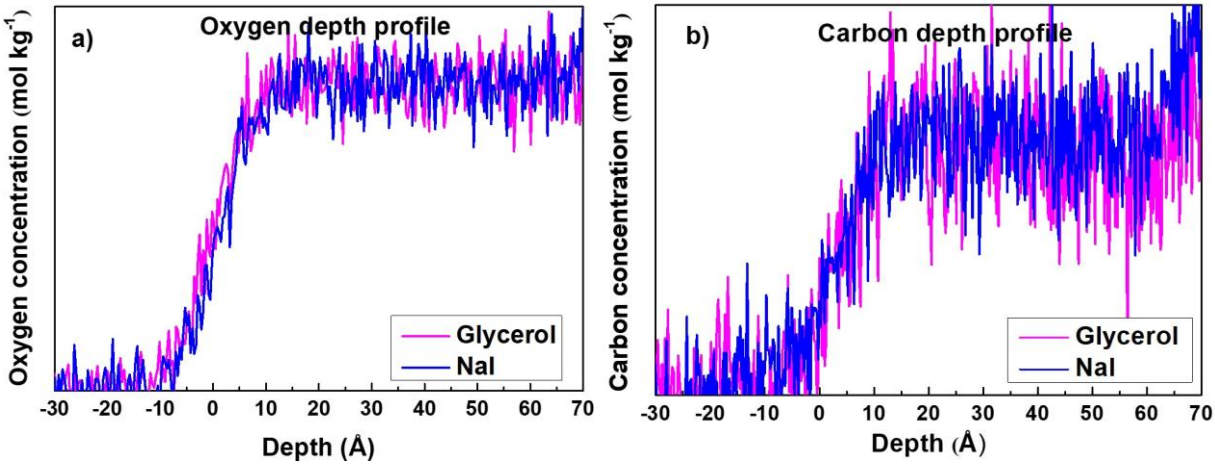

Figure 2-5: (a) Oxygen depth profile comparison between pure glycerol (pink) and 1 m NaI glycerol solution (blue), and (b) carbon depth profile comparison between pure glycerol (pink) and 1 m NaI glycerol solution (blue). This comparison shows that the onsets of the oxygen and carbon depth profiles of glycerol solutions overlap, which means that the experimental conditions are identical between these measurements. Hence a direct comparison between different measurements can be made within the experimental uncertainty.

2.1.7. Deconvolution of NICISS CDP

The I^- CDP shown in Figure 2-4 is the raw CDPs as measured by NICISS. These NICISS CDPs (raw CDP) show counts and a finite concentration at negative depths. As the liquid surface is a step function located at zero depth no ions or other materials are present at negative depths. Count rates at negative depth and the finite gradient at the onset of counts are due to two effects, namely 1) the inelastic energy loss distribution of He projectiles during backscattering and, 2) the finite energy resolution of the NICISS instrument. Both features are measured with a gas phase measurement. The distribution of inelastic energy losses during backscattering is the main contribution to the width

of the gas phase peak. The centre of the peak is used to calibrate (or offset) the zero of depth in a NICISS CDP and thus the spread in the gas phase peak leads to count rates (proportional to the concentration) at negative depth in a NICISS CDP as observed in Figure 2-4 (for further illustration, see Figure I-2 in Appendix Chapter I and Figure III-2 in Appendix Chapter III).

The measured NICISS CDPs can be deconvoluted using a genetic algorithm described previously [197]. In this genetic algorithm, the intensity of the deconvoluted profiles is considered a free parameter. These free parameters create a profile by selecting many sets of numbers between 0 to 1 generated using a random number generator. The profile generated from these free parameters is then convoluted with a Gaussian curve (determined from the elemental gas phase measurement) and compared with the steps of the NICISS spectrum. For these generated deconvoluted profiles there are two variable fitting parameters; one for the step gradient region and another for the bulk region which is used to constrain the fitting procedure after the removal of the gradient energy spread (gradient concentration onset below zero depth). In the deconvolution code, a certain range for selecting the best-fitted profile is also included. The mathematical error for the deconvoluted profile is the standard deviation of various best-fitting profiles generated from the genetic algorithm within the selected range. Further uncertainty arises from selecting the centre of a gas phase spectrum and the reproducibility of NICISS CDPs. Both uncertainties are accounted for within the error bars as standard error (see Section 2.1.8). All the NICISS CDP presented here are repeated typically a few months apart from the first electrolyte solution measurement and repetition is done with a freshly prepared electrolyte solution.

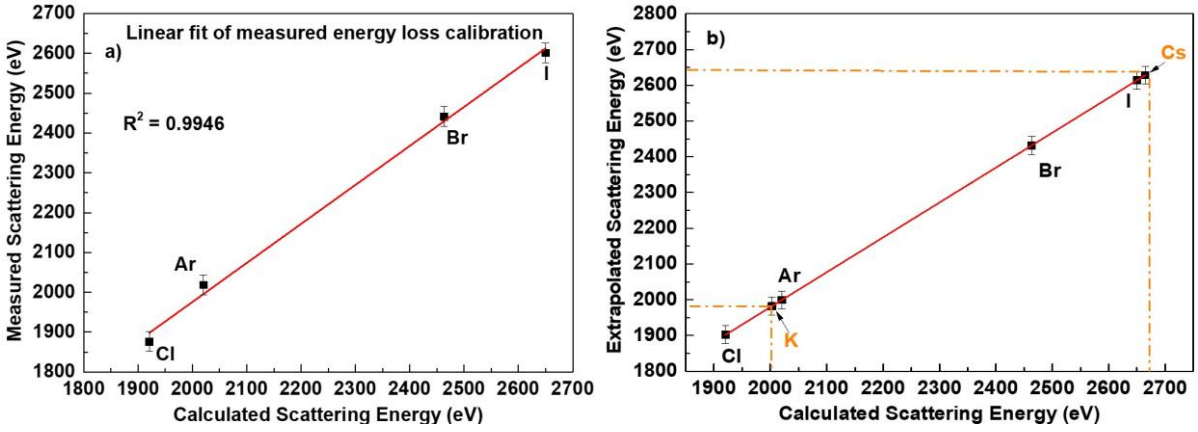

Figure 2-6: (a) Linear fit of calculated scattering energy and measured scattering energy of 3 keV He projectiles obtained using gas phase measurement of the elements following the procedure described by Zhao et al [195]. (b) Extrapolation/Interpolation of backscattering energy obtained using the equation of linear fit. The uncertainty associated with scattering energy calibration following this procedure is ± 25 eV. This is determined from the difference in scattering energy obtained using the linear fit equation and the measured gas phase scattering energy together with the standard error within the fitting of a Gaussian curve as discussed below in section 2.1.8.

For the deconvolutions, FWHM of the gas phase measurement is an input parameter. Na^+, K^+, and Cs^+ calibration by gas phase measurements were not possible. In these cases, the procedure to obtain the energy loss calibration is described in the earlier section 2.1.5 and shown in Figure 2-6. Therefore, for elements with no gas phase measurement, the FWHM of an element similar in mass is used, e.g., for K^+ the FWHM from the Cl^- gas phase measurement is used. This selection does not influence the deconvoluted CDPs in a significant manner since the difference between the FWHM of every elemental Gaussian curve (i.e., chlorine, bromine and, iodine) is significantly smaller than the uncertainty of scattering energy calibration (depth calibration).

In Figure 2-7, an average of all deconvolution solutions (200 repeated deconvolutions) for the I^- CDP is shown, and the vertical error bars represent the standard error between deconvolution results from two freshly prepared and measured sets of electrolyte solutions (in the present case for glycerol solutions) together with the mathematical error involved in the deconvolution procedure (Section 2.1.8). A deconvoluted profile provides us with a CDP in which no counts are present at negative depths. However, the deconvolution procedure also introduces unrealistic oscillations. For example, the oscillations present beyond 30 Å depth in the deconvoluted profile shown in Figure 2-7 are a result of a deconvolution procedure where oscillatory fits perform better than smooth fits, due to the extra mathematical degrees of freedom introduced when allowing oscillations. Hence, to avoid discussing features resulting from the artifacts arising from deconvolution, we point out that only the first maximum (Region 1 of Figure 2-7) and the following depletion region (Region 2 of Figure 2-7) are the features that are significant as they have been fitted with higher constraints. We assume that beyond these regions, the CDP of an ion is described by its bulk concentration in glycerol and all investigated solvents (observed in NICISS CDP in Figures I-4,5, and 6 in the Appendix chapter I). Also, from the comparison of deconvoluted CDPs, we conclude a significant difference between spectra only when the comparison of the NICISS CDPs shows similar differences in the spectra. It can also be interpreted based on the vertical error bars showing which features in a CDP are relevant and thus should be discussed. Region 1 and Region 2 are also referred to as "the interface" and “the surface” region at solvent surfaces respectively.

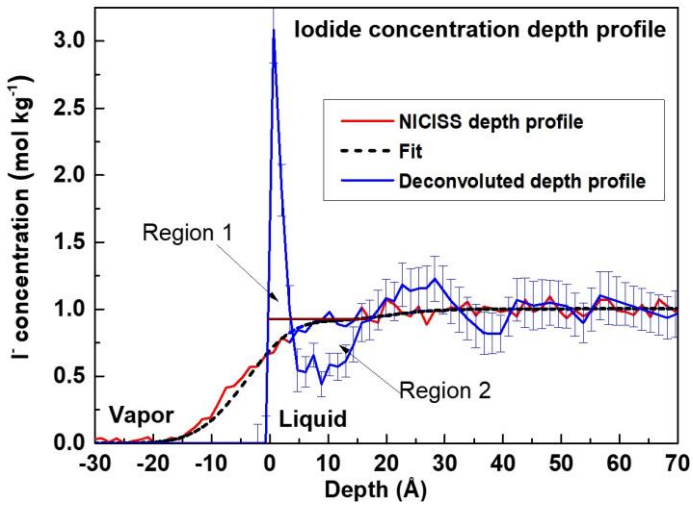

Figure 2-7: Deconvoluted CDP of I^- (blue) with its NICISS CDP (red) and fit for the deconvolution of CDP (dashed black line) for 1 m KI glycerol solutions. The error in the depth calibration of iodide CDP is ± 1.7 Å. In the current investigation, the first maximum peak (Region 1) and adjacent sub-surface depletion (Region 2) are of significant interest.

It is worth noting that the deconvolution procedure here is based on the experimental measurements because the deconvolution uses as input the shape of the respective gas phase spectra. A gas phase spectrum can be considered as a response of the experimental measurement procedure to a delta function with the delta function being represented by the dilute gas phase used as a target. The gas phase represents less than a monolayer of a sample thus energy losses due to stopping power are excluded.

2.1.8. NICISS Measurement Uncertainty Estimation

1. The error in the gas phase spectrum is a result of the uncertainty involved in statistically selecting the Gaussian centre of each gas-phase peak. Error bars are calculated in the following manner:
    a. A gas-phase spectrum is fitted using a Gaussian curve (see Figure I-2 in Appendix Chapter I (a) & (b)) and the centre of the Gaussian fit is determined.
    b. The peak centre is moved towards the positive or negative shoulder of the peak until the determined Gaussian fit is deemed unsuitable to fit the gas phase spectrum.
    c. This overall shift made without compromising the centre of the Gaussian fit corresponds to the error involved in the zero-depth calibration using a gas phase peak. On average, this value corresponds to ± 5 – 8 eV (~0.6 – 0.8 Å, depending on the element).
2. In the error bar calculation of a gas phase measurement, the uncertainty of correctly positioning the gas phase tip over the liquid sample is also accounted for. The uncertainty of positioning the tip is ± 1. 0 mm. This value corresponds to ± 5 eV in energy loss which is calculated from equation 1 by accounting for the wrong TOF value of ± 1. 0 mm.

a. NICISS photon peak observation is sensitive to such small variations in TOF length. Hence, it can be used to correctly align the gas phase tip setup. This uncertainty is only included in cases where the positioning of the tip cannot be corrected.

3. The overall uncertainty in a deconvoluted CDP comes from 1) gas phase measurement (for calibration of the depth profile), 2) reproducibility of the NICISS CDP and their deconvolution solutions, and 3) mathematical error for deconvolutions which is the standard deviation of various best fitting profiles generated from the genetic algorithm within the selected range. The latter two uncertainty combined present the error in the concentration of a CDP whereas the earlier uncertainty (vertical error bars) accounts for the error in depth (horizontal error bar).
4. For comparing spectra with multiple errors, an averaging procedure is followed. Errors are averaged using the standard error propagation, i.e., overall error = $(\sqrt{(a)^2 + (b)^2})$ where (a) and (b) are the error involved with 2 different gas phase spectra or two different components of errors.

2.2. Surface Tension Measurement:

Surface tension (γ) is defined as the surface energy per unit area that can be measured for solvents using various methods. In the current work, a pendent drop method is used. In zero gravity, a solvent will form a spherical drop to minimize its surface energy per unit area. However, in normal conditions gravitation and capillarity forces will influence the shape of a drop hanging from the capillary. This information underpins the surface tension measurement using the Pendent drop method. A pendant drop at equilibrium follows the Young-Laplace equation [198] relating to the Laplace pressure across the interface with a curvature of the interface and the surface (or interfacial) tension (γ):

$$\boldsymbol{\gamma}\left(\frac{\mathbf{1}}{\boldsymbol{R_1}}+\frac{\mathbf{1}}{\boldsymbol{R_2}}\right)=\Delta\boldsymbol{P_0}-\Delta\boldsymbol{\rho g z} \qquad (8)$$

Where z is the distance from an arbitrary reference place chosen at the end of the drop, g is the acceleration due to gravity, $\Delta\rho$ is the difference between the density of the liquid and the surrounding atmosphere. ΔP_0 is the reference pressure at $z = 0$ written as $\Delta P_0 = \Delta P + \Delta\rho g z$ and ΔP is the difference in Laplace pressure, in the drop and outside the drop.

Surface tension measurements were performed using PAT1 (Sinterface Technologies) pendent drop-based instrument at 20 ºC. The drop-shape analysis was done using the commercially available program used by Sinterface Technologies. For pendent drop measurement, the density of the solution is required as it defines the gravitational forces acting on the drop hence the shape of the drop. For pure solvent and the electrolyte solutions, the density values were measured at 20 ºC using density bottles (Pycnometers) which follow a linear trend with electrolyte concentration (see Figure 2-8 (a)). While performing surface tension measurements, the capillary was cleaned thoroughly

using a 10% NaOH solution followed by rinsing with ethanol and water multiple times and flushing with a water-ethanol-air cycle using the stepper motor to clean the pumping line.

Surface tension increment above the Jones-Ray concentration regime increase linearly with inorganic electrolyte concentration [134] (see Figure 2-8 (b)). Hence, by taking the gradient of this linear increase, we can extract surface excess information. However, the surface excess calculation is performed against the activity of an electrolyte in a solution which requires the activity coefficient information for an electrolyte. Activity coefficient information is scarcely available for solvents other than water therefore, surface excess data for inorganic electrolytes are not included in this work. The purpose of surface tension measurement is to provide complementary information for the NICISS CDP trends.

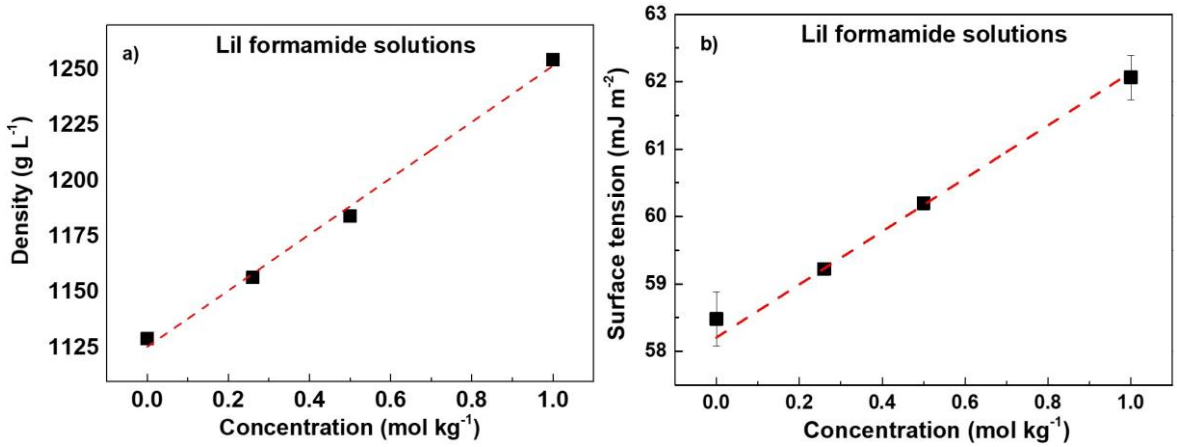

Figure 2-8: A linear trend for change in (a) density, and (b) surface tension with varying concentrations of LiI in formamide electrolyte solutions. Error bars are smaller than the data points in some cases.

For glycerol electrolyte solutions measurements, the solution was slowly sucked into a 3 mm outer diameter capillary and pushed slowly using a stepper motor-controlled pump to form a 30 µL solution drop. Time-dependent measurement was performed over the 5-second range with 0.5-sec intervals. A surface tension value of 63.0 ± 0.4 mJ m^{-2} was achieved for pure glycerol and set as a standard value to achieve before continuing with electrolyte solution measurement.

In the case of formamide electrolyte solutions, the solutions were filled (and pushed out) throughout the line (with tubing made of PTFE) using a stepper motor. The same drop volume as for glycerol electrolyte solutions was used. The surface tension of formamide was measured first and subsequent electrolyte solutions measurements were only performed if a surface tension of 58.5 ± 0.4 mJ m^{-2} was achieved. The surface tension of each drop was measured every 0.5 seconds for 20 seconds. The same protocols as formamide solutions were followed for propylene carbonate and benzyl alcohol solutions. For propylene carbonate solutions, the surface tension value achieved was 41.8 ± 0.2 mJ·m^{-2} and for benzyl alcohol, the surface tension value was measured as 40.0 ± 0.4 mJ·m^{-2}. Surface tension measurements of solutions were repeated 4 – 7 times with freshly formed drops and the standard deviation within the surface tension value of each drop acquired is taken as the uncertainty.

2.3. Fourier Transform Infrared (FTIR) Spectroscopy:

In FTIR spectroscopy a spectrum is obtained for liquid, solid and gaseous samples by absorbance of light at a specific wavelength which represents a unique vibration mode of a chemical bond or species. IR absorbance corresponds to the derivative of dipole moment over changing the bond length and the properties of different bonds with different dipole moment provides chemical-specific bonding information. In a more precise explanation, infrared spectra result from the transition between quantized vibrational energy states ranging from a simple coupled motion of two atoms to a very complex movement of each atom. This complex movement creates vibration at a specific wavenumber, which absorbs light of varying wavelengths producing an interferogram. This interferogram is the raw data that is converted into absorbance/ transmission infrared spectrum using the Fourier transform algorithm. Interferrrogram is generated using a Michelon interferogram which splits a polychromatic beam into two radiation beams with different paths. One of these beams is reflected from a fixed mirror and another from the perpendicularly moving mirror (against the direction of the beam). These beams later get recombined following the superposition principle and pass through a sample (or get absorbed or reflected from a sample) to the detector. The moving mirror produces a beam of various interference depending on its distance from the beamsplitter, which results in a beam of new wavelength focused towards the sample manifesting absorbance at different wavenumber [199]. Depending on the chemical bonds present in a sample, these beams will shows adsobansce for the new wavelength and produce vibrational peaks specific to the derivative of dipole moment over changing the bond length. The infrared spectrum range is from 13000 cm^{-1} to 0 cm^{-1}, and this spectral range is divided into three parts: Near-Infrared region (13000 cm^{-1} – 4000 cm^{-1}), Mid- Infrared region (4000 cm^{-1} – 400 cm^{-1}), and Far- Infrared region (400 cm^{-1} – 0 cm^{-1}). All investigations related to the current thesis are focused on the Mid- Infrared region (MIR).

FTIR instrument used for current research work is purchased from Bruker optics Inc, Vertex model 80v with an external adapter for running FTIR measurements in UHV condition simultaneously with the XPS instrument. In the current model of the FTIR instrument, a silicon carbide heated at 1200 K is used as a MIR source (Globar) that produces light for the wavenumber range of 5000- 370 cm^{-1} [200]. For MIR region investigation, a KBr beam splitter is used and all the presented results in this thesis were performed in attenuated total reflection (ATR) mode of FTIR spectroscopy. ATR-FTIR utilizes the total internal reflection property of light bouncing above the critical angle which results in the formation of evanescent waves (waves that decay exponentially over depth). Based on this exponential decay, the probing depth of ATR-FTIR lies from ~ 0.5 µm to 2.0 µm, essentially making it a surface-sensitive measurement compared to the transmission mode of FTIR. However, in the current thesis, most of the discussion is in the depth range of 1-3 nm hence ATR-FTIR measurement is considered a bulk measurement.

ATR-FTIR measurements were performed with a diamond ATR crystal and IR signals were recorded using a DLaTGS detector with KBr windows. Electrolyte solution drops were deposited onto the ATR crystal and FTIR measurements were done at normal room temperature (20 °C, as set on the thermostat) and atmospheric conditions. ATR-FTIR measurements were performed for 100 background and sample scans for a scan range of 4000 – 400 cm^{-1} with 2 cm^{-1} resolution. Each electrolyte solution measurement was repeated twice with a freshly formed drop. Presented spectrums were baseline and ATR corrected using the function available in the OPUS software (version 8.2.28).

2.4. X-Ray Absorption Spectroscopy (XAS):

In X-ray absorption spectroscopy (XAS), a sample is bombarded with X-rays of certain energies and some of these X-rays are absorbed by the atoms of the sample. These absorbed X-rays lead to the excitation or ejection of core electrons from the atoms of the sample. This absorption is measured as transmission (difference in initial and final transmitted signal), fluorescence (signals resulting from excited electrons filling the core hole (orbitals)), and auger spectrums (signal results from ejected electrons that are filled by the excited electrons) [201]. Each element has a specific energy range of absorption and scanning over this range results in a XAS spectrum. A XAS spectrum has three main features: an absorption edge which occurs when an electron has enough energy to excite from its core orbital, a large steep peak and shoulder formation just above the edge, and slowly dampening oscillating features as shown in Figure 2-9. The region just below the edge and short energy over the shoulder (up to 100 eV from the edge) is called the X-ray absorption near edge structure (XANES) region which provides electronics and local geometric information for the atom of interest. The oscillating features in the figure up to 700 eV (depending on the order presented within a sample) are called extended x-ray absorption fine structure (EXAFS) region which provides quantitative geometrical information about the atom.

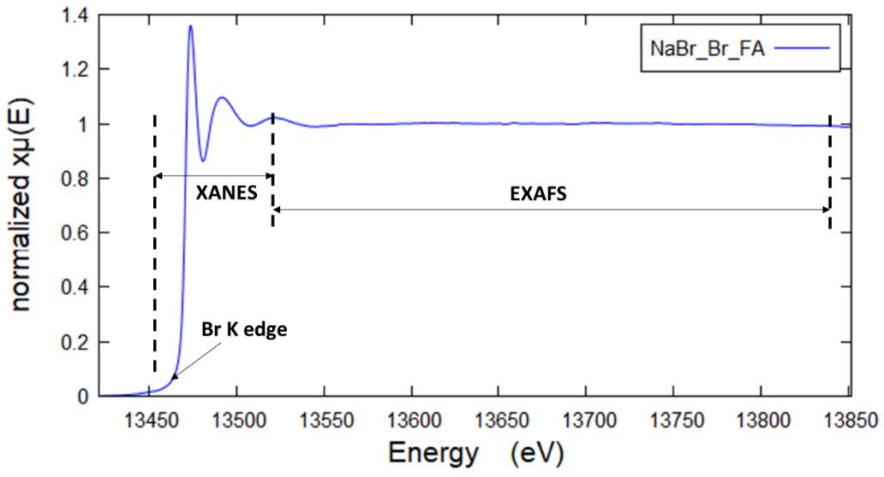

Figure 2-9: X-ray absorption spectrum (XAS) of Br Kedge from 10mM NaBr formamide (FA) electrolyte solutions. The figure here illustrates the main features in an elemental X-ray absorption spectrum.

All the presented XAS data were acquired at the Australian Synchrotron XAS beamline [202]. Electrolyte solutions of 10 mM concentrations were prepared at Flinders University following a similar procedure as discussed in a later section (Section 2.6) and degassed on-site just before the XAS measurements. This electrolyte concentration was selected to avoid the oversaturation of the detector due to higher fluorescence signal [203]. Bromide electrolyte solutions were slowly injected into quartz capillary (Hilgenberg gmbh) of the outer wall thickness of 0.010 mm and 80 mm in length. Special care was taken while injecting the solutions to avoid any bubble formation inside the capillary and the capillary was sealed after filling the sample to avoid any unwanted water gain during the measurements. Br K edge spectrums were calibrated against the first maximum (edge) of the first derivative of the Br K edge spectrum of standard KBr pellets. Transmission spectrums of KBr pellets were collected simultaneously while collecting fluorescence spectrums of Br K edge in electrolyte solutions. Caesium electrolyte solutions were slowly filled in a rectangular metallic sample cell consisting of two apertures of 7.5 mm radius. These sample cells were sandwiched in a 3-layer arrangement with Kapton foils (0.025 mm thickness) in between and on the top that are held together with screws. The solution was filled in the middle layer of the sample cell using a syringe. This sample cell setup was used as the walls of quartz capillary were too thick for X-rays penetration at lower excitation energy (5 – 9 KeV). Cs L_3 edge spectra were calibrated against the first maximum (edge) of the first derivative of the Cs L_3 edge spectrum of standard CsCl pellets.

Cs L_3 edge and Br K edge fluorescence spectra were collected with 100 elements solid state Ge-detector at room temperature. The excitation energies of 5 – 9 KeV and 9 - 19 KeV were selected for Cs L_3 and Br K edge measurements respectively; and the slit size was selected to keep an x-ray beam spot of ~ 1mm. All the spectrums presented here are triplicate scans collected from three different positions on the solutions-filled capillaries/sample cell to avoid bubble formations on a single focused spot. Collected data were pre-processed using Sakura pre-processing software and triplicates scans were averaged, and background subtracted using the Athena XAS data processing package [204].

2.5. Thermal Gravimetric Analysis (TGA):

TGA measures the mass change of a system with changing temperature and provides indirect information regarding the loss of compound from the sample of interest. TA instruments model 2950 was used for TGA measurements in this thesis. Liquid or solid samples of mass 18 – 35 milligrams (mg) were loaded into an aluminium crucible and the weight of samples was calibrated using the same aluminium crucible beforehand. TGA measurements were performed in a nitrogen purging environment with a temperature variation rate of 10 $^{o}C \cdot min^{-1}$ and the temperature range were selected based on the system of interest i.e., for glycerol measurement a temperature range of 30 – 200 ^{o}C was selected.

2.6. Materials and Sample Preparation

2.6.1. Solvents Selected

The focus of this thesis is to gain diverse information for ion specificity at various solvent surfaces. So solvent selection was done with criterion to explore the influence of two important factors for the ion specificity at solvent surfaces: 1) hydrogen bonding nature and, 2) dielectric permittivity. The hydrogen bonding interaction between solvent molecules at the interfaces is one of the interactions that define the magnitude of surface tension, thus the magnitude of intermolecular forces at the interface. Comparing the ion specificity in hydrogen-bonded and non-hydrogen-bonded solvents will allow us to test the influence of hydrogen bonding nature which have been indicated as one of the enablers of SIE [205]. The dielectric permittivity (ε_r) is related to a solvent's ability to solvate ionized species (i.e., electrolytes). Hence, the varying dielectric constant of the solvent will allow for testing the role of solvation in defining SIE. Further, at the interfaces, the varying ε_r also provides the opportunity to test the influence of image charge repulsion for specific ion adsorption at the interface. To investigate the influence of dielectric permittivity, formamide (high dielectric permittivity), glycerol (intermediate dielectric permittivity), and benzyl alcohol (low dielectric permittivity) were selected. Benzyl alcohol (protic) and propylene carbonate (aprotic) were selected to explore the influence of hydrogen bonding nature for ion specificity in ion CDPs at the vapour-solvent interface (Figure 2-10).

Within the above-listed properties, the need for vacuum suitability also dictated the selection of solvents, electrolyte solution concentration, and their measurement temperature. Therefore, NICISS measurements had to be conducted at varying temperatures between the solvent and with respect to surface tension measurements to limit the evaporation inside the vacuum chamber. For interfacial consideration, the surface tension of solvents increases linearly with the decreasing temperature suggesting that the intermolecular force at the interfaces increases at a lower temperature. I assume that this linear change in surface tension thus a linear change in intermolecular forces at surfaces does not change the SIE trend [206].

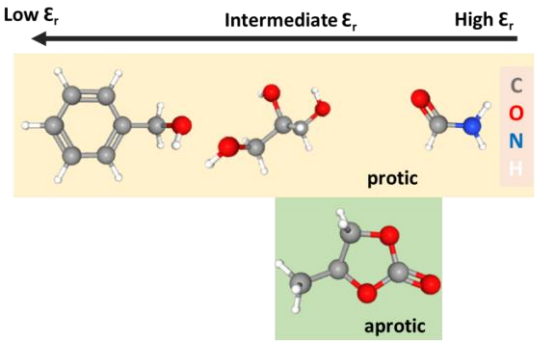

Figure 2-10: Investigated solvents in this thesis[c]. See Table 2-1 for details of their physical and chemical properties.

[c] Molecular structures are obtained from the PubChem database https://pubchem.ncbi.nlm.nih.gov.

Table 2-1: Physical and Chemical Properties of solvents investigated here[d] [e].

Physical/Chemical properties	Solvent			
	Glycerol	Formamide (FA)	Propylene carbonate (PC)	Benzyl Alcohol (BA)
Formula	$C_3H_8O_3$	CH_3NO	$C_4H_6O_3$	C_7H_8O
Density (g L^{-1}) at 20 ºC	1260	1129	1204	1045
Dielectric permittivity at 20 ºC	46.5	111.0	66.1	13.0
Dipole moment[f] at 20 ºC (Debye)	2.66	3.73	5.36[g]	1.67
Polarizability[h] ($Å^3$)	8.14	4.22	8.55	12.89
Surface tension at 20 ºC (mJ m^{-2})	63.0 ± 0.4	58.5 ± 0.4	41.8 ± 0.2	40.0 ± 0.4
Vapour Pressure at 20 ºC (bar)	3.3×10^{-6}	1.1×10^{-5}	3.1×10^{-5}	1.2×10^{-4}
NICISS measurement temperature (ºC)	20 ± 1	6 ± 1	1 ± 1	-5 ± 1
NICISS measurement pressure (bar)	$1 – 3 \times 10^{-8}$	$6 – 9 \times 10^{-8}$	7×10^{-8} -– 1×10^{-7}	9×10^{-8} -– 2×10^{-7}
Freezing /Boiling point (ºC)	17.0/290.0	3.0/210.0	-48.8/242.0	-15.0/205.0

[d] Data are obtained from the PubChem database https://pubchem.ncbi.nlm.nih.gov unless otherwise indicated.
[e] Density and surface tension values are reported as measured here.
[f] 207. Lide, D.R., *CRC handbook of chemistry and physics*. Vol. 87. 2006: CRC press.
[g] 208. Chernyak, Y., *Dielectric constant, dipole moment, and solubility parameters of some cyclic acid esters.* Journal of Chemical & Engineering Data, 2006. **51**(2): p. 416-418.
[h] 209. Bosque, R. and J. Sales, *Polarizabilities of solvents from the chemical composition.* Journal of chemical information and computer sciences, 2002. **42**(5): p. 1154-1163.

2.6.2. Electrolytes (salts) selected:

The salts lithium chloride (LiCl), lithium bromide (LiBr), sodium chloride (NaCl), sodium bromide (NaBr), sodium iodide (NaI), potassium fluoride (KF), potassium bromide (KBr), potassium iodide (KI), rubidium bromide (RbBr), caesium fluoride (CsF) and caesium bromide (CsBr) (Sigma Aldrich, purity > 99%) and caesium chloride (CsCl) (Alfa Aesar, purity > 99%) were roasted at 400 ^{o}C overnight to remove impurities before the sample preparation. To avoid oxidation of lithium iodide (LiI), a newly purchased bottle of LiI (Sigma Aldrich, purity > 99%) was stored in a glove box under a nitrogen atmosphere and used without further purification. Multiple batches of LiI were purchased for each set of measurements at separate times for the duration of my PhD.

Table 2-2: Lists of electrolytes investigated for each solvent. Electrolyte concentrations were selected based on their solubilities in the solvents and the backscattering signals obtained from NICISS measurements[i].

Electrolytes (NICISS measurement concentration)	Glycerol (At 1.0 mol kg^{-1})	Formamide (At 1.0 mol kg^{-1})	Propylene carbonate (At 0.5 mol kg^{-1})	Benzyl alcohol (At 0.5 mol kg^{-1})
LiCl	X	X		X
LiBr	X	X	X	X
LiI	X	X	X	X
NaCl	X	X		
NaBr	X	X		
NaI	X	X	X	X
KF	X			
KBr	X	X		
KI	X	X		
CsF	X	X		
CsCl	X	X		
CsBr	X	X		

[i] better backscattering signals are achieved with higher electrolyte concentration

2.6.3. Sample Preparations:

In specific ion investigations, salts are dissolved in a solvent for which ionic interaction with the solvent molecule is of interest. During such investigation, the presence of any impurity like water in a solution can influence the SIE. Different SIE can emerge as ions tend to interact easily with a water molecule or organic impurity. Hence, avoiding such a scenario is vital in the collection of data for specific ion investigations. Due to the hygroscopic nature of most salts in this investigation, a trustworthy procedure to remove water content and organic impurities for salts is essential. Figure 2-11 shows that a small amount of unknown organic impurities changes the oxygen step of the NICISS spectrum and affects the results. The oxygen step is changed as the surface-active organic impurity has adsorbed at the interface hence changing the backscattering of the He projectiles. NICISS can observe such subtle changes at the interface. Hence the data presented in this thesis are carefully evaluated keeping such observations in mind.

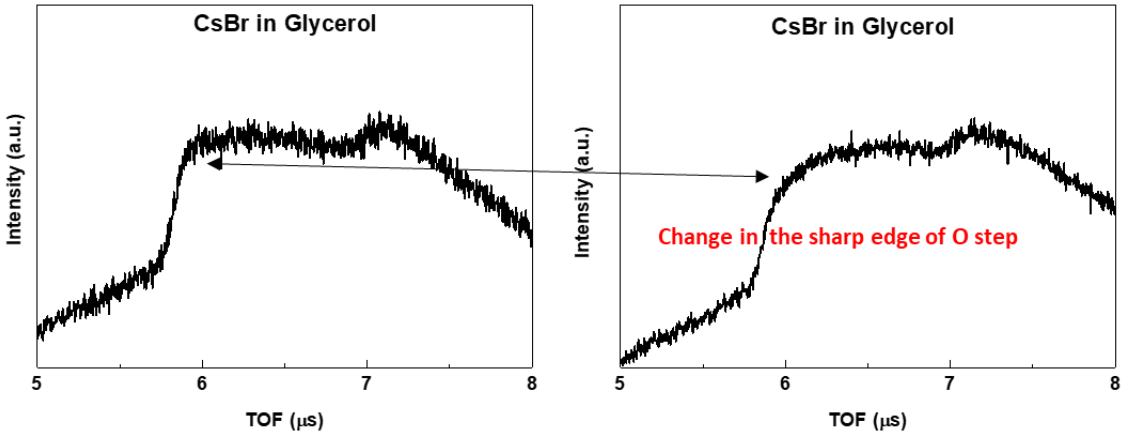

Figure 2-11: Change in oxygen step height of CsBr NICISS spectrum due to the presence of organic impurity. The change in the sharp edge of the O step indicates that surface active impurities are depleting the O at the interface.

Distillation or degassing is required to remove water content from the non-aqueous solvents, as high content of water will influence the ion specificity. The procedure to remove and determine the water content was different for each solvent investigated and dependent upon the instrument availability. For glycerol, the solvents were degassed in a custom-made vacuum setup for a period of 12 – 24 hours. The degassed solvents were stored in separate glass bottles with the estimated volume required for each measurement and used within a fortnight. Due to the viscous nature of glycerol, the preparation of saturated solutions takes 12 – 24 hours. To avoid any additional water gain during the stirring process was carried out under a vacuum as well. TGA measurements (Figure 2-12) were performed to account for water absorbed by salts in this duration. Degassed glycerol solutions had < 0.5 weight percentage (wt.%) of water which further decreased during the measurements in the NICISS UHV chamber.

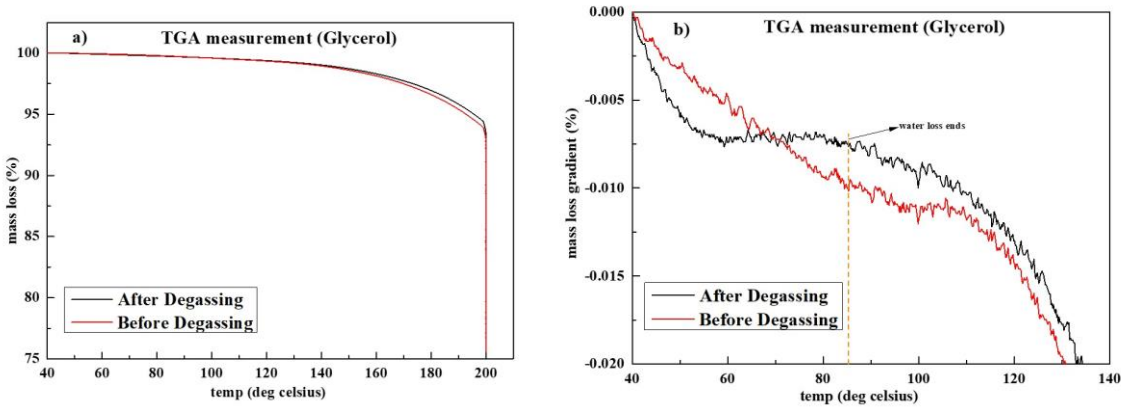

Figure 2-12: TGA measurement of glycerol before (red) and after degassing (black). (a) overall mass percentage loss TGA spectrum of glycerol, (b) mass loss gradient of glycerol to account for water content absorbed in glycerol (85.49 °C is the cut-off point for water loss in glycerol under N_2 environment [210]).

Formamide (FA) was purchased from Sigma Aldrich and the same salts and protocol mentioned above were followed to prepare formamide solutions. For FA purification, distillation was performed under low pressure (vacuum) due to its high boiling point (210 ºC). Distilled FA was stored in separate sealed vials in the measured volume required to make the solutions. Glass bottles were opened just before the addition of salts to reduce any water content and stirring was performed under the fume hood. For propylene carbonate (HPLC grade, purity ~ 99.7 %) and benzyl alcohol (purity ≥ 99.0%), newly purchased bottles from Sigma Aldrich were used as received and the required volume for a series of electrolyte solution measurements was separated and stored in the glass bottle. This procedure was done to avoid repeated opening of newly purchased bottles leading to a chance of gaining moisture. Electrolyte solution stirring was done in clean sealed glass bottles under the fume hood. All the glass bottles used for the storage of solutions were cleaned in bulk for a series of measurements. Cleaning was done with 10% NaOH solutions then water, followed by flushing with acetone–water and ethanol-water combinations. These cleaned glass bottles were then baked in the oven overnight at 150 ºC.

ATR-FTIR spectroscopy was used to detect water content in FA, PC, and BA electrolyte solutions[j]. The deliberate addition of water into FA, PC, and BA were conducted to measure the detection limit of water content using ATR-FTIR spectroscopy which was >1 wt.% (Figure 2-13). Hence, this detection limit was used as a reference for checking the water content in all electrolyte solutions (except for the glycerol sets). Mazzini and Craig performed a structured investigation and suggested that the SIE will be affected due to water presence in case there are enough water molecules present to form a full solvation shell around the ion. Through SEC, they measured that >0.2 wt.% of water is needed to create a full solvation shell around ions in formamide and propylene carbonate at an electrolyte concentration of 0.05 moles kg^{-1}. Since all the electrolyte solutions investigated here are

[j] TGA instrument was out of commission during these measurements.

at least of 10 times higher concentration. It is assumed that > 2.0 wt.% will be required to potentially influence the herein presented results. All the electrolyte solutions investigated in this thesis are suggested to have >1.0 wt.% water content as measured from TGA and FTIR spectroscopy. Further, in NICISS measurements, the amount of water can be considered much less because of degassing inside the vacuum chamber.

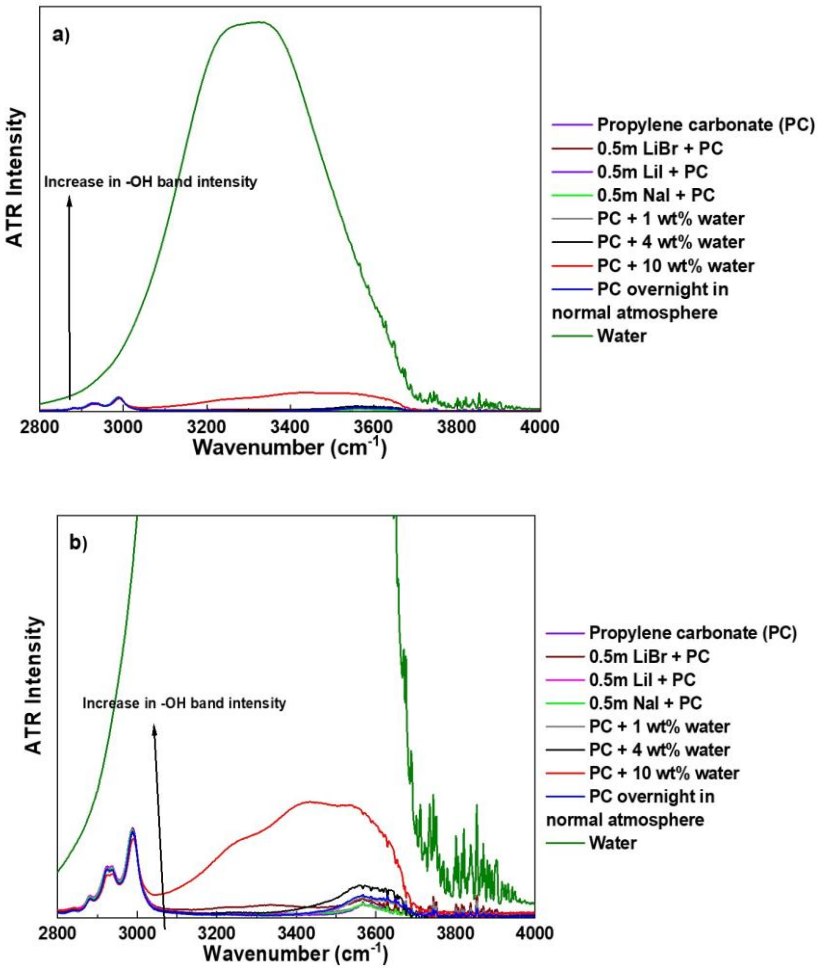

Figure 2-13: (a) and (b) ATR-FTIR spectrum of stretching -OH group (located between 3200-3800 cm^{-1}) of pure PC, PC with the addition of varying wt.% of water, and 0.5 m LiCl, LiI, LiBr and NaI PC electrolyte solutions. With an increasing percentage of water, the H-OH groups' presence starts to become more visible in the broad -OH IR range. When water is added at 1.0 wt.%, there is a slight increase in intensity at stretching -OH band suggesting. Hence using ATR-FTIR, we can measure > 1 wt.% of water. The absence of this peak in these regions suggests water content is less than > 1.0 wt.%. Based on this procedure, it can be suggested that all the electrolyte solutions prepared for NICISS, and surface tension measurement has less than > 1.0 wt.% of water. Thus, the effect of water presence toward ion specificity in herein investigated electrolyte solutions is assumed to be minima

CHAPTER 3 : ION SPECIFICITY IN THE MEASURED CONCENTRATION DEPTH PROFILE OF IONS AT THE VAPOUR-GLYCEROL INTERFACE

This chapter is a reformatted and edited version of a manuscript for a journal article published in a peer-reviewed journal. See the Contextual Statement section for details on the contribution of the co-author to the published version of the manuscript.

Reference for the published version:

Kumar, A., Craig, V.S., Page, A.J., Webber, G.B., Wanless, E.J. and Andersson, G., 2022. Ion specificity in the measured concentration depth profile of ions at the Vapour-Glycerol interface. Journal of Colloid and Interface Science, 626, pp.687-699.

3.1. Introduction:

The overall aim of this chapter is to quantitatively determine the concentration depth profiles (CDPs) of individual cations and anions of a large set of monovalent salts at the interface of glycerol. The CDPs are investigated under the same conditions. The aim is to identify and understand the specific ion trends that are manifest and to investigate what drives the ion specific adsorption and desorption of anions and cations at solvent surfaces. The solvent studied here is glycerol. Glycerol has been chosen for a combination of reasons including its ability to dissolve a wide range of electrolytes, its low vapour pressure and its high surface tension (~ 63 $mJ{\cdot}m^{-2}$) which is comparable to water (~ 73 $mJ{\cdot}m^{-2}$) [211]. SIE in glycerol have been previously investigated in the bulk [212-214] and at the surfaces [148, 152] (see 1.5.3). Studies of the vapour-glycerol interface have shown that the hydroxyl groups of glycerol face into the bulk solvent and the CH_2 and CH groups extend into the vapour phase [215-218]. Based on the current understanding of the orientation of water at the vapour-liquid interface [219]. The surface dipole of glycerol has the opposite orientation to that of water.

3.2. Results

The current investigation focuses on four different comparisons of ion CDPs:

1) Comparison between different anion CDPs with a common cation.

2) Comparison between a single anion's CDP with varying cations.

3) Comparison between cation CDPs with varying anions.

4) Comparison between the CDPs of the ions comprising a single salt.

Cations with common anions are not compared explicitly, as the zero-depth scale for cations cannot be measured directly (see 2.1.5 and 2.1.7). Therefore, the resulting uncertainty in the profile of cations prevents meaningful comparison between different cations (see Figure I-7 in the Appendix chapter I). However, comparing the same cation in different salts is not affected as the offset error in the zero-depth calibration is the same.

3.2.1. Observation of Specific Ion Series in Anion CDPs:

Examination of the ordering of anions with a common cation mirrors specific ion effect studies into the Hofmeister series for anions, as this probes the relative strength of the anion's affinity for the interface. The CDPs of Cl^-, Br^- and I^- with Li^+ and Na^+ as common cations are compared in Figure 3-1 (a) and (b), respectively, while the CDPs of Br^- and I^- with K^+ as the common cation are compared in Figure 3-1 (c). The CDPs of Cl^-, I^- and Br^- show a non-monotonic distribution (except for KBr), where ions are present in enhanced concentration close to the Vapour-glycerol interface, followed by a strong depletion in the subsurface region. In Region 1, for lithium salts (Figure 3-1 (a)) all three anions show a similar maximum peak concentration. For the sodium salts (Figure 3-1 (b)), Cl^- ions have a similar peak concentration to that of I^- while Br^- has the lowest peak concentration. For the potassium salts (Figure 3-1 (c)), the I^- peak concentration is enhanced in Region 1 whereas Br^- shows a depletion (no peak). In Region 2, Cl^- shows a slightly stronger depletion than I^- for the lithium salts. For the sodium salts a similar but smaller difference is present and is difficult to discern within the uncertainties.

3.2.2. Observations of Counterion Effects on Ion CDPs:

3.2.2.1. Anion Depth Profiles in The Presence of Various Cations

In considering classic Hofmeister effects the influence of the counterion is usually neglected. As such the ordering of the anions in the Hofmeister series is usually assumed to be independent of the cation. Here we explore how changing the cation influences the depth profile of a common anion. The CDPs for Cl^- in 1 m LiCl, NaCl and CsCl glycerol electrolytes are compared in Figure 3-2 (a), showing that the Cl^- CDPs in Region 1 are the same in each case. In the case of the CsCl glycerol solution, the Cl^- CDP has a somewhat larger depletion in Region 2 (subsurface region) compared to LiCl and NaCl solutions. In contrast, comparison of the Br^- CDPs (Figure 3-2 (b)) clearly shows that the cation identity strongly influences the Br^- peak in Region 1 as observed in the raw NICISS CDPs (see Figure I-5 (b) in Appendix chapter I). The magnitude of the Br^- peak in Region 1, as shown in Figure 3-2 (b), is strongly influenced by the counter-cation ($Li^+ > Na^+ > K^+$) while in Region 2 the depletion order is reversed. The CDPs for I^- (Figure 3-2 (c)) paired with Li^+, Na^+ or K^+ counterions have similar peak concentrations in Region 1 and in this respect are similar to the Cl^- CDPs. Whilst differences appear to be present in Region 2 the measurements are within uncertainty in this region.

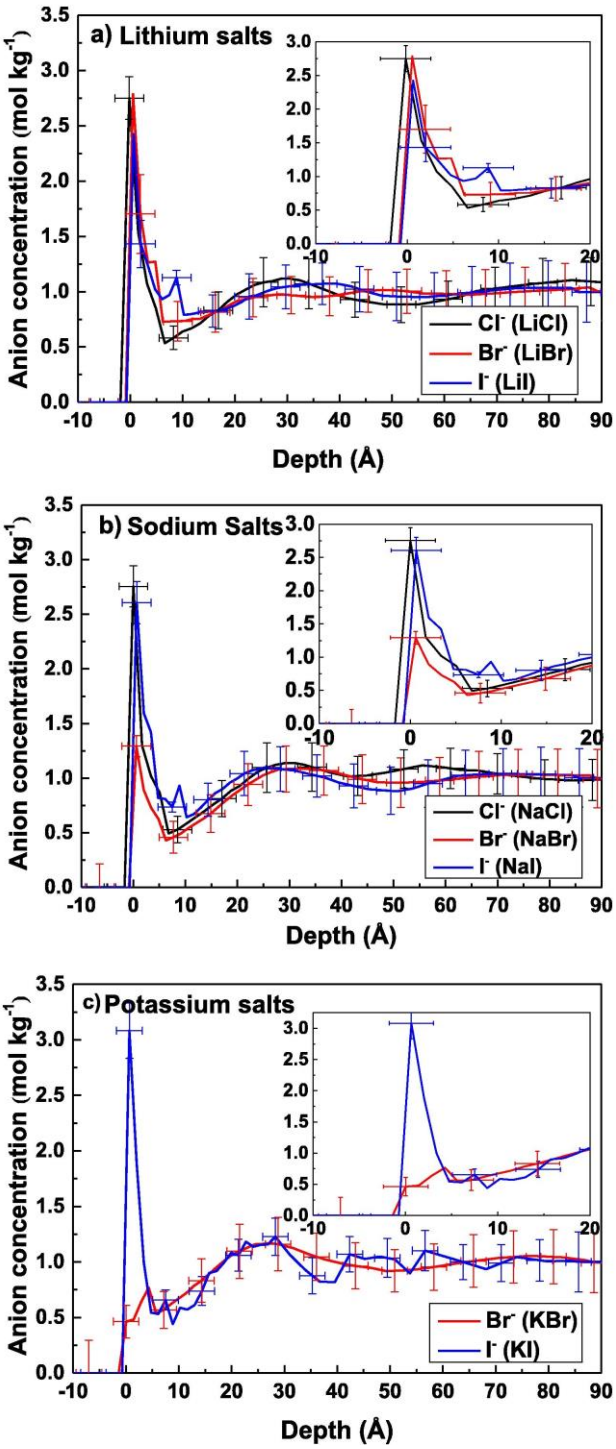

Figure 3-1: Deconvoluted CDPs of Cl^- (black), Br^- (red), and I^- (blue) anions in 1 m solutions in glycerol with (a) Li^+ as the counterion, (b) Na^+ as the counterion, and (c) K^+ as the counterion. The insets show the outermost layer (Region 1) of the ion CDP. For lithium salts, Cl^-, Br^-, and I^- have a similar peak concentration at the glycerol surface. For sodium salts, the peak concentration of anions follows the order $Cl^- = I^- > Br^-$. For potassium salts I- exhibits a strong peak concentration near the interface whereas Br^- is depleted near the interface. For clarity, error bars are only included every 5 data points.

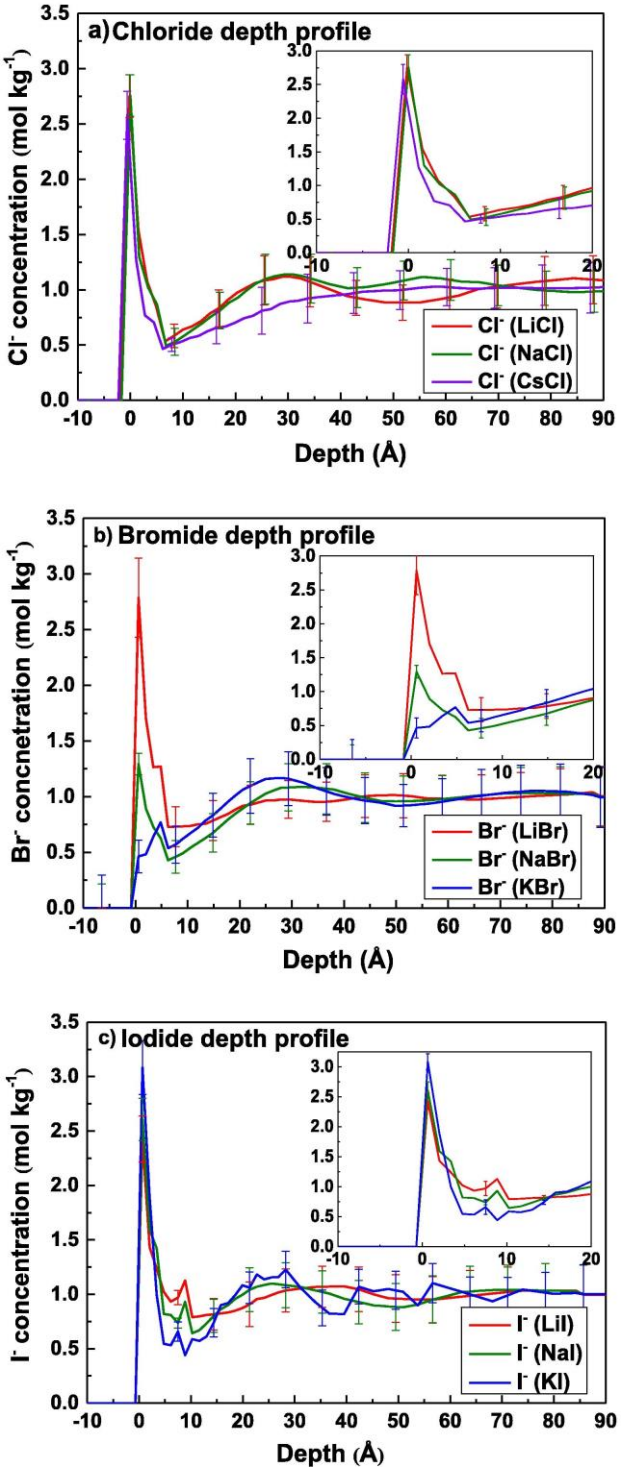

Figure 3-2: CDPs in 1 m solutions for Li^+ (red), Na^+ (green), K^+ (green) and Cs^+ (black) salts of (a) Cl^-, (b) Br^-, and (c) I^- in glycerol. Insets in each figure shows the region of the outermost layer of the CDP (Region 1). The Br^- CDP in Region 1 shows a specific ion order for cations i.e., $Li^+ > Na^+ > K^+$ while Cl^- and I^- CDPs remain unchanged with varying counter-cation. Since each of these ion CDP comparisons have been calibrated with the same gas phase measurement, the potential offset error in the depth scale is the same in each measurement and for the sake of clarity they are not included. For clarity concentration error bars are included for every 5 data points.

3.2.2.2. Cation Depth Profiles in the Presence of Various Anions

In the previous section we examined how cations influence the CDP of a particular anion, here we examine how anions influence the CDP of a particular cation. The CDP for K^+ paired with F^-, Br^- and I^- counterions are compared in Figure 3-3 (a). The CDP's show that K^+ is depleted at the surface in all cases. Since the K^+ NICISS CDPs have a less favourable signal to noise ratio than other heavier ions, differences are more difficult to discern (see Figure I-6 (a) in the Appendix Chapter I). However, K^+ when paired with Br^- is more depleted from glycerol surfaces than when paired with F^- and I^-; for the latter anions the degree of K^+ depletion at the surface is similar (Figure 3-3 (a)). The CDPs for Cs^+ from CsF and CsCl solutions are compared in Figure 3-3 (b) and show Cs^+ has a sharp maximum in concentration near the vapour-glycerol interface and that it has a higher peak concentration when paired with F^- than with Cl^-.

It is desirable to include CsBr in this comparison, but a direct comparison as shown for Cs^+ in CsF and CsCl is not possible as the Cs^+ and Br^- steps cannot be fully separated in the TOF spectra. However, a TOF spectrum for CsBr can be constructed from the TOF spectra for CsCl and NaBr, as in these spectra the peaks are separated. To do so, the region of the TOF spectra of CsCl that corresponds to Cs^+ is combined with the region of the TOF spectra of NaBr that corresponds to Br^-. The difference between the measured TOF spectra for CsBr and the constructed TOF spectra for CsBr can then be determined and is shown in Figure 3-3 (c). The difference spectrum is examined in two regions. The Cs^+ TOF region is between approximately 3.67 µs - 3.82 µs and the Br^- region is approximately from 3.82 µs – 4.00 µs (regions marked in Figure 3-3 (c)). In the difference spectrum a negative distribution indicates a relative depletion in the measured CsBr spectra compared to the constructed CsBr spectra. Thus, a negative distribution in the difference spectrum for Cs^+ or Br^- ions indicates the depletion of Cs^+ and Br^- ions relative to Cs^+ from CsCl and Br^- from NaBr respectively. Examining the Cs^+ region, Cs^+ shows a depletion when Cs^+ from CsCl is used to construct the CsBr spectrum. Furthermore, when replacing the Cs^+ from CsCl with Cs^+ from CsF, (see Figure I-8 in the Appendix Chapter I) this depletion region for CsBr becomes even larger. This overall comparison of Cs^+ profile shows a Hofmeister effect of the anions on the Cs^+ concentration at the vapour-glycerol interface i.e., Cs^+ (CsF) > Cs^+ (CsCl) > Cs^+(CsBr). The zero in the TOF difference spectrum (dashed black line in Figure 3-3(c)) was determined from the region above 4.0 µs where the CsBr solution TOF spectrum has reached the bulk concentration.

For Br^-, the depletion is pronounced at shorter TOF, and this disappears for longer TOF, reaching bulk concentration (above 4.0 µs). This depletion feature for Br^- becomes more pronounced when Br^- from LiBr is used for constructing the CsBr TOF spectrum (see Figure I-9 in the Appendix Chapter I). Furthermore, after using Br^- from the KBr TOF spectrum for constructing the CsBr spectra, the difference in Br^- region becomes negligible (see Figure I-10 in the Appendix Chapter I) evidently suggesting similar Br^- CDPs in KBr and CsBr solutions, as shown in Figure 3-2 (b). These

comparisons suggest that the cations affect the location of the Br^- ion relative to the vapour-glycerol interface in the order $Li^+ > Na^+ > K^+ = Cs^+$.

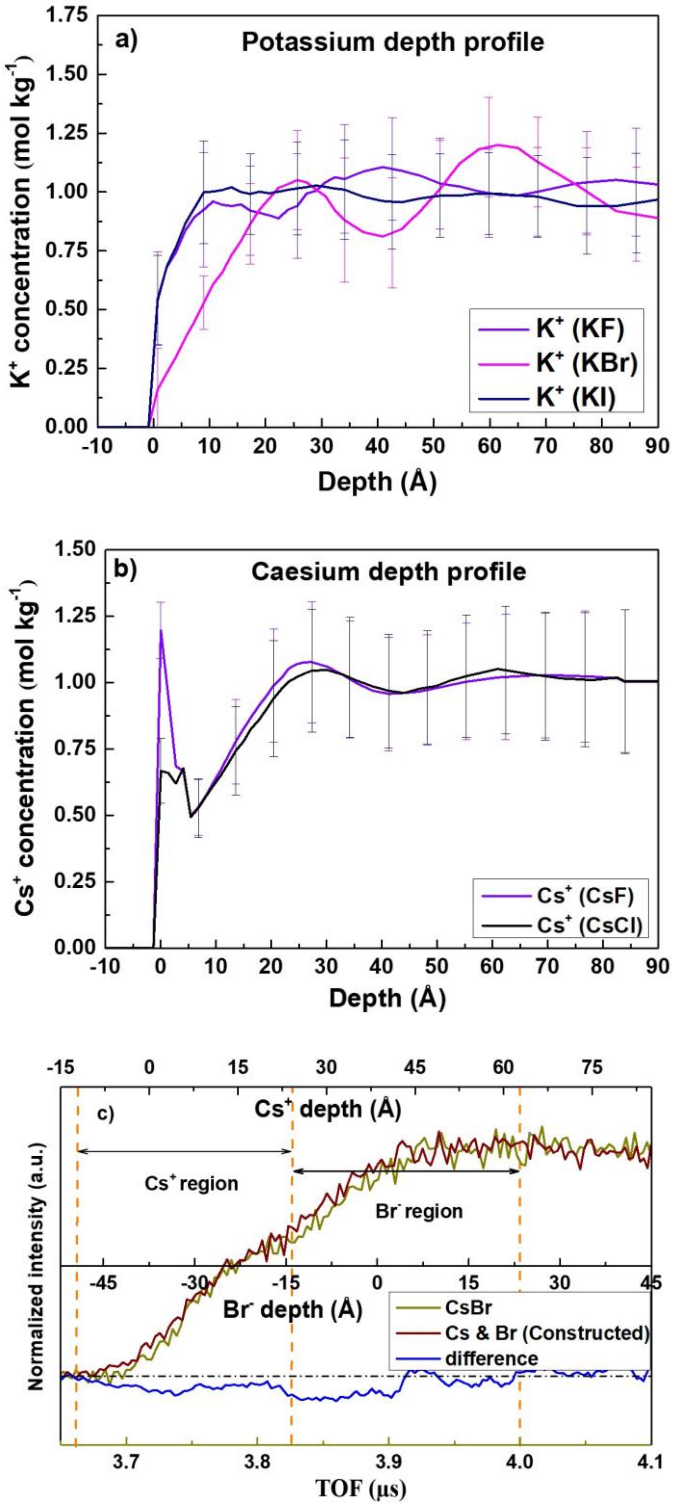

Figure 3-3: (a) Comparison of the CDPs of K^+ in 1 m KF (violet), 1 m KBr (pink) and 1 m KI (dark blue) glycerol solutions. (b) Comparison of the CDPs of Cs^+ in a 1 m CsF (red) and 1 m CsCl (black) solutions in glycerol. (c) Difference (blue) between the TOF spectrum of 1 m CsBr (olive) and that of the constructed 1 m CsCl and 1 m NaBr TOF spectrum (brown). This difference in TOF spectrum is averaged over 3 data points. For clarity, error bars are included for Figures 5(a) and (b) only for every 5 data points.

3.2.3. Surface Tension of Glycerol Electrolyte Solutions

The surface excess of solutes in solution, Γ_B, can be determined from surface tension measurements using the Gibbs adsorption isotherm, wherein an increase in the surface tension with increasing concentration of solute means there is an overall depletion of the solute at the surface. Here we have measured the surface tension of a range of solutions containing different salts at a concentration of 1 m in glycerol. For most electrolyte solutions it has been observed that the surface tension increases linearly with concentration for a wide range of electrolytes up to a few molal in both aqueous [9] and glycerol solutions [152]. As the change in surface tension is linear, the surface tension increment (STI) ($mJ \cdot m^{-2} \cdot (mol \cdot kg^{-1})^{-1}$) can be conveniently employed to compare the overall degree of depletion of the electrolyte from the interface for different salts.

From the surface tension measurements, the STI of the various electrolyte solutions has been calculated and the values are presented in Table 3-1. Quantitative conversion of these data to surface excess requires knowledge of the mean activity of the ions in glycerol at this concentration. The activity is only known for a few of the systems studied here. (See Table I-1, 2, and 3 in the Appendix Chapter I for surface excess data derived from both NICISS CDPs and surface tension measurements assuming that the activity coefficient of salts in glycerol is 1.0). Regardless of the unavailability of the activity coefficient data, the surface tension increment allows a qualitative discussion of the trends. It is evident that the anion identity has a significant influence on the magnitude of the STI and implies that the anion concentration at the interface follows the series $Cl^- < F^- < Br^- < I^-$ with the last in the series being the most depleted from the surface.

These STI data are consistent with the NICISS measurements in two ways. It is evident that the magnitude of the surface tension increment is more strongly influenced by the anion than the cation. For the anions the STI follows the series $Cl^- < F^- < Br^- < I^-$ and for the cations the STI order is variable and dependent upon the anion, suggesting that the depletion of cations at the interface is anion dependent. This dependency was shown clearly with the NICISS data in section 3.2.2.2.

Table 3-1: Measured surface tension increments (STI), $\Delta\gamma$ ($mJ \cdot m^{-2} \cdot (mol \cdot kg^{-1})^{-1}$) for electrolytes in glycerol, calculated from surface tension measurements of solutions at a concentration of 1 m. Here the STI of a particular electrolyte in glycerol is tabulated at the intersection of the column containing the anion and the row containing the cation

Cations/Anions	F^-	Cl^-	Br^-	I^-
Li^+		0.4 ± 0.3	0.8 ± 0.3	1.7 ± 0.4
Na^+		0.2 ± 0.3	0.9 ± 0.3	0.9 ± 0.4
K^+	0.7 ± 0.2		1.3 ± 0.2	1.8 ± 0.4
Cs^+	1.0 ± 0.3	0.7 ± 0.5	1.1 ± 0.3	

3.2.4. Anion and Cation Depth Profiles of electrolytes

Various computational works investigating inorganic ions at the vapour-solvent interface have shown that ion enhancement can occur at the solvent surface, which is counteracted by depletion of the counterion in the surface region [112, 129, 220]. To investigate this trend directly in experiments, we compare the anion and cation concentration depth profiles obtained from KI in Figure 3-4(a) and CsCl in Figure 3-4(b), dissolved in glycerol. (See Table I-1 and 2 in the Appendix Chapter I for surface excesses obtained from ion CDPs obtained using NICISS). In both cases the anion has an enhanced concentration nearest to the interface followed by a strong subsurface depletion, while the cation is depleted throughout the interface. The net effect is an overall depletion of ions from the glycerol interface (a similar trend was observed for KBr electrolyte solutions in see Figure I-11 in the Appendix Chapter I).

Ideally, by integrating the ion CDPs over a certain depth range, the surface excess of both the anion and cation and hence of the overall salt could be obtained from NICISS CDPs and compared to the surface excess values calculated from surface tension measurements. However, previous comparisons [221] of surface excess calculated from surface tension measurements and NICISS CDPs were for a surfactant solutions which have a much greater magnitude of surface excess. Simple monovalent inorganic ions have a small surface excess and experimental uncertainties preclude accurate determination of the surface excess from NICISS measurements. Hence, we do not compare the surface excess values obtained from both techniques.

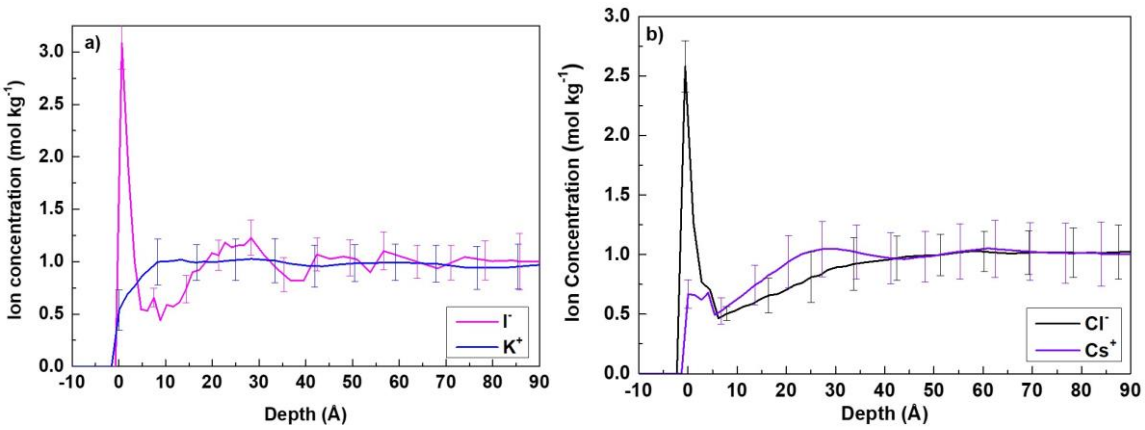

Figure 3-4: **Anion and cation CDPs of (a) 1 m KI glycerol solutions with I^- (pink) and K^+ (blue) CDPs and (b) 1 m CsCl glycerol solutions with Cl^- (black) and Cs^+ (violet) CDPs. The uncertainty between depth calibration of cation and anion is ± 3.6 Å. For the sake of clarity, the error bars for depth calibration are not included in the figures. The presented error bars in the ion concentration are the standard error between deconvolution solutions of two repeated NICISS measurements which for clarity is shown only for 1 in 5 data points.**

3.3. Discussion

Here NICISS has been used to measure the CDPs of individual ions in glycerol solutions, in order to determine how the concentration profile near the interface is influenced by the identity of the ion. The strength of this technique is that the CDP of each ion can be determined independently. These experiments reveal four key results for ions at glycerol surfaces.

- Anions are mostly enhanced in concentration relative to the bulk in the outermost region of the interface and Cl^- and I^- ions are enhanced in concentration to a greater degree than Br^- (Section 3.2.1).
- The degree to which Br^- ions are enhanced in concentration in the outermost region of the interface is strongly dependent on the counterion, such that the enhancement is greatest for Li^+ and follows the series $Li^+ > Na^+ > K^+ = Cs^+$. In contrast, the CDPs of Cl^- and I^- were unaffected by the identity of the counterion. (Sections 3.2.1 and 3.2.2).
- The concentration of cations at the glycerol interface depends on the identity of the anion. Cs^+ and K^+ have lower concentrations at the vapour-solvent interface when paired with Br^- than when paired with I^- or F^-. The Cs^+ concentration at the vapour-glycerol interface follows a Hofmeister series in terms of anion effect (Section 3.2.2.2).
- These experiments directly measured the concentration depth profiles of ions at the glycerol interface and show that anions have an enhanced concentration in the outermost region of the interface (Region 1) followed by a significant subsurface depletion (Region 2). In contrast, cations are depleted throughout the interface (Section 3.2.4). These results offer direct experimental evidence in support of a number of computational studies reporting accumulation of anions in the outermost region of the interface (Region 1) [112, 129, 144, 160].

Interpreting interfacial manifestations of SIE is complicated. Measurements of STI average the concentration of both anion and cations across the interface. As such surface tension measurements are not able to discern the individual contributions of the cations or anions without further assumptions such as assignment of a surface excess to a reference ion [222, 223]. Moreover, extraction of the individual contribution of specific ions to the surface tension increment requires the assumption that the surface excess of an anion is independent of the cation and vice-versa, which is known not to be the case. Further, surface tension measurements are unable to reveal anything about the distribution of ions within the interface. This is important, as simulations show that the ion distribution is non-monotonic and dependent on the specific nature of the ion [112].

The non-monotonic distribution of ions within the interface complicates comparison between different experimental techniques for probing the interface, as each technique varies in depth sensitivity. For example, X-ray photoelectron spectroscopy typically probes depths of 2 - 10 nm [166], whereas surface sensitive non-linear optical techniques typically probe depths of between 0.3 and 0.8 nm [157, 224]. The variability and uncertainty in experimental depth sensitivity also complicates

comparison of experiments with computational and simulation studies. This highlights the importance of NICISS as a tool for mapping the depth distribution of ions within the interface. As shown here, the technique is able to measure the non-monotonic distribution of ions within the interface with high depth resolution whilst simultaneously differentiating between ionic species. As such the technique allows direct comparison between the spatial distribution of ions of varying types and charge at the vapour-solvent interfaces. Further, the effect of different counterions on this distribution can be measured. These direct experimental observations can be used to interpret and compare different techniques for the investigation of interfaces. For example, the detailed ion depth profiles illustrate why simulation studies show an excess of ions at the interface whilst thermodynamic analysis of surface tension measurements reveals a depletion of ions within the interface - the ion distribution is non-monotonic, and the techniques are probing different depths. The technique is also powerful for understanding the detailed manifestation of SIE. For example, the influence of counter ions on the distribution of an ion within the interface can be revealed. This interdependency between ions complicates interpretation of SIE and has led researchers to move beyond interpretations based on the Hofmeister series.

Collins [65, 66] proposed the law of matching water affinities to explain these effects in aqueous systems. This affinity, as defined by Collins [65], accounts for the charge density of ions and counter-ions in interacting with water molecules. If the ion and counter-ion have similar charge density, then contact ion pairs will be formed and when the charge density differs the ions will preferentially interact with water molecules. This idea was later expanded to include non-aqueous solvents through a consideration of Volcano plots [68] and described as the "Law of matching effective ion sizes (MEIS)" for the monovalent ions [68]. These ideas go beyond the Hofmeister series as they encompass the observation of series reversals with changing counterion, whereas the Hofmeister paradigm assumes that the counterion is irrelevant. The MEIS can be extended to include the interaction of ions with interfaces. Ions with a relatively strong affinity for the solvent will be withdrawn from the interface and ions with a weaker affinity for the solvent will be relatively abundant at the interface. Our NICISS results show that cations are depleted from the interface whilst anions are adsorbed at the outermost region of the interface, except for Br^- when it is paired with either Cs^+, K^+ or Na^+. This is in accord with the surface tension measurements that show an overall depletion of ions at the interface. Taken together with the NICISS data this implies that the overall depletion is primarily due to the strong depletion of cations from the interface.

Do these observations align with the Collins paradigm and the MEIS? To determine the relevant affinity of the anions for glycerol we have calculated their solvation free energies in glycerol using Gregory and co-worker's IonSolvR database (see Appendix Chapter I and the reference for methodology details) [225]. The solvation free energies for Cl^-, Br^-, and I^- in bulk glycerol are -234.2 $\pm$ 6.1 $kJ{\cdot}mol^{-1}$, -332.0 $\pm$ 6.1 $kJ{\cdot}mol^{-1}$ and -92.5 $\pm$ 6.2 $kJ{\cdot}mol^{-1}$, respectively ($\pm$ are standard error in solvation free energy from MD trajectory). The Br^- solvation energy is much more favourable than

both Cl^- and I^-. Within the Collins paradigm this infers that it is more favourable for Cl^- and I^- anions to be at the interface, as observed. But this does not explain why Br^- is found at the interface in the presence of Li^+ but not in the presence of Cs^+, K^+ or Na^+ counterions.

The MEIS suggests that the Br^- ion will have a strong affinity for Cs^+ , K^+ and Na^+ but not so for Li^+ as the hydrated ion size [226] for Br^- (0.330 nm) is similar to Cs^+ (0.329 nm), K^+ (0.331 nm) and Na^+ (0.358 nm) but quite different to Li^+ (0.382 nm). As the cations are strongly depleted from the interface this will draw the Br^- from the interface into bulk when the counterion is Cs^+, K^+ or Na^+. In contrast the Li^+ is different in size to the Br^- and as such there is no drive for association and the Br^- remains at the interface when Li^+ is the counterion. We note that the influence of matching effective ion sizes is not manifest when the anion is either Cl^- or I^- (which have very similar hydrated ion size to Br^- at 0.332 and 0.331 nm respectively), presumably due to the dominant effect of their much lower solvation free energy.

3.3.1. Comparison with Previous Investigations of the Vapour-Glycerol Interface and Outlook

Now we compare our results with previous investigations of ions at the vapour-glycerol interface. Allen and co-workers [152] have investigated the adsorption of anions to the interface, with Na^+ as the counterion using Vibrational Sum Frequency Generation (VSFG) spectroscopy. They concluded that I^- exhibits a larger degree of disturbance on the hydrogen bond network than Br^- at the surface of glycerol. This indirectly implies a greater concentration of I^- at the glycerol surface than Br^- which is consistent with the NICISS CDPs presented here for sodium electrolyte solutions. Allen and co-workers had discussed the higher concentration of I^- at glycerol surfaces based on its larger ionic size and polarizability akin to the aqueous electrolyte surfaces, however they did not investigate NaCl glycerol solutions due to solubility issues. Our observations here of an enhancement of Cl^- at glycerol surfaces, suggest that the trend observed for water of larger and more polarisable anions being surface enhanced does not extend to glycerol electrolyte surfaces.

Allen and co-worker's investigation on glycerol electrolyte solution surfaces was inspired by Nathanson and co-worker's molecular beam scattering experiments [146]. Employing molecular beam scattering experiments, Nathanson and co-workers studied the reaction probability pathways of DCl interaction at the vapour-glycerol interface. One of the interesting reaction pathways in these experiments was the nonreactive DCl molecule desorption. A small percentage of DCl molecules are immediately scattered from the glycerol surface without any desorption, because some of the available interaction sites (hydroxyl moiety) for DCl molecules (i.e., D→H exchange interaction) are occupied by electrolytes present at the glycerol surface. From this reaction pathway, the fraction of ion occupied interaction sites can be inferred. Comparing this reaction pathway, the authors observed that each of LiI, NaI and KI glycerol solutions had a similar fraction of nonreactive desorption of DCl, suggesting the absence of any cation influence on the fraction of occupied interaction sites at glycerol surfaces for the I- anion. This observation is supported by our NICISS

CDPs of I^- in LiI, NaI and KI solutions surfaces measured here (Figure 4 (c)) showing that the I^- concentration at the glycerol surface does not vary with the counterion. Additionally, Nathanson and co-workers observed that NaBr and NaI glycerol solution had a similar fraction of nonreactive DCl desorption, suggesting a different specific ion trend than observed here for the anion CDPs of sodium salts. This difference emphasizes another important observation of single ion contributions and the role of anion-cation interactions, since molecular beam scattering experiments measure the effect of the overall salt. The authors rationalised these observations as owing to competing effects between ion-solvent and ion-counterion interactions and suggested that the DCl molecular reaction pathways are further complicated by ion coordination at glycerol surfaces.

Hence the coordination of ions (i.e., the number of solvent molecules within the solvation shell of the ions) at the glycerol surface and in bulk solution will help elucidate the herein observed organization of ions, as well as observations made by Nathanson and co-workers at the vapour-glycerol interface. The solvation shell essentially encompasses most ion-solvent interactions and defines the effective ionic size [128, 227, 228]. Unfortunately, knowledge of the ion solvation shell in glycerol (and other non-aqueous solvents) is limited in the bulk and is non-existent for ions near interfaces. Recently, it has been shown with Extended X-ray Absorption Fine Structure (EXAFS) measurements that it is possible to obtain accurate solvation shell data in the bulk. Watanabe[87] showed that EXAFS can be used to measure the solvation shell of ions at solvent surfaces and these have now been accurately measured by Bera and co-workers [229]. In the near future we plan to perform similar experiments with inorganic ions in aqueous and non-aqueous solvents and compare this with CDP of ions in aqueous and non-aqueous solvents to gain insight into the driving parameters for ionic adsorption at solvent surfaces.

3.4. Conclusion

In last few decades, a range of investigations have covered the topic of ion specificity of the adsorption and desorption of ions at solvent surfaces with a strong emphasis on the vapour-water interface [230-232]. Only a few investigations have studied non-aqueous solvent surfaces [148, 233]. Based on our comprehensive measurements of CDPs of several combinations of cations and anions we have identified four key results regarding the adsorption and desorption of monovalent ions at glycerol surfaces. These results confirm previous observations from experiments and computational studies with direct measurements. In the current work, we compare the CDPs of different ion combinations using 12 different glycerol electrolyte solutions to determine the specificity of ions in the CDPs at glycerol surfaces. In general anions are adsorbed to the outermost region (Region 1) of the vapour- glycerol interface, with Br- being the exception. These results prove that the concept of larger and more polarisable ions present at a vapour-water interface [116] does not apply for all solvents. Quantum chemical calculations of free energies of solvation for these anions in glycerol, show that ions with a weak affinity for the solvent are abundant at the interface (Cl^- and I^-), whereas ions with a strong affinity for the solvent may be depleted from the interface (Br^-) depending on the

nature of the counterion. These observations are consistent with the concept of MEIS [68], wherein counterions with a similar hydrated size to the Br- ion lead to strong ion-ion interactions which draws the anion away from the interface.

The cation CDPs were influenced by the nature of the anion. In contrast, the anion CDPs were only influenced by the cation in the case of Br^-. An overall salt depletion at glycerol surfaces is evident from the surface tension measurements whilst NICISS showed that anions are enhanced at the interface. By measuring CDPs of the cations we show that the absence of cations in the interface is responsible for the overall salt depletion. This highlights the importance of directly measuring the individual CDP of the anion and cation simultaneously with NICISS. Based on these results it is important to acknowledge that the cation influence on the anion CDP cannot be ignored and consideration of anion-cation interactions is vital for future ion specific investigations at solvent surfaces. In this journey of exploring the complex nature of ion specificity at solvent surfaces we have also demonstrated the advantage of NICISS as a technique for specific ion investigations which will be thoroughly utilized in upcoming investigations with various solvents.

Our current work, which concentrates on a single solvent, is unable to reveal vital information on the influence of several solvent properties on SIE at interfaces. In particular the polarizability and dielectric permittivity of the solvent, the molecular orientation of the solvent molecules at the surface and the resultant dipole moment at the vapour-solvent interface may all be important. Additionally, the role of the solvent on the individual ion-ion and ion-solvent interactions on the adsorption of ions at surfaces also needs to be evaluated [95, 142]. Investigation of the adsorption of ions at various solvent surfaces and determining the solvation shell with EXAFS are examples how these questions will be investigated along with important contributions from computational studies.

.

CHAPTER 4 : SPECIFIC ION EFFECTS AT FORMAMIDE SURFACES: A REVERSE HOFMEISTER SERIES IN ION CONCENTRATION DEPTH PROFILES

4.1. Introduction:

Current chapter uses NICISS to determine the concentration depth profiles (CDPs) of a range of monovalent anions and cations in formamide (FA). Eleven FA electrolyte solutions were investigated to obtain Cl^-, Na^+, K^+, Br^-, I^- and Cs^+ CDPs. Herein, I aim to understand how the nature of the ions impacts their organisation in the interfacial region of FA and to observe the solvent perturbation towards fundamental SIE. FA is an important solvent for SIE investigation as it represents the simplest amide compound with the biologically important peptide linkage that is thought to have a significant role in the creation of life during the prebiotic earth [234]. It is also an interesting solvent as it acts as the point of series reversal for ion-solvent interaction in the SIE series for two different experiments [71]. It is a polar solvent with highly structured hydrogen bonding, a high dielectric constant (111.0), high surface tension (58.5 mJ m^{-2}), and large polarizability (4.22 $Å^3$) compared to water (1.49 $Å^3$) [209]. These properties of FA make it a relevant non-aqueous solvent to compare against the previously reported SIE trends at water surfaces (see 1.5.3). It also has compatible vapour pressure for measurements employing ultra-high vacuum (UHV) based techniques.

4.2. NICISS Results:

The current investigation focuses on comparisons of CDPs in four different ways:

- Comparison of anions with a common cation.
- Comparison of cations with a common anion.
- Comparison of an anion with different cations.
- Comparison of a cation with different anions.

For the present work it is worth noting that there is some FA evaporation in the UHV chamber in which the experiments are conducted. The evaporation results in an increase of the concentration of the electrolyte solution by 15-20 % over the course of an experiment (the vapour pressure depression is ion-specific, and the evaporation rates differ between each electrolyte solutions [235, 236]). Zhang and Cremer[184] have reported a concentration dependent SIE reversal. Hence, it is important that the consequence of the concentration changes for the SIE investigation is discussed. In Figure II-4 of the Appendix chapter II, I^- convoluted CDPs of KI FA solutions with varying electrolyte concentration clearly shows that above 0.1 m electrolyte solutions, the CDPs of I^- do not change. Thus, it is assumed that a small change in the electrolyte concentration due to evaporation in a high electrolyte concentration regime as used in this chapter should not affect the SIE comparisons.

4.2.1. Comparison of Anions with a Common Cation.

In this section we discuss the CDPs of anions when they are paired with one specific counter-cation. In Figure 4-1 (a), the anions, Cl^-, Br^- and I^- of lithium salts are compared. Cl^- exhibits an enhanced ion concentration in Region 1, followed by a strong depletion in Region 2, whereas Br^- has a peak with concentration slightly lower than the bulk electrolyte concentration in Region 1 and a depletion in Region 2. I^- is depleted in Region 1 and reaches the bulk electrolyte concentration in Region 2. The Cl^-, Br^- and I^- CDPs for sodium salts are shown in Figure 4-1 (b) and potassium salts in Figure 4-1 (c). The CDPs of the anions are similar regardless of the cation. Note that KCl solutions were not investigated because the K and Cl TOF steps cannot be separated in a NICIS spectrum when using He projectiles. Andersson and co-workers [237] have previously measured CDPs for anions of LiI and LiCl at the vapour-FA interfaces and found that the trend of Cl^- and I^- are in disagreement with the measurements we report here. This disagreement could arise from differences in the sample preparation, in particular difference to the present work, the salts had not been roasted. Hua et.al. [238] showed that “as received” salts from suppliers contain organic impurities which influence ionic organisation at solvent surfaces. In this work we roasted the salts at 400˚C before use to remove organic impurities.

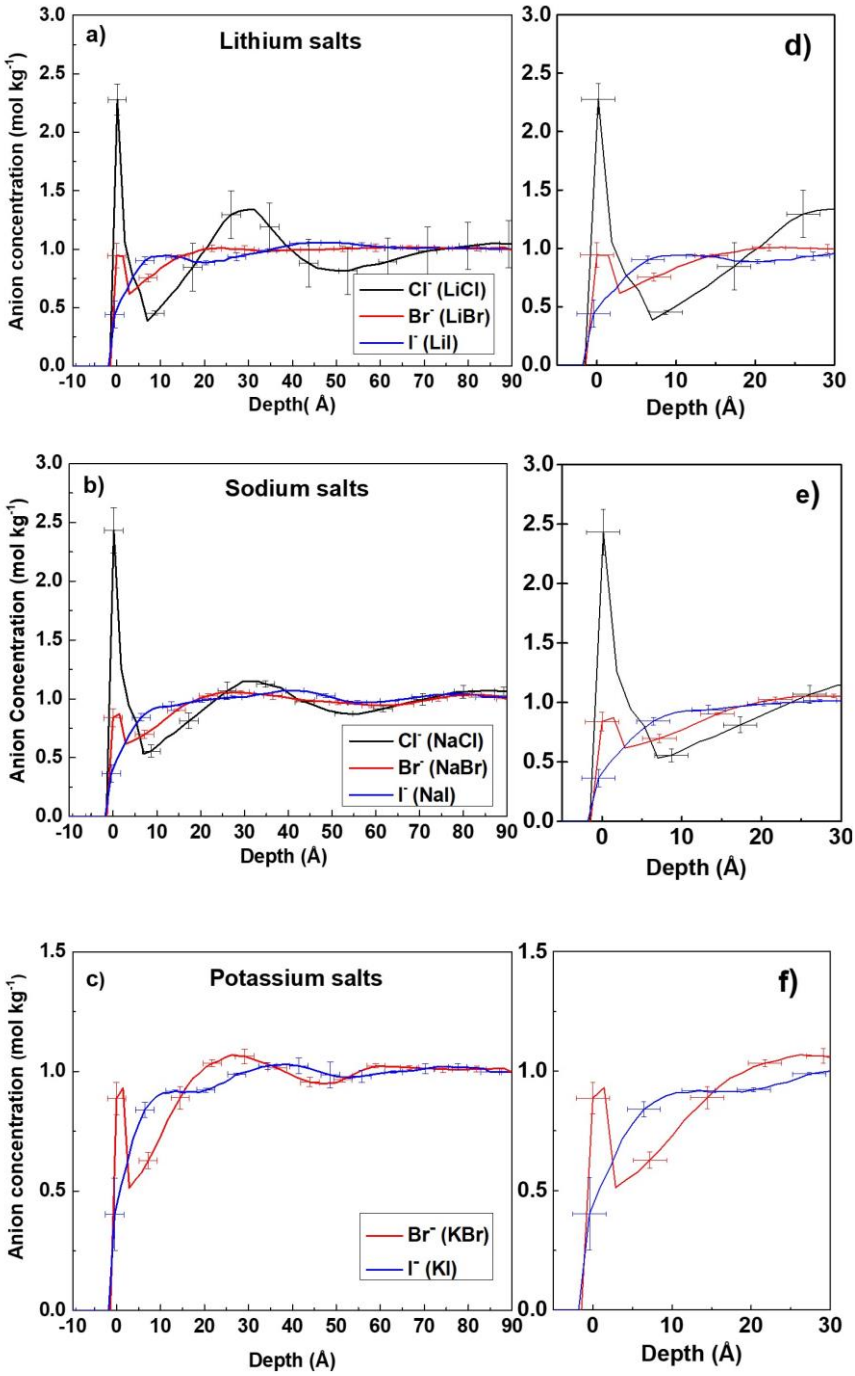

Figure 4-1: Concentration depth profiles of Cl^- (black), Br^- (red), and I^- (blue) ions in 1 m FA electrolyte solutions with (a) Li^+, (b) Na^+, and (c) K^+ as counterions. Panels (d), (e), and (f) are same CDPs comparisons as (a), (b), and (c) respectively but specific to Region 1 and Region 2. For clarity, error bars are only included for every 5th data point.

4.2.2. Comparison of Cations with a Common Anion.

The comparison of CDPs of Na^+ and Cs^+ for chloride salts (Figure 4-2 (a)) show that both cations are depleted in Region 1 and Cs^+ is more depleted in Region 2 compared to Na^+. A similar trend is observed for Na^+ and K^+ CDPs for bromide salts (Figure 4-2 (b)), where K^+ is more strongly depleted in Region 1 than Na^+. It should be noted that the Cs^+ CDP of CsBr could not be obtained directly as

Cs and Br elemental TOF steps could not be separated in the NICISS spectrum using He^0 projectiles. Additionally, the CDPs for iodide salts with different cations could not be compared due to the large uncertainties involved (See Figure II-5 in the Appendix chapter II).

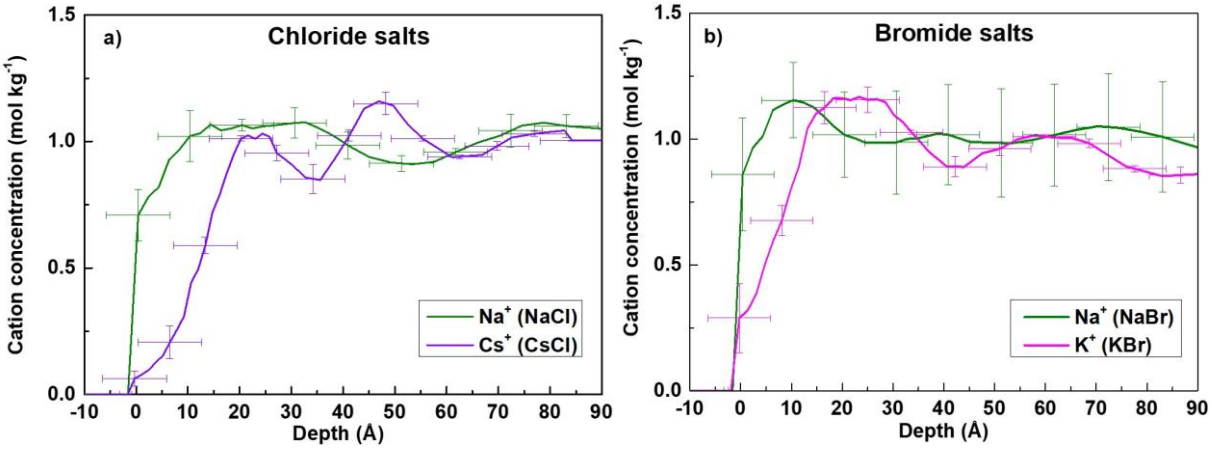

Figure 4-2: Comparison of (a) Na^+ (green) and Cs^+ (violet) CDPs, and (b) Na^+ (green) and K^+ (pink) CDPs, of chloride and bromide salts in FA respectively. For clarity, error bars are only included for every 5th data point.

4.2.3. Comparison of an Anion with Different Cations

In this section we examine the effect of counterions on CDPs of anions measured using NICISS. Cl^-, Br^- and I^- CDPs in FA with various cations are compared in Figure 4-3 (a), (b) and (c), respectively. In Figure 4-3 (a), we observe that the Cl^- are enriched in Region 1 and depleted in Region 2. Further, the Cl^- CDPs do not change with the cation within experimental uncertainty. Note that the oscillations in the bulk region are not considered significant as explained earlier (Section 2.1.7). Br^- has a peak in Region 1 with a depletion in Region 2 (Figure 4-3 (b)) and we see that the Br^- CDPs are the same in both Region 1 and Region 2, regardless of the cation. The I^- CDPs (Figure 4-3 (c)) are depleted in Region 1 and reach their bulk electrolyte concentration in Region 2 while not showing a counterion effect. In summary, whilst each anion exhibits a distinct CDP, these CDPs are largely independent of the counterion.

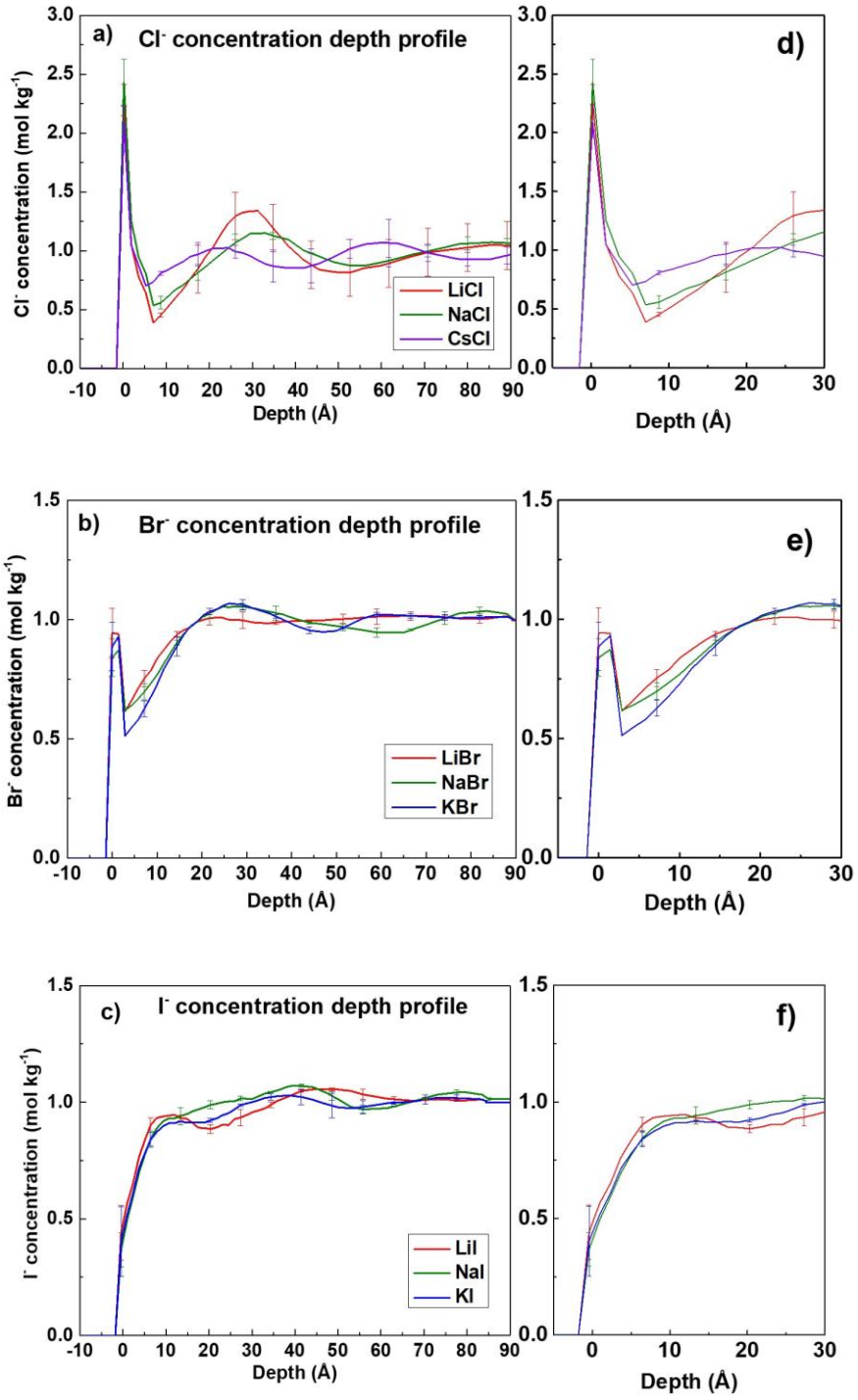

Figure 4-3: (a) Concentration depth profiles of Cl^- ions at the surface of 1 m LiCl (red), 1 m NaCl (blue) and 1 m CsCl (black) FA solutions, (b) Concentration depth profiles of Br^- ions at the surface of 1 m LiBr (red), 1 m NaBr (black) and 1 m KBr (blue) FA, and (c) Concentration depth profiles of I^- ions at the surface of 1 m LiI (black), 1 m NaI (red) and 1 m KI (blue) FA solution. Panels (d), (e), and (f) are same CDP comparisons as (a), (b), and (c) respectively but specific to Region 1 and Region 2. The uncertainty arising from the gas phase calibration will be unchanged for a given ion hence for clarity the depth scale error bars are not included in the figures. Error bars in the concentration are determined from multiple deconvolutions and are only presented for every 5th data point.

4.2.4. Comparison of a Cation with Different Anions

In Figure 4-4 (a), (b), and (c) CDPs of Na^+, K^+, and Cs^+ ions with different counter-anions are shown. The Na^+ CDPs (Figure 4-4 (a)) with Cl^-, Br^- and I^- show a slight depletion in Region 1 which transitions to the bulk concentration in Region 2. However, differences between these CDPs cannot be discerned outside of the uncertainty. The K^+ ion CDPs (Figure 4-4 (b)) with Br^- and I^- show a depletion in Region 1 and a slight enhancement in Region 2. The K^+ ion CDPs are same within the experimental uncertainty when paired with Br^- or I^- ions (the raw NICISS CDPs show weak differences within noise, Figure II-6 in the Appendix chapter II). Cs^+ CDPs with F^- and Cl^- counter-anions (Figure 4-4 (c)) show a strong and similar depletion in Region 1, followed by an slight enhancement in Region 2.

For He projectiles, Cs^+ and Br^- ions have very similar TOF complicating the analysis for CsBr solutions. In order to compare the Cs^+ and Br^- CDPs of CsBr in FA electrolyte solutions with those of the other counterions, we followed the same procedure as described in previous chapter (Section 3.2.2.2) [239]. In Figure 4-4 (d), we have constructed a CsBr TOF profile using the Cs step from CsCl and the Br step from NaBr FA electrolyte solutions and compared it with that of the CsBr TOF profile. The differences in the TOF regions between the profile can be used to examine both Cs (3.63 – 3.78 µS) and Br (3.79 – 3.95 µS) ions. In Figure 4-4 (d) we find there is no difference between Cs^+ in CsCl or CsBr solutions in the Cs TOF region, nor is there a difference between Br^- of NaBr or CsBr in the Br TOF region. The same is found for Cs^+ and Br^- ions when the TOF spectrum is constructed using the Cs step from CsF and the Br step from KBr. This is presented in Figure II-7 (a) and (b) in the Appendix chapter II. Hence, we conclude that the Cs^+ CDP at the FA surface is not influenced by the type of anion. Overall, all the presented data in this section for cation CDPs show minimal influence of the counter-anion, except for I- in the NaI solution, which shows a minor perturbation.

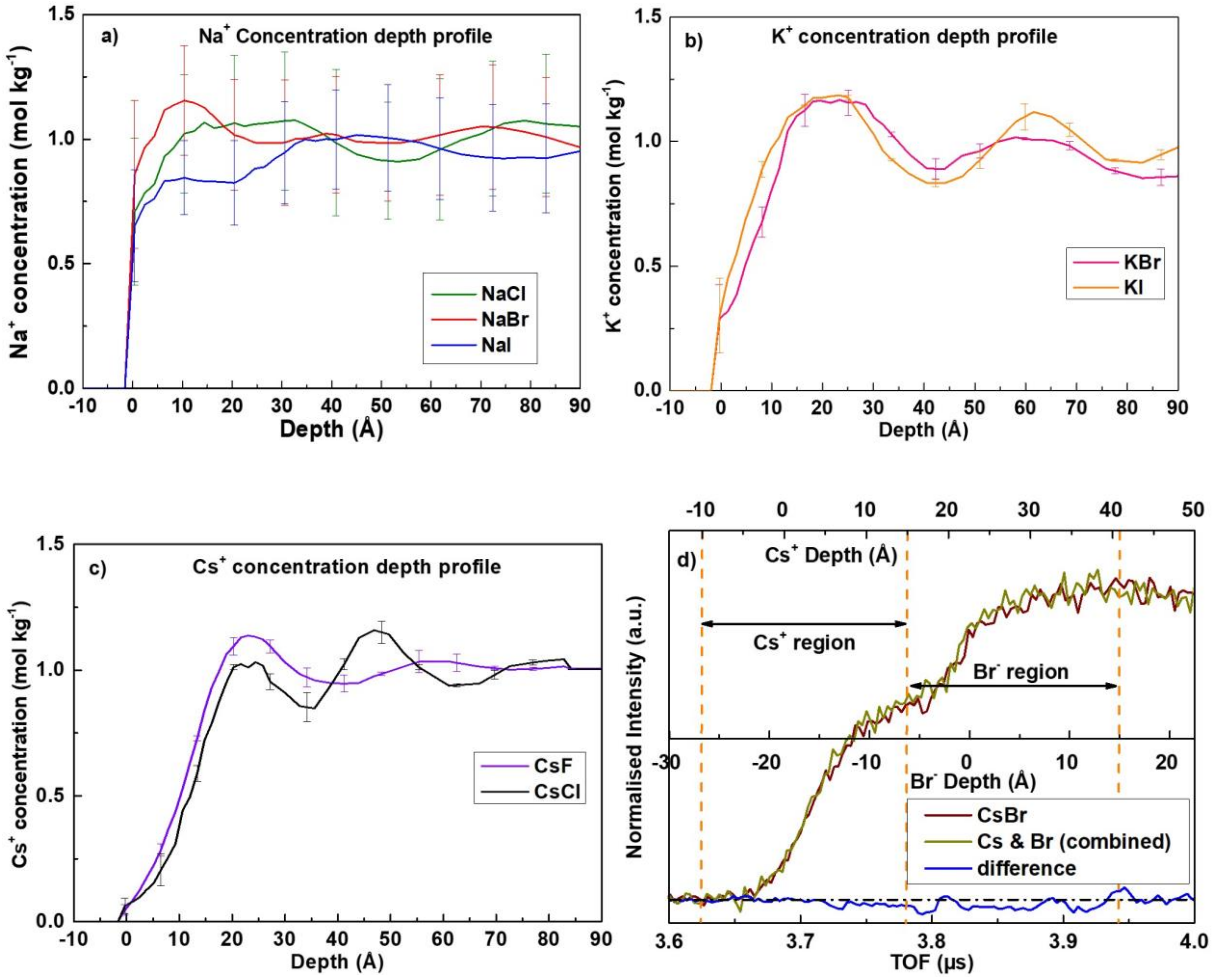

Figure 4-4: (a) Comparison of the concentration depth profile of Na^+ ions in 1 m NaCl (green) and 1 m NaBr (red) and 1 m NaI (blue) FA solutions (b) Comparison of the concentration depth profile of K^+ ions in 1 m KBr (pink) and 1 m KI (orange) FA solutions, (c) Comparison of the concentration depth profile of Cs^+ in 1 m CsF (purple) and 1 m CsCl (black) FA solutions), and (d) The difference (blue) between the measured TOF spectrum of 1 m CsBr (brown) FA solution and a TOF spectrum constructed from 1 m CsCl and 1 m NaBr (pale yellow) FA solutions. Na^+ ion CDP's have larger errors compared to other CDPs due to greater noise in the raw NICISS CDPs.

4.3. Surface Tension of Formamide Electrolytes

The change in surface tension (often expressed as a surface tension increment (STI) per mole of substance) of a solvent upon addition of electrolyte is related to the surface excess of the electrolyte[105]. In Table 4-1, we present the surface tension increments (STI) for 11 electrolyte solutions. We find that the STIs are larger than what is observed in other solvents such as water[134] and glycerol[239], indicating a greater level of overall electrolyte depletion at the surface. It is notable that there are only small variations in the STIs between different electrolytes. Within these small variations it is evident that the anions (when paired with common cation) exhibit a reverse Hofmeister series at FA surfaces, i.e., $Cl^- \geq Br^- > I^-$ (noting that CsF is an exception). The cations have a similar influence on the STIs and hence no clear trend is evident. This is consistent with the strong depletion

of all the cations through measured CDPs and variations in the level of enhancement of anions in Region 1.

Table 4-1: Measured surface tension increments (STI) $\Delta\gamma$ (mJ m^{-2} (mol kg^{-1})$^{-1}$) for electrolytes in FA, calculated from surface tension measurements of solutions at a concentration of 1 molal. The STI of a monovalent inorganic electrolyte in FA is tabulated at the intersection of the column containing the anion and the row containing the cation.

Cations/ Anions	F^-	Cl^-	Br^-	I^-
Li^+		2.2 ± 0.1	2.2 ± 0.1	3.3 ± 0.3
Na^+		2.3 ± 0.1	2.5 ± 0.1	2.9 ± 0.1
K^+			2.3 ± 0.1	2.9 ± 0.1
Cs^+	2.8 ± 0.1	2.3 ± 0.1	2.6 ± 0.1	

4.4. X-ray Absorption Near Edge Structure of Formamide Electrolytes

X-ray absorption studies have long been used to probe the bulk structure of solutions. Of interest here is that techniques such as X-ray absorption spectroscopy of the near edge structure (XANES), provides element specific information. In Figure 4-5, we have measured the XANES spectra of Br^- paired with Li^+, Na^+, K^+, Rb^+, and Cs^+ and observe that it has negligible changes in the XANES region as a function of counter-cation. Hence, the local structure of Br^- in FA is unaffected by the nature of the cation. In addition, in Figure 4-6, the XANES spectra of Cs^+ paired with F^-, Cl^- and Br^- are compared. The fluorescence signal recorded for Cs^+ are weaker due to stronger attenuation of X-rays at lower excitation energy. Within the noise, we suggest that the local coordination structure of Cs^+ is similar when paired with varying counter-ion. We suggest this with confidence as for electrolyte solution of water (see Figure II-8 in the Appendix chapter II) and DMSO (not included here) a larger difference in the XANES spectra is observed. It should be noted that the edge peak intensity for Caesium L_3 edge is higher compared to Bromide K edge because electrons can transition to lower unoccupied orbital from L_3 shell which is forbidden from the K shell.

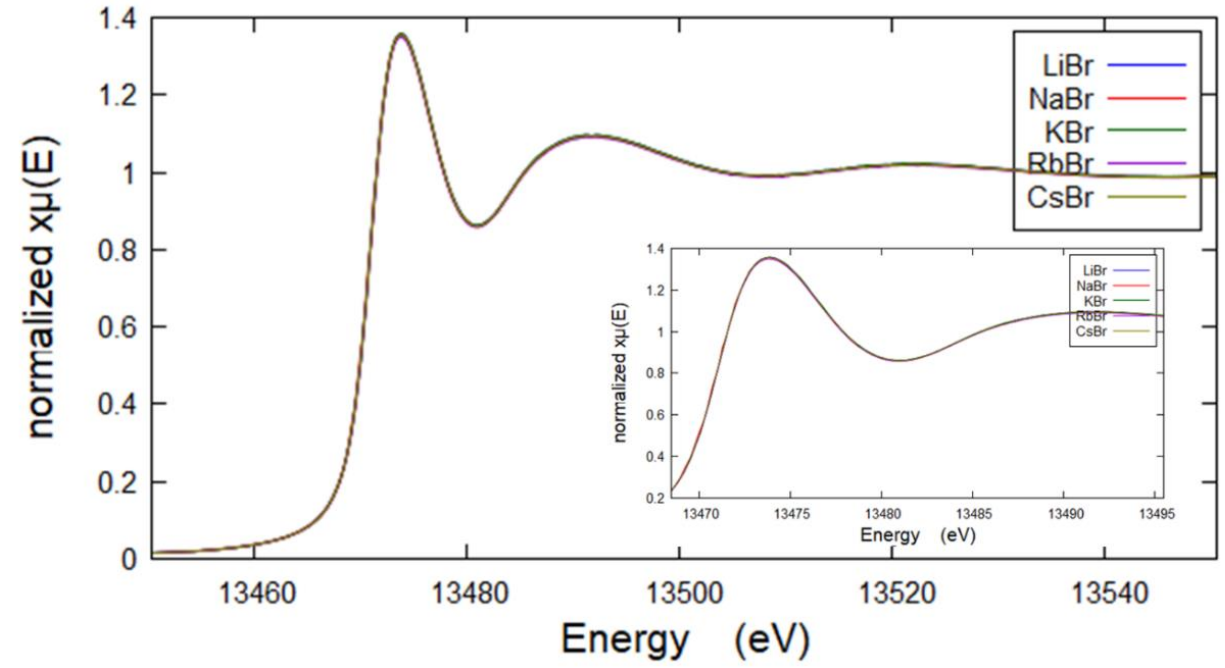

Figure 4-5: Bromide K edge X-ray absorption (xμ) near edge spectrum (XANES) of LiBr (blue), NaBr (red), KBr (green), RbBr (violet), and CsBr (dark yellow) in FA. Inset showing the edge peak of bromide XANES data.

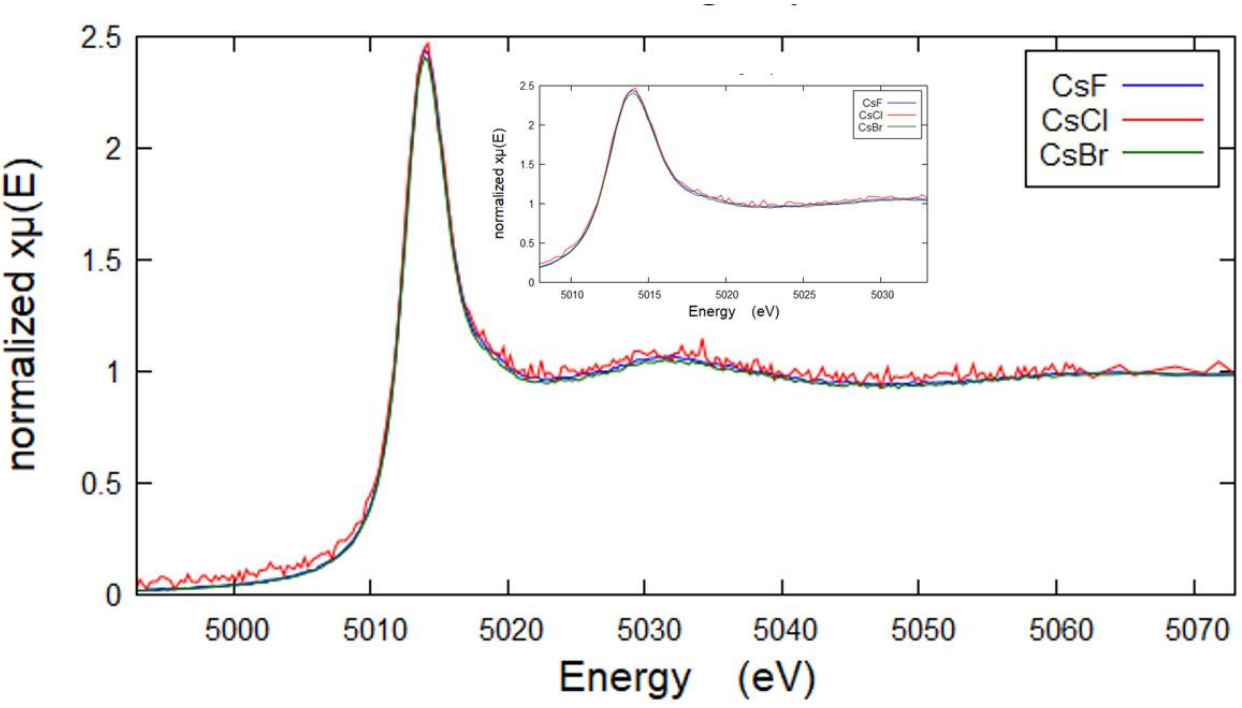

Figure 4-6: Caesium L_3 edge X-ray absorption (xμ) near edge spectrum (XANES) of CsF (blue), CsCl (red), and CsBr (green) in FA. Inset showing the edge peak of Caesium XANES data. The uncertainty due to averaging of noisy triplicate scans are larger compared to the scans presented in Figure 4-5 (see Figure II-9 in the Appendix chapter II).

4.5. Discussion

For SIE investigation in electrolyte solutions, FA provides a valuable comparison to water, as like water it has a highly structured hydrogen bonded network and consequently has a high surface tension and dielectric permittivity. FA has an acceptor number (AN)[k] and a donor number (DN)[l] of 39.8 and 24, respectively, which is different to the AN (54.8) and DN (18) of Water[240].

Here, NICISS has been used to measured and compare the CDPs of individual ions at FA surfaces. This work shows that Cl^- is in excess at the interface (i.e., Region 1) and its counter-cations are strongly depleted from the interface, resulting in an overall negative surface excess. Whilst the latter is evident from STI, the former information can only be obtained with this level of detail from NICISS CDPs (Figure II-10 in the Appendix chapter II for direct comparisons between CDPs of ions of an electrolyte solutions). When considering anions paired with a common cation, anions are concentrated in Region 1 in the order $Cl^- > Br^- > I^-$ and depleted in Region 2 in the same order. This anion enhancement at the vapour-FA interface follows the reverse Hofmeister series, opposed to anions at the vapour-water interface which follow the Hofmeister series (see Figure 1-5) [136]. Notably cations are all strongly depleted from the interface. The CDPs for cations of chloride salts (NaCl and CsCl) and bromide salts (NaBr and KBr) show a SIE trend where larger ions are more depleted at the vapour-FA interface (Figure 4-1).

Implicit in the discussion of the Hofmeister or Lyotropic series is the assumption that the series is not influenced by the nature counterion. Whilst this is sometimes correct, it is known that this assumption is often violated[68, 242]. As NICISS provides information on the CDP specific to a particular ion, we have investigated the influence of the counterion, noting that the arrangements of both the anions and cations at FA surfaces are largely independent of the nature of the counterion (Figure 4-2 and Figure 4-3). Thus, it is evident that there is negligible anion-cation interaction at FA surfaces. This is in stark contrast to the results at glycerol and water surfaces. At glycerol surfaces, we observed that the Br^- organisation was strongly influenced by the nature of the counter-cations[239]. Further, at water surfaces the I^- concentration was higher with Li^+ compared to K^+ as the counter-cation[140]. The organisation of ions at FA surfaces follows the "Hofmeister paradigm", wherein the nature of the counterion can be ignored when considering the effects of the ion. XANES comparisons presented in Figure 4-5 and Figure 4-6 reflects our observations here; the arrangement of Br^- at the interface is independent of the nature of its paired counter cation (see Figure 4-3 (b)) and the depletion of Cs^+ at the interface is independent of the nature of its paired counter anion (see Figure 4-4 (c) and (d)). We attribute the lack of influence of the counterion to the structure of FA, as

[k] Acceptor number (AN) is an empirical measure for the effectiveness of anion solvation. 240.Mayer, U., V. Gutmann, and W. Gerger, *The acceptor number ? A quantitative empirical parameter for the electrophilic properties of solvents.* Monatshefte für Chemie/Chemical Monthly, 1975. **106**(6): p. 1235-1257.
[l] Donor number (DN) is an empirical measure for the effectiveness of cation solvation. 241.Gutmann, V., *Empirical parameters for donor and acceptor properties of solvents.* Electrochimica Acta, 1976. **21**(9): p. 661-670.

the anions and cations interact at physically separated locations on the FA molecules. Anions in FA have a competition for interaction site with the hydrogen dipole of C-H group and N-H group, while cations will preferentially interact with the C=O group of the FA structure [243]. However, it should be noted that F^- may be more likely to show a counterion effect as the F^- often leads to series reversals due to its high electronegativity and unfavourable solvation[68]. Our investigation of fluoride salts was limited here due to solubility limits and the weak backscattering of projectiles from fluoride ions in solutions.

Why would the ionic series be different between water and FA? Mazzini et al. previously suggested that the series reversal for ionic interactions can result from differences in their polarizabilities [71]. Their work was built on Collins' concepts of the law of matching water affinity [65]. Mazzini et al. proposed that ions that are more polarisable interact more favourably with a highly polarizable solvent, and ions that are less polarizable interact more favourably with a less polarizable solvent. Within this framework, ions that do not interact strongly with the solvent are expected to be present at the interface. As such, a change in polarizability of the solvent could drive a series reversal. This explanation is in accordance with the experiments of Mazzini et al. with methanol, FA, DMSO, and PC in the bulk [71].

Polarizability is associated with dispersion forces; however more recent work strongly suggests that the electrostatic interactions play a greater role in determining the relevant strength of SIE. Gregory et al.[89] have characterised the site-specific electrostatic interactions of ions with water through the parameter þ*,* and demonstrated that in a great variety of experiments the strength of ions SIE is highly correlated with þ. This concept can successfully be extended to non-aqueous solvents by considering the tendency of a solvent to donate electron pairs to a cation through the donor number (DN) or to accept electron density from an anion through the acceptor number (AN) [89]. In this case, the change in electrostatic interaction energy between ion and solvent molecules can be indicated using the DN and AN for cations and anions, respectively. Water (54.8) has a much higher AN than FA (39.8) [240]. Therefore, the series reversal observed for the anions may be related to a reduction in the strength of electrostatic interactions in FA compared to water due to the greater Lewis acidity of water. As such, we might expect that the anion series reversal observed at the vapour-FA and vapour-water interface would be reflected by the difference in AN for these solvents (as observed by Gregory et al. in another investigation [88]), but the precise mechanism of this reversal is unclear. What is also not clear is whether the reversal observed is due interfacial or bulk ionic effects.

In case of bulk ionic effect, within the Collins concept, we can suggest that the relative affinity of ions for water (or solvent) determines the comparative strength of their affinity with solvents surfaces - ions of higher solvent affinities are more strongly depleted from the surface, since they prefer to reside in the bulk solution. To determine the relative solvation affinities of anions, we have calculated their solvation free energies (binding energy) in FA (obtained from IonSolvR database [225]). The

solvation free energies of Cl^-, Br^-, and I^- in bulk FA are -257.9 ± 1.3, -187.3 ± 2.6 and -130.5 ± 1.3 KJ mol^{-1} respectively, suggesting that the preference of ion for FA bulk is strongest for Cl^- then Br^- and least for I^-. This solvation free energy trend agrees with the interaction trend suggested from NMR measurements and infers that the I^- should be more enhanced at the vapour-FA interface compared to Br^- and Cl^-. This would be in contrast with the NICISS CDPs and STI trend measured here in case Collin's paradigm would apply. This highlights that we are yet to develop a framework for understanding how the vapour-solvent interface perturbs SIE. To better understand SIE, we need to understand how the interface changes interaction between ions and solvent compared to the bulk.

4.6. Conclusion

In the current work we have investigated and compared concentration depth profiles (CDPs) of various anions and cations at the vapour-FA interfaces. The anion CDPs as a function of a common cation shows that anions are present at the interface following a reverse Hofmeister series (i.e., Cl^- > Br^- > I^-) with most presence for Cl^- at vapour-FA interface and the least for I^-. We also observe a reverse Hofmeister series for the cations at the surface over a limited data range, in which the decreasing concentration of the ions follows the series Na^+ > K^+ and Na^+ > Cs^+ for bromide and chloride counter-ions, respectively. However, all cations were observed to be depleted from the interface relative to the bulk. These results for the first time show the reversal of the Hofmeister series at the FA interface compared to that of water. It was also found that the arrangement of ions at the interface were largely independent of the counterion present for both the cations and anions, indicating weak anion-cation interactions. These observations show that the ions at FA surfaces follow a "Hofmeister paradigm" where the specific identity of the counterion is unimportant. Both reversal of the Hofmeister series and minimal anion-cation interactions are qualitatively consistent with the STIs of the FA electrolyte solutions. The observed series reversal is consistent with explanations based on both the polarizability of the solvent and electrostatic interactions between the ions and the solvent. Further information from the study of other solvents is needed to unravel the role that the solvent plays in the organisation of ions at interfaces and to understand how the bulk ionic interactions dictates the surface presence.

CHAPTER 5 : WEAK SPECIFIC ANION TRENDS IN MEASURED CONCENTRATION DEPTH PROFILES AT PROPYLENE CARBONATE AND BENZYL ALCOHOL SURFACES

5.1. Introduction

In the current chapter, we have investigated ionic presence/absence at the propylene carbonate (PC) and benzyl alcohol (BA) surfaces. PC is an aprotic solvent while BA is a protic solvent. Both solvents are selected due to their distinct physical and chemical properties as listed in Table 2-1. Both solvents have similar surface tension values as measured here. PC and BA has a surface tension value of 41.8 ± 0.2 and 40.0 ± 0.4 mJ m^{-2} respectively. Their surface tension value suggests that both solvents have similar interfacial intermolecular interactions, even though the hydrogen bonding nature of both solvents is different. Thus, these solvents are selected to investigate the effect of hydrogen bonding towards ion specificity at solvent surfaces. Comparing the ion specificity in hydrogen-bonded and non-hydrogen-bonded solvents allows us to test the influence of hydrogen bonding nature which have been indicated as one of the enablers of SIE [205]. Hence, based on previous descriptions, both solvents are expected to show differing ion specificity and the ion specific trend should be prevalent at the BA surfaces. In addition, BA and PC have lower vapour pressure thus making these solvents as attractive choice for UHV based NICISS measurements.

A collaborative MD simulation and SFG work for PC suggests that at a vapour-solvent interface, PC molecules are lying flat at the molecular axis where the C=O group has a slight tit at the molecular axis and the methyl group at the end of the carbonate ring protruding in the vapour phase [244, 245]. For BA, angle-resolved NICISS have measured that the BA molecules are titled at an angle of 68º ± 8º at the molecular axis with hydroxyl moiety (-OH group) pointing inwards towards the solvent's bulk[196]. Furthermore, BA is also a solvent with low dielectric permittivity and makes for an interesting comparison with the SIE trend observed at FA (high dielectric constant solvent) and glycerol (intermediate dielectric constant solvent) surfaces in Chapter 3 and Chapter 4 respectively.

5.2. Results and Discussion

All ion concentration depth profiles (CDPs) presented here are a result of the deconvolution of the respective spectra. Details related to deconvolution and the uncertainty associated are described in Sections 2.1.7 and 2.1.8 respectively. In Figure 5-1, the deconvoluted CDP of I^- (green) is shown along with definitions of the main regions of interest in the CDPs presented here. The concentration of I^- is depleted at <0.5 nm depth region which is defined as Region 1. Region 1 is also referred to as 'the interface'. A concentration similar to the bulk electrolyte concentration is observed at the depths of 0.5 – 2.5 nm, which is defined as Region 2. In the present work, only Region 1 and Region

2 are of interest. At larger depths beyond 2.5 nm, it is expected that the ions have reached their bulk concentration as shown in Figure 5-1.

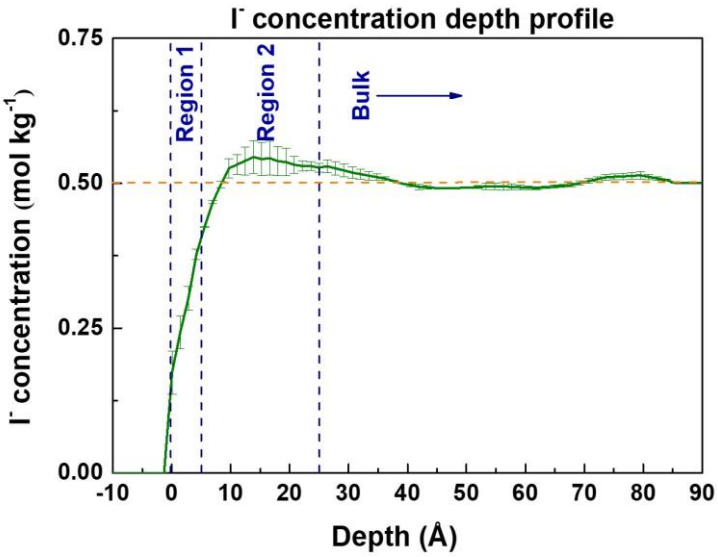

Figure 5-1: I^- concentration depth profile of 0.5m NaI with BA solutions showing the region of interest for herein presented results. The dashed orange line represents the bulk electrolyte concentration.

5.2.1. Electrolytes in Propylene Carbonate:

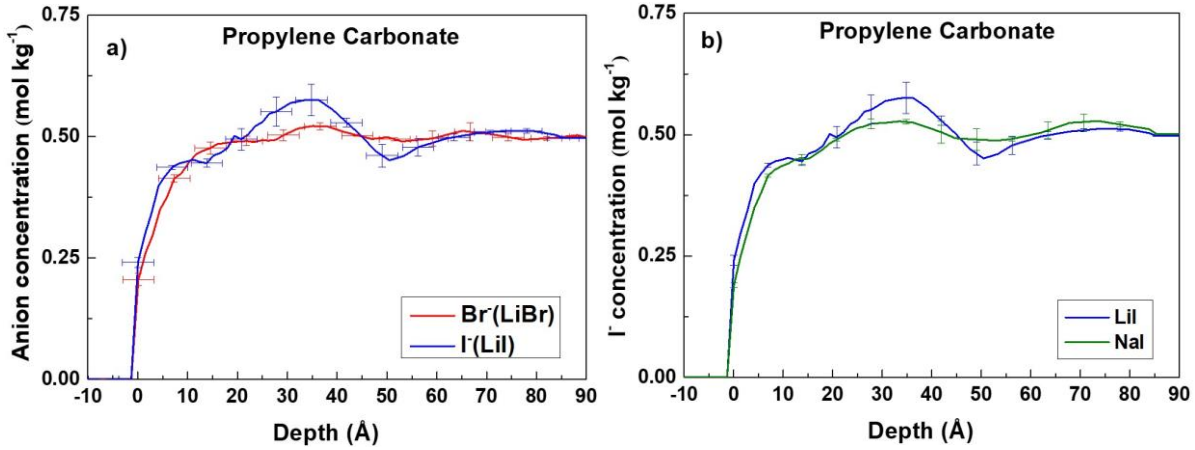

Figure 5-2: Concentration depth profile comparison of (a) Br^- (red) and I^- (blue) of lithium salts and (b) of I^- with varying counter-ion as Li^+ (blue) and Na^+ (green) in propylene carbonate solutions. In (b), I^- CDPs of both electrolyte solutions compared are calibrated using the same gas phase measurements. Thus, the error in depth calibration will be the same and not included for clarity. Error bars are only included in every 5 data points for clarity.

The CDPs of anions with Li^+ as a common counter-cation for PC are shown in Figure 5-2 (a). Both anions are depleted in Region 1 and then reach the bulk electrolyte concentration in Region 2. Hence, no specific anion effects are observed in ion CDPs at PC surfaces. In Figure 5-2 (b), I^- CDPs paired with varying counter-cations (Li^+ and Na^+) at PC surfaces are presented. I^- is depleted in Region 1 and reaches its bulk concentration in Region 2 when paired with Li^+ and Na^+. Hence, no

counter-ion effects are observed for I^- CDPs. All investigated anion CDPs at PC surfaces follow a monotonic trend (within experimental and deconvolution uncertainty).

In Figure 5-3, Surface tension increment (STI) relative to the pure solvent for PC solutions is presented where LiI electrolyte solutions had the largest STI while LiBr the least. NaI had a similar STI compared to LiBr electrolyte solutions within the uncertainty. Based on the STI, we observe specific anion and specific cation trends for decreasing electrolyte depletion as LiI > LiBr and LiI > NaI respectively with the greater sign (>) indicating a stronger depletion (i.e., LiI is strongly depleted than LiBr).

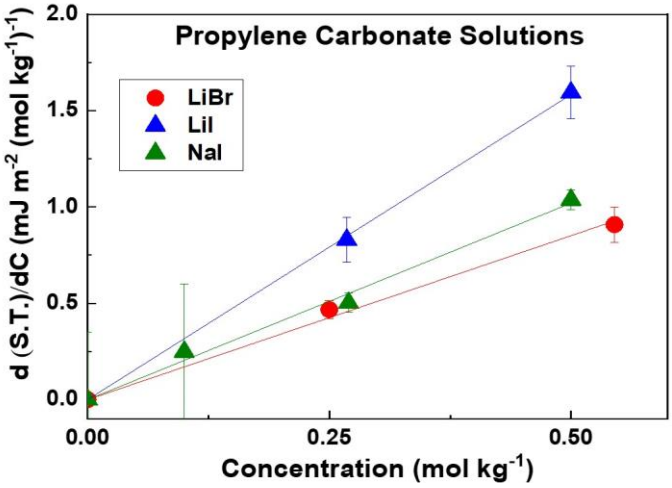

Figure 5-3: Surface tension increment (STI) relative to the pure solvent at varying electrolyte concentration (d(S.T.)/dC) comparisons of 0.5m LiBr (red), LiI (blue) and NaI (green) in propylene carbonate solution.

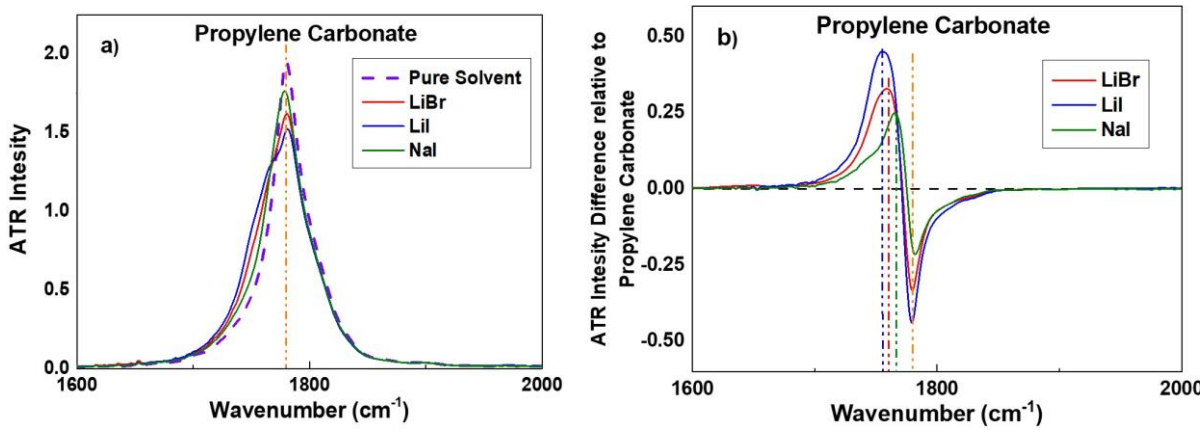

Figure 5-4: (a) Comparison of ATR-FTIR spectrums of pure PC (dashed purple line) with 0.5 m, LiBr (red), LiI (blue) and NaI (green) electrolyte solution and (b) difference in ATR-FTIR spectrum of electrolyte solution compared to the pure solvent. The dashed orange line shows the centre for the C=O group of PC. The dashed red, blue and green lines in Figure 4 (b) are drawn to visualise the peak shift in LiBr (red), LiI (blue) and NaI (green) electrolyte solution respectively compared to the pure solvent (orange).

As discussed in the previous chapters [239], based on Collins' framework, if ionic interaction is favourable in the bulk, then their presence at the solvent surfaces will be opposed and vice versa. We define this as the bulk vs surface affinity approach. Therefore, to investigate the bulk interaction of ions we have performed ATR-FTIR measurements of PC electrolyte solutions. It should be noted that for current investigations in comparison to NICISS CDPs, ATR-FTIR measurements can be considered the bulk of the solvent and discussed here as such because NICISS measurement is of the nanometres (nm) range and ATR-FTIR is in micrometres (μm).

Within the investigated IR range, propylene carbonate of the IR spectrum shows various changes due to electrolyte presence. Cations are known to preferentially interact with the negative dipole which is located on O of the PC molecules. Hence for cation interactions, we focus on vibrational changes recorded for C=O, whereas similar observation of vibration changes is observed for O-C-O stretch and discussed in the Figure III-5 of the Appendix Chapter III. In the propylene carbonate ATR-FTIR spectrum, the changes in dipole moment derivative for anions interactions site i.e., C-H bonds are small and similar as discussed in the Figure III-6 and 7 of the Appendix Chapter III. This is expected because PC favours asymmetric solvation of cations over anions as reported previously [246] thus the anion specificity in ion-solvent interaction is weaker.

In Figure 5-4 (a), the ATR-FTIR spectrum for the C=O band (carbonyl moiety) i.e., the peak at ~ 1780 cm^{-1} is presented of pure PC (dashed purple) with LiBr (red), LiI (blue) and NaI (green) electrolyte solutions. Figure 5-4 (a) shows a shoulder formation for C=O stretch in electrolyte solutions corresponding to new peak assignments within 1756 – 1766 cm^{-1}. These new peak assignments are representative of cation interacting with the negative dipole i.e., O of the C=O group. These peaks appear as cations interact with the O of the C=O group and weaken the C=O bond leading to a redshift compared to the pure solvent. Therefore, the larger red shift in the peak assignment (and increase in the peak intensity) due to cation interaction with the negative dipole is indicative of stronger cation interaction. This has been reported previously by various vibrational spectroscopy studies investigating PC electrolyte solutions [247-250].

Cations' effect towards dipole moment changes for PC is significant as shown in Figure 5-4 (a) and (b). Presenting Figure 5-4 (a) in terms of differences in the spectrum from the pure solvent (Figure 5-4 (b)), we observe a shoulder formation i.e., a new peak at ~ 1756 cm^{-1} in the case of LiI electrolyte solution. For LiBr and NaI solution this peak can be assigned at ~ 1760 and ~ 1766 cm^{-1} respectively. As mentioned before, the red shift in the peak (and increasing intensity) to the lower wavenumber created from shoulder formation (Figure 5-4 (b)) compared to ~ 1780 cm^{-1} corresponds to increasing cation interaction with the C=O moiety of PC. This observation of the strongest cation interaction with propylene carbonate based on ATR-FTIR results follows the order of LiI > LiBr and LiI > NaI for specific anion and specific cation trends respectively with the greater sign (>) indicating a stronger interaction (i.e., LiI has stronger interaction than LiBr). In context of the bulk vs surface affinity

approach, we expect that the strong interacting cations will be partitioned more in the bulk compared to PC surfaces and vice versa. Based on the cation interactions suggested from the ATR-FTIR spectroscopy, the depletion of cation for electrolyte solutions should follow the order of LiI > LiBr and LiI > NaI for specific anion and specific cation effect.

The STI of an electrolyte solution is the experimental evidence for the strength of depletion of the electrolyte i.e., the larger STI means larger depletion of electrolytes in conjunction with the Gibbs equation (Section 1.5.1). Reiterating the earlier observation, the STI trend as shown in Figure 5-3 is LiI > LiBr and LiI > NaI. NICISS CDPs show similar depleted CDPs for anions in LiI and LiBr electrolyte solutions and for I^- in LiI and NaI electrolyte solutions (Figure 5-2 (a) and (b)). The latter observation suggests that the variation in the STI of constituting electrolyte solution of LiI and NaI is caused by the cations. This suggests that Li^+ is more depleted compared to Na^+ at PC surfaces when paired with I^-. This trend of specific cation effect of electrolyte solution depletion is akin to the above-mentioned trend from the ATR-FTIR measurements. Hence, the bulk vs surface affinity approach correlates well with the cation specificity observed at PC surfaces. Further, this trend is also supported by the bulk binding energy (solvation-free energy) data of Li^+ (-95.0 kJ mol^{-1}) and Na^+ (-71.9 kJ mol^{-1}) [251].

Interestingly, the earlier observation of similar anion CDPs for lithium salts (Figure 5-2 (a)) but variation in their STI (Figure 5-3) infers stronger depletion for Li^+ when paired with I^- than when paired with Br^-. Similarly, in the bulk of PC electrolyte solutions, Li^+ interaction is stronger with the C=O group of PC molecule in the LiI electrolyte solution compared to the LiBr electrolyte solution. Each observation suggests that Li^+ behaves differently when paired with Br^- compared to I^-, depicting the role of anion-cation interaction. It should be noted that NICISS measurements compared to the surface tension measurements are performed at a lower temperature (see Section 2.6). We expect that these temperature differences do not cause a variation in the SIE within the STI (as observed previously for aqueous electrolyte solutions, see Figure III-3 of the Appendix Chapter III). However, the lowering of temperature should lower the STI differences between electrolytes solutions. Thus, we only compare the ion CDPs and STI differences together if there is a large enough difference as observed for LiI and NaI electrolyte solutions and not for the NaI and LiBr electrolyte solutions.

5.2.2. Electrolytes in Benzyl Alcohol

In Figure 5-5 (a), anion CDPs paired with Li^+ as a common counter-ion for BA are shown. These anions (Cl^-, Br^-, and I^-) show monotonic CDP and are depleted in Region 1 then reach the bulk electrolyte concentration in Region 2. Hence, no specific anion effects are observed for anion CDPs at BA surfaces. In Figure 5-5 (b) for I^- CDP paired with Li^+ at the vapour-BA interfaces, I^- follows a monotonic depletion trend as observed for anions in Figure 5-5 (a). Similar CDP is observed for I^- paired with Na^+ suggesting no counter-cation effects on anions CDPs. Therefore, no counter-ion

effects are observed for I^- CDPs. All anions have similar CDPs at BA surfaces which follows a monotonic depletion trend.

In Figure 5-6, STI relative to the pure solvent for BA electrolyte solutions are compared. Here, NaI has the largest STI while LiCl the smallest; LiBr and LiI have a similar STI within the uncertainty and fall between the STIs of NaI and LiCl electrolyte solutions. The decreasing depletion of electrolytes at BA surfaces from STI follows the specific anion and specific cation trend of LiI = LiBr > LiCl and NaI > LiI respectively. Interestingly, we observe that the STI trend between LiI and NaI has flipped at BA surfaces compared to the PC surfaces (Figure 5-3).

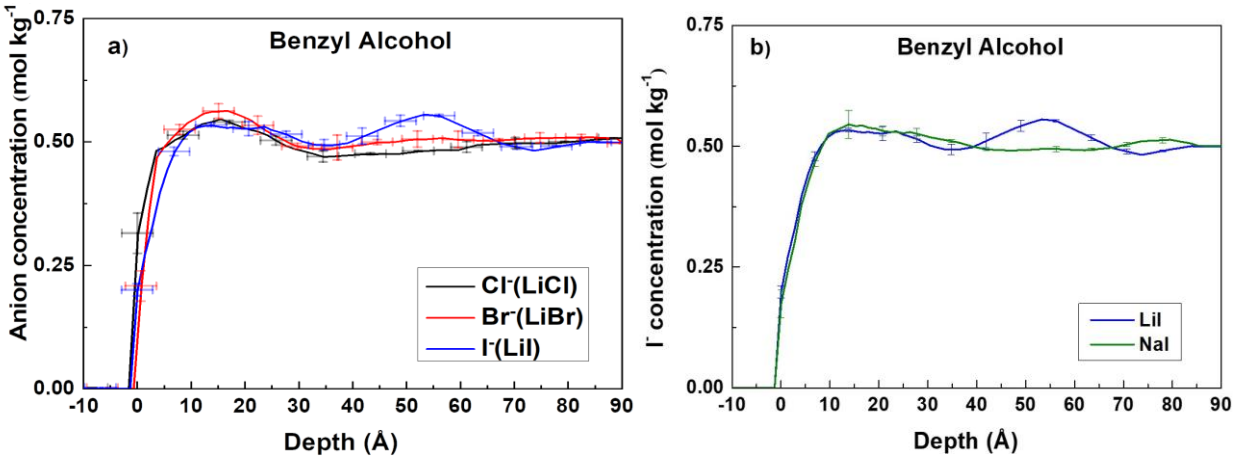

Figure 5-5: Concentration depth profile comparison of (a) Cl^- (black), Br^- (red), and I^- (blue) with common counter-ion as Li^+ and (b) I^- with varying counter-ion as Li^+ (blue) and Na^+ (green) in propylene carbonate solutions

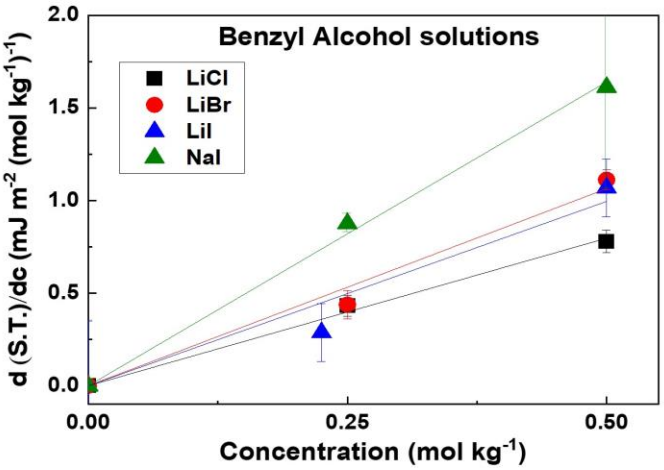

Figure 5-6:Surface tension increment (STI) relative to the pure solvent comparisons at varying electrolyte concentration (d(S.T.)/dC) of LiCl (black), LiBr (red), LiI (blue) and NaI (green) in BA electrolyte solutions.

As noted earlier, the NICISS measurement is performed at a lower temperature compared to the surface tension measurements. Thus, it can be suggested that the small difference observed for LiCl compared to LiBr and LiI will diminish at the lower temperature (see Figure III-3 of the Appendix

Chapter III). As such, the specific anion effect based on the STI of lithium electrolyte solutions can suggested to be the same when interpolated to lower NICISS measurement temperature. In that case, the weaker specific anion effects for the STI of lithium electrolyte solutions is considered to be consistent with the absence of a specific anion effect observed from the anion CDPs. It is expected that the difference in the STI of NaI will persist due to a much larger STI compared to the rest of the electrolyte solution.

Since anions CDPs are unaffected by the anion identity and the counter-ion identity, we can discuss that the STI change is mostly due to differences in the cations' preference for the bulk thus cation depletion. Therefore, for the iodide electrolyte solution comparison we expect that the Li^+ paired with I^- is less depleted than the Na^+ paired with I^-. Coincidentally, in the bulk through ATR-FTIR data (Figure III-9 of the Appendix Chapter III) we observe that the NaI electrolyte solutions shows a distinct behaviour i.e., blue shift for the hydroxyl moiety IR band compared to other electrolyte solutions and pure benzyl alcohol. However, the shift in the hydroxyl moiety IR band, especially a blue shift is ambiguous [252] and therefore not discussed here (for detailed description see *ATR-FTIR results of electrolytes in Benzyl alcohol* in the Appendix Chapter III).

We have also calculated the bulk solvation-free energy data for single anion interaction with BA in the bulk from the IonSolvR database [225]. The bulk solvation-free energies for Cl^-, Br^-, and I^- in BA are -368.5 ± 0.5, -362.6 ± 0.5, and -241.15 ± 0.5 kJ mol^{-1} respectively (the errors are the standard error in the binding energy of the equilibrated MD trajectory). Within the previously discussed Collins framework, this would mean that the favourable interaction of the anion in the bulk of BA decreases in order as $Cl^- > Br^- > I^-$. Suggesting that the anionic presence at BA surfaces should follow the decreasing ion concentration order as $I^- > Br^- > Cl^-$. This is in contrast with the NICISS CDPs which shows weaker variation in anions CDPs for lithium salts (Figure 5-5 (a)). Thus, the bulk vs surface affinity approach does not work for anions at BA surfaces. This observation suggests that we need to develop a different framework for relating bulk interaction to the surface presence as this approach correlates well with ions at PC surfaces but not with the ions at BA surfaces.

Nevertheless, in the current investigation, we have measured various interesting results for anionic CDPs at PC and BA surfaces. The NICISS CDP for anions follows similar depletion and ion specificity trends at PC (aprotic) and BA (protic) surfaces. This means, that the ion specificity in anionic distribution at solvent surfaces is independent of the hydrogen bonding (for the limited sets investigated here). Based on our knowledge, this is the first experimental evidence suggesting that the ion specificity in anion distributions is independent of the hydrogen bonding nature at solvent surfaces.

Further, the counter-cation effect for I^- CDPs is also negligible for Li^+ and Na^+ at both PC and BA surfaces. Perhaps, the strong depletion of anions from the interface consequently leads to no counter-ion (cation) effect for their CDPs. Because if anions are absent in the interfacial region, cations will consequently be absent in the interfacial region to maintain electroneutrality. Thus,

cations' absence in the interfacial region can lead to a weaker influence. Unfortunately, due to weaker backscattering signals from cations at currently investigated electrolyte concentration, the cation distribution cannot be obtained here and for a detailed understanding this observation should be further investigated using surface potential and/or phase-sensitive SFG measurements [127, 253].

From current results, we also observe a strong solvent perturbation since the STI trend between LiI and NaI depletion is reversed at PC surfaces compared to the BA surfaces. This perturbation is mostly related to the change in cations' depletion in PC and BA as NICISS measurement show similar anion CDPs. Thus, the cation effect in overall electrolyte depletion is dominant. Future work is needed to understand the strong role of cations in electrolyte solution depletion and their solvent perturbation. Earlier, Levin and co-workers had observed that while keeping the anionic behaviour constant and by changing the hydrated radius of the cation, they could predict the correct STI and the SIE trends within the STI for aqueous electrolyte solutions [117]. To understand currently observed cationic behaviour, Levin et al.'s approach sound reasonable. However for this test, a framework to explain ion specificity at various solvent surfaces needs to be developed.

5.3. Conclusion

Employing NICISS in the current work we have investigated and compared concentration depth profiles (CDPs) for limited sets of monovalent electrolytes at the propylene carbonate and benzyl alcohol surfaces. We have measured that the ion specificity (specific anion effect and counter-ion effect) for the anionic organisation at vapour-solvent interface is weak and follow a similar trend for both protic and aprotic solvents. This is an important observation suggesting that the hydrogen bonding nature of solvent does not define anionic CDPs at the PC and BA interfaces.

At PC surfaces, the decreasing electrolyte depletion trend observed from surface tension measurements are LiI > NaI and LiI > LiBr while anions show similar NICISS CDPs. Considering the similar NICISS CDPs for anions, this STI trend can be suggested to be dominated by the cations. This dominant cation trend is consistent with the ion interaction in the bulk of PC as observed from the ATR-FTIR spectroscopy. Similarly, at BA surfaces, the decreasing electrolyte depletion trend observed from surface tension measurements are LiBr = LiI > LiCl and NaI > LiI while anions show similar NICISS CDPs. The earlier trend is expected to be consistent with the weaker specific anion trend observed from NICISS measurement if interpolated at the lower temperature. Further, the bulk solvation free energy data suggests that the bulk vs surface affinity approach discussed for ions at PC surfaces do not persist for ions at BA surfaces. Hence, a different framework is needed to relate bulk behaviour of ion to its solvent surface presence.

CHAPTER 6 : DISCUSSION AND CONCLUSION

6.1. Overview

Inorganic electrolytes at solvent surfaces have been an interesting topic of investigation since the observation that most of these electrolytes increase the surface tension of water [101]. In doing so, some inorganic electrolytes increase the surface tension value more compared to the other electrolytes and follow ion specific trend [105]. In this interesting topic of investigation, the surface tension change only provides the total excess of electrolytes (constitute the anions and cations) and does not provide any information regarding the location or distribution of ions along the depth scale at water (or solvent) surfaces. This information on the distribution of ions is relevant for various interfacial processes [69, 194, 254-256] and has a significant impact on our understanding of atmospheric chemistry [257]. Herein, I have investigated ion specificity at 4 non-aqueous solvent surfaces and directly measured the separate concentration depth profiles (CDPs) of anions and cations at these solvent surfaces. A summary of these experimental findings is listed below.

In chapter 3, a large set of electrolytes to examine the specific ion trend at non-aqueous solvent surfaces i.e., glycerol surfaces are investigated. It was observed that the Cl^- and I^- were equally enhanced at the vapour-glycerol interface independent of the counter-ion but Br^- concentration was dependent on the counter-cation (i.e., Li^+, Na^+, K^+ and Cs^+). This counter-cation dependence for Br^- concentration at the vapour-glycerol interface followed the Laws of Matching effective ion size (MEIS) [68], where ions of similar effective ion sizes have stronger anion-cation interaction thus cations can draw Br^- away from the interface, but if their association is weaker (as expected in case of Li^+), Br^- can partition to the interface. Furthermore, the enhanced presence of Cl^- at the interface dismisses the belief that only large polarizable ions can adsorb at the vapour-solvent interfaces [112, 116]. Within this large set of electrolytes investigated, it was also observed that Cs^+ and K^+ were relatively depleted compared to the anions. In their depletion, a specific ion trend was observed where Cs^+ and K^+ presence is expected to depend upon its counter-anion. Finally in this chapter, direct experimental results are provided that support previous computational studies describing the anion enhancement at the vapour-solvent interface with overall inorganic electrolyte depletion.

In chapter 4, presence/absence of ions at the formamide (FA) surfaces were investigated, where a specific ion series reversal is observed at the compared to the specific ion series reported at aqueous surfaces. In this chapter, both specific anion and limited set of cation series were reversed at the FA surfaces. These results were further complemented by the surface tension increment (STI) trend observed for these inorganic electrolyte solutions. Further, the trend in the STI of formamide electrolyte solutions for sodium and potassium halides complied by Marcus are also in agreement with current observation [258]. Interestingly, at FA surfaces for the investigated electrolyte sets, we observed a negligible counter-ion effect that were similar to the bulk coordination of bromide and

caesium electrolyte solutions. The ion specificity at FA surfaces followed a different trend compared to glycerol and water surfaces which warranted a strong solvent effect for ionic presence.

To further investigate the solvent effect, in chapter 5, the presence of ions at the propylene carbonate (aprotic) and benzyl alcohol (protic) surfaces were studied. In this chapter, electrolytes solubility posed an experimental limitation. However, within the limited set of data acquired, interesting results were observed. NICISS CDPs for all anions investigated in PC and BA were depleted at the vapour-solvent interface irrespective of their identity and the counter-ion; and followed a similar specific ion trend. These two solvents were also selected to observe the effect of hydrogen bonding on ionic presence at the vapor-solvent interfaces. Therefore, similar ion specificity at the vapour-PC and vapour-BA interface showed that the ion specificity for anion distribution in these systems is independent of the hydrogen bonding nature. Interestingly, we observed a varying STI trend at both solvent surfaces. Since anion CDPs were similar, a variation in STI meant a specific cation trend for overall electrolyte depletion from PC and BA surfaces. Further, the specific cation followed the opposite depletion trend between PC and BA solvent surfaces, suggesting a cationic interaction reversal between the PC and BA surfaces. The explanation of bulk interaction relation to surface affinity showed a good correlation with the depletion of herein investigated ions at the PC surfaces but at the BA surfaces, only a partial trend could be inferred and the anion CDPs were found to be in contrast with this explanation.

6.2. Common Specific Ion Trend at the Vapour-Solvent Interface:

Based on the data collected in chapters 3, 4, and 5 it is observed that only anions of lithium salts and iodide of LiI and NaI salts are common for specific anion effect and counter-ion effect respectively at these selected vapour-solvent interfaces. These observations are summarised in Table 6-1. In this table, the SIE at the vapor-water interfaces is also included as a reference that is not investigated here as discussed in Appendix Chapter IV. I have included the specific anion trend reported at the vapor-water interfaces from Pegram and Record's solute partition model (see Figure 1-5) [135, 136]. Whereas the counter-ion effect data is taken from Perrine et al. investigation [140]. At the vapour-water interfaces it is reported that the specific anion follows a decreasing presence trend as $I^- > Br^- > Cl^-$. Whereas for the counter ion effect the trend is, I^- paired with Li^+ is more abundant at the vapour-water interfaces than when paired with K^+. This trend is selected from the anion/oxygen ratio of 2 M LiI and KI aqueous electrolyte solutions presented by Perrine et al.

Looking at the trend presented in Table 6-1, we see that for lithium salts and iodide salts the trend at the vapour- glycerol, vapour-PC, and vapour- BA interfaces are the same. Whereas, at the vapour-FA interface, the counterion effect is similar but the specific anion effect is different. This specific anion trend at the vapour-FA interface is the opposite of reports at the vapor- water interface. Further, the counter-ion effect is also different for water but akin to glycerol, PC and BA interfaces. Categorising this ion specificity in terms of solvents for the limited sets of electrolytes, it can be

suggested that the anions at the vapour-water interface follow the fundamental Hofmeister series [136]. Following, the anions at glycerol, PC, and BA interfaces are at a verge of ion specificity reversal (i.e., gradual change). This reversal finally occurs for ions at the vapour-FA interface in terms of the specific anion effects.

Table 6-1: Common ion specificity at solvent surfaces. The greater sign (>) indicates a stronger presence (i.e., I^- has stronger presence than Br^-).

Ion Specificity	**Solvent**				
	Water[136, 140]	Glycerol	Benzyl Alcohol (BA)	Propylene Carbonate (PC)	Formamide (FA)
Anion effect	$I^- > Br^- > Cl^-$	$I^- = Br^- = Cl^-$	$I^- = Br^- = Cl^-$	$I^- = Br^-$	$Cl^- > Br^- > I^-$
Counter-ion effect	I^- (LiI) > I^- (KI)	I^- (LiI) = I^- (NaI)	I^- (LiI) = I^- (NaI)	I^- (LiI) = I^- (NaI)	I^- (LiI) = I^- (NaI)

As mentioned in the introduction, Mazzini et al. [71] provided an explanation that qualitatively accounted for series reversal in 5 solvents i.e., water, methanol, FA, PC, and DMSO. They provided that the SIE trend for ion-solvent interactions in presence of a surface is a result of the competition of ion and solvent polarizability against surface polarizability and charge. Within this framework, it was suggested that more polarizable ions will have stronger ion-solvent interaction in highly polarizable solvents and thus have a weaker interaction with surfaces. Whereas a less polarizable ion will interact weakly with a highly polarizable solvent therefore ions will favour the involved surfaces. Their experiments involved the presence of two varying surfaces i.e., Dextran present in SEC columns and PMETAC surface of the polyelectrolyte brush. Within these surfaces, ions in a more polarizable solvent followed the reverse Hofmeister series and ions in formamide with intermediate polarizability were on the verge of ion specificity reversal i.e., ions in FA showed an inconsistent trend when Dextran surfaces were involved compared to the PMETAC structure. They suggested this inconsistent trend between two experiments as a gradual change for specific ion series reversal in formamide [71].

Based on the experiments conducted in the dissemination for lithium salts (see Table 6-1) and its series categorization, it is observed that the ions at more polarizable vapour-solvent interface i.e., glycerol, PC, and BA are on the verge of reversal (gradual change) and SIE is reversed at intermediately polarizable the vapour-FA interface. This suggests that Mazzini et al.'s presented rationale does not work for ionic adsorption at the vapour-solvent interfaces investigated here. But this conclusion is not straightforward as Mazzini et al's discussion was based on sodium salts and

current discussion is based on lithium salts; and it is known that the combined pair of ions often results in different ion specificity as observed in Chapter 3 and suggested by them. They also suggested that the involvement of different surfaces might lead to reversal or variation as the polarizability and charge of the surfaces is changed and so is the competition of ion, solvent, and surfaces (also previously shown by Schwierz et al. [14]). Further, the understanding of what this match of ionic polarizability and solvent polarizability fundamentally means is not clear. Because polarizability is a vector component, the match of ion polarizability could be any directions which could depend on the solvent structure, solvents' charge distribution, ionic charge, anion-cation interactions, and even the combination of all these parameters.

6.3. Ionic Adsorption at the Vapour-Solvent Interface and its Correlating Concepts

Until now the investigation of ion specificity for inorganic ions has been limited to aqueous surfaces and only a few selected studies have explored the presence/absence of inorganic ions at non-aqueous surfaces [231, 233]. In this thesis, I have investigated the ion specificity of inorganic ions at 4 non-aqueous solvent surfaces. In this section, I explore if the data collected for ion specificity at non-aqueous solvent surfaces align with various concepts proposing the parameters driving the specific ion adsorption/desorption at the vapour-water interfaces. Within the large lists of parameters suggested for specific ionic adsorption, the few selected parameters of importance as discussed below are ionic size and polarizability [112, 114, 116], cavitation energy [116, 259], dispersion interaction [121, 122, 260], variation in the dipole moment of the ion and the solvent [128, 259], and desolvation energy [131, 136] (which is interchangeable with the hypothesis discussed here within Collins framework).

Various studies have reported ionic size and polarizability as the important driving parameters for anion adsorption at the vapour-water interface [112, 114, 116]. Jungwirth and Tobias [112, 113] qualitatively explained that ions are stabilised at the vapour-water interface as water molecules induce a non-net zero dipole towards the asymmetrically solvated ions at the interface. This induced dipole polarizes the large and more polarizable ion which leads to an energy gain that compensates for the electrostatic energy penalty for ionic adsorption at the vapour-water interface. In bulk, this dipole is zero as ions are symmetrically solvated. Therefore, it is suggested that only large and more polarizable ions (I^- and Br^-) has enhanced concentration at the interface compared to their bulk concentration. Whereas the small and less polarizable ions (Cl^- and F^-) has depleted concentration at the interface compared to their bulk concentration. This explanation cannot be extended to non-aqueous solvent interfaces as it disagrees with the experimental observation made in Chapters 3 and 4 i.e., even smaller, and less polarizable Cl^- is present at the vapour-glycerol and vapour-FA interfaces.

Based on Jungwirth and Tobias's seminal simulation [112, 113], a model description for ion enhancement and overall electrolyte depletion was proposed (see Figure 1-4). It was suggested that the less polarizable ions behave classically and are repelled from the interface following a monotonic distribution. Whereas the large polarizable ions minimize their Gibb's free energy for ionic adsorption at the interface by distributing non-monotonically from the interface [129]. In Figure 3-4 and Figure II-10 of the Appendix chapter II, we observe that for CsCl electrolyte solution, the Cl^- concentration depth profile is organised non-monotonically whereas, Cs^+ is depleted from the interface monotonically. This CDP is similar to the anion and cations of KI glycerol electrolyte solution and NaCl formamide electrolyte solution. Thus, the model description for ion enhancement and overall electrolyte depletion agrees with inorganic electrolyte organisation at the vapour-glycerol and vapour-formamide interfaces.

Adding onto the classical explanations, Levin et al. [116, 117, 261] postulated that the large polarizable ions are present at the interface based on the competing effect of electrostatic self-energy (repulsive electrostatics) and the driving cavitation energy. Levin et al. explained that the cavity formed in the bulk of the solvent (water) to accommodate larger polarisable ions expels ions to the interface. The image charge repulsion of ions at the interface is overcome by large polarizable ions like I^- through their charge redistribution into the high dielectric medium. Smaller and less polarizable ions like Cl^- and most cations cannot fulfil the same conditions as the cavity formed to accommodate small ions does not perturb the bulk hydrogen bonded network significantly and the large image charge repulsion compared to the driving cavitation energy disfavours their adsorption at the interface. Afterwards, calculating the ion density profile using the non-linear Poisson Boltzmann equation they defined the contribution of anions and cations. Within the cation contribution, they included a variable parameter 'a_h' for the hydrated radius of the cations. By changing the hydrated radius of the cation and keeping the anion contribution fixed (following their model calculations), they were able to correctly match the surface tension increment of sodium halide electrolyte solutions and their SIE trend. Employing this model, they were also able to qualitatively account for SIE in the surface potential change at water surfaces as reported by Frumkin [163]. Based on this description two observations can be expected for ionic adsorption at the vapour-solvent interface of differing dielectric permittivity:

1) the magnitude of electrostatic self-energy (repulsive electrostatics) should decrease for solvents with lower dielectric permittivity as the magnitude of electrostatic self-energy is inversely proportional to the sum of both medium's permittivity (i.e., vapour and solvent).
2) large polarizable ions can have higher adsorption at the interface of solvents with lower dielectric permittivity as these ions face lesser electrostatic repulsion in lower dielectric solvent and therefore can redistribute their charges in solvent and stay asymmetrically solvated.

Observation 2) is already refuted in chapter 3 and chapter 4 as discussed above. For observation 1), the implication will be that a single ion will face the opposing electrostatics of the magnitude inversely proportional to the dielectric permittivity order. In the solvents investigated, the decreasing dielectric permittivity order follows formamide (111.0) > propylene carbonate (66.1) > glycerol (46.5) > BA (13.0). Hence, a large polarizable ion can be expected have higher enhancement at the vapour-BA interface and the least enhancement at the vapour-FA interface. This decreasing I^- enhanced concentration should follow the trend as BA > Glycerol > PC > FA. In Figure 6-1 (a) and (b), the I^- CDPs of LiI and NaI electrolyte in FA, BA, and PC are compared respectively. Here, we observe that the I^- CDPs are similar in mentioned solvents within the uncertaintity and does not vary with the counter-ion. Thus, from the combined results observed in chapter 3, 4, and 5 and from the results shown in Figure 6-1 (a) and (b), it is observed that I^- CDPs are equally depleted at the vapor-solvent interfaces (except for the vapour-glycerol interface), independent of the dielectric permittivity of the solvent. Therefore, observation 1) does not work either.

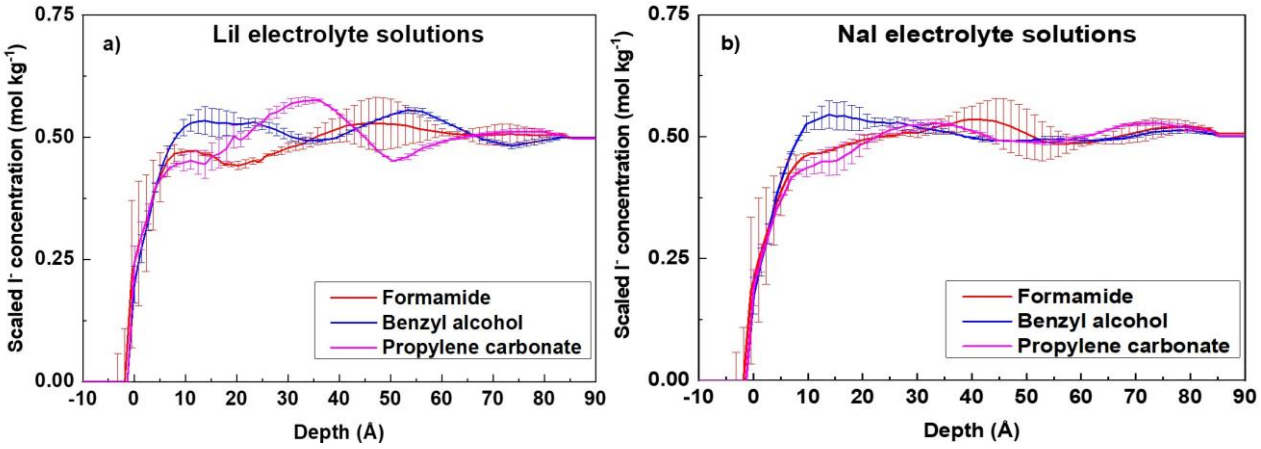

Figure 6-1: I^- CDPs of (a) LiI and (b) NaI in formamide(red), benzyl alcohol (blue), and propylene carbonate (pink). The I^- CDPs in formamide electrolytes are scaled by a factor of x1/2 for comparison. The error in depth calibration is ±2.7 Å which is calculated by accounting for the error in each gas phase measurement used for calibration of presented spectra.

One interesting observation of Levin et al. [117, 261] model was that upon changing the cation's hydrated radius they were able to correctly predict the STI and surface potential of various electrolyte solutions. From Figure 6-2 (a), we see that the STI for LiI electrolyte solutions follows the decreasing trend as FA ≥ PC > BA > glycerol. In Figure 6-2 (b), it is observed that the LiI electrolyte solutions follows the decreasing trend as BA > FA > PC ≥ glycerol. There is a variation in the order between PC, FA, and BA for LiI compared to NaI. Additionally, from the ion CDPs we see that the I^- profiles in Figure 6-1 (a) and (b) do not change at the vapour-solvent interfaces. Therefore, this variation in STI can be related to the role of cation depletion. For glycerol, a consistently lower STI due to higher anion adsorption is observed in Chapter 3. Thus, the difference in STI cannot be purely attributed to the role of the cation and is not included in the above comparisons.

The experimental results in Figure 6-2 (a) and (b) show that cations are playing an important role in the overall STI trend at non-aqueous solvent surfaces. Hence, Levin et al.'s model could potentially predict the ion specificity at the vapour-solvent interface by correctly accounting for the cationic contribution in the STI through its varying solvated radius. However, a fundamental explanation for varying the cations' solvated radius was not discussed. Further, the limitation of not gaining suitable backscattering signals in NICISS measurements to obtain a large set of cation CDPs has disallowed for quantifying the cations' role. Hence, this important observation should be followed up on in the future. It should also be noted that Levin et al.'s [116, 117, 261] postulation does not consider the effect of solvent polarisation which is important. Further, the cavitation energy cost for inserting an ion in glycerol, FA, PC, and BA is not known. Therefore, correction of these observations will be vital for predicting the ion specificity at the vapour-solvent interface.

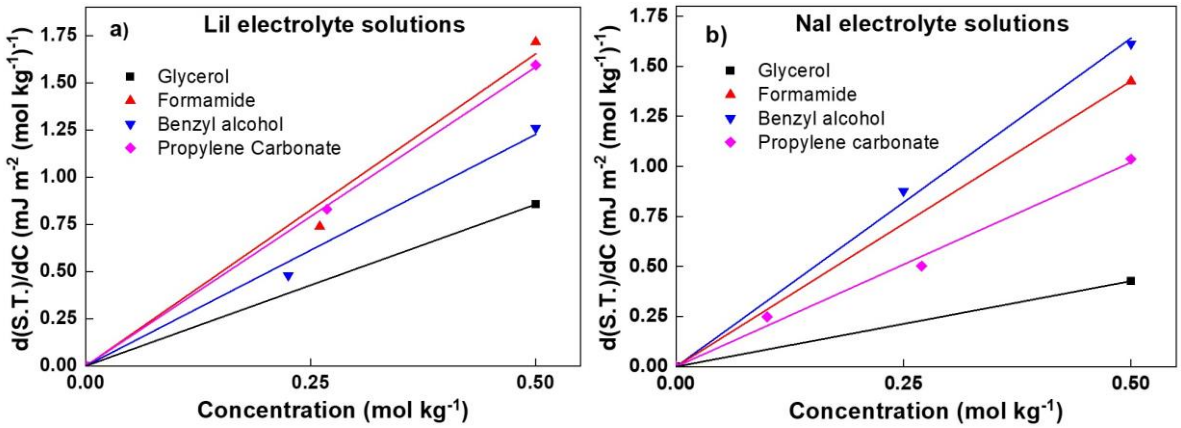

Figure 6-2: Surface tension increment (STI) comparisons of 0.5m (a) LiI and (b) NaI relative to the pure solvent of glycerol (black), formamide (red), benzyl alcohol (blue) and propylene carbonate (pink)at varying electrolyte concentration (d(S.T.)/dC). For some electrolyte solutions, surface tension data were collected only at a single concentration and the linear trend is included for the visual representation.

Dispersion interaction at solvent surfaces have also been considered as an important parameter for predicting ion specificity [104, 121, 122, 260]. Dispersion interaction contribution is a result of ion-solvent, ion-ion, and ion-surface interaction that is related to the ionic size and polarizability but also to the solvent molecular size and polarizability. The dispersion interaction becomes stronger with the solvent molecular size and polarizability because of the involvement of additional van der Waals interactions (dispersion interaction is a part of the van der Waals interactions) [262]. This additional van der Waals interactions decreases the perturbation of ions (reorganisation ability) in the bulk of the larger and more polarisable solvents[152].

Further, in an electrolyte solution when an ion is moving to the interface, dispersion interaction starts to play an opposing role if there is an imbalance of dispersion interaction in the bulk and at the interface i.e. if an ion loses solvent molecules from its solvation shell while approaching the interface [140]. This opposing dispersion interaction is expected to be stronger in solvents of larger molecular

size and polarizability. This means that ionic adsorption at glycerol, PC and BA interfaces will be more opposed compared to the FA interface as PC and BA are of larger molecular size and polarizability (see Table 2-1) compared to FA. For, the PC and BA interfaces, the aforementioned thought seems true as all the investigated anion CDPs are depleted due to stronger dispersion interactions. However, Cl^- and I^- show enhancement at the glycerol interface which is also of larger solvent molecular size and polarizability. In addition, the depletion observed for I^- CDPs at vapour-FA interface compared to vapour-glycerol interface is in contrast with mentioned notion. This suggests that the relationship of dispersion interaction with adsorption of inorganic ions at the vapour-solvent interface is not linearly correlated.

From another point of view, ions can adsorb at the vapour-solvent interface of larger molecular size and polarizability by overcoming the dispersion interactions if ions have a tightly bound solvation shell [140]. This notion might be true for Cl^- adsorption at the vapour-glycerol interface, as it is known that Cl^- forms a strong bidentate coordination in glycerol [263]. However, the ionic coordination information in the bulk and at the vapour-glycerol interface is required to gain clarity on this assumption. Such coordination information is harder to measure experimentally and only a few such investigations exist [87, 229]. Therefore, these details can mainly be acquired and discussed using computational simulations at the vapour-solvent interface.

Employing accurate DFT-D simulation of solvent cluster and extended vapour-water interface model, Baer and Mundy [128] reported that as iodide approaches the vapour-water interfaces there is an increase in its dipole moment and decrease in the solvents' bulk dipole moment value. This concomitant change of dipole moment of the solvent and the ion helps stabiles the ions against the image charge repulsion through counteracting cavitation/polarization. Based on their observations, Baer and Mundy [128] suggested that the first solvation shell and the polarization response of the anion at the vapour-water interface are important driving parameters for ionic adsorption. Similar observations were made by Wick and Xantheas [259] earlier for Cl^- and I^- who also suggested the cavitation and the anisotropy of solvation structure (related to the ion polarizability) as important driving parameters for ionic adsorption at the vapour-water interface. The accurate simulations of Baer and Mundy has not been carried out for ions at non-aqueous solvent interfaces and does not include the contribution of counter-ion, which is important as presented in Chapters 3, 4 and 5.

Above discussed observation further puts the spotlight on two important parameters for ionic adsorption at the vapour-solvent interface, 1) molecular orientational effects and 2) surface potential. Surface potential is a measure of the average change in the molecular orientation at the interface due to dielectric discontinuation of the vapour and the solvent. Thus, the molecular orientational effect is already incorporated into this parameter. Further, the change in molecular orientation at the interface due to a change in dipole response is expected to change the surface potential at the vapour-solvent interface and influence the local – electrostatic/dispersion contribution for ionic

adsorption. Therefore, the significance of surface potential in ionic adsorption discussion seems obvious. Indeed, the change in surface potential at the vapour-water interface is suggested as one of the important driving parameters for ionic adsorption [264] but a detailed investigation of this driving parameter is lacking at the vapour-solvent interface. Experimentally, surface potential measurement and/or phase-sensitive SFG measurements performed by Allen and co-workers can shed some light on this discussion [127, 151, 253]. However, to the best of my knowledge, such information is not available for non-aqueous solvents currently.

The surface tension of a solvent relates to the overall magnitude of the intermolecular forces at the interface. Within various intermolecular forces, polarity (related to the hydrogen bonding nature) at the solvent surface also defines the surface tension value of a solvent. Based on the surface tension value of a solvent one can indirectly judge the polarity (or percentage of polarity) at the interface. If a solvent is highly polar, it will have a higher surface tension value and the obvious example is water. Water has the larger surface tension value in solvents mainly because most of the water molecules participate in the hydrogen bonding. In this context, the trend for decreasing polarity of solvent from its surface tension data can be suggested as glycerol (63.0 mJ m^{-2}) > formamide (58.5 mJ m^{-2}) > benzyl alcohol (40.0 mJ m^{-2}). To test the role of polarity for ionic adsorption at the vapour-solvent interface, in Figure 6-3 the Cl^- CDP of LiCl in glycerol, FA, and BA is compared. In Figure 6-3, it is observed that Cl^- is most enhanced at the vapour-glycerol interface followed by a lesser enhancement at the vapour-FA interface and a depletion at the vapour-BA interface. This means that Cl^- has the most presence at the most polar solvent interface (glycerol) and the least at the least polar solvent interface (BA). This infers a tempting relationship between ionic adsorption and the polarity of the vapour-solvent interface. However, in Figure 6-1 (a) and (b), it is observed that I^- is equally depleted at the vapour–FA and vapour-BA interface. Thus, this relationship does not hold for all anions investigated here.

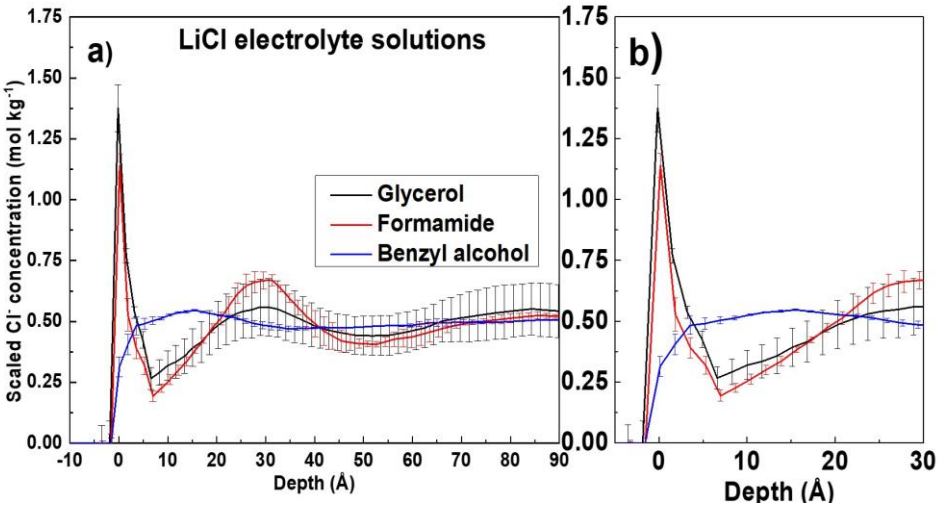

Figure 6-3: Cl^- CDP of LiCl electrolyte in glycerol (black), formamide (red), and benzyl alcohol (blue). The Cl^- CDPs in glycerol and formamide solution are scaled by a factor of x1/2 for comparison. The error in depth calibration is ±2.3 Å which is calculated by accounting for the error in the gas phase measurement used for calibration of presented spectra.

6.3.1. Inadequacy of the Hypothesis for Relating Bulk Interaction of Ions to their Surface Presence:

Within the Collins framework [65, 66], a hypothesis is tested against the data throughout this thesis to explain ionic presence at solvent surfaces. This hypothesis simply defines that if an ion prefers the bulk of solvent, it will be depleted from the interface as the opposing forces at the interface will be stronger. However, if the ion's interaction in the bulk is weak, then these ions can approach the solvent interface and will experience lesser opposing forces. This hypothesis is analogous to the desolvation energy [131] (or dehydration energy in water) explanation which suggests that the larger desolvation energy requirement will oppose ionic adsorption at the vapour-solvent interface. An ion will only have a larger desolvation energy if its interaction is favoured in the bulk of the solvent. For a coherent discussion let us call this approach the "bulk vs surface affinity" approach.

In Water, the ion's bulk solvation vs surface affinity approach has been investigated and proposed by various research groups. Based on the experimental data, Cheng et al.[131] have proposed that the source of the SIE within the anion partition to the air-water interface is the dehydration energy of an ion which was later supported by Pegram and Record through the solute partition model [136]. Levin et al.'s [116, 117] cavity model description has an essence of this approach as the driving cavitation energy expels the large ions to the interface. The calculation of the magnitude of this driving cavitation energy is based on the cavity (or volume) formed in a solvent bulk to accommodate an ion of a certain hydrated radius. Similarly, Horinek et al. [123] has explained that ion-specific effect at water surfaces arises from the hydrophobic solvation of ions. The hydrophobic solvation of an ion is also calculated by accounting for a cavity formed in the bulk of the solvent which is

proportional to the radius of the hard-charged ion. So, there are collective (but inexplicit) agreement in the literature for this approach (for further examples see [122, 265-267]).

Building onto the collective set of literature utilizing the bulk vs surface affinity approach, we extended this approach to explain ionic presence at the vapour-glycerol interface. The counter-ion effect for Br^- CDPs at the vapour-glycerol interface was correlated based on the change in anion-cation interaction in the bulk using the law of matching effective ion size (MEIS) [68]. The role of anion-cation interactions became dominant for Br^- adsorption at the vapour-glycerol interface because Br^- had larger solvation-free energy thus a stronger preference for the bulk of glycerol. Anions at the vapour-PC interface showed weaker specific anion effect and counter-ion effect in their CDPs. Whereas, the overall electrolyte STI suggested a strong cation-specific depletion. This cation-specific depletion trend agreed with the bulk ion-solvent interaction information gained from ATR-FTIR measurements suggesting a good correlation with bulk vs surface affinity approach. A negligible counter-ion effect for ion CDP at the vapour-FA interface was also observed in the bulk coordination through XANES, suggesting a connection between the ion interaction in the bulk and at the vapour-FA interface. However, this approach fails to describe the specific anions effects as presented in chapter 4. A distinct behaviour in NaI in BA electrolyte solution through the ATR-FTIR measurement analogous to the observation at the surface tension increment infers that the bulk vs surface approach is pertinent for NaI presence/absence at the vapour-BA interface. Although, the direct interpretation of IR data seems ambiguous (see Appendix chapter III). Further, the absence of a specific anion effect on anion CDPs at the vapour-benzyl alcohol interface is in direct contrast with the bulk solvation-free energy data presented in chapter 5. Overall, the collection of data in this thesis suggests that the bulk vs surface approach is not a valid hypothesis to explain ion specificity at all the vapour-solvent interface. However, the interpretation or parameter under investigation that relates bulk interaction with surface affinity varies between each solvent, model, and even the with type of measurement as observed for ion-water interactions in the bulk [70]. In this thesis alone I have looked through ranges of data for specific ion-solvent interaction information i.e., bulk IR interaction, NMR downfield shift, bulk coordinating information from XANES and, bulk solvation free energy data set. The variation in correlating features or the measure of the feature suggests that this approach is not unified, and a better framework is missing which is not achieved in this thesis.

This dichromatic view also does not consider the change in the ionic solvation environment in the bulk of the solvent and at the interface. Otten et al. observed that the ions approaching the vapour-water interface lose water-water interaction out of their solvation shell as water-water interaction is unfavourable at the interface compared to the bulk environment due to the dielectric discontinuity. This loss of water-water interaction compensates for the desolvation penalty of ion-water interactions at the interface [132]. Based on this observation, it can be suggested that there could be multiple driving/opposing parameters defining the specific ion adsorption at the vapor-solvent interface. Perhaps, to relate ionic bulk interaction to its surface presence, subtle interaction (or cancellation) of

multiple driving/opposing parameters needs to be accounted for [268], which potentially are a complex interplay of ion-solvent, ion-ion, and solvent-solvent interactions [7, 266]. Within these varying compensative interactions defining the bulk vs surface affinity approach, a refined inclusion of electrostatic contribution is not trivial [230]. This electrostatic contribution in bulk has been recently quantified as the site-specific electrostatic interaction using the parameter þ (pronounced "Sho") [89]. The site-specific electrostatic interaction can correctly predict the ion specificity in various non-aqueous solvents by the inclusion of the solvent's Lewis strength. Thus, with correct scaling of the site-specific electrostatic interaction of various solvents, þ can be advocated as one of the candidates for developing a stronger framework for understanding the changes in ionic interaction in the bulk and its relationship at the interface. To further, advance this framework, the anion-cation interactions in the bulk can be included using the modified electrostatic approach of Miranda-Quintana and Smiatek (Section 1.4) [93, 95, 269].

6.4. Conclusion

This thesis presents quantitative interfacial information for a range of monovalent ions in 4 non-aqueous solvents of protic and aprotic nature. From the CDPs, it is observed that ions at the vapour-solvent interfaces show ranges of complexity and that at the interface ion specificity is strongly influenced by the solvent. In chapter 1, I have presented a literature review for specific ion effects that points to the obvious need of investigating SIE at non-aqueous solvent surfaces. This has been addressed in chapters 3, 4, and 5. Within this literature review, I also discuss the theoretical developments made in the field and introduce various surface-sensitive techniques capable of conducting SIE investigation at the vapour-solvent interface. From this description one of the important information needed to gain better insights into ion specificity at solvent surfaces is the single ion CDP information. This is achieved here by employing NICISS. Further to complement the SIE trend observed from NICISS measurement, I have also conducted surface tension measurements of ranges of electrolyte solutions.

In Chapter 3, I investigated 12 electrolyte solutions and presented the ion specificity at the vapour-glycerol interface. A few important points to take from this chapter is:

- Smaller ions can also absorb at the vapour-solvent interface in contrast to suggestions made until now in the literature.
- The role of counter-ion is strong and so is the role of anion-cation interaction. Thus, the effect of anion and cation observation should not be considered additive at the vapour-solvent interface.
- Ion specificity changes with the solvent and often large sets of investigated electrolyte solutions show the true complexity of ion specificity.

In Chapter 4, the discussion of the SIE at formamide surfaces with 11 electrolyte solutions is presented but with additional comparison for cations. The important observations are:

- A complete series reversal of SIE is observed at the vapour-formamide interface in comparison to SIE at the vapour-water interface. This is observed through both NICISS and surface tension measurements.
- Further, the counter-ion effect is negligible suggesting ions at formamide surfaces follow the "Hofmeister paradigm" where the counter-ion effect can be ignored.
- Even though a negligible counter-ion effect is observed, the cations' role in overall electrolyte depletion and its influence in defining the site-specific electrostatic interaction of anion with formamide structure is important.

In Chapter 5, we moved on to investigate the ion specificity at aprotic and protic solvent surfaces i.e., at PC and BA surfaces respectively. Here it was observed that:

- The hydrogen bonding does not influence the ion specificity within the anion CDPs at vapour- PC and vapour - BA interfaces.
- Further, we also observed that cation plays a dominant role in defining STIs, but their role varies between protic and aprotic solvents.
- This dominant role of cation for electrolyte depletion at solvent surfaces demonstrates that cation specificity should not be considered “weak” compared to the anions while investigating the vapour-solvent interface.

Finally, in the current chapter, I have compiled the overall trend for lithium salts and iodide salts and observed that anion specificity is similar at the vapour-glycerol, vapour-PC, and vapour-BA interfaces. This supports the observation from Chapter 5 that anion specificity is not significantly influenced by the hydrogen bonding nature. The experimental results obtained in this thesis are compared against previous theories/hypotheses and the hypothesis discussed in this thesis to explain the ion specificity at the vapour-solvent interface. Both previous theories/hypotheses and current hypothesis in entirety cannot explain the experimental results for ions at solvent surfaces. Discissions of the current chapter depicts that the parameter(s) defining ionic presence/absence at the vapour-solvent interface is not yet determined. Although there are collections of parameters that are identified as important i.e., ionic size and polarizability of an ion, molecular size and polarizability of the solvent, surface potential change due to electrolyte presence, solvated cationic behaviour, anion-cation interactions, and site-specific electrostatic interaction. It is clear that to determine the driving parameter(s) of ion specificity at the vapour-solvent interface, a different framework is needed to understand how the interface changes the interaction between ions and solvent compared to the bulk. This can only be achieved through large-scale experimental and computational approach. For this approach, a baseline collection of data is presented here and hopefully, this contribution will stimulate further developments in this research direction.

CHAPTER 7 : FUTURE WORKS

Conclusions achieved in this thesis are based on the limited but exhaustive set of quantitative information measured for the ion specificity at 4 non-aqueous solvent surfaces. To explain the experimental results, I tried to re-introduce the qualitative hypothesis that the ionic preference at solvent surfaces is related to the ionic interaction in the bulk of a solvent. This hypothesis did not work as much as I would have hoped. Thus, a more refined and predictable theory is still needed to discuss all the presented results. To support the effort to come up with a refined predictable theory a larger collection of cation's CDPs data is needed some of which is measured here but not in the number that is required. This gap of information should be filled in the future by employing advanced surface-sensitive techniques and/or by developing the NICISS setup to achieve higher count rates.

SIE within concentrated electrolytes solution (high electrolyte concentration) is an elusive topic of research for widespread importance because the validity of the Debye- Hückel theory is diminished in high salt concertation regimes [64]. The validity of the Debye- Hückel theory is diminished as the screening length defined for charge separation in dielectric medium shows a re-entrant behaviour at a concentration greater than 1 M. Previously, concentrated aqueous electrolyte solutions have been investigated in vacuum-based techniques because high electrolyte concentration decreases the vapour pressure of water hence making it more accessible for forming a stable vapour-liquid interface [270, 271]. With a specialized setup, NICISS measurements for concentrated electrolyte solutions can be performed. Furthermore, with higher concentrations, even the smaller cations' cross-section can potentially be measured. Hence, in future, a large range of SIE for both anions and cations with high salts concentration should be investigated on water surfaces. Closer to the end of my PhD, I started developing the current NICISS setup to perform concentrated aqueous electrolyte solutions measurements. The progress in the development of the new setup and protocol is discussed in Appendix chapter IV. While developing this setup, I encountered multiple problems and have anticipated a few problems that will have to be fixed to achieve a useful dataset for studying ion specificity of concentrated electrolyte solutions. Concentrated electrolyte solutions can also be investigated with a non-aqueous solvent like glycerol and formamide that has higher electrolyte solubility.

Current work is only limited to monoatomic ions, but divalent and trivalent ions as well as polyatomic ions show interesting and complex features of ion specificity. A successful investigation of ions at PC surfaces has allowed for future SIE studies employing NICISS with application-based alkali metal ion battery systems. For such studies, the possible solvent choices can be ethylene carbonate, diethyl ethyl carbonate, adiponitrile and dimethyl sulfoxide with polyatomic ions. Recently, divalent ions at glycerol surfaces have been investigated which showed that the anions paired with common divalent cations show similar ion CDPs [272]. Trivalent ions follow interesting SIE trends called Irving -William's series [273] that is discussed based on charge transfer between ion and the solvent. This

series should be tested in non-aqueous solvents as well employing XAS and NICISS. The lanthanide groups of ions have displayed an interesting phenomenon where heavier lanthanide ions create inverted bilayer self-assembly at water surfaces [59]. The reasoning behind this phenomenon can be examined in detail by gaining ions and their counter-ion CDP information in model systems like glycerol solutions. This would also be another test to see if these thermodynamically unfavourable inverted bilayers can form in non-aqueous solvents.

The investigation related to ions with macromolecules are the centre point of SIE discussions as these were the original systems used to define the Hofmeister series and Lyotropic series [5]. Amongst a vast range of the macromolecular system, the ionic influence on the thermal response of thermoresponsive polymers is interesting and widely investigated. For such SIE systems, the important knowledge gap is the information regarding the distribution of ions within the polymer structure at the solvent surface and the variation in ionic distribution during the conformational change. The advantage of NICISS to gain ion and elemental CDP for such systems present an obvious opportunity for future endeavours. A study motivated to gain such information was attempted during my PhD as discussed in Appendix chapter V. While attempting these measurements, I observed that the NICISS probing depth at 3 KeV primary energy creates a limitation for gaining more accurate and direct depth information. This limitation can be resolved by employing NICISS with higher primary energy of ion beam. Such measurements require further set-up of the instrument, calibration measurements and determination of stopping power. Protocols for such calibrations, set-up, and measurements are already in place and should be followed in near future.

APPENDIX CHAPTER I: ION SPECIFICITY IN THE MEASURED CONCENTRATION DEPTH PROFILE OF IONS AT THE VAPOUR-GLYCEROL INTERFACE

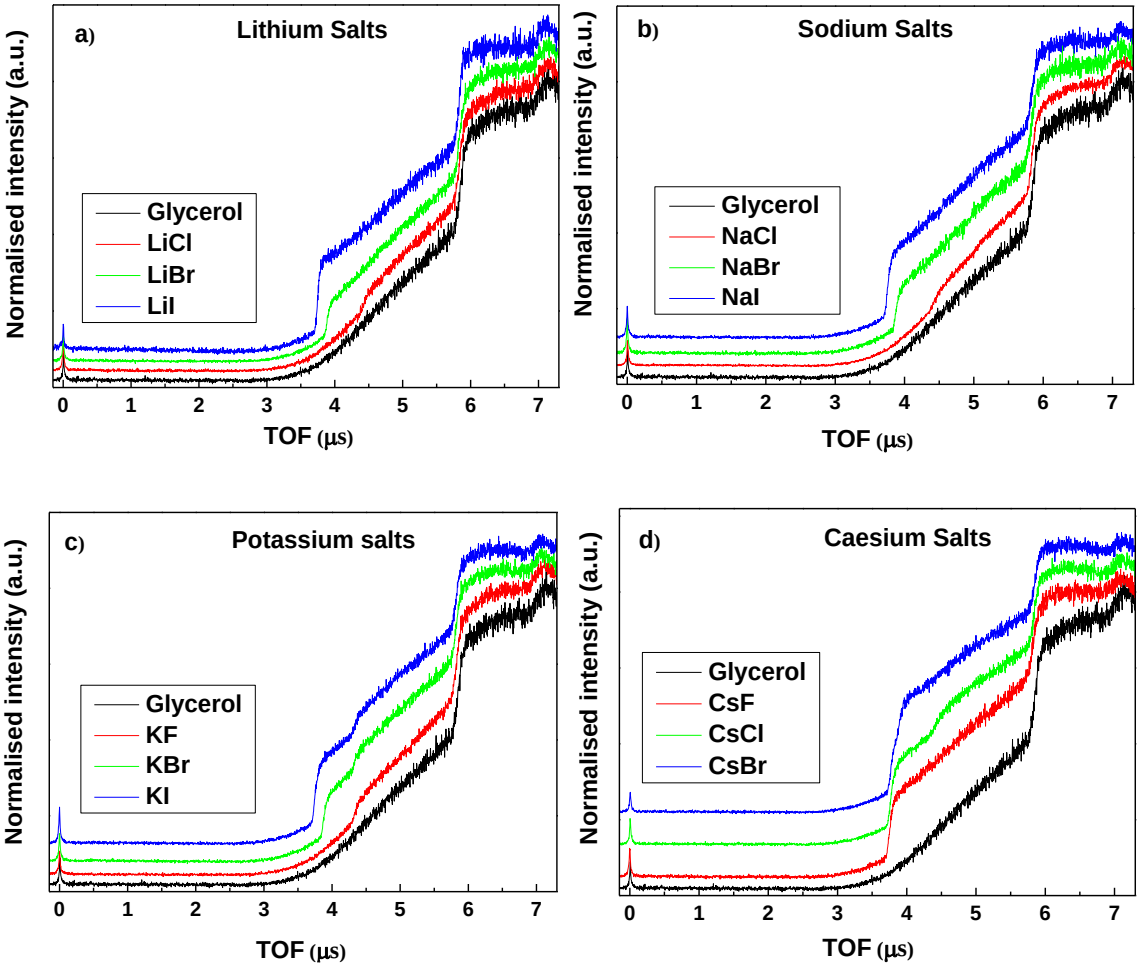

Figure I-1: Time-of-flight (TOF) spectra of 3 keV He ions backscattering from 1 molal concentration solution of (a) lithium salts, (b) sodium salts, (c) potassium salts and (d) caesium salts in glycerol compared to glycerol TOF spectrum (black in all figures).

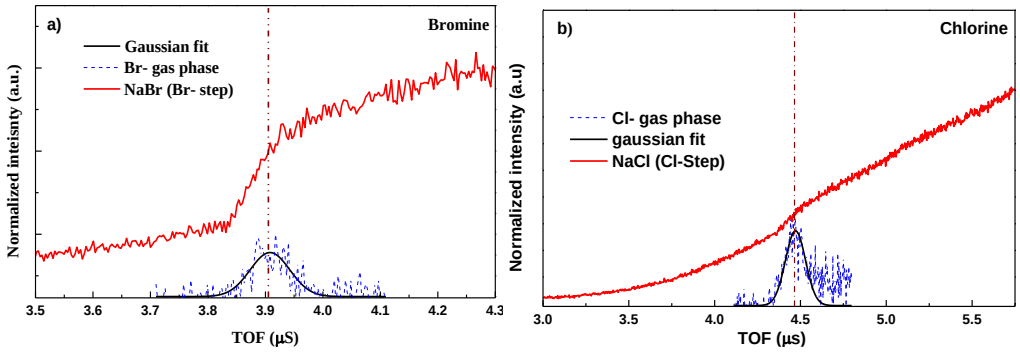

Figure I-2: Gas phase peaks of (a) bromine and (b) chlorine compared to the Br^- step from NaBr and the Cl^- step from NaCl glycerol solutions respectively. The black curve shows the Gaussian fitting of the gas phase measurement, and the dotted blue line shows the centre of the gas phase peaks used for zero depth calibration of each ion's concentration depth profile (CDP).

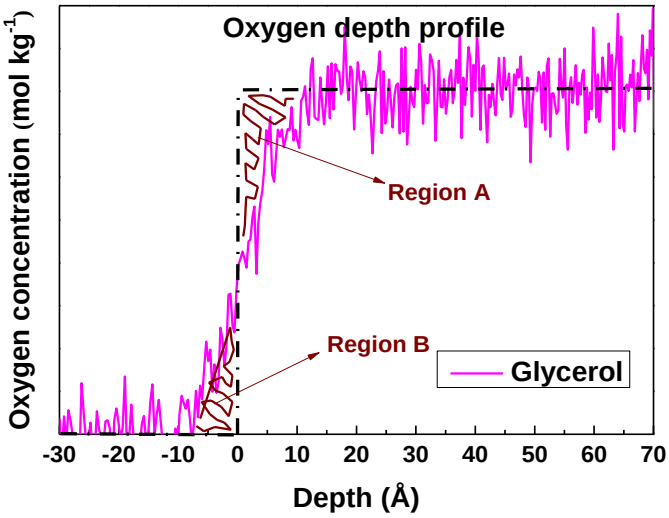

Figure I-3: Oxygen CDP of glycerol (pink) displaying the Gibbs dividing plane for pure glycerol (dashed black line). This figure illustrates that the area under Region A and Region B are approximately the same. Hence, the dashed black line represents the Gibb's dividing plane for glycerol. Similar plots have been presented using solvent concentration depth profile previously [221]. It should be noted that the oxygen depth profile presented here is calibrated using the linear fit equation discussed in Figure 2-6 and not using measured gas phase spectrum. Therefore, the error associated in the depth calibration is ~ ± 7 Å.

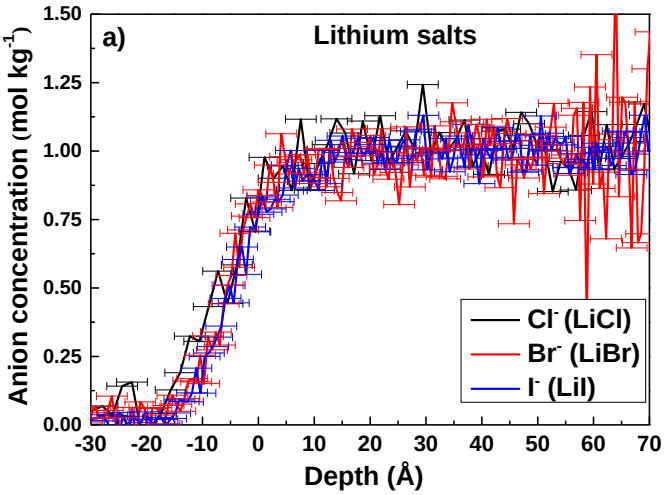

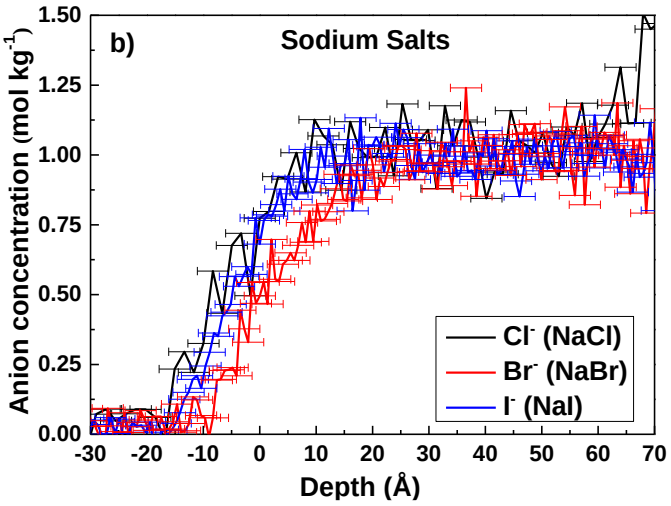

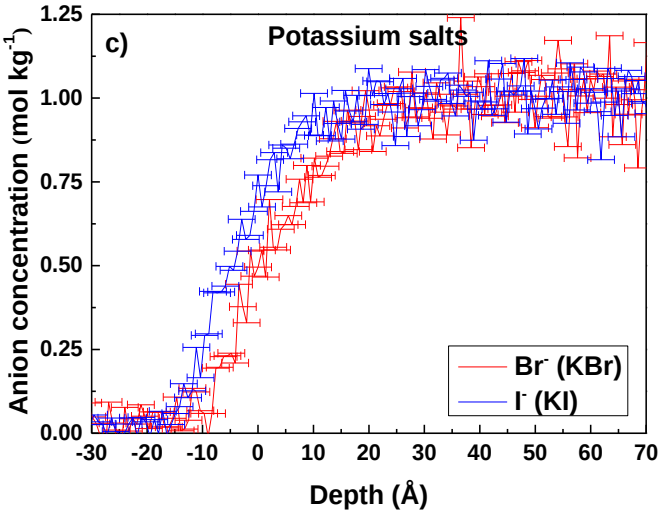

Figure I-4: (a) Measured CDP of Cl^- (black), Br^- (red), and I^- (blue) ions in 1 m glycerol solutions with Li^+ as the counterion, (b) CDP of Cl^- (black), Br^- (red), and I^-(blue) ions in 1 m glycerol solutions with Na^+ as counterion, and (c) CDP of Br^- (red) and I^- (blue) in 1 m glycerol solutions with K^+ as counterion. The depth scale error is of ± 2.4 Å for comparisons between anions of lithium and sodium salts while for comparisons of potassium salts anions error present is ± 2.2 Å. This uncertainty is due to selecting the centre of gaussian fit for gas phase spectrums.

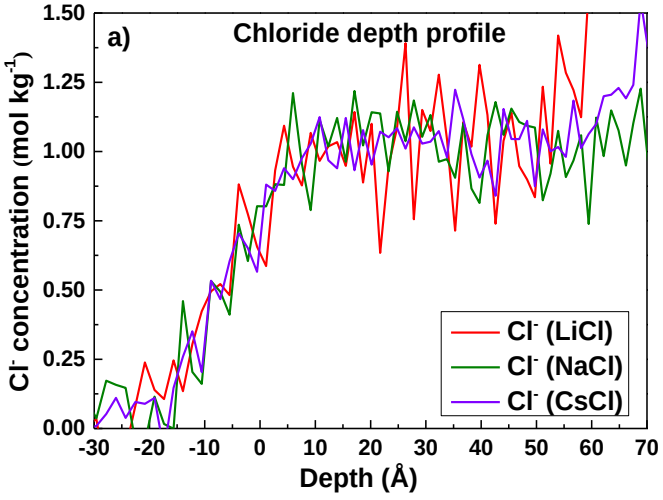

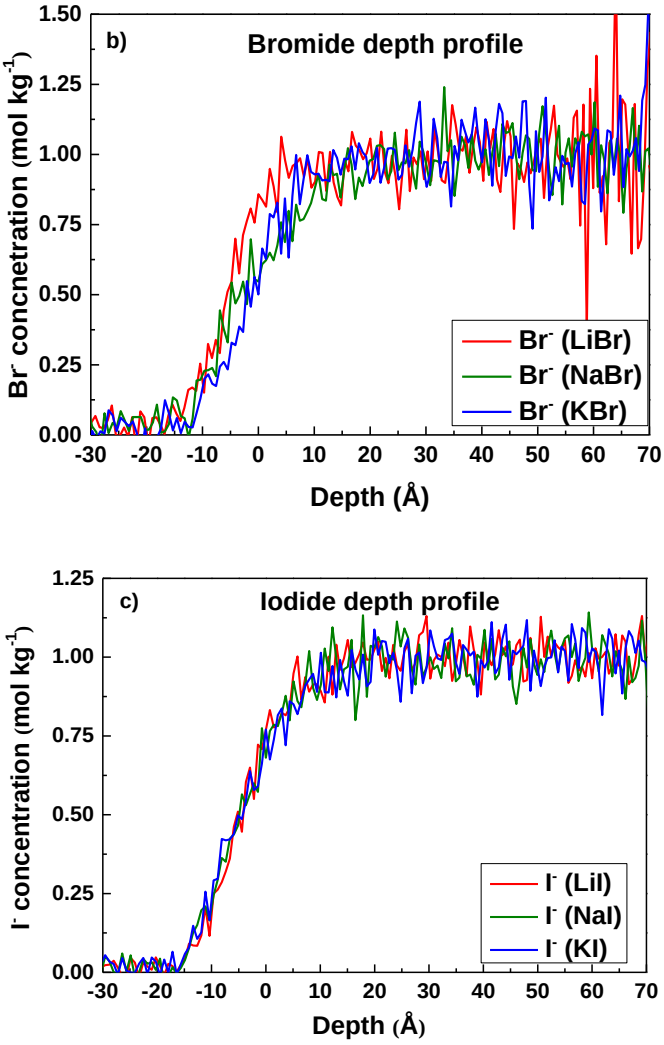

Figure I-5: (a) CDP of Cl^- at the surface of 1 m LiCl (red), 1 m NaCl (green) and 1 m CsCl (yellow) glycerol solutions. (b) CDP of Br^- ions at the surface of 1 m LiBr (red), 1 m NaBr (green) and 1 m KBr (blue) glycerol solutions. (c) CDP of I^- at the surface of 1 m LiI (red), 1 m NaI (green) and 1 m KI (blue) glycerol solution.

The CDP obtained for each anion are not influenced by the different cations except for the case of bromide. The Br^- concentration at the Vapour-glycerol interface is dependent on its counteraction as Br^- concentration follows an order for electrolyte solution as LiBr > NaBr > KBr. All ion concentration depth profile has been calibrated with same gas phase measurements; the uncertainty associated with each comparison are the same. As chloride is lighter than the other anions investigated, the probability for backscattering of the He projectile is smaller and therefore the signal to noise ratio in these depth profiles is lower than that in the bromide and iodide spectra.

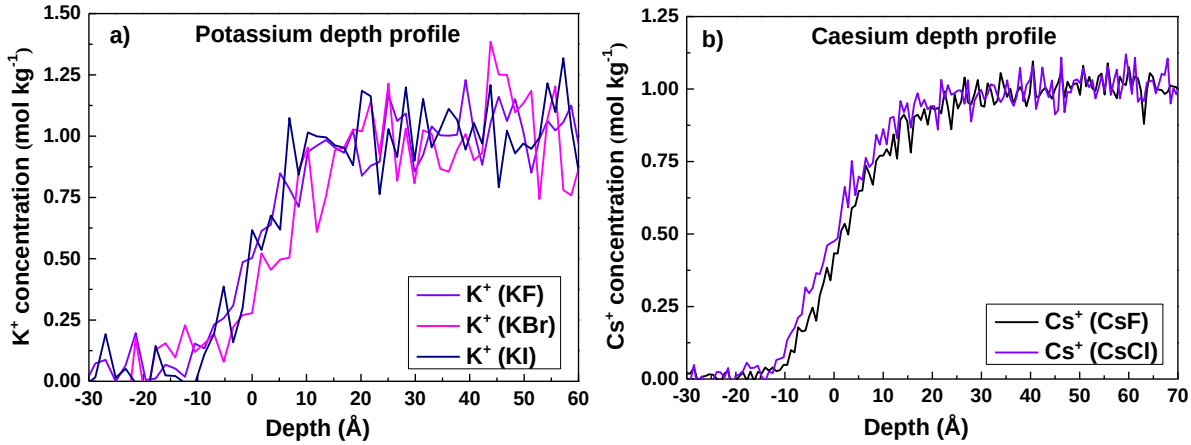

Figure I-6: (a) Comparison of the concentration depth profile of K^+ in 1 m KF (violet), 1 m KBr (pink) and 1 m KI (dark blue) glycerol solution with 3 data points average. (b) Comparison of the concentration depth profile of Cs^+ in a 1 m CsF (violet) and 1 m CsCl (black) solutions in glycerol.

The onset of the CDPs for Cs^+ is different for the counteranions F^- and Cl^- which show that Cs^+ when paired with F^- anion is found closer to Vapour-glycerol interface than when paired with Cl^-. Due to smaller signal to noise ratio the onset of K^+ CDPs in KF, KBr and KI glycerol solution does not differ much paired with various anions (Figure I-6 (a)). However, looking at the smoothed K^+ CDPs comparisons in Figure I-6 (a), the K^+ onset in KBr solutions is further away than K^+ onset in KF and KI solutions. This onset order is consistent with their counter-anion presence nearby the Vapour-glycerol interface where Br^- paired with K^+ onset is further away than I^- paired with K^+ showing that anions presence from vapour-glycerol interface strongly influences their counter-cation.

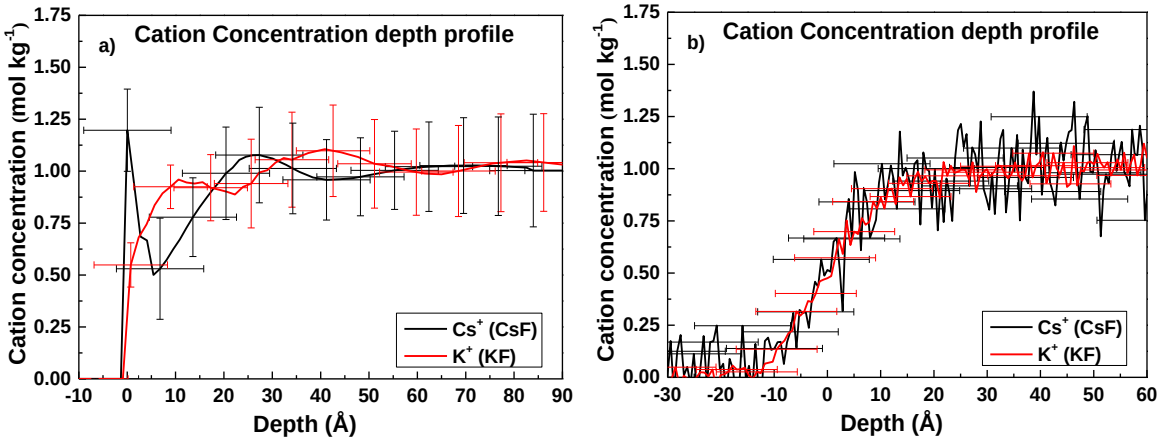

Figure I-7: Comparisons between CDPs of K^+ of KF (black) and Cs^+ of CsF (red) electrolytes in 1 m glycerol solutions (a) deconvoluted CDPs (b) NICISS CDPs. Since the zero-depth calibration is determined through extrapolation, as shown in Figure S4, the uncertainty involved in the depth scale is ± 5.9 Å.

Comparing two different cations CDPs in Figure I-7 (a), we can see that Cs^+ has a stronger presence in the near surface region than K^+ of fluoride electrolyte solutions. However, NICISS CDPs in Figure I-7 (b) shows that these differences fall within the uncertainty. So, it is avoided to make strong conclusions from the presented cation comparison.

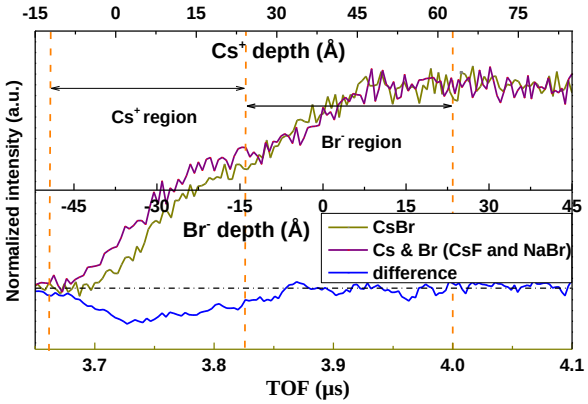

Figure I-8: TOF spectrum difference (blue) between CsBr TOF spectrum (green) and TOF spectrum constructed with CsF and NaBr (brown). In this figure, the Cs^+ region has a stronger depletion compared to Figure 3-3 (c) presented in the main text since Cs^+ of CsF is closer to the Vapour-glycerol interface than Cs^+ of CsCl (see Figure 3-3 (c)).

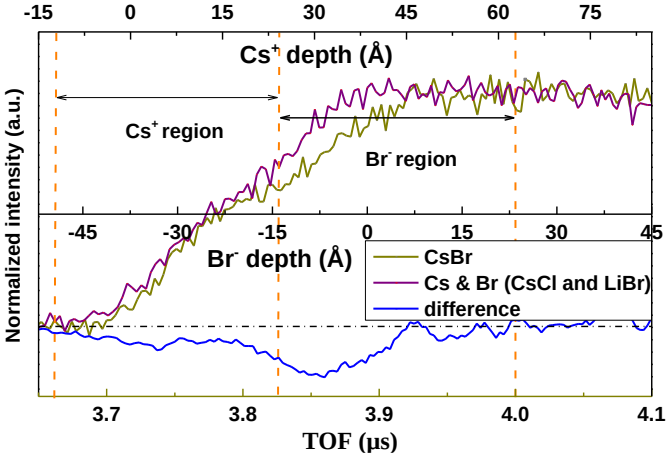

Figure I-9: TOF spectrum difference (blue) between CsBr TOF spectrum and constructed TOF spectrum (purple) with CsCl and LiBr.

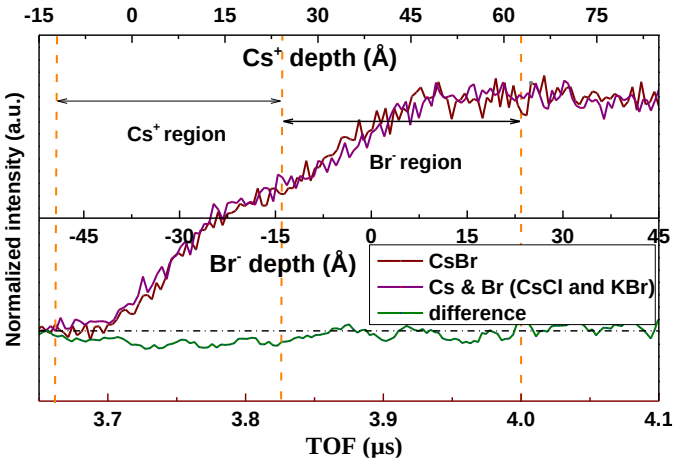

Figure I10: TOF spectrum difference (green) between CsBr TOF spectrum (purple) and the TOF spectrum (brown) constructed from CsCl and KBr. In this figure, the Br^- region has no depletion compared to Figures I-8 and I-9 because Br^- of KBr expected to have similar onset at Vapour-glycerol interface.

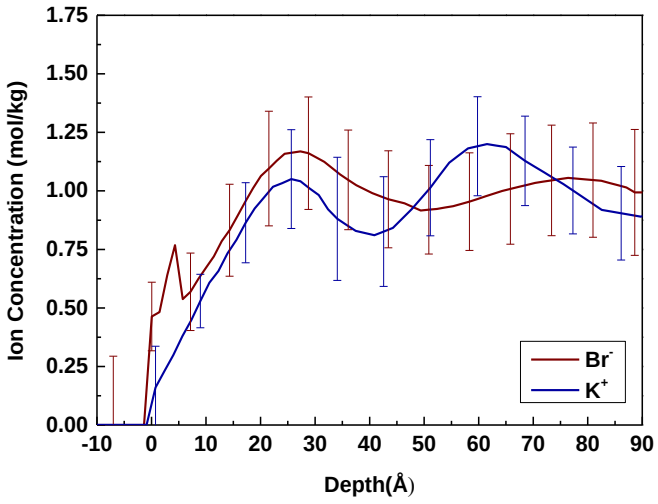

Figure I-11: Anion and cation CDPs comparisons of 1 m KBr glycerol solutions with Br^- (brown) and K^+ (blue) concentration depth profiles. The uncertainty in the depth calibration between both ion concentration depth profile is of ± 3.6 Å and for the sake of clarity error bars are not included in this figure.

Surface Excess derived from the concentration depth profiles of ions

The procedure to derive the surface excess of ions from concentration depth profiles has been described previously [221]. The error bars for the surface excess are a result of uncertainty in zero depth calibration and noise present in each NICISS spectrum. Here we only present the surface excess calculated from the as measured NICISS profile because the accuracy is highest in these profiles.

Table I-1: Surface excess derived from measured NICISS concentration depth profile of anions.

Anions only of glycerol electrolyte solution	Surface excess derived from as measured NICISS CDP of each ion (anions only) (10^{-10} mol cm^{-2})
LiCl	1.0 ± 1.0
LiBr	0.5 ± 1.0
LiI	0.5 ± 1.0
NaCl	0.7 ± 1.0
NaBr	-0.1 ± 1.0
NaI	0.5 ± 1.0
KBr	-0.1 ± 1.0
KI	0.4 ± 1.0
CsCl	0.8 ± 1.0

Table I-2: Surface excess derived from measured NICISS concentration depth profile of cations.

Cation only of glycerol electrolyte solutions	Surface excess derived from as measured NICISS CDP of each ion (cation only) (10^{-10} mol cm^{-2})
KF	0.2 ± 2.0
KBr	-0.2 ± 2.0
KI	0.2 ± 2.0
CsF	-0.03 ± 2.00
CsCl	-0.3 ± 2.0

Surface Excess derived from surface tension measurement

The surface excess from surface tension is derived using the Gibbs adsorption isotherm (see section 1.5.1). To derive the surface excess from the surface tension value we assume that the surface tension change is linear[134] for simple glycerol electrolytes as observed previously[152] and that the activity coefficient is 1.

Table I-3: Surface excess derived from measured surface tension values of glycerol electrolytes.

Electrolytes dissolved in glycerol	Surface excess (10^{-10} mol cm^{-2})
LiCl	-0.21
LiBr	-0.41
LiI	-0.80
NaCl	-0.10
NaBr	-0.42
NaI	-0.49
KF	-0.30
KBr	-0.61
KI	-0.82
CsF	-0.40
CsCl	-0.42
CsBr	-0.41

Free energy of solvation calculation methodology

The solvation free energy of an anion X^- in bulk solution is defined as the change in Gibbs free energy for the reaction $X^-_{(g)} \rightarrow X^-_{(soln)}$, i.e.

$$\Delta \boldsymbol{G}_{\mathbf{solv}} = \Delta \boldsymbol{G}(\mathbf{X}^-_{(\mathbf{soln})}) - \Delta \boldsymbol{G}(\mathbf{X}^-_{(\mathbf{g})}) \qquad (9)$$

Both $\Delta \boldsymbol{G}(\mathbf{X}_{(\mathbf{soln})})$ and $\Delta \boldsymbol{G}(\mathbf{X}_{(\mathbf{g})})$ can be approximated directly using quantum chemical calculations, i.e.

$$\Delta \boldsymbol{G}_{\mathbf{solv}}(\mathbf{298\ K}) \sim \langle \Delta \boldsymbol{G}(\mathbf{X}^-_{(\mathbf{soln})}) \rangle - \left[\boldsymbol{E}(\mathbf{X}^-_{(\mathbf{g})}, \boldsymbol{T} = \mathbf{0\ K}) + {}^{\mathbf{3}}/_{\mathbf{2}}\, \boldsymbol{kT} \right] \qquad (10)$$

where $\langle \Delta G(\mathrm{X}_{(\mathrm{soln})}) \rangle$ is the free energy of the solvated anion (approximated via time-averaging an MD ensemble energy), $E(\mathrm{X}^{-}_{(\mathrm{g})}, T = 0\ \mathrm{K})$ is the 0 K energy of the ion in vacuum, and $^{3}/_{2}\, kT$ is the equilibrium thermal energy at temperature T (for the Boltzmann constant k). Here, $\langle \Delta G(\mathrm{X}_{(\mathrm{soln})}) \rangle$ is calculated using the IonSolvR database[274]. For full computational details of IonSolvR records, the reader is referred to the ref[225]. Briefly however, each record in the IonSolvR database consists of an ab initio MD trajectory calculated using the density functional tight binding method and an NVT ensemble via a Nosé [275]-Hoover [276] chain [277, 278] (NHC) thermostat set to 298 K. Each trajectory consisted of a single anion solvated by 64 glycerol molecules in a periodic box. Time-averaging was performed across the final 30 ps of each 100 ps MD trajectory (30,000 MD frames in total). For the gas-phase anion energy, the quantum chemical level of theory was kept identical to that used for the respective solvated anion MD trajectory, viz. 3rd order density functional tight binding (DFTB3) [279] using the 3ob-3-1 parameter [280-282] set and Grimme's D2 dispersion [283, 284] with Becke-Johnson [285, 286] dampening (i.e., D3(BJ)).

APPENDIX CHAPTER II: SPECIFIC ION EFFECTS AT FORMAMIDE SURFACES: A REVERSE HOFMEISTER SERIES IN THE CONCENTRATION DEPTH PROFILES

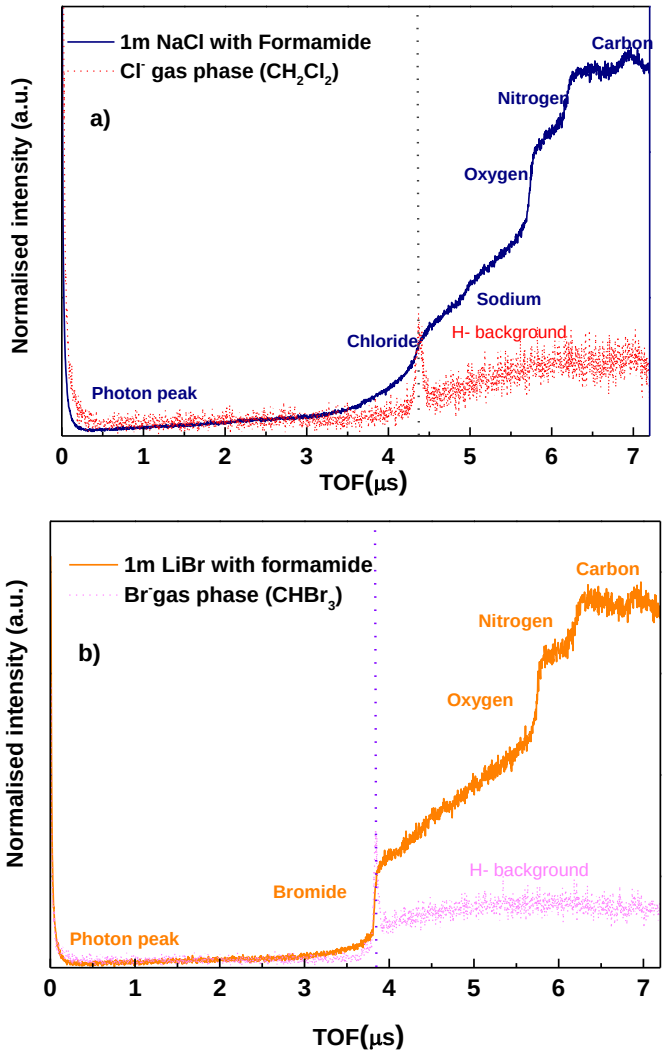

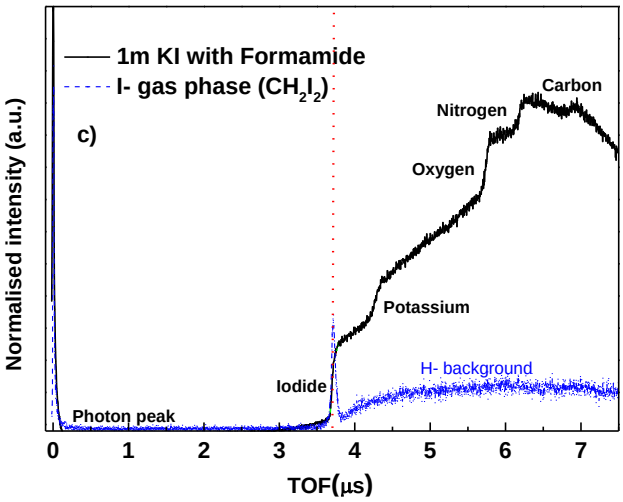

Figure II-1: NICISS TOF spectrum of (a) 1 m NaCl in Formamide (dark blue) and dichloromethane in the gas phase (red), (b) 1 m LiBr in Formamide (orange) and bromoform in the gas phase (pink) and (c) 1 m KI in Formamide (black) and diiodomethane in the gas phase TOF spectrum (blue).

Gas Phase Calibration

The zero-depth calibration and inelastic energy losses of each element was measured and calibrated using a gas phase measurement[189]. For Cl^-, Br^- and I^-, the calibration was obtained by measuring gas phase NICIS spectrum of dichloromethane (CH_2Cl_2), bromoform ($CHBr_3$) and diiodomethane (CH_2I_2) respectively (see Figure II-1 (a), (b) and (c) comparison between NICIS gas phase spectrum and elemental step in electrolyte solution). Gas phase measurements for Na^+, K^+ and Cs^+ were not possible due to the lack of stable gas phase sources. Therefore calibration for these cations was carried out using the procedure developed by Zhao et al.[195] (see Figure II-2). For the deconvolution of cations, the FWHM of a neighbouring element measured in the gas phase was used.

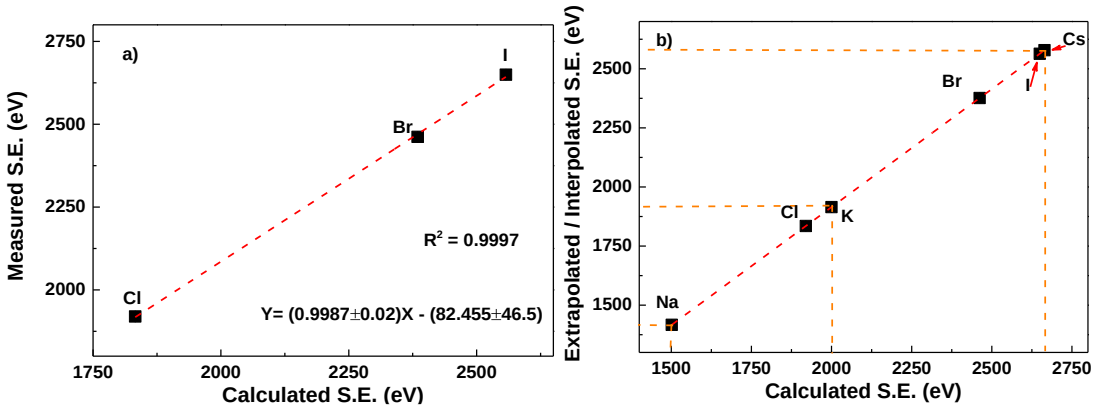

Figure II-2: (a) Scattering energy from gas phase measurements versus the calculated scattering energy from Equation 1, showing a linear relationship. (b) The derived scattering energy values obtained using the linear fit equation shown in the inset of the figure (a). The uncertainty in the scattering energy obtaining following this procedure is ±12 eV. The error bars in the figures are smaller than the data points.

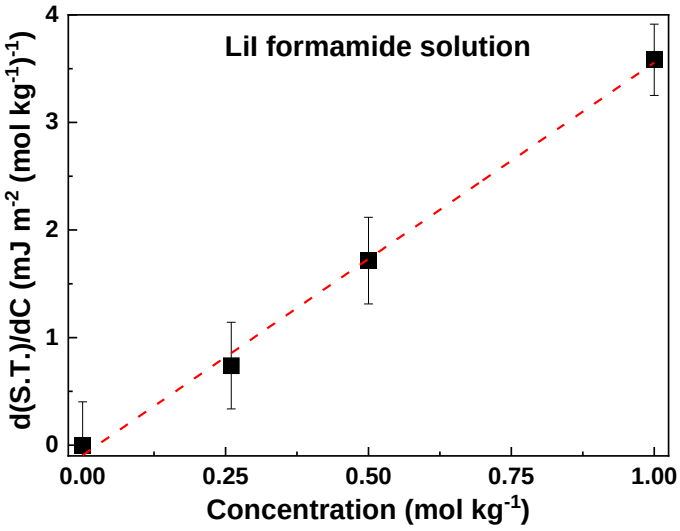

Figure II-3: Surface tension increment (STI) relative to the pure solvent for varying concentration (d(S.T./dC) of LiI electrolyte solutions.

Concentration effect on ion CDPs for KI formamide electrolyte solutions

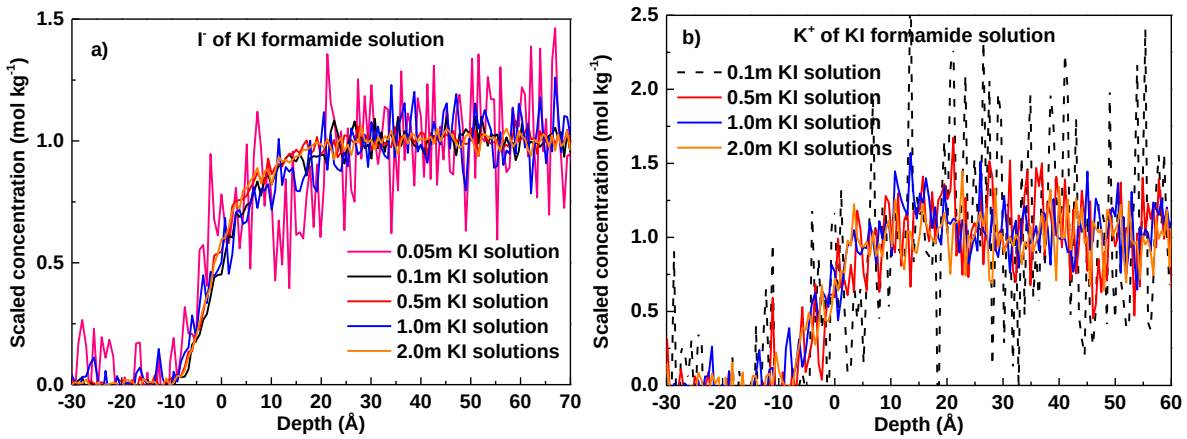

Figure II-4: Convoluted CDPs of (a) I^- and (b) K^+ at 0.05 m (pink), 0.1 m (black), 0.5 m (red), 1 m (blue) and 2 m (orange) KI formamide solution. Convoluted I^- at 0.05 m KI solutions clearly has different features than convoluted I^- CDPs. K^+ convoluted CDP is shown (black dotted line) to demonstrate that signal for K^+ is weak at lower concentration. All the CDPs presented here are scaled to 1 m bulk concentration for better comparisons. Depth profile of I^- is calibrated using the same gas phase measurement hence uncertainty involved will be same which is ± 1.1 Å. K^+ zero depth is calibrated following the procedure discussed earlier in the section and uncertainty involved is ± 2.3 Å which is same for all K^+ profile presented here.

We have investigated KI formamide solutions at concentrations from 0.05 m to 2 m. KI electrolyte solutions were selected for this test to overcome the challenge of getting enough backscattering signals for reasonable CDPs and that K^+ and I^- TOF steps in NICIS spectra are well separated (See Figure II-1). In Figure II-4, I^- convoluted CDPs of KI formamide solutions clearly show that above 0.1 m electrolyte solutions, the CDPs of I^- does not show any difference within the experimental uncertaintity. Therefore, we assume that a small change in the electrolyte concentration due evaporation in a high concentration electrolyte solution regime (> 0.5 m) should not affect the current SIE investigation. In Figure II-4, we also see that the I^- CDP onset is higher for 0.05m KI electrolyte solutions compared to higher concentrations solution. Further the I^- CDP shows a depletion at higher depth before reaching the bulk electrolyte concentration. This is interpreted as a depletion for I^- in the subsurface depth region with higher concentration in the outermost region of the Vapour-formamide interfaces.

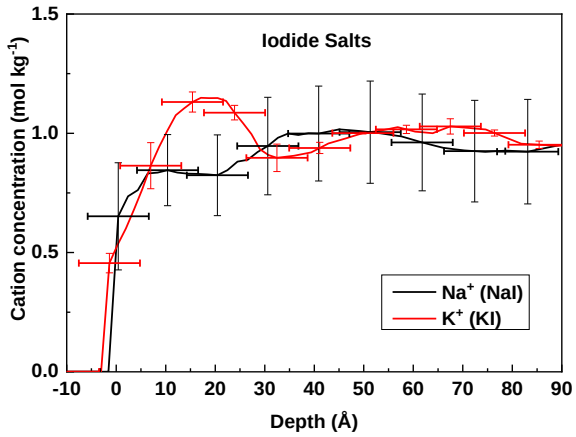

Figure II-5: Comparison of Na^+ (black) and K^+ (red) CDPs of iodide salts in formamide electrolyte solutions.

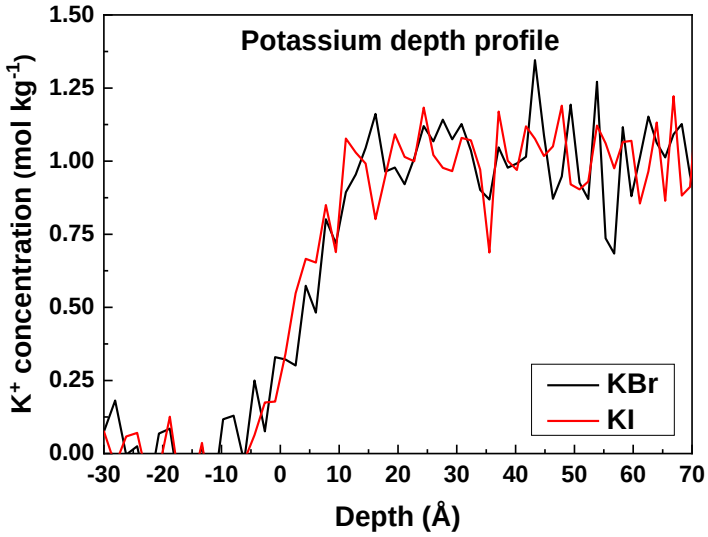

Figure II-6: Comparison of cation concentration depth profile for (a) K^+ paired with Br^- and I^-. No effect of counter-anion is observed in K^+ CDPs within the noise.

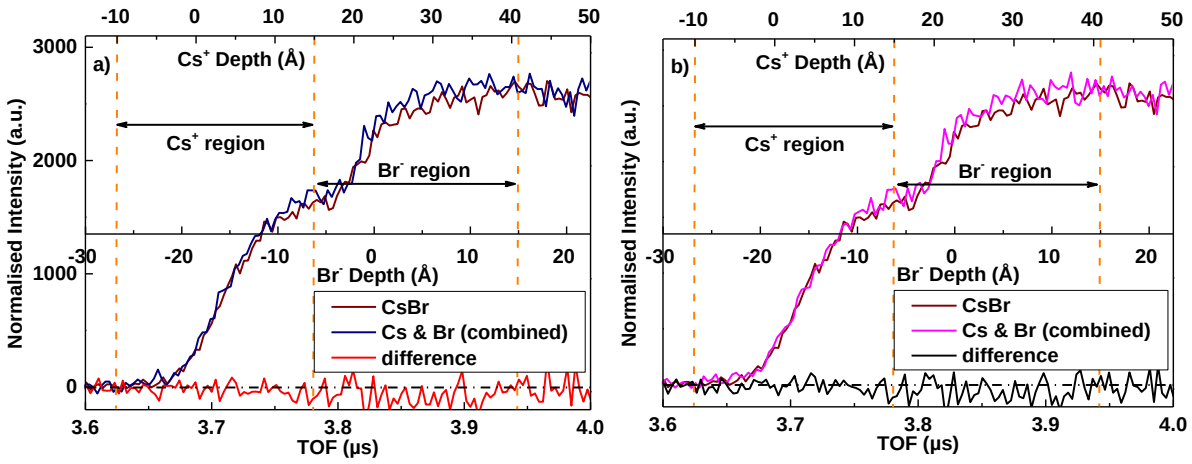

Figure II-7: The difference (red in panel (a) and black in panel (b)) between the TOF spectrum of CsBr (brown) and the constructed TOF spectrum of (a) CsCl and KBr formamide solution (navy blue) and (b) CsF and KBr formamide solutions (pink). These profiles show that there is no difference in the Cs^+ and Br^- regions for different combinations of counter-ions, as observed in Figure 4-2 (d).

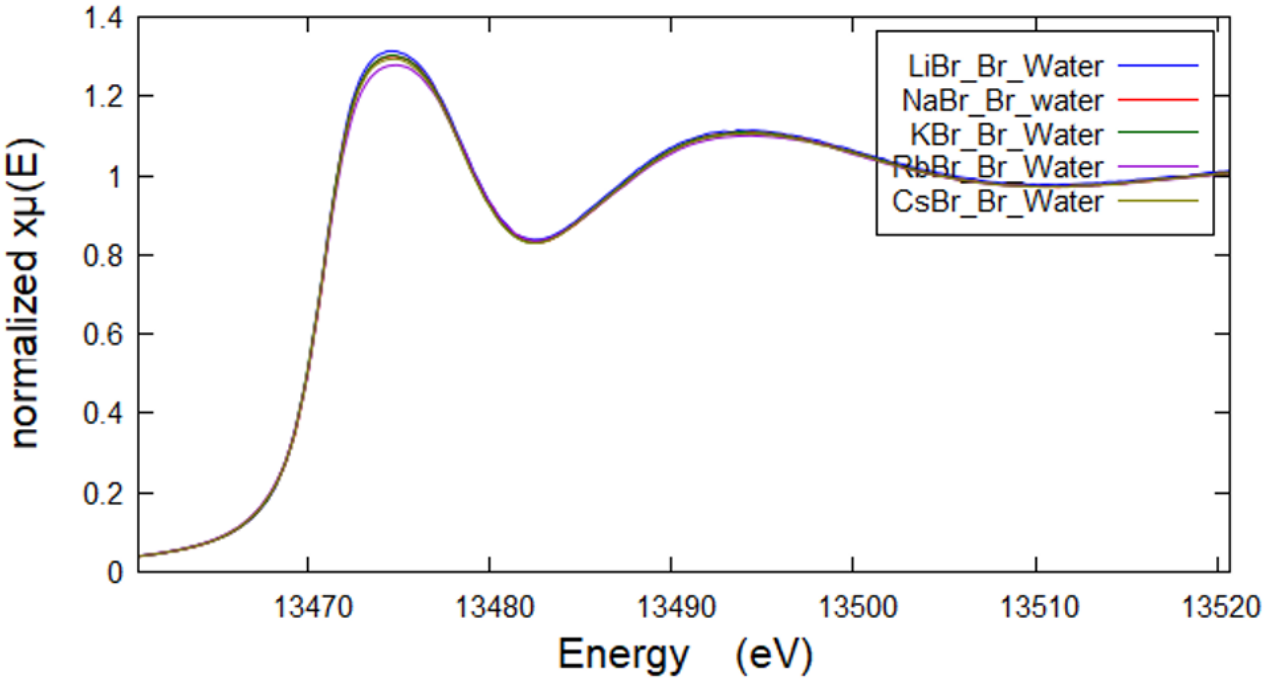

Figure II-8: Bromide K edge X-ray absorption (xµ) near edge spectrum (XANES) of LiBr (blue), NaBr (red), KBr (green), RbBr (violet), and CsBr (dark yellow) in water.

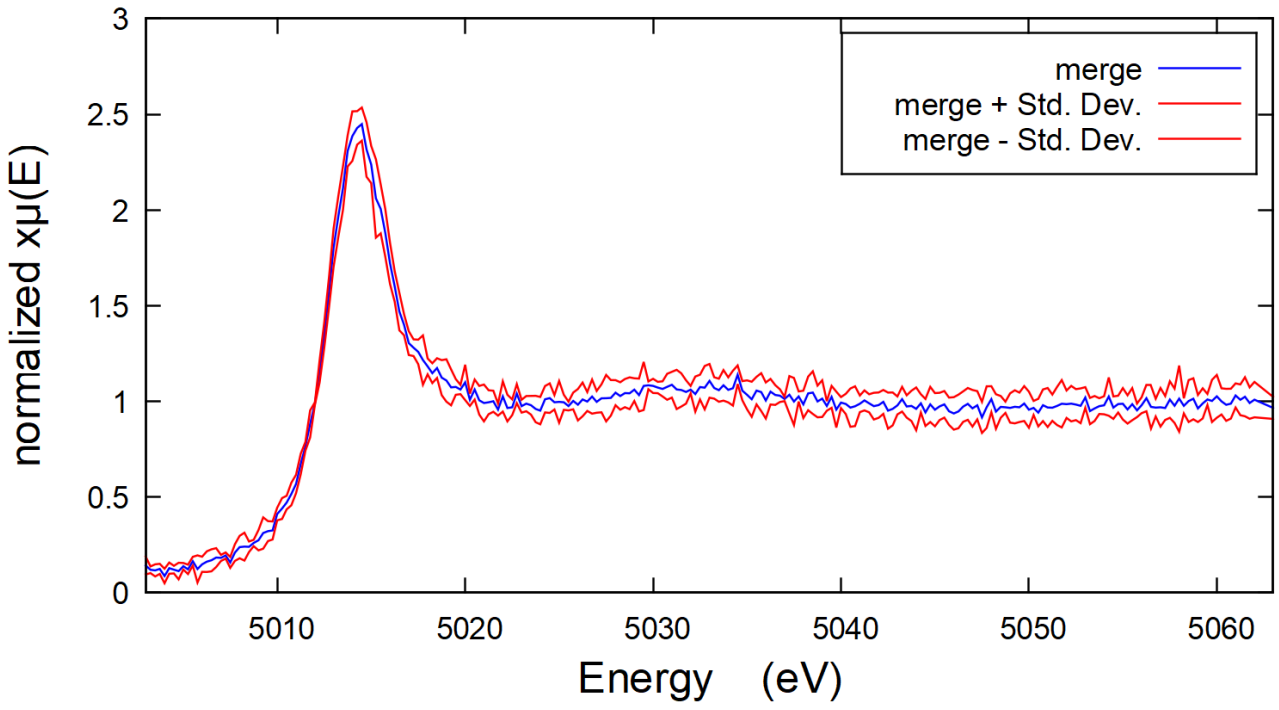

Figure II-9: Merged Caesium L_3 edge X-ray absorption (xμ) near edge spectrum (XANES) of CsCl with formamide. Standard deviations (Std. Dev.) '+' and '- 'of merged triplicate scans for CsCl formamide solution (red curves).

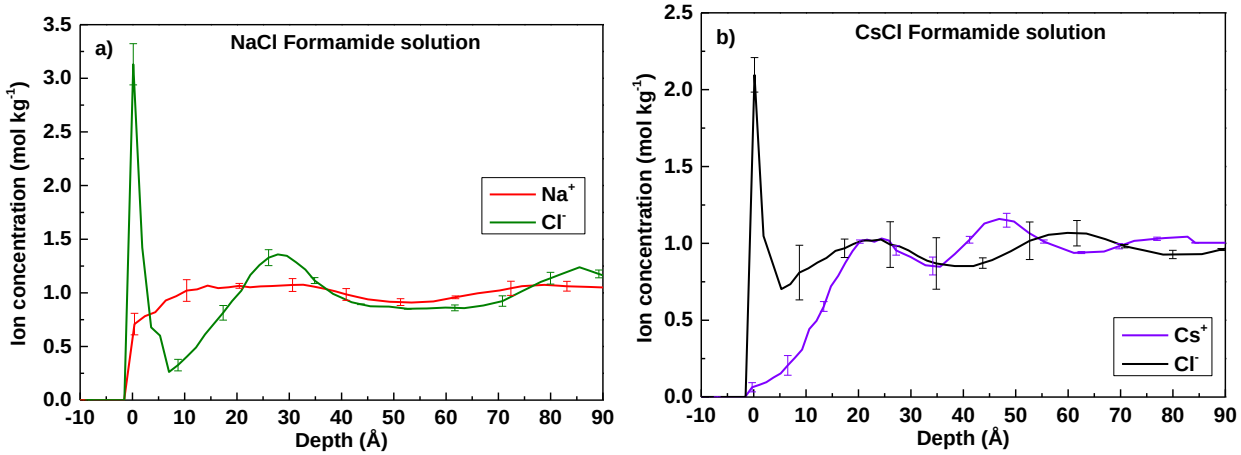

Figure II-10: Concentration depth profiles for 1 m (a) NaCl and (b) CsCl formamide electrolyte solutions. The depth calibration uncertaintity involved here is ± 4.6 Å.

APPENDIX CHAPTER III: WEAKER ION SPECIFICITY IN MEASURED CONCENTRATION DEPTH PROFILES OF ANIONS AT PROPYLENE CARBONATE AND BENZYL ALCOHOL SURFACES

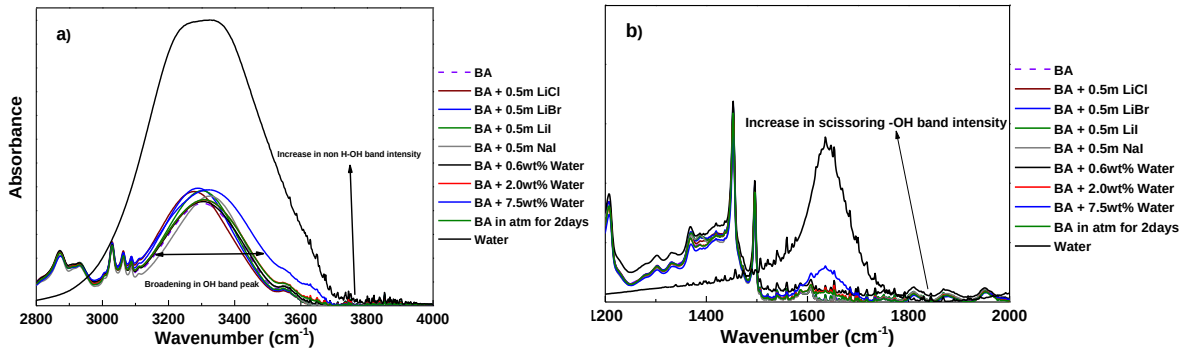

Figure III-1: ATR-FTIR spectrum for (a) broad -OH band and (b) scissoring -OH band (located around 1620 cm^{-1}) of pure benzyl alcohol, benzyl alcohol with the addition of varying wt.% of water and 0.5 m LiCl, LiI, LiBr and NaI benzyl alcohol electrolyte solutions. With an increasing percentage of water, the H-OH vibration presence starts to become more visible in respective IR bands.

As observed, when water is added at 0.6 wt.%, there is a slight increase in the intensity at the scissoring -OH band which suggest presence of free H-OH molecules present in benzyl alcohol. This observation infers, using ATR-FTIR, we can measure the presence of water at ~0.6 wt.% and no observation of peak in these regions suggest water content is less than 0.6 wt.%. Hence, following this procedure, we can say that all the electrolyte solutions prepared for NICISS, and surface tension measurement has water less than 0.6 wt.% and the effect of water presence on ion specificity in benzyl alcohol electrolyte solutions can be ignored[71].

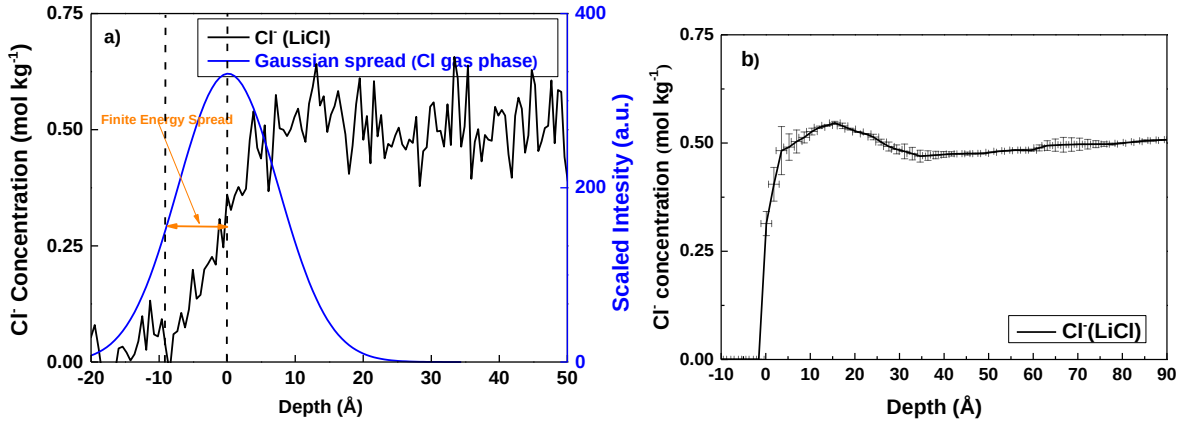

Figure III-2: (a) NICISS depth profile figures depicting the finite energy spread present in convoluted Cl^- depth profile of 0.5 m LiCl benzyl alcohol solutions (black) together with the gaussian spread present in chlorine gas phase measurement (blue) and (b) showing deconvoluted profile using the centre of Gaussian fit (E_0), Gaussian FWHM and convoluted Cl^- depth profile as input parameters[169, 287]. The deconvolution procedure is done on an energy loss scale since the backscattering event is correlated to He^0 losing energy while passing through the sample. It should be noted that the intensity of the gas phase gaussian fit is not a relevant parameter for the deconvolutions procedure and it is presented in figure (a) just to avoid confusion with the y-axis scale of convoluted Cl^- depth profile. The depth error bar presented in figure (b) is the error involved with the determination of E_0 of Chlorine from the Gaussian spread. Whereas the concentration error bar is the standard error presented between repeated Cl^- concentration depth profile measurements[239].

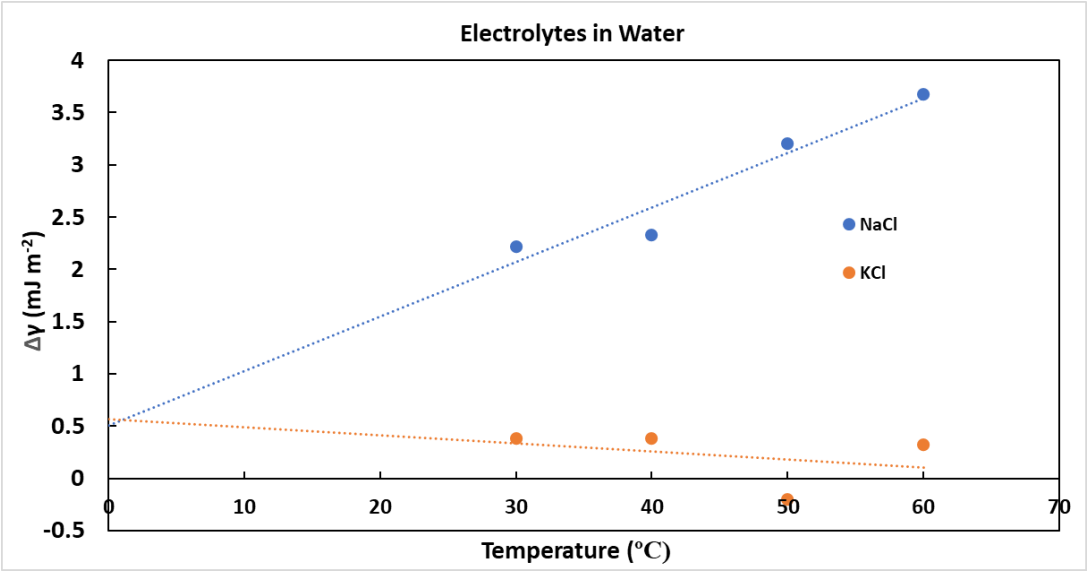

Figure III-3: Surface tension increment relative to the pure water for NaCl (blue) and KCL (orange) at varying temperature. The blue and orange trendline are linear fit of STI caused NaCl and KCl aqueous electrolyte solutions at varying temperature. As it can be seen from the interpolated trendline, lowering the measurement temperature does not change the SIE order but the STI difference between both electrolyte solutions starts to decrease [206].

ATR-FTIR results of electrolytes in propylene carbonate

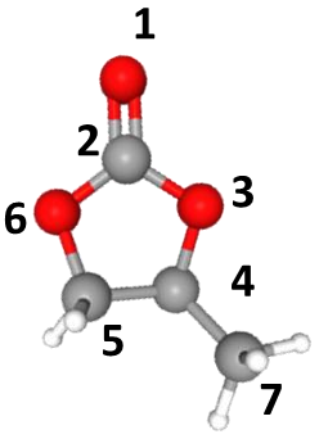

Figure III-4: Bond number assignment for propylene carbonate molecules.

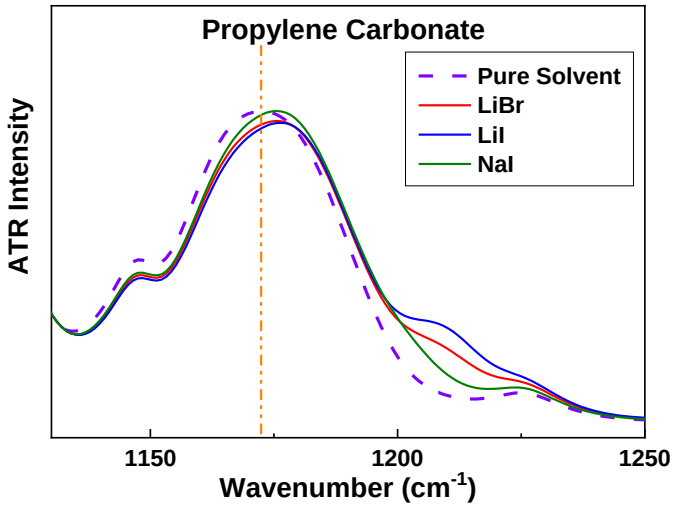

Figure III-5: ATR-FTIR spectrum for O-C-O IR peak of PC, 0.5m LiBr, 0.5m LiI and 0.5m NaI electrolyte solutions. There are weak blue shifts in the peak observed at ~1173 cm^{-1} and a shoulder formation in the range of 1200 – 1240 cm^{-1}. This shoulder formation follows the same trend observed for C=O band in the main text. This trend is also assigned to strong cation interaction at the negative dipole but mostly through the C-O_6-C [249].

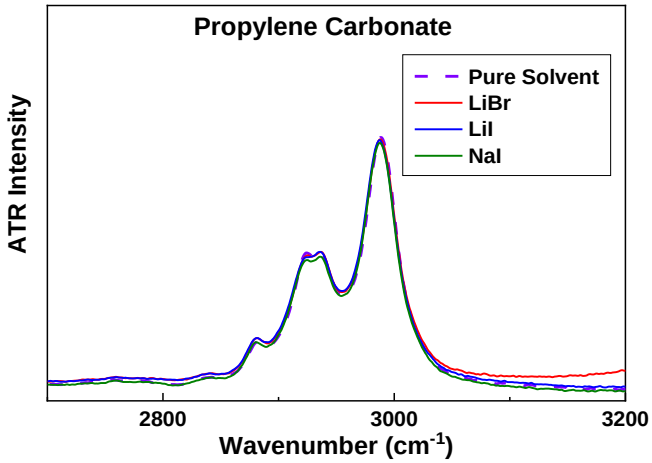

Figure III-6: ATR-FTIR spectrum for CH_2 and CH_3 IR peaks of PC, 0.5m LiBr, 0.5m LiI and 0.5m NaI electrolyte solutions. The IR peaks are similar for all PC and its electrolyte solutions suggesting weaker dipole derivative change caused by anions.

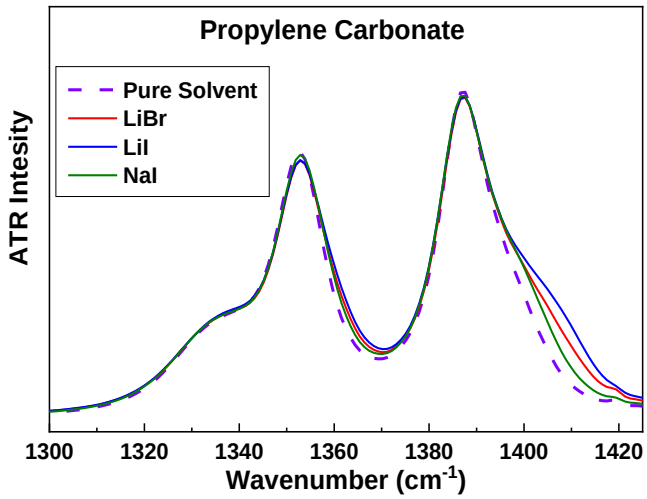

Figure III-7: ATR-FTIR spectrum of PC, 0.5m LiBr, 0.5m LiI and 0.5m NaI electrolyte solutions. Both shoulder peaks at ~ 1336 cm^{-1} and a very strong peak at ~ 1355 cm^{-1} is specific to the bending mode of C_7- H at the end of the PC ring. Whereas the IR peak observed at ~1391 cm^{-1} is a result of the combined IR contribution of the bending mode of C_7- H and the wagging mode of the C_5- H group. All presented IR peaks for the locations of anion interaction suggest weaker dipole derivative change. Thus, anion interaction is considered weak and similar within the experimental uncertainty.

The additional shoulder formation Figure III-7 at ~1400 – 1420 cm^{-1} (following the same trend as presented in the main section) is probably caused by the weak cation interaction at the C-O group on the PC ring [249]. Thus, affecting the ring structure and the C_5- H group. This is inferred because a direct anion interaction with the C-H group will be a result of halide interaction with the hydrogen dipole which should cause a shift in IR peak at ~ 1391 cm^{-1}.

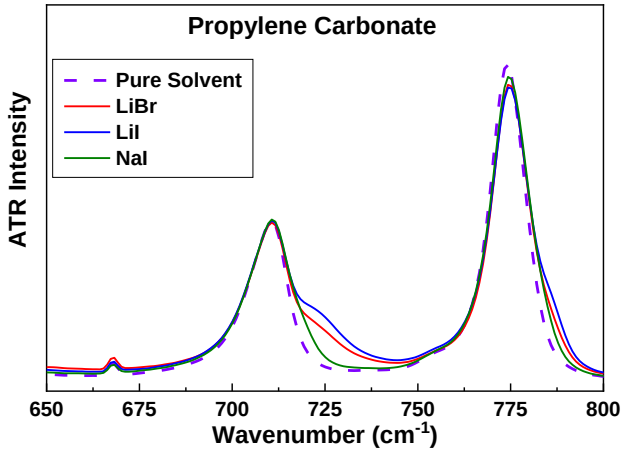

Figure III-8: ATR-FTIR spectrum for CH2 and CH3 IR peaks of PC, 0.5m LiBr, 0.5m LiI and 0.5m NaI electrolyte solutions. Both strong IR peaks are presented and the shoulder formation within these peaks corresponds to the PC ring deformation due to strong cation interaction at the C=O group.

ATR-FTIR results of electrolytes in Benzyl alcohol

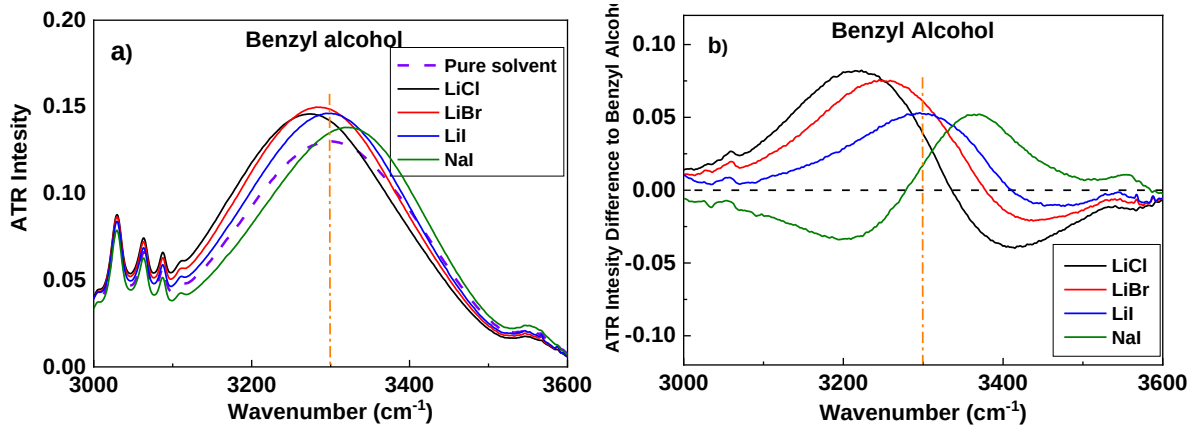

Figure III-9: Comparison of (a) ATR-FTIR spectrums of hydroxyl moiety (-OH group) of pure benzyl alcohol solvent (dashed purple line) with 0.5 m LiCl (black), LiBr (red), LiI (blue) and NaI (green) electrolyte solution and (b) difference in ATR-FTIR spectrum of electrolyte solution compared to pure solvent. The dashed orange line shows the centre for H-OH band of benzyl alcohol.

Figure III-9 (a) and (b) show the ATR-FTIR spectrums of benzyl alcohol electrolyte solutions with pure BA and the difference in the ATR-FTIR spectrum with pure BA respectively. In Figure III-9 (a), the ATR-FTIR spectrum of benzyl alcohol has a broad band at ~ 3150 – 3450 cm^{-1} that represents the hydrogen-bonded (H bonded) OH groups of BA - with the small intensity peak (bump-like feature) at ~ 3450 – 3650 cm^{-1} denoting the non- H bonded OH groups[288]. For the latter case, the change in peak intensity is small and within the experimental uncertainty. The earlier case represents the -OH stretch with the positive and negative dipole i.e., hydrogen and oxygen of the hydroxyl group respectively. Based on the charge available on the BA molecules, anions and cations will favourably interact at these dipoles[288].

From Figure III-9 (b), we see that all Lithium electrolyte solutions show a red or weak blue shift. However, the NaI electrolyte solution shows a strong blue shift. The red shift in the -OH bond is related stronger interaction of anion with the hydrogen dipole thus creating a weaker -OH bond.

A blue shift in the IR spectrum especially for the -OH bond is harder to interpret. This blue shift can be interpreted in two ways:

1) A qualitatively suggested structure-breaking effect caused by cations and anions on the BA intermolecular bonding[289].
2) Na^+ is interacting strongly with the electron donating part (i.e., oxygen) of benzyl alcohol with stronger interaction energy than the -OH bond itself.

The latter case is suggested to be an improper hydrogen bond (exception case) in which the bond length of the electron donating group and Na^+ is shorter in length compared to the -OH bond length[252]. For the earlier case, the structure-breaking effect corresponds to the breaking of a greater number of hydrogen bonds which should be related to the stronger interaction of ions with the solvent.

In either case, the blue shift is suggested to be caused by stronger Na^+ interaction (for iodide salts). Following the bulk vs surface affinity approach, this can explain the larger STI of NaI compared to LiI. However, the discussion of an improper hydrogen bond is a complex argument that needs computational aid. Further, the interpretation of ionic influence towards the hydrogen bond network (structure making or breaking effect) is not just the ion interaction with the opposite charge dipole but with the angular movement of the dipole change as well[290]. Thus, the IR interpretation will be oversimplified in terms of structure breaking effect. Another possible interpretation is the strong influence of anion interaction on the positive charge of carbon of the C-O group that can cause this blue shift. Interaction of anion at C-O moiety can influence the length of the C-O bond thus affect the -OH group IR spectrum by shortening the bond. However, this will also influence the C-O group IR peak which shows a weak or minimal change (Figure III-10). Therefore, this interaction can be ignored.

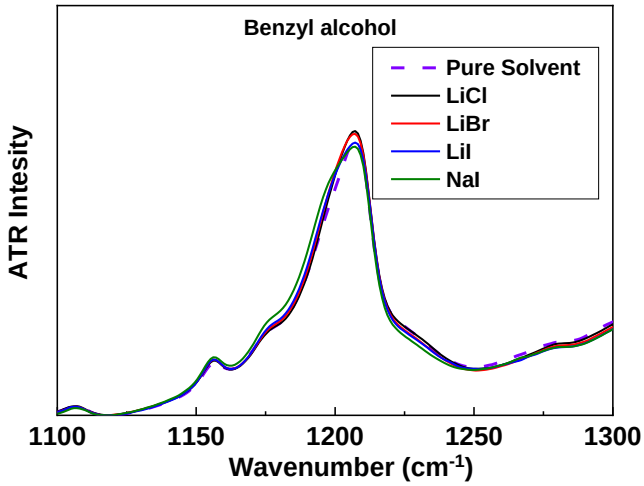

Figure III- 10: ATR-FTIR spectrum of C-O group present on the BA molecules for 0.5m LiCl, 0.5m LiBr, 0.5m LiI and 0.5m NaI electrolyte solutions. The IR peak has shown minimal change between pure solvent and various electrolyte solutions.

For specific anions trend of lithium salts, we observe that the decreasing redshift trend follows Cl^- > Br^- > I^- (Figure III-9). This means that the electrotactic interaction of anion is getting stronger with the positive dipole, but this strengthening of electrostatic interaction follows order as Cl^- > Br^- >I^-. Based on the bulk vs surface affinity approach this would mean that Cl^- should be more depleted than Br^- or I^-. This is in contrast with the STI trend and NICISS CDPs for ions at BA surfaces but in agreement with solvation free energy data of ions presented in Chapter 5.

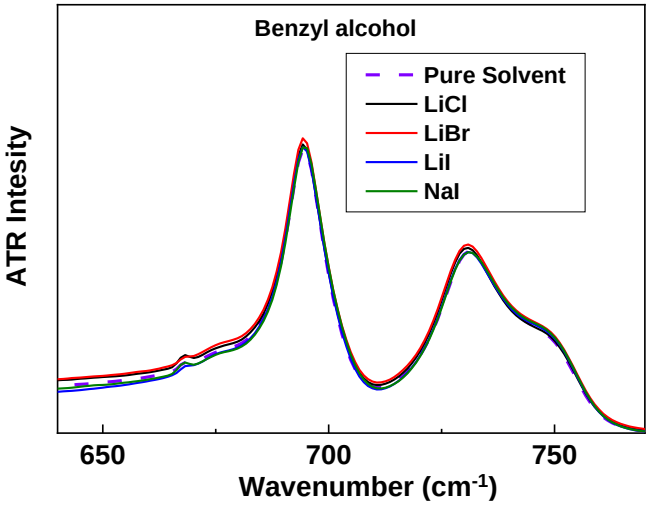

Figure III-11: ATR-FTIR spectrum of benzyl alcohol solution showing no evidence of cation-pi interaction IR peak. If there was a cation-pi interaction with the benzene ring of benzyl alcohol, then a new signature IR peak will appear between 640 – 770 cm^{-1} [291]. Due to weak intensity, the small peak at ~665 cm^{-1} cannot be assigned as a cation-pi interaction peak with confidence.

APPENDIX CHAPTER IV: NICISS MEASUREMENT OF IONS AT SALTY WATER SURFACES

The motivation of the current thesis was to gain a detailed understanding of SIE at various solvent surfaces and the most important and investigated solvent for SIE is water. Hence, measuring concentration depth profiles at water surfaces seems like an obvious selection. However, NICISS is a UHV-based technique and performing water measurement in a vacuum is challenging and requires specialised setups. Andersson and co-workers[270, 292] have previously investigated aqueous electrolyte solutions surfaces with a specialised set-up (sample holder) but with a different design of the instrument. To perform measurements in the current design, I have modified the current sample holder setup. The modified sample holder is of a fully enclosed metal housing with two sample apertures to let the ion beam in and out (backscatter) to the TOF detector as shown in Figure IV-1 (a). This enclosed housing is the same as used in this thesis but with a closed cap and two apertures in front of the rotating wheel. This cap also has a metal divider in place between two apertures to stop any unwanted backscattered projectiles (like projectiles backscattering from the metal end of the aperture) from making their way to the TOF detector.

To conduct the NICISS experiment using this cap, I had to minimise the ion beam spot size to <1mm and determine the correct sample position and rotational angle so the ion beam can be focused on the 1st aperture and the backscattered projectiles make it out the 2nd aperture (see Figure IV-1). This was achieved in a trial-and-error fashion by running NICISS measurements with formamide (as a test solvent) at various, X-direction (left and right direction to the ion beam), Z-direction (upwards and downwards direction to the ion beam), and angles (sample holder orientation).

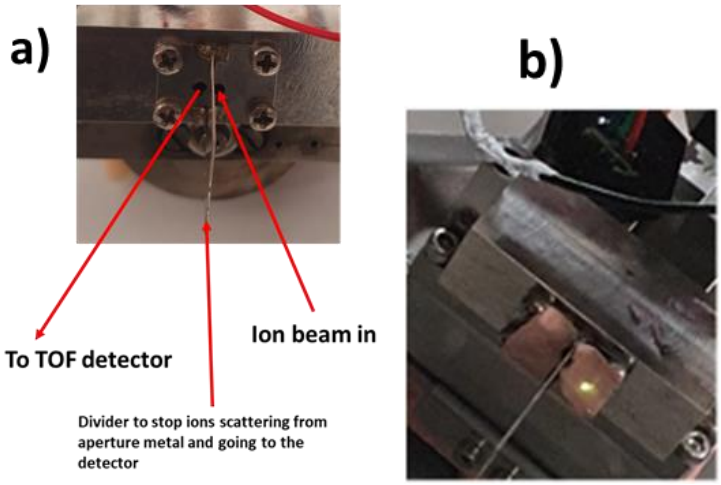

Figure IV-1: (a) Reduced aperture setup for NICISS liquid sample holder and (b) Ion beam spot on fluorescence sample covered copper tape attached to the liquid sample holder.

However, the count rate using formamide as a test solvent was low compared to normal measurements (due to small apertures) making the trial-and-error determination a lengthy process. To expedite the process, a metal sample with drop-casted P3HT polymer solutions was used with silicon-based surfactant impurity (Figure IV-2 (a)). This sample was used as silicon-based surfactant impurities are highly surface adsorbing solutes and its TOF step can be observed quickly in a NICISS spectrum as shown in Figure IV-2 (b). Further, this sample arrangement also allows for the ion beam current measurement at the wheel of the sample holder. Hence, I could optimise the ion beam better for the best suitable count rates. Following these procedures, a relatively good sample position was successfully obtained.

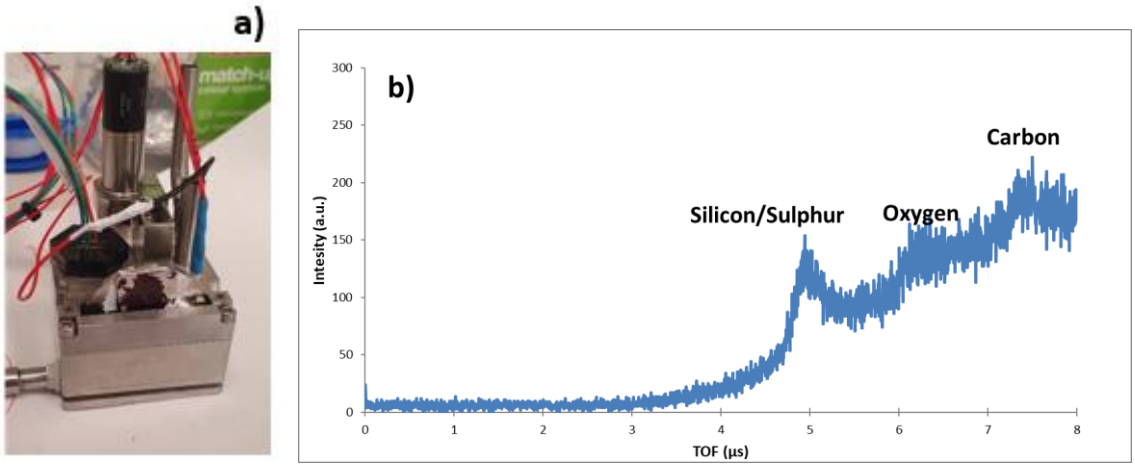

Figure IV-2: (a) NICISS sample holder arrangement to measure current inside the cap and (b) NICISS spectrum of attached polymer layer plate onto the liquid sample holder.

The next challenge was controlling the evaporation of an aqueous electrolyte solution in the UHV chamber. Adding high salt concentration in water will result in the solution's vapour pressure depression and lowering of the solution's freezing point temperature. Hence, NICISS measurement was conducted by setting up the sample holder at a temperature just above the solution's freezing point. Even after the addition of a salt concentration of 4 molal, solvent evaporation was fast (< 30 minutes) and to gain reasonable NICIS spectra minimum of 8 hours of measurement is needed (depending on the count rate which is already low in the herein discussed sample holder setup).

Previously Andersson and co-workers [270, 271, 292] used to vent the vacuum analysis chamber and directly introduce the sample holder into the position for a NICISS measurement. Following this procedure, after 4 or 5 pumped-down cycles a reasonable spectrum was collected. However, the current NICISS instrument has a 2-stage pumping down system where the sample has to be first introduced into the liquid load lock chamber separated by a gate valve from the UHV analysis chamber. Once optimal pressure is reached then a sample can be introduced into the UHV analysis chamber. But this 2-stage pumping down setup is disadvantageous for high vapour-pressure solvent

(i.e., water) measurements as the duration taken to introduce the sample holder into the analysis position with an aqueous solution is long enough that most of the solution is evaporated.

To remedy this challenge, I used the filling line available on the liquid sample holder stage (Figure IV-3 (a)) to continuously top up the water when the solution level is low for NICISS measurement. However, another problem occurred following this procedure. The filling line inside the NICISS liquid manipulator is situated close to the cooling line. This cooling line is used to control liquid sample holder temperature and the sample stage has to be set to – 7 °C to reduce electrolyte solutions evaporation[m]. This cooling line creates a problem that when pure water is added to the filling line, it quickly freezes before reaching the sample holder (Figure IV-3 (b)) due to metal temperature conduction. If more solvent is added to remove this ice block the line becomes full and floods the liquid manipulator chamber leading to forced venting of the liquid manipulator chamber. This happens as in the current setup we have minimal control over the volume of the liquid inside the line. We have minimal control over the volume inside the UHV chamber line as only one gate valve is used in the filling line situated outside the UHV chamber[n]. Further, we cannot fill the electrolyte solution, as the presence of dried salts leads to internal corrosion of the line which will be hard to clean and create complications for the longer operation of the instrument.

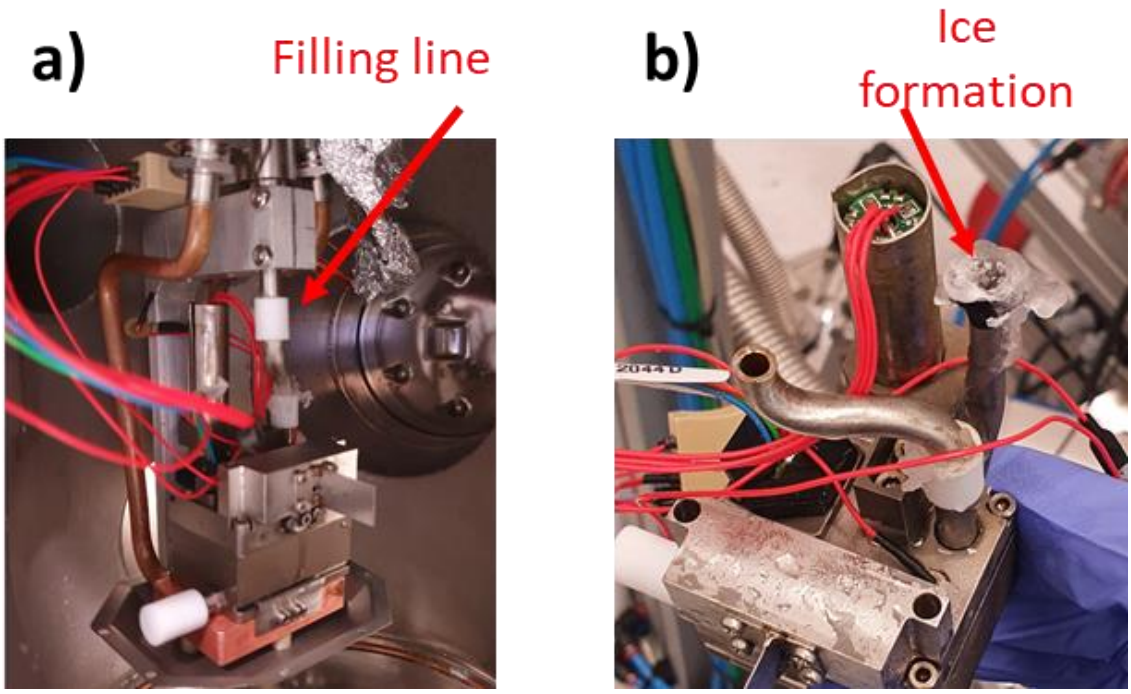

Figure IV-3: (a) Showing arrangement of sample holder for continuous filling of solvent and (b) Ice formation in the filling line.

[m] The sample holder setup temperature is decided based on the concentration of electrolytes added to the solutions. The higher the concentration, the lower the sample holder temperature is set to.
This temperature is determined through the Van Hoff't equation with the assumption of ideal activity coefficient.
[n] This filling line was designed for the gas phase measurements.

To overcome this challenge, I designed a new sample holder (Figure IV-4 (a)) set up the Peltier module. Taking advantage of the Peltier effect, we can lower the sample holder temperature to – 7 °C while keeping the sample stage temperature (hence the cooling line) above the water's freezing point temperature (see Figure IV-4 (b)).

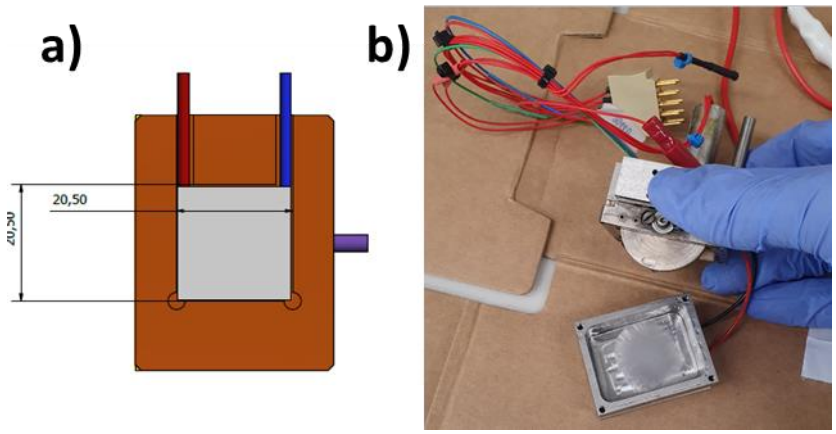

Figure IV-4: (a) Design of the new NICISS sample holder reservoir for attachment of the Peltier module and (b) showing the ice formation in the reservoir as evidence of the successful working of the new reservoir.

After overcoming above listed challenges, the successful NICISS spectrum of 4 molal LiBr aqueous electrolyte solutions was measured at – 7 °C (Figure IV-5 (a)). However, the energy loss due to continuously evaporating water molecules leads to the broadening of projectiles' energy loss. This broadening can be subtracted following the procedure employed by Andersson[292] previously.

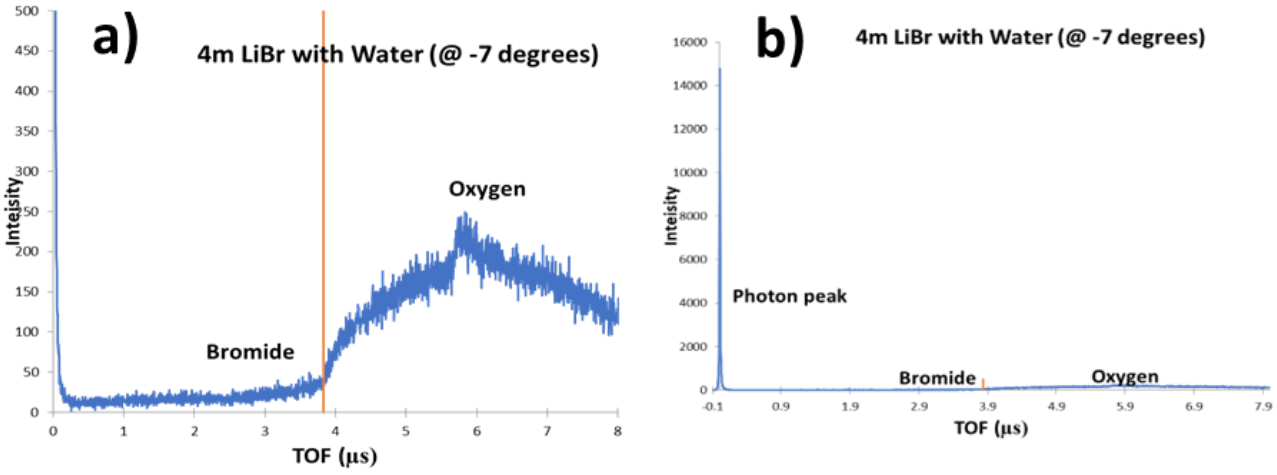

Figure IV-5:(a) Scaled NICISS TOF spectra of 4 molal (m) LiBr with water solutions at – 7 °C and (b) Rescaled NICISS TOF spectrum illustrating the difference in counts of photons and the sample of interest. The orange line shows the Br^- step for the LiBr electrolyte solution. The difference in counts is due to the backscattering of projectiles from the gas phase layer formed in front of the liquid sample due to solvent evaporation.

However, additional problems will need to be fixed even after the vapour phase energy loss contribution is determined. The challenges (or problems) that need to be addressed before a successful NICISS aqueous electrolyte solutions measurement can be obtained are:

1) A controlled flow rate (in a manually controlled valve) to avoid accidental venting of the NICISS instrument. This happens due to a delay in receiving the signal from the level sensor that indicates the optimum solvent level for NICISS measurement.
2) An automatic top-up system needs to be built to reduce the labour extensive work required to finish one set of measurements.
3) Then following Andersson's method, we will still require 4 – 5 days to measure to get a useful NICISS spectrum. Hence further avenues to improve the count rate must be explored.

APPENDIX CHAPTER V: IONS WITHIN POLYMER STRUCTURE AT THE VAPOUR-FORMAMIDE INTERFACE

Employing NICISS measurements, we can directly gain ionic organisation information within the polymeric structure due to its elemental sensitivity and high-resolution depth profile. Thus, I attempted to investigate the ionic presence/absence within the stimulus (temperature) responsive polymer structure at the vapour-formamide interface. The stimulus (temperature) responsive polymer selected was polypropylene oxide/ polypropylene glycol (PPO). PPO has been used in commercially relevant applications since the 1970s [293]. PPO is a stimulus-responsive polymer with an LCST of 20 ^{o}C in water which can be varied up to 50 ^{o}C depending on the molecular weight of the polymeric chain[294]. PPO is known for its high surface activity and segregates into many interfaces[295].

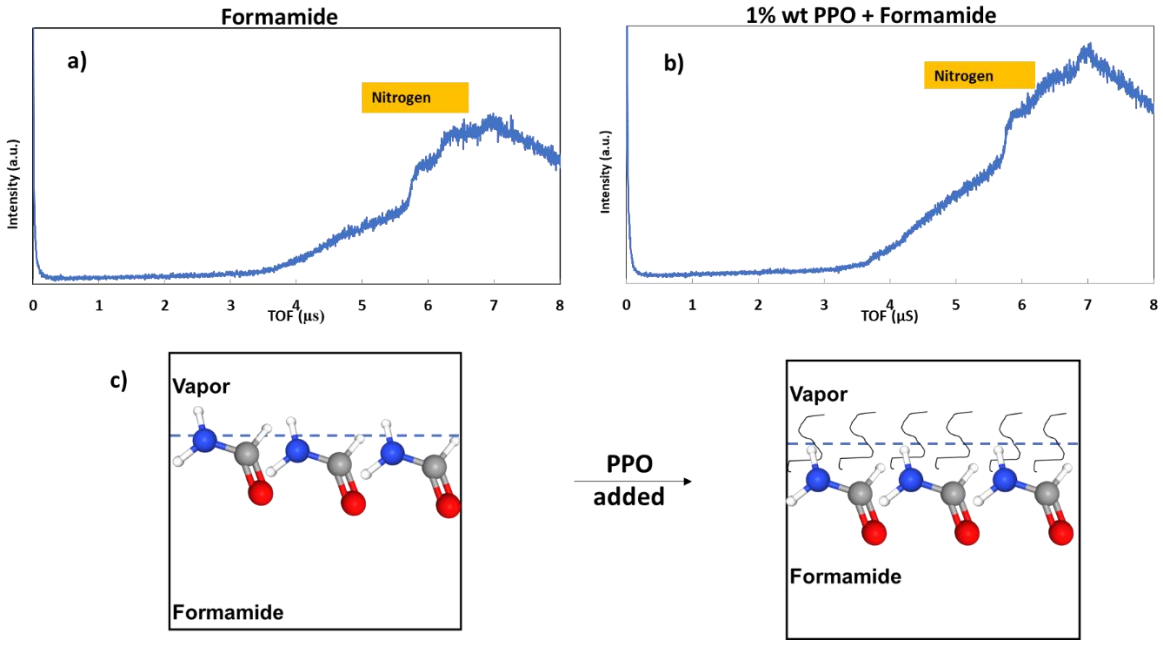

Figure V-1: The comparison of NICISS TOF spectrum of (a) pure formamide, (b) 1 weight per cent (1% wt.) of PPO in formamide, and (c) scheme for interpretation of the nitrogen step depletion observed in figure 1 (b).

In Figure V-1 (a) and (b), NICIS spectra of pure formamide and formamide with 1 wt. % PPO is shown respectively. It is observed that the nitrogen step of formamide changes (diminishes) in presence of PPO. The change in nitrogen step in Figure V-1 (b) compared to Figure V-1 (a) represent the depletion of formamide and stronger absorption of PPO at the solvent surface. This is concluded based on that the PPO adsorption at the interface interferes with the backscattering signal from the formamide molecule causing a diminished nitrogen step. The nitrogen step is used to interpret this depletion as PPO molecules do not have any nitrogen group within their structure. Therefore, the

change in the nitrogen step only represents the change in solvent (formamide) concentration at the interface.

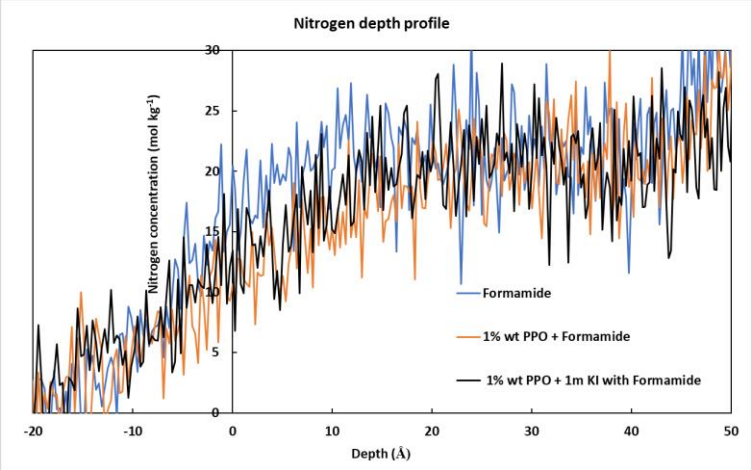

Figure V-2: Nitrogen depth profile comparison of pure formamide (blue curve), in presence of 1 weight per cent (1% wt.) of PPO (orange curve) and with 1 molal KI electrolyte solution with 1 % wt. of PPO (black curve).

In Figure V-2 it is observed that the nitrogen raw (convoluted) NICISS depth profile of formamide occurs at the lower depth. Whereas the nitrogen raw NICISS depth profile is shifted to a higher depth for 1 m KI electrolyte solution with 1 % wt. of PPO followed by nitrogen raw NICISS depth profile of 1% wt. of PPO with formamide solutions. This variation in nitrogen step between PPO solution with and without the electrolyte demonstrates that the PPO gets salted in from the interfaces into the bulk. A well-observed behaviour of iodide salts. Similarly, the I^- depth profile of the KI electrolyte solution shift to a higher depth at formamide surfaces in presence of PPO compared to just KI with formamide electrolyte solution (Figure V-3). This means that PPO pushes I^- further away from the formamide surfaces.

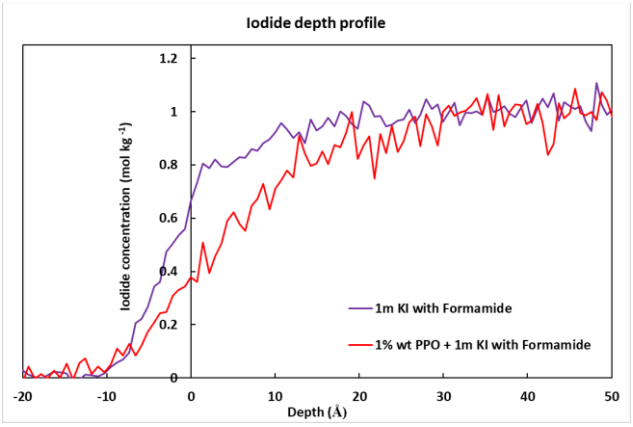

Figure V-3: NICISS concentration depth profile of Iodide in 1m KI with formamide solution (purple curve) and presence of 1 weight per cent (1% wt.) of PPO with 1m KI with formamide solution (red curve).

From depletion observed in nitrogen and I^- depth profile we gain information on PPO presence. The depletion region in the nitrogen depth profile directly relates to PPO presence. The depletion region in the I^- depth profile is also related to PPO presence but in the sense that it is pushing I^- away from surfaces. Hence, comparing the overall depletion regions of Nitrogen and I^- we can comment if ions bind directly to the PPO at formamide surfaces.

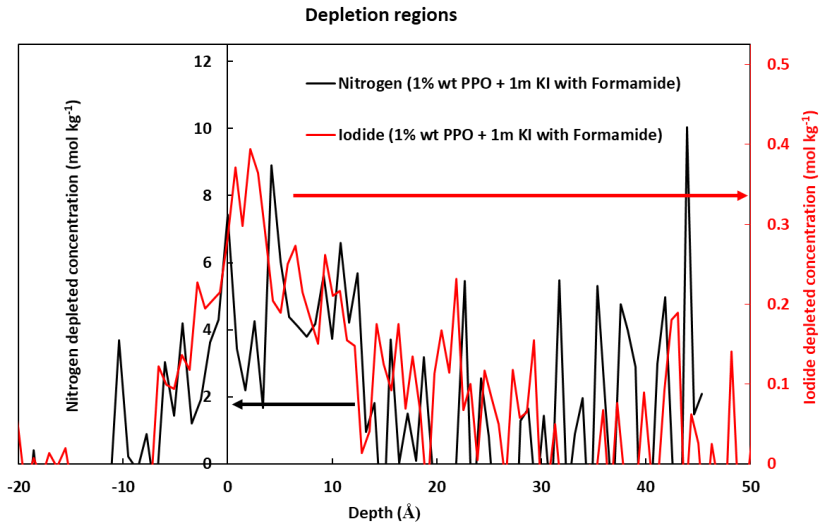

Figure V-4: Nitrogen (black curve) and Iodide (red curve) depletion concentration depth profiles in 1m KI formamide solution with 1 weight per cent (1% wt.) of PPO. Nitrogen and iodide depletion concentration in formamide solution is of two different scales as pointed out with arrows.

In Figure V-4 we plot the depletion depth profile of nitrogen and I^- by subtracting the nitrogen and I^- depth profile of 1m KI formamide electrolyte solutions and 1m KI formamide electrolyte solution with 1 wt. % PPO respectively. Following this procedure, we can locate the nitrogen absence at the formamide surfaces (representative of PPO presence) and the I^- absence in electrolyte solutions with polymeric presence. If both nitrogen and I^- are absent (depleted) at the same depth locations means that I^- does not bind to the PPO. As for an ion to be binding to the polymeric system, it has to locate nearby the polymer accumulation region.

From Figure V- 4 we can see that the I^- depleted depth region is located closer to the formamide surface compared to nitrogen-depleted depth regions as there is a slight overlap in their depletion region. This means that I^- is located at the higher depths in formamide solutions where PPO is also present meaning I^- binds to the end of the PPO structure in formamide. This information is of high importance and further location of ions within PPO can similarly be determined at formamide surfaces. However, we have observed that due to the presence of PPO, the higher limit of probing depth of He projectiles at 3 KeV is reached.

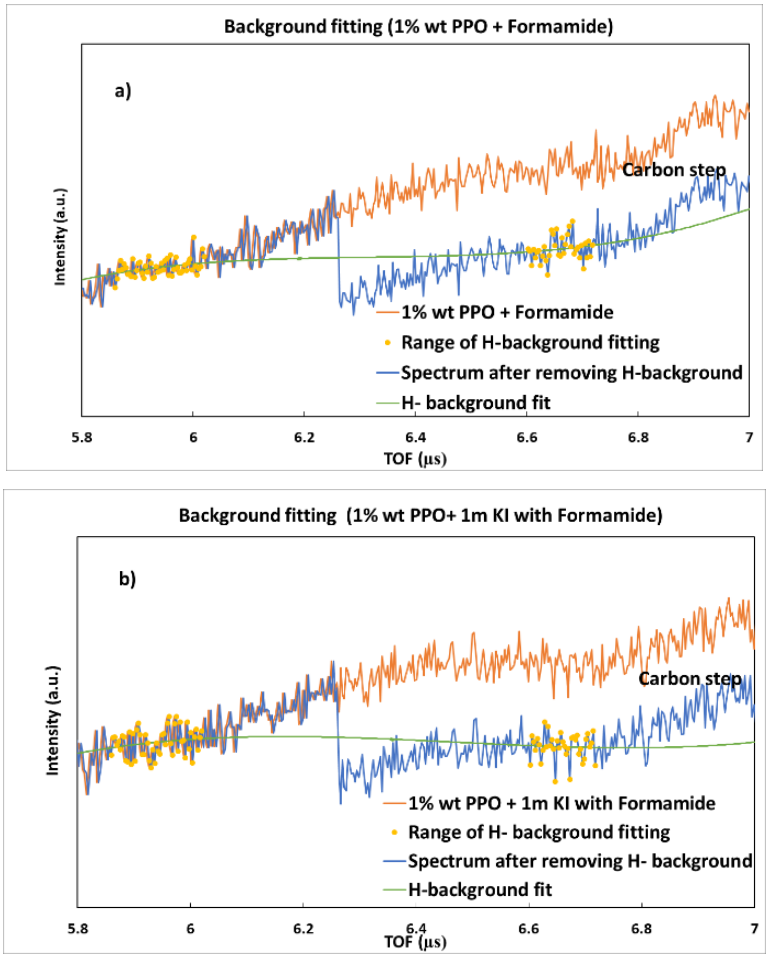

Figure V-5: Hydrogen background fitting for the nitrogen step in (a) formamide solution with 1 weight per cent (1% wt.) of PPO and (b) 1m KI formamide solution with 1% wt. of PPO. Yellow data points in both curves represent the boundary conditions selected for fitting the nitrogen step with the 3rd-order polynomial curve (green curve).

In Figure V-5 (a) and (b), the hydrogen background removal fit (green curve) of the nitrogen step is shown with 1% wt. of PPO and 1m KI formamide solution with 1% wt. of PPO respectively. The H-background of the nitrogen step in Figure V-5 (a) shows a smooth linear fit with a 3rd-order polynomial, whereas in Figure V-5 (b) the H-background seems to follow a curved trend. This suggests that a smooth linear background cannot be removed from the nitrogen step of 1m KI formamide solution with 1% wt. of PPO within the selected fitting range. We cannot extend the fitting range (yellow data points) in the presented figures as this range will start to overlap the carbon step. This means that in Figure V-5 (b) the He backscattered projectiles have researched the probing depth of NICISS at 3 KeV. To overcome the issue of probing depth, we will have to move to a higher primary energy of NICISS measurement i.e., 7 KeV which requires, further energy calibrations, stopping power measurements, ion beam focusing parameter adjustments, time delay determination, and depth resolution estimation.

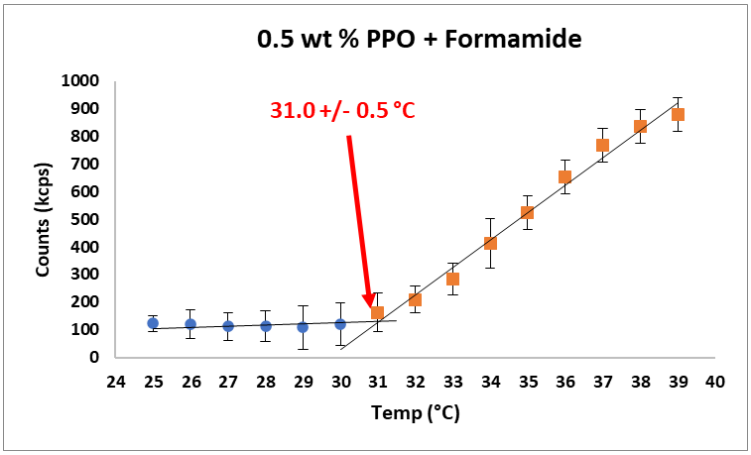

Figure V-6: Dynamic Light Scattering (DLS) results showing the LCST for 0.5 wt.% PPO in formamide at 31.0 °C. Error bars are calculated based on the standard deviation between 3 repeated sets of measurements.

Determination of ionic organisation or binding location with biomimicking polymer structure will help us understand the ionic interaction with these polymers hence providing insights for unravelling SIE[296]. From DLS measurement, I determined that at 0.5 wt. % PPO in formamide has a LCST of 31.0 +/- 0.5 °C (Figure V-6). Further, I have performed NICISS measurement of pure formamide solution at two different (Figure V-7) which can also be conducted at a much higher temperature with a newly built Peltier module attachment for liquid reservoir setup (see Appendix chapter IV).

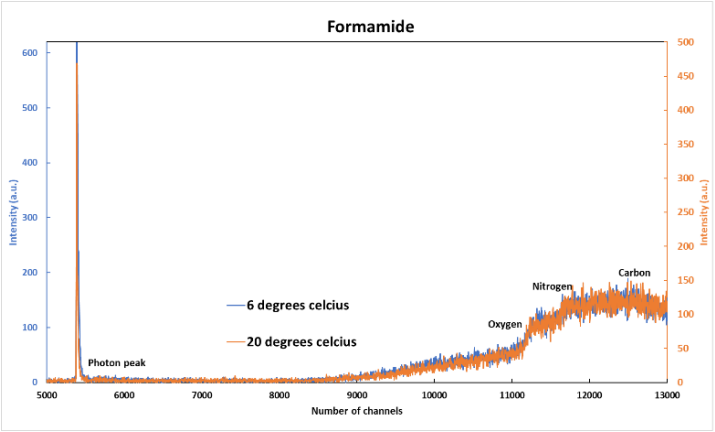

Figure V-7: Raw NICISS spectrum showing formamide measurement at 6 degrees Celsius (blue curve) and 20 degrees Celsius (orange curve).

Hence, in future with higher primary energy projectiles, we can directly determine the ionic binding location during the conformational change of biomimicking PPO in formamide solutions i.e., before LCST, at the LCST, and after the LCST. However, to gain such information we will have to determine the structural arrangement of PPO in formamide which is not available at this time. Initial X-ray scattering measurements (at the Advanced photon source - GUP 80053) have been performed during my short visit to Prof. Mark Schlossman' s group at the University of Illinois, Chicago.

APPENDIX CHAPTER VI: NICISS DEPTH RESOLUTION

Throughout this thesis, I have mentioned that NICISS has a high-depth resolution of ~ 2Å. Even though I have not made the direct use of this depth resolution. This resolution is not required for concentration depth profile comparisons unless we discuss our results only in terms of depth profile due to the convolution of the NICISS spectrum. The best resolution (without additional uncertainty) in a NICISS spectrum is achieved in the convoluted depth profile. Thus, here I have used the convoluted depth profile to demonstrate the NICISS depth resolution.

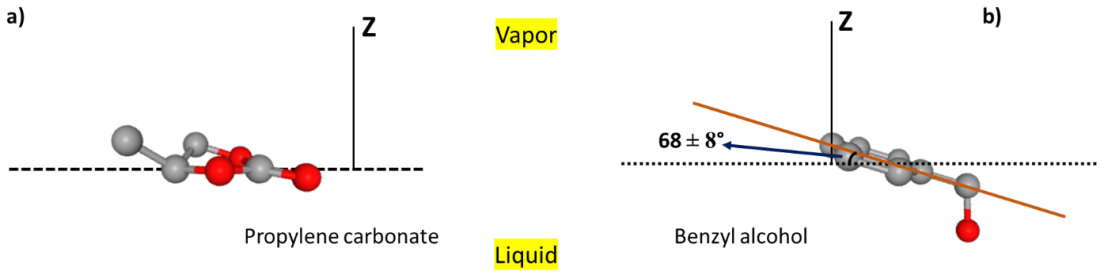

Figure VI-1: Orientation of (a) Propylene carbonate (PC) and (b) Benzyl alcohol (BA) at the vapour-solvent interface. The orientation of the PC has been determined by an MD simulation[244] and SFG measurements[245]. The orientation of BA has been determined by Andersson[196] employing the angle-resolved mode of NICISS. The carbon atoms are shown in grey colour and oxygen in red colour. Here, the hydrogen atoms of the solvent molecules are not included for clarity.

In Figure VI-1 (a) and (b) the orientation of propylene carbonate (PC) and benzyl alcohol (BA) molecules are presented respectively. You et al suggested that the PC molecules are lying flat at the interfaces with the methyl group at the end of the PC ring protruding in the vapour phase. Similar observations were reported by Wang et al [245] through SFG-assisted molecular dynamics simulation with the additional observation that the C=O group has a slight tilt pointing inwards in bulk. However, the tilt angle was too small to be discerned within the noise. For BA molecules, Andersson[196] measured the orientation at the interface as the -OH group of BA pointing inwards into the bulk while the BA molecules showed a tilt against the interfacial plane of 68 ± 8 º at the interface[º].

The current discussion is for the normal mode of NICISS. In normal mode, the orientational differences will be flat for C atoms of PC and BA, as NICISS measures the average backscattered projectiles (the interface is considered flat, (see 2.1.5) and would not be able to differentiate between the methyl group of the PC ring and the C atom of C=O group or the C atom of C-O bond in BA. Since the O atom of PC and BA molecules are orientated differently (i.e., pointing inwards) the O of

[º] In angle-resolved NICISS mode, the depth resolution is 0.5 – 0.7 Å 170. Andersson, G., T. Krebs, and H. Morgner, *Angle resolved ion scattering spectroscopy reveals the local topography around atoms in a liquid surface.* Physical Chemistry Chemical Physics, 2005. **7**(15): p. 2948-2954.

BA will show a depletion away from the interface (an onset at a lower depth in the NICISS depth profile).

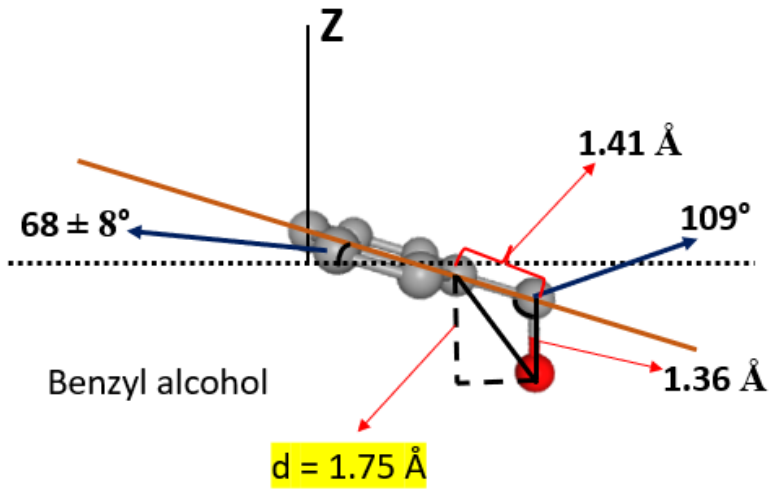

Figure VI-2: Calculation of the height of the triangle which is the distance (d) between the C atom on the benzene ring and the O atom of the BA. All the values used for calculation are shown in the figure.

Based on the orientation depicted in Figure VI-1 (a) and (b), the position for O of the C=O group of the PC molecule and the C on the benzene ring of the BA molecule is the same within the experimental uncertainty. Thus, by calculating the distance 'd' between the C atom on the benzene ring and the O atom of BA we can calculate the approximate depth difference between the O atoms of PC and BA. From the approximate calculation as shown in Figure VI-2 we get a value of d = ~1.75 Å.

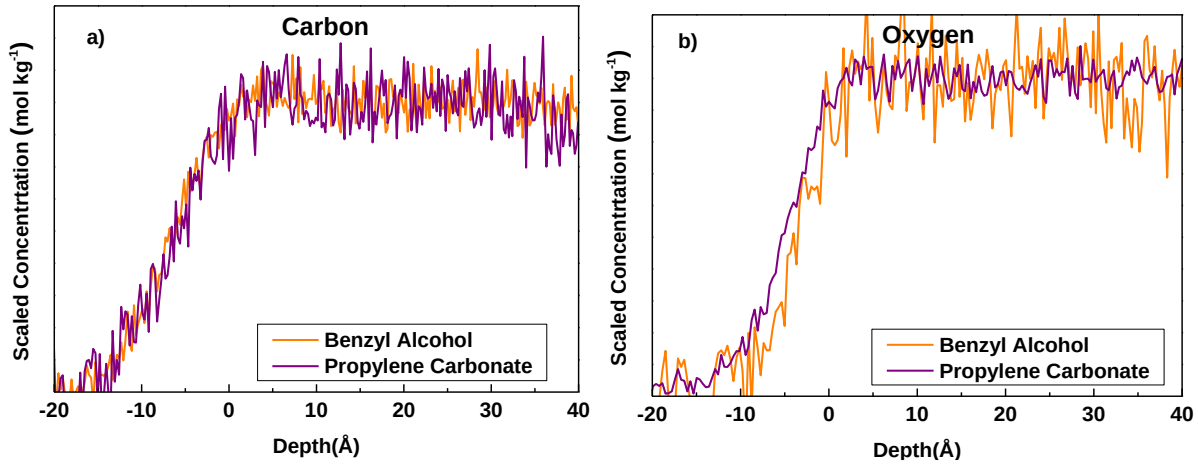

Figure VI-3: Convoluted NICISS depth profile of (a) Carbon (C) and (b) Oxygen (O) of propylene carbonate (purple) and Benzyl alcohol (orange) at the vapour-solvent interface. The uncertainty involved here is the same for both solvents' carbon and oxygen depth profiles and in the same direction. The noise in the oxygen depth profile of benzyl alcohol is larger as it has lesser number of O atoms in its molecular structure.

In Figure VI-3, (a) and (b), the convoluted NICISS depth profile of Carbon and Oxygen of PC and BA are presented. Carbon depth profiles are overlapping for both solvents which is obvious as the interface of both solvents have carbon coverage and NICSS will measure both carbons at the same depth. Interestingly, the oxygen depth profile of PC and BA show clear differences. The oxygen depth profile onset of BA is shifted to higher depths compared to the oxygen depth profile onset of PC. This means that the O atoms are located slightly below the interface in the case of BA. By shifting the profile to overlap the oxygen depth profile onset of PC, we get a value of 1.61 ± 0.30 Å. This value is in reasonable agreement with the calculated value of d.

Note: the error presented here is due to 1) depth determination by shifting the curve and (2) repetition measurements done a year apart (Oct 2021 and Sep 2022). Additional uncertainty that is not accounted here is the difference in the O atom location of PC and BA at the interfaces due to the suggested tilt at the interface for PC molecules.

BIBLIOGRAPHY

1. Works, A., Clarendon Press london 1927. **7**: p. 933b.
2. Helfferich, F.G., *Ion Exchange: Past, Present, and Future*. 1986, Springer Netherlands. p. 23-32.
3. Gregory, K.P., et al., *Lewis Strength Determines Specific-Ion Effects in Aqueous and Nonaqueous Solvents.* The journal of physical chemistry. A, 2019. **123**(30): p. 6420-6429.
4. Debye, P.H., Erich *Zur Theorie der Elektrolyte. I. Gefrierpunktserniedrigung und verwandte Erscheinungen.* Physikalische Zeitschrift, 1923. **24**: p. 185-206.
5. Zhang, Y. and P.S. Cremer, *Interactions between macromolecules and ions: the Hofmeister series.* Current Opinion in Chemical Biology, 2006. **10**(6): p. 658-663.
6. Zhang, Y. and P.S. Cremer, *Chemistry of Hofmeister Anions and Osmolytes.* Annu. Rev. Phys. Chem., 2010. **61**(1): p. 63-83.
7. Okur, H.I., et al., *Beyond the Hofmeister Series: Ion-Specific Effects on Proteins and Their Biological Functions.* The Journal of Physical Chemistry B, 2017. **121**(9): p. 1997-2014.
8. Craig, V.S.J., B.W. Ninham, and R.M. Pashley, *The effect of electrolytes on bubble coalescence in water.* Journal of Physical Chemistry, 1993. **97**(39): p. 10192-10197.
9. Henry, C.L., et al., *Ion-Specific coalesence of bubbles in mixed electrolyte solutions.* Journal of Physical Chemistry C, 2007. **111**: p. 1015.
10. Henry, C.L. and V.S.J. Craig, *Ion-specific influence of electrolytes on bubble coalescence in nonaqueous solvents.* Langmuir : the ACS journal of surfaces and colloids, 2008. **24**(15): p. 7979-7985.
11. Humphreys, B.A., et al., *Specific ion modulated thermoresponse of poly(N -isopropylacrylamide) brushes.* Phys. Chem. Chem. Phys., 2016. **18**(8): p. 6037-6046.
12. Murdoch, T.J., et al., *Specific ion effects on thermoresponsive polymer brushes: Comparison to other architectures.* Journal of Colloid And Interface Science, 2018. **526**: p. 429-450.
13. Koelsch, P., et al., *Specific ion effects in physicochemical and biological systems: Simulations, theory and experiments.* Colloids and Surfaces A: Physicochemical and Engineering Aspects, 2007. **303**(1-2): p. 110-136.
14. Schwierz, N., D. Horinek, and R.R. Netz, *Reversed anionic Hofmeister series: the interplay of surface charge and surface polarity.* Langmuir, 2010. **26**(10): p. 7370.
15. Leontidis, E., *Investigations of the Hofmeister series and other specific ion effects using lipid model systems.* Adv Colloid Interface Sci, 2017. **243**: p. 8-22.
16. Gadsby, D.C., *Ion channels versus ion pumps: the principal difference, in principle.* Nature Reviews Molecular Cell Biology, 2009. **10**(5): p. 344-352.
17. Sutera, S.P. and R. Skalak, *The History of Poiseuille's Law.* Annual Review of Fluid Mechanics, 1993. **25**(1): p. 1-20.
18. Dole, G.J.M., *The viscosity of aqueous solutions of strong electrolytes with special reference to barium chloride.* 1929. **51**: p. 2950-2964.
19. Sprung, Ann Physik, 1876. **1**: p. 159.
20. Arrhenius, S., *Über die innere Reibung verdünnter wässeriger Lösungen.* Zeitschrift für Physikalische Chemie, 1887. **1**(1): p. 285-298.
21. .Wagner, J., ibid, 1890. **31**: p. 5.
22. W.Herz, Z.Anorg.Chem, 1914. **89**: p. 393.
23. Schneider, K. 1910: Rostock.
24. Frank, H.S. and M.W. Evans, *Free volume and entropy in condensed systems III. Entropy in binary liquid mixtures; partial molal entropy in dilute solutions; structure and thermodynamics in aqueous electrolytes.* The Journal of Chemical Physics, 1945. **13**(11): p. 507-532.
25. Washabaugh, M.W. and K.D. Collins, *The systematic characterization by aqueous column chromatography of solutes which affect protein stability.* The Journal of Biological Chemistry, 1986. **261**(27): p. 12477-12485.
26. Hamaguchi, K. and E.P. Geiduschek, *The effect of electrolytes on the stability of the deoxyribonucleate helix.* Journal of the American Chemical Society, 1962. **84**(8): p. 1329-1338.
27. Kunz, W., J. Henle, and B.W. Ninham, *'Zur Lehre von der Wirkung der Salze' (about the science of the effect of salts): Franz Hofmeister's historical papers.* Current Opinion in Colloid & Interface Science, 2004. **9**(1-2): p. 19-37.
28. Kunz, W., *Specific Ion Effects, Evidences*, in *Encyclopedia of Applied Electrochemistry*, G. Kreysa, K.-i. Ota, and R.F. Savinell, Editors. 2014, Springer New York: New York, NY. p. 2045-2050.
29. Voet, A., *Quantitatvie Lyotropy.* Chemical Reviews, 1937. **20**: p. 169-179.

30. Freundlich, H., *Die Doppelbrechung des Vanadinpentoxydsols.* Zeitschrift für Elektrochemie und angewandte physikalische Chemie, 1916. **22**(1-2): p. 27-33.
31. Pearson, R.G., *Hard and soft acids and bases.* Journal of the American Chemical society, 1963. **85**(22): p. 3533-3539.
32. FREUNDLICH, H., Kapillarchemie, 1930. **1**(4th edition): p. 57-61 & 98-99.
33. Diesselhorst, H. and H. Freundlich, *On the double refraction of vanadine pentoxydsol.* Phys. Z, 1915. **16**: p. 419-425.
34. Mazzini, V. and V.S.J. Craig, *What is the fundamental ion-specific series for anions and cations? Ion specificity in standard partial molar volumes of electrolytes and electrostriction in water and non-aqueous solvents.* Chemical Science, 2017. **8**(10): p. 7052-7065.
35. Nostro, P.L., et al., *Specific ion effects on the growth rates of Staphylococcus aureus and Pseudomonas aeruginosa.* Physical biology, 2005. **2**(1): p. 1.
36. Broering, J.M. and A.S. Bommarius, *Evaluation of Hofmeister Effects on the Kinetic Stability of Proteins.* The Journal of Physical Chemistry B, 2005. **109**(43): p. 20612-20619.
37. Bilanicová, D., et al., *Specific anion effects on enzymatic activity in nonaqueous media.* The Journal of Physical Chemistry B, 2008. **112**(38): p. 12066.
38. Kunz, W., P. Lo Nostro, and B.W. Ninham, *The present state of affairs with Hofmeister effects.* Current Opinion in Colloid & Interface Science, 2004. **9**(1-2): p. 1-18.
39. Schweitzer, F., P. Mirabel, and C. George, *Multiphase Chemistry of N_2O_5 , $ClNO_2$, and $BrNO_2$.* The Journal of Physical Chemistry A, 1998. **102**(22): p. 3942-3952.
40. Shaloski, M.A., et al., *Reactions of N_2O_5 with Salty and Surfactant-Coated Glycerol: Interfacial Conversion of Br^- to Br^{2-} Mediated by Alkylammonium Cations.* The Journal of Physical Chemistry A, 2017. **121**(19): p. 3708-3719.
41. Shcherbina, A., L. Talley, and D. Rudnick, *Direct Observations of North Pacific Ventilation: Brine Rejection in the Okhotsk Sea.* Science, 2003. **302**(5652): p. 1952-5.
42. Henry, C.L. and V.S.J. Craig, *The link between ion specific bubble coalescence and Hofmeister effects is the partitioning of ions within the interface.* Langmuir : the ACS journal of surfaces and colloids, 2010. **26**(9): p. 6478-6483.
43. Millero, F.J., F. Huang, and A.L. Laferiere, *Solubility of oxygen in the major sea salts as a function of concentration and temperature.* Marine Chemistry, 2002. **78**(4): p. 217-230.
44. Versteegden, L.R., et al., *A salt-based method to adapt stiffness and biodegradability of porous collagen scaffolds.* RSC Advances, 2019. **9**(63): p. 36742-36750.
45. Metrick, M.A., et al., *Million-fold sensitivity enhancement in proteopathic seed amplification assays for biospecimens by Hofmeister ion comparisons.* Proceedings of the National Academy of Sciences, 2019. **116**(46): p. 23029.
46. Tang, J., *Hofmeister interaction in the driver's seat.* Nature Nanotechnology, 2019. **14**(12): p. 1091-1092.
47. Somasundar, A., et al., *Positive and negative chemotaxis of enzyme-coated liposome motors.* Nature nanotechnology, 2019. **14**(12): p. 1129-1134.
48. Schneider, L., et al., *Directional cell migration and chemotaxis in wound healing response to PDGF-AA are coordinated by the primary cilium in fibroblasts.* Cellular physiology and Biochemistry, 2010. **25**(2-3): p. 279-292.
49. Roussos, E.T., J.S. Condeelis, and A. Patsialou, *Chemotaxis in cancer.* Nature Reviews Cancer, 2011. **11**(8): p. 573-587.
50. Trompette, J.L., *The comparative breakdown of passivity of tin by fluorides and chlorides interpreted through the 'law of matching affinities' concept.* Corrosion Science, 2015. **94**: p. 288-293.
51. Serajuddin, A.T., *Salt formation to improve drug solubility.* Advanced drug delivery reviews, 2007. **59**(7): p. 603-616.
52. Wang, K., et al., *Flocculation-to-adsorption transition of novel salt-responsive polyelectrolyte for recycling of highly polluted saline textile effluents.* Chemical Engineering Journal, 2020: p. 127410.
53. Liu, J., et al., *Wettability Alteration and Enhanced Oil Recovery Induced by Proximal Adsorption of Ions on Calcite.* Physical Review Applied, 2018. **10**(3).
54. Geise, G.M., et al., *Specific ion effects on membrane potential and the permselectivity of ion exchange membranes.* Phys. Chem. Chem. Phys., 2014. **16**(39): p. 21673-21681.
55. Lukanov, B. and A. Firoozabadi, *Specific ion effects on the self-assembly of ionic surfactants: a molecular thermodynamic theory of micellization with dispersion forces.* Langmuir : the ACS journal of surfaces and colloids, 2014. **30**(22): p. 6373-6383.
56. Lo Nostro, P., et al., *Hofmeister effects in supramolecular and biological systems.* Biophysical Chemistry, 2006. **124**(3): p. 208-213.

57. Wydro, P., *The interactions between cholesterol and phospholipids located in the inner leaflet of humane erythrocytes membrane (DPPE and DPPS) in binary and ternary films—The effect of sodium and calcium ions.* Colloids and Surfaces B: Biointerfaces, 2011. **82**(1): p. 209-216.
58. Castellana, E.T. and P.S. Cremer, *Solid supported lipid bilayers: From biophysical studies to sensor design.* Surf Sci Rep, 2006. **61**(10): p. 429-444.
59. Yoo, S., et al., *Specific Ion Effects in Lanthanide–Amphiphile Structures at the Air–Water Interface and Their Implications for Selective Separation.* ACS Applied Materials & Interfaces, 2022. **14**(5): p. 7504-7512.
60. Bu, W., et al., *Observation of a rare earth ion-extractant complex arrested at the oil-water interface during solvent extraction.* J Phys Chem B, 2014. **118**(36): p. 10662-74.
61. Liang, Z., et al., *Nanoscale view of assisted ion transport across the liquid–liquid interface.* Proceedings of the National Academy of Sciences, 2019. **116**(37): p. 18227-18232.
62. Zhang, T., et al., *Cation effects on phosphatidic acid monolayers at various pH conditions.* Chemistry and Physics of Lipids, 2016. **200**: p. 24-31.
63. Liu, G., D. Parsons, and V.S.J. Craig, *Re-entrant swelling and redissolution of polyelectrolytes arises from an increased electrostatic decay length at high salt concentrations.* Journal of Colloid and Interface Science, 2020. **579**: p. 369-378.
64. Perez-Martinez, C.S., A.M. Smith, and S.J.F.d. Perkin, *Underscreening in concentrated electrolytes.* 2017. **199**: p. 239-259.
65. Collins, K.D., *Charge density-dependent strength of hydration and biological structure.* Biophysical Journal, 1997. **72**(1): p. 65-76.
66. Collins, K.D., *Ions from the Hofmeister series and osmolytes: effects on proteins in solution and in the crystallization process.* Methods, 2004. **34**(3): p. 300-311.
67. Collins, K.D., G.W. Neilson, and J.E. Enderby, *Ions in water: Characterizing the forces that control chemical processes and biological structure.* Biophysical Chemistry, 2007. **128**(2-3): p. 95-104.
68. Mazzini, V. and V.S.J. Craig, *Volcano Plots Emerge from a Sea of Nonaqueous Solvents: The Law of Matching Water Affinities Extends to All Solvents.* ACS Central Science, 2018. **4**(8): p. 1056-1064.
69. Salis, A. and B.W. Ninham, *Models and mechanisms of Hofmeister effects in electrolyte solutions, and colloid and protein systems revisited.* Chem. Soc. Rev., 2014. **43**(21): p. 7358-7377.
70. Mazzini, V. and V.S.J. Craig, *Specific-ion effects in non-aqueous systems.* Current Opinion in Colloid & Interface Science, 2016. **23**: p. 82-93.
71. Mazzini, V., G. Liu, and V.S.J. Craig, *Probing the Hofmeister series beyond water: Specific-ion effects in non-aqueous solvents.* The Journal of Chemical Physics, 2018. **148**(22): p. 222805.
72. Lo Nostro, P., et al., *Specific Anion Effects on the Kinetics of Iodination of Acetone.* ChemPhysChem, 2016. **17**(16): p. 2567-2571.
73. Mazzini, V., *Specific ion effects in non-aqueous solutions*, in *Department of Applied Mathematics*, P. Thesis, Editor. 2017, Australian Nantional University.
74. Parker, A.J., *The effects of solvation on the properties of anions in dipolar aprotic solvents.* Quarterly reviews /, 1962. **16**(2): p. 163-187.
75. Butler, R.N. and M.C.R. Symons, *Solvation spectra. Part 29.—Nuclear magnetic resonance studies of electrolyte solutions : ion-solvent interactions in methanol.* Transactions of the Faraday Society., 1969. **65**(0): p. 2559-2566.
76. Melendres, C.A. and H.G. Hertz, *Magnetic relaxation of quadrupolar nuclei in nonaqueous electrolyte solutions.* The Journal of Chemical Physics, 1974. **61**(10): p. 4156-4162.
77. Labban, A.K.S. and Y. Marcus, *The solubility and solvation of salts in mixed nonaqueous solvents. 1. Potassium halides in mixed aprotic solvents.* Journal of Solution Chemistry, 1991. **20**(2): p. 221-232.
78. Labban, A.-K.S. and Y. Marcus, *The Solubility and Solvation of Salts in Mixed Nonaqueous Solvents. 2. Potassium Halides in Mixed Protic Solvents.* Journal of Solution Chemistry, 1997. **26**(1): p. 1-12.
79. Marcus, Y., G. Hefter, and T.-S. Pang, *Ionic partial molar volumes in non-aqueous solvents.* Journal of the Chemical Society, Faraday Transactions, 1994. **90**(13): p. 1899-1903.
80. Jenkins, H.D.B. and Y. Marcus, *Viscosity B-coefficients of ions in solution.* Chemical reviews, 1995. **95**(8): p. 2695-2724.
81. Marcus, Y. and G. Hefter, *Standard partial molar volumes of electrolytes and ions in nonaqueous solvents.* Chemical reviews, 2004. **104**(7): p. 3405-3452.
82. Marcus, Y., *Ions in Solution and their Solvation.* 2015.
83. Peruzzi, N., et al., *Hofmeister phenomena in nonaqueous media: the solubility of electrolytes in ethylene carbonate.(Report).* Journal of Physical Chemistry B, 2012. **116**(49): p. 14398-14405.
84. Peruzzi, N., et al., *The Solvation of Anions in Propylene Carbonate.* Journal of Solution Chemistry, 2015. **44**(6): p. 1224-1239.
85. Parsons, D.F. and A. Salis, *Hofmeister effects at low salt concentration due to surface charge transfer.* Current opinion in colloid & interface science, 2016. **23**: p. 41-49.

86. Mazzini, V. and V.S.J. Craig, *What is the fundamental ion-specific series for anions and cations? Ion specificity in standard partial molar volumes of electrolytes and electrostriction in water and non-aqueous solvents.* Chem. Sci., 2017. **8**(10): p. 7052-7065.
87. Watanabe, I., *EXAFS of bromide ion in solvents and at air/solution interface.* Journal of Molecular Liquids, 1995. **65-66**: p. 245-252.
88. Gregory, K.P., et al., *Lewis Strength Determines Specific-Ion Effects in Aqueous and Nonaqueous Solvents.* The Journal of Physical Chemistry A, 2019. **123**(30): p. 6420-6429.
89. Gregory, K.P., et al., *The electrostatic origins of specific ion effects: quantifying the Hofmeister series for anions.* Chemical Science, 2021. **12**(45): p. 15007-15015.
90. Krishnamoorthy, A.N., et al., *Preferential solvation and ion association properties in aqueous dimethyl sulfoxide solutions.* Physical Chemistry Chemical Physics, 2016. **18**(45): p. 31312-31322.
91. Krishnamoorthy, A.N., C. Holm, and J. Smiatek, *Specific ion effects for polyelectrolytes in aqueous and non-aqueous media: the importance of the ion solvation behavior.* Soft matter, 2018. **14**(30): p. 6243-6255.
92. Narayanan Kirshnamoorthy, A., et al., *Electrolyte solvents for high voltage lithium ion batteries: ion correlation and specific anion effects in adiponitrile.* Physical Chemistry Chemical Physics, 2018. **20**(40): p. 25701-25715.
93. Miranda-Quintana, R.A. and J. Smiatek, *Theoretical Insights into Specific Ion Effects and Strong-Weak Acid-Base Rules for Ions in Solution: Deriving the Law of Matching Solvent Affinities from First Principles.* ChemPhysChem, 2020. **21**(23): p. 2605-2617.
94. Yang, J., et al., *Artificial neural networks for the prediction of solvation energies based on experimental and computational data.* Physical Chemistry Chemical Physics, 2020.
95. Miranda-Quintana, R.A. and J. Smiatek, *Specific Ion Effects in Different Media: Current Status and Future Challenges.* The Journal of Physical Chemistry B, 2021. **125**(51): p. 13840-13849.
96. Sarri, F., et al., *The curious effect of potassium fluoride on glycerol carbonate. How salts can influence the structuredness of organic solvents.* Journal of Molecular Liquids, 2018. **255**: p. 397-405.
97. Sarri, F., et al., *Specific ion effects in non-aqueous solvents: The case of glycerol carbonate.* Journal of Molecular Liquids, 2018. **266**: p. 711-717.
98. Krienke, H., R. Fischer, and J. Barthel, *Ion solvation in nonaqueous solvents on the Born—Oppenheimer level.* Journal of molecular liquids, 2002. **98**: p. 331-356.
99. Adamson, A.W.G.A.P., *Physical chemistry of surfaces*. 1997, New York: Wiley.
100. Guggenheim, E.A. and N.K. Adam, *The thermodynamics of adsorption at the surface of solutions.* Proceedings of the Royal Society of London. Series A, Containing Papers of a Mathematical and Physical Character, 1933. **139**(837): p. 218-236.
101. Heydweiller, A., *Über physikalische Eigenschaften von Lösungen in ihrem Zusammenhang. II. Oberflächenspannung und elektrisches Leitvermögen wässeriger Salzlösungen.* Annalen der Physik, 1910. **338**(11): p. 145-185.
102. Wagner, C., Physik. Z., 1924. **25**(474).
103. Onsager, L. and N.N.J.T.J.o.c.p. Samaras, *The surface tension of Debye-Hückel electrolytes.* 1934. **2**(8): p. 528-536.
104. Ninham, B.W. and V. Yaminsky, *Ion binding and ion specificity: The Hofmeister effect and Onsager and Lifshitz theories.* Langmuir, 1997. **13**(7): p. 2097-2108.
105. Weissenborn, P.K. and R.J. Pugh, *Surface tension and bubble coalescence phenomena of aqueous solutions of electrolytes.* Langmuir, 1995. **11**(5): p. 1422-1426.
106. Jungwirth, P. and D.J. Tobias, *Specific ion effects at the air/water interface.* Chemical reviews, 2006. **106**(4): p. 1259-1281.
107. Knipping, et al., *Experiments and simulations of ion-enhanced interfacial chemistry on aqueous NaCl aerosols.* Science (New York, N.Y.), 2000. **288**(5464): p. 301.
108. Perera, L. and M.L. Berkowitz, *Many-body effects in molecular dynamics simulations of Na+(H2O)n and Cl−(H2O)n clusters.* The Journal of Chemical Physics, 1991. **95**(3): p. 1954-1963.
109. Perera, L. and M.L. Berkowitz, *Stabilization energies of Cl−, Br−, and I− ions in water clusters.* The Journal of Chemical Physics, 1993. **99**(5): p. 4222-4224.
110. Perera, L. and M.L. Berkowitz, *Structure and dynamics of Cl−(H2O)20 clusters: The effect of the polarizability and the charge of the ion.* The Journal of Chemical Physics, 1992. **96**(11): p. 8288-8294.
111. Hu, J., et al., *Reactive uptake of Cl2 (g) and Br2 (g) by aqueous surfaces as a function of Br-and I-ion concentration: The effect of chemical reaction at the interface.* The Journal of Physical Chemistry, 1995. **99**(21): p. 8768-8776.
112. Jungwirth, P. and D.J. Tobias, *Ions at the Air/Water Interface.* The Journal of Physical Chemistry B, 2002. **106**(25): p. 6361-6373.

113. Jungwirth, P. and D.J. Tobias, *Molecular Structure of Salt Solutions: A New View of the Interface with Implications for Heterogeneous Atmospheric Chemistry.* The Journal of Physical Chemistry B, 2001. **105**(43): p. 10468-10472.
114. Dang, L.X. and T.-M. Chang, *Molecular Mechanism of Ion Binding to the Liquid/Vapor Interface of Water.* The Journal of Physical Chemistry B, 2002. **106**(2): p. 235-238.
115. Chang, T.-M. and L.X. Dang, *Recent Advances in Molecular Simulations of Ion Solvation at Liquid Interfaces.* Chemical Reviews, 2006. **106**(4): p. 1305-1322.
116. Levin, Y., *Polarizable Ions at Interfaces.* Physical Review Letters, 2009. **102**(14): p. 147803.
117. Levin, Y., A.D.D. Santos, and A.J.P.r.l. Diehl, *Ions at the air-water interface: an end to a hundred-year-old mystery?* 2009. **103 25**: p. 257802.
118. Noah-Vanhoucke, J. and P.L. Geissler, *On the fluctuations that drive small ions toward, and away from, interfaces between polar liquids and their vapors.* Proceedings of the National Academy of Sciences, 2009. **106**(36): p. 15125-15130.
119. Cheng, J., et al., *Experimental anion affinities for the air/water interface.* 2006. **110**(51): p. 25598-25602.
120. Stairs, R., *Calculation of surface-tension of salt-solutions - effective polarizability of solvated ions.* Can. J. Chem.-Rev. Can. Chim., 1995. **73**(6): p. 781-787.
121. Boström, M., D.R.M. Williams, and B.W. Ninham, *Surface tension of electrolytes: Specific ion effects explained by dispersion forces.* Langmuir, 2001. **17**(15): p. 4475-4478.
122. Boström, M., W. Kunz, and B.W. Ninham, *Hofmeister Effects in Surface Tension of Aqueous Electrolyte Solution.* Langmuir, 2005. **21**(6): p. 2619-2623.
123. Horinek, D., et al., *Specific ion adsorption at the air/water interface: The role of hydrophobic solvation.* Chemical Physics Letters, 2009. **479**(4): p. 173-183.
124. Schwierz, N., D. Horinek, and R.R. Netz, *Reversed anionic Hofmeister series: the interplay of surface charge and surface polarity.* Langmuir : the ACS journal of surfaces and colloids, 2010. **26**(10): p. 7370.
125. Schwierz, N., et al., *Reversed Hofmeister series—The rule rather than the exception.* Current Opinion in Colloid & Interface Science, 2016. **23**: p. 10-18.
126. Horinek, D., S.I. Mamatkulov, and R.R. Netz, *Rational design of ion force fields based on thermodynamic solvation properties.* The Journal of Chemical Physics, 2009. **130**(12): p. 124507.
127. Verreault, D. and H.C. Allen, *Bridging the gap between microscopic and macroscopic views of air/aqueous salt interfaces.* Chemical Physics Letters, 2013. **586**: p. 1-9.
128. Baer, M.D. and C.J. Mundy, *Toward an Understanding of the Specific Ion Effect Using Density Functional Theory.* The Journal of Physical Chemistry Letters, 2011. **2**(9): p. 1088-1093.
129. Petersen, P.B. and R.J. Saykally, *On the Nature of ions at the Liquid Water Surface.* Annual Review of Physical Chemistry, 2006. **57**(1): p. 333-364.
130. Duignan, T.T., *The surface potential explains ion specific bubble coalescence inhibition.* Journal of Colloid and Interface Science, 2021. **600**: p. 338-343.
131. Cheng, J., et al., *Experimental anion affinities for the air/water interface.* The Journal of Physical Chemistry B, 2006. **110**(51): p. 25598-25602.
132. Otten, D.E., et al., *Elucidating the mechanism of selective ion adsorption to the liquid water surface.* Proceedings of the National Academy of Sciences, 2012. **109**(3): p. 701.
133. Winter, B. and M. Faubel, *Photoemission from Liquid Aqueous Solutions.* Chemical Reviews, 2006. **106**(4): p. 1176-1211.
134. Craig, V., J. Cui, and T. Brazier, *On the Surface Tension of Electrolyte Solutions*, in *AQUA INCOGNITA: Why Ice Floats on Water and Galileo 400 years on*. 2014, Connor Court (Australia).
135. Pegram, L.M. and M.T. Record, *Partitioning of atmospherically relevant ions between bulk water and the water/vapor interface.* Proceedings of the National Academy of Sciences, 2006. **103**(39): p. 14278.
136. Pegram, L.M. and M.T. Record, *Hofmeister Salt Effects on Surface Tension Arise from Partitioning of Anions and Cations between Bulk Water and the Air−Water Interface.* The Journal of Physical Chemistry B, 2007. **111**(19): p. 5411-5417.
137. Pegram, L.M. and M.T. Record, *Quantifying accumulation or exclusion of H +, HO −, and Hofmeister salt ions near interfaces.* Chemical Physics Letters, 2008. **467**(1-3): p. 1-8.
138. Ghosal, S., et al., *Electron Spectroscopy of Aqueous Solution Interfaces Reveals Surface Enhancement of Halides.* Science, 2005. **307**(5709): p. 563.
139. Brown, M.A., et al., *Ion spatial distributions at the liquid–vapor interface of aqueous potassium fluoride solutions.* Physical Chemistry Chemical Physics, 2008. **10**(32): p. 4778-4784.
140. Perrine, K.A., et al., *Specific cation effects at aqueous solution− vapor interfaces: Surfactant-like behavior of Li^+ revealed by experiments and simulations.* Proceedings of the National Academy of Sciences, 2017. **114**(51): p. 13363-13368.

141. Sloutskin, E., et al., *The surface structure of concentrated aqueous salt solutions.* The Journal of Chemical Physics, 2007. **126**: p. 054704.
142. Cheng, M.H., et al., *Ambient Pressure X-ray Photoelectron Spectroscopy and Molecular Dynamics Simulation Studies of Liquid/Vapor Interfaces of Aqueous NaCl, RbCl, and RbBr Solutions.* The Journal of Physical Chemistry C, 2012. **116**(7): p. 4545-4555.
143. Höfft, O., et al., *Interaction of NaI with solid water and methanol.* The Journal of Physical Chemistry B, 2006. **110**(34): p. 17115-17120.
144. Höfft, O., et al., *Surface segregation of dissolved salt ions.* The Journal of Physical Chemistry B, 2006. **110**(24): p. 11971-11976.
145. Dempsey, L.P., J.A. Faust, and G.M. Nathanson, *Near-Interfacial Halogen Atom Exchange in Collisions of Cl2 with 2.7 M NaBr–Glycerol.* The Journal of Physical Chemistry B, 2012. **116**(40): p. 12306-12318.
146. Muenter, A.H., J.L. DeZwaan, and G.M. Nathanson, *Interfacial Interactions of DCl with Salty Glycerol Solutions of KI, NaI, LiI, and NaBr.* The Journal of Physical Chemistry C, 2007. **111**(41): p. 15043-15052.
147. DeZwaan, J.L., S.M. Brastad, and G.M. Nathanson, *Evidence for Interfacial [FDCl]− in Collisions between DCl and F− in KF−Glycerol Solutions.* The Journal of Physical Chemistry C, 2008. **112**(39): p. 15449-15457.
148. Dempsey, L.P., S.M. Brastad, and G.M. Nathanson, *Interfacial Acid Dissociation and Proton Exchange Following Collisions of DCl with Salty Glycerol and Salty Water.* The Journal of Physical Chemistry Letters, 2011. **2**(6): p. 622-627.
149. Zhuang, X., et al., *Mapping molecular orientation and conformation at interfaces by surface nonlinear optics.* Physical Review B, 1999. **59**(19): p. 12632.
150. Liu, D., et al., *Vibrational Spectroscopy of Aqueous Sodium Halide Solutions and Air−Liquid Interfaces: Observation of Increased Interfacial Depth.* The Journal of Physical Chemistry B, 2004. **108**(7): p. 2252-2260.
151. Hua, W., et al., *Cation effects on interfacial water organization of aqueous chloride solutions. I. Monovalent cations: Li+, Na+, K+, and NH4+.* The Journal of Physical Chemistry B, 2014. **118**(28): p. 8433-8440.
152. Huang, Z., et al., *Salty glycerol versus salty water surface organization: bromide and iodide surface propensities.* The Journal of Physical Chemistry A, 2013. **117**(29): p. 6346-6353.
153. Raymond, E.A. and G.L. Richmond, *Probing the molecular structure and bonding of the surface of aqueous salt solutions.* The Journal of Physical Chemistry B, 2004. **108**(16): p. 5051-5059.
154. Feng, R.-r., et al., *Spectroscopic evidence for the specific Na^+ and K^+ interactions with the hydrogen-bonded water molecules at the electrolyte aqueous solution surfaces.* The Journal of Chemical Physics, 2009. **130**(13): p. 134710.
155. Bian, H.-t., et al., *Specific Na+ and K+ cation effects on the interfacial water molecules at the air/aqueous salt solution interfaces probed with nonresonant second harmonic generation.* The Journal of Chemical Physics, 2009. **130**(13): p. 134709.
156. Petersen, P.B. and R.J. Saykally, *Probing the Interfacial Structure of Aqueous Electrolytes with Femtosecond Second Harmonic Generation Spectroscopy.* The Journal of Physical Chemistry B, 2006. **110**(29): p. 14060-14073.
157. Ishiyama, T. and A. Morita, *Molecular dynamics study of gas− liquid aqueous sodium halide interfaces. Ii. Analysis of vibrational sum frequency generation spectra.* The Journal of Physical Chemistry C, 2007. **111**(2): p. 738-748.
158. Petersen, P.B. and R.J. Saykally, *Confirmation of enhanced anion concentration at the liquid water surface.* Chemical Physics Letters, 2004. **397**(1): p. 51-55.
159. Petersen, P.B., et al., *Direct experimental validation of the Jones–Ray effect.* Chemical Physics Letters, 2004. **397**(1-3): p. 46-50.
160. Petersen, P.B., et al., *Enhanced Concentration of Polarizable Anions at the Liquid Water Surface: SHG Spectroscopy and MD Simulations of Sodium Thiocyanide.* The Journal of Physical Chemistry B, 2005. **109**(21): p. 10915-10921.
161. Petersen, P.B. and R.J. Saykally, *Adsorption of Ions to the Surface of Dilute Electrolyte Solutions: The Jones−Ray Effect Revisited.* Journal of the American Chemical Society, 2005. **127**(44): p. 15446-15452.
162. Piatkowski, L., et al., *Extreme surface propensity of halide ions in water.* Nature Communications, 2014. **5**(1): p. 1-7.
163. Frumkin, A., *Phasengrenzkräfte und Adsorption an der Trennungsfläche Luft. Lösung anorganischer Elektrolyte.* Zeitschrift für Physikalische Chemie, 1924. **109U**(1): p. 34-48.
164. Randles, J., *Ionic hydration and the surface potential of aqueous electrolytes.* Discussions of the Faraday Society, 1957. **24**: p. 194-199.
165. Jarvis, N.L. and M.A. Scheiman, *Surface potentials of aqueous electrolyte solutions.* The Journal of Physical Chemistry, 1968. **72**(1): p. 74-78.

166. Ottosson, N., et al., *Photoelectron spectroscopy of liquid water and aqueous solution: Electron effective attenuation lengths and emission-angle anisotropy.* Journal of Electron Spectroscopy and Related Phenomena, 2010. **177**(2-3): p. 60-70.
167. Dupuy, R., et al., *Core level photoelectron spectroscopy of heterogeneous reactions at liquid–vapor interfaces: Current status, challenges, and prospects.* The Journal of Chemical Physics, 2021. **154**(6): p. 060901.
168. Morgner, H., *The characterization of liquid and solid surfaces with metastable helium atoms*, in *Advances in Atomic, Molecular, and Optical Physics*. 2000, Elsevier. p. 387-488.
169. Andersson, G. and H. Morgner, *Impact collision ion scattering spectroscopy (ICISS) and neutral impact collision ion scattering spectroscopy (NICISS) at surfaces of organic liquids.* Surface Science, 1998. **405**(1): p. 138-151.
170. Andersson, G., T. Krebs, and H. Morgner, *Angle resolved ion scattering spectroscopy reveals the local topography around atoms in a liquid surface.* Physical Chemistry Chemical Physics, 2005. **7**(15): p. 2948-2954.
171. Shen, Y.R., *Surface properties probed by second-harmonic and sum-frequency generation.* Nature, 1989. **337**(6207): p. 519-525.
172. Bryant, S.J., et al., *Deep eutectic solvents as cryoprotective agents for mammalian cells.* Journal of Materials Chemistry B, 2022. **10**(24): p. 4546-4560.
173. Weng, L. and G.D. Elliott, *Polymerization Effect of Electrolytes on Hydrogen-Bonding Cryoprotectants: Ion–Dipole Interactions between Metal Ions and Glycerol.* The Journal of Physical Chemistry B, 2014. **118**(49): p. 14546-14554.
174. Karlsson, B.C.G. and R. Friedman, *Dilution of whisky – the molecular perspective.* Scientific Reports, 2017. **7**(1): p. 6489.
175. Goodenough, J.B. and Y. Kim, *Challenges for rechargeable Li batteries.* Chemistry of materials, 2010. **22**(3): p. 587-603.
176. Ponrouch, A. and M.R. Palacín, *Post-Li batteries: promises and challenges.* Philosophical Transactions of the Royal Society A: Mathematical, Physical and Engineering Sciences, 2019. **377**(2152): p. 20180297.
177. Marshall, M., *How the first life on Earth survived its biggest threat — water*. 2020, Nature. p. 210-213.
178. Saladino, R., et al., *A possible prebiotic synthesis of purine, adenine, cytosine, and 4 (3H)-pyrimidinone from formamide: implications for the origin of life.* Bioorganic & medicinal chemistry, 2001. **9**(5): p. 1249-1253.
179. Saladino, R., et al., *One-Pot TiO2-Catalyzed Synthesis of Nucleic Bases and Acyclonucleosides from Formamide: Implications for the Origin of Life.* ChemBioChem, 2003. **4**(6): p. 514-521.
180. Saladino, R., et al., *On the prebiotic synthesis of nucleobases, nucleotides, oligonucleotides, pre-RNA and pre-DNA molecules.* Prebiotic chemistry, 2005: p. 29-68.
181. Saladino, R., et al., *Formamide chemistry and the origin of informational polymers.* Chemistry & Biodiversity, 2007. **4**(4): p. 694-720.
182. Saladino, R., et al., *Genetics first or metabolism first? The formamide clue.* Chemical Society Reviews, 2012. **41**(16): p. 5526.
183. Senske, M., et al., *The temperature dependence of the Hofmeister series: thermodynamic fingerprints of cosolute–protein interactions.* Physical Chemistry Chemical Physics, 2016. **18**(43): p. 29698-29708.
184. Zhang, Y. and P.S. Cremer, *The inverse and direct Hofmeister series for lysozyme.* Proceedings of the National Academy of Sciences, 2009. **106**(36): p. 15249-15253.
185. Parsons, D.F. and B.W. Ninham, *Importance of Accurate Dynamic Polarizabilities for the Ionic Dispersion Interactions of Alkali Halides.* Langmuir, 2010. **26**(3): p. 1816-1823.
186. Andersson, G., *Ion Scattering Spectroscopy*, in *Reference Module in Chemistry, Molecular Sciences and Chemical Engineering*. 2013, Elsevier.
187. Smith, D.P., *Scattering of Low-Energy Noble Gas Ions from Metal Surfaces.* Journal of Applied Physics, 1967. **38**(1): p. 340-347.
188. Niehus, H. and G. Comsa, *Ion scattering spectroscopy in the impact collision mode (ICISS): Surface structure information from noble gas and alkali-ion scattering.* Nuclear Instruments and Methods in Physics Research Section B: Beam Interactions with Materials and Atoms, 1986. **15**(1-6): p. 122-125.
189. Andersson, G. and H. Morgner, *Determining the stopping power of low energy helium in alkanethiolates with Neutral Impact Collision Ion Scattering Spectroscopy (NICISS).* Nuclear Instruments and Methods in Physics Research Section B: Beam Interactions with Materials and Atoms, 1999. **155**(4): p. 357-368.
190. Brongersma, H.H., et al., *Surface composition analysis by low-energy ion scattering.* Surface Science Reports, 2007. **62**(3): p. 63-109.
191. Andersson, G. and H. Morgner, *Thermodynamics and structure of liquid surfaces investigated directly with surface analytical tools***, in *Surface and Interface Science*, K. Wandelt, Editor. 2017, Annalen der Physik. p. 1600230.
192. Ridings, C. and G.G. Andersson, *Deconvolution of NICISS profiles involving elements of similar masses.* Nuclear Inst. and Methods in Physics Research, B, 2014. **340**: p. 63-66.

193. Andersson, G., *Ionenstreuspektroskpie als Methode zur Untersuchung von Oberflachen organischer Flussigkieten*. 1998, University of Witten/Herdecke.
194. Zhao, X., G.M. Nathanson, and G.G. Andersson, *Competing Segregation of Br– and Cl– to a Surface Coated with a Cationic Surfactant: Direct Measurements of Ion and Solvent Depth Profiles.* The Journal of Physical Chemistry A, 2020. **124**(52): p. 11102-11110.
195. Zhao, X., G.M. Nathanson, and G.G. Andersson, *Experimental Depth Profiles of Surfactants, Ions, and Solvent at the Angstrom Scale: Studies of Cationic and Anionic Surfactants and Their Salting Out.* The Journal of Physical Chemistry B, 2020. **124**(11): p. 2218-2229.
196. Andersson, G., *Angle resolved ion scattering spectroscopy at surfaces of pure liquids: topography and orientation of molecules.* Physical Chemistry Chemical Physics, 2005. **7**(15): p. 2942-2947.
197. Andersson, G. and H. Morgner, *Investigations on solutions of tetrabutylonium salts in formamide with NICISS and ICISS: Concentration depth profiles and composition of the outermost layer.* Surface Science 2000. **445**: p. 89-99.
198. Young, T., *III. An essay on the cohesion of fluids.* Philosophical transactions of the royal society of London, 1805(95): p. 65-87.
199. Griffiths, P.R., *Fourier transform infrared spectrometry*. 2nd ed. ed, ed. J.A. De Haseth. 2007, Hoboken, N.J.: Hoboken, N.J. : John Wiley & Sons, Inc.
200. Smith, D.R., R.L. Morgan, and E.V. Loewenstein, *Comparison of the Radiance of Far-Infrared Sources.* Journal of the Optical Society of America, 1968. **58**(3): p. 433-434.
201. Bunker, G. *Introduction to XAFS: A Practical Guide to X-ray Absorption Fine Structure Spectroscopy*. 2010.
202. Glover, C., et al., *Status of the X-Ray Absorption Spectroscopy (XAS) Beamline at the Australian Synchrotron.* AIP Conference Proceedings 2007.
203. Heald, S.M., *Strategies and limitations for fluorescence detection of XAFS at high flux beamlines.* Journal of Synchrotron Radiation, 2015. **22**(2): p. 436-445.
204. Ravel, B. and M. Newville, *ATHENA, ARTEMIS, HEPHAESTUS: data analysis for X-ray absorption spectroscopy using IFEFFIT.* Journal of Synchrotron Radiation, 2005. **12**(4): p. 537-541.
205. Thomas, A.S. and A.H. Elcock, *Molecular Dynamics Simulations of Hydrophobic Associations in Aqueous Salt Solutions Indicate a Connection between Water Hydrogen Bonding and the Hofmeister Effect.* Journal of the American Chemical Society, 2007. **129**(48): p. 14887-14898.
206. Sadeghi, M., V. Taghikhani, and C. Ghotbi, *Measurement and correlation of surface tension for single aqueous electrolyte solutions.* International Journal of Thermophysics, 2010. **31**(4): p. 852-859.
207. Lide, D.R., *CRC handbook of chemistry and physics*. Vol. 87. 2006: CRC press.
208. Chernyak, Y., *Dielectric constant, dipole moment, and solubility parameters of some cyclic acid esters.* Journal of Chemical & Engineering Data, 2006. **51**(2): p. 416-418.
209. Bosque, R. and J. Sales, *Polarizabilities of solvents from the chemical composition.* Journal of chemical information and computer sciences, 2002. **42**(5): p. 1154-1163.
210. Castelló, M., J. Dweck, and D. Aranda, *Thermal stability and water content determination of glycerol by thermogravimetry.* Journal of Thermal Analysis and Calorimetry, 2009. **97**(2): p. 627-630.
211. *CRC handbook of chemistry and physics: 1st student edition: Editor-in-chief: R C Weast. CRC Press, Inc, Boca Raton, Florida and Wolfe Medical Publications, London. 1988. £19.95 ISBN 0-8493-0740-6.* Biochemical Education, 1989. **17**(2): p. 103-103.
212. Hammadi, A. and D.C. Champeney, *Ion–Solvent Interactions of Some Alkali Halides in Glycerol from Density and Viscosity Data.* Journal of Chemical & Engineering Data, 1998. **43**(6): p. 1004-1008.
213. Hammadi, A., *Electrical Conductance, Density, and Viscosity in Mixtures of Alkali-Metal Halides and Glycerol.* International Journal of Thermophysics, 2004. **25**(1): p. 89-111.
214. Kameche *, M., et al., *Ionic mobility and ionic association of singly charged ions in glycerol.* Molecular Physics, 2005. **103**(9): p. 1231-1239.
215. Krebs, T., G. Andersson, and H. Morgner, *Electron energy loss spectroscopy of liquid glycerol.* Chemical Physics, 2007. **340**(1): p. 181-186.
216. Oh-e, M., H. Yokoyama, and S. Baldelli, *Structure of the glycerol liquid/vapor interface studied by sum-frequency vibrational spectroscopy.* Applied Physics Letters, 2004. **84**(24): p. 4965-4967.
217. Benjamin, I., M. Wilson, and A. Pohorille, *Scattering of Ne from the liquid–vapor interface of glycerol: A molecular dynamics study.* The Journal of Chemical Physics, 1994. **100**(9): p. 6500-6507.
218. Wiens, J.P., et al., *Collisions of Sodium Atoms with Liquid Glycerol: Insights into Solvation and Ionization.* Journal of the American Chemical Society, 2014. **136**(8): p. 3065-3074.
219. Du, Q., et al., *Vibrational spectroscopy of water at the vapor/water interface.* Physical Review Letters, 1993. **70**(15): p. 2313-2316.
220. Netz, R.R. and D. Horinek, *Progress in Modeling of Ion Effects at the Vapor/Water Interface.* Annual Review of Physical Chemistry, 2012. **63**(1): p. 401-418.

221. Andersson, G., T. Krebs, and H. Morgner, *Activity of surface active substances determined from their surface excess.* Physical Chemistry Chemical Physics, 2005. **7**(1): p. 136.
222. Henry, C.L. and V.S.J. Craig, *The Link between Ion Specific Bubble Coalescence and Hofmeister Effects Is the Partitioning of Ions within the Interface.* Langmuir, 2010. **26**(9): p. 6478-6483.
223. Kasimir P. Gregory, G.E., Hayden Robertson, Anand Kumar, Erica J. Wanless, Grant B. Webber, Vincent S. J. Craig, Gunther G. Andersson, Alister J. Page, *Understanding Specific Ion Effects and the Hofmeister Series.* Physical Chemistry Chemical Physics, 2022: p. 10.1039/d2cp00847e.
224. Ishiyama, T., T. Imamura, and A. Morita, *Theoretical studies of structures and vibrational sum frequency generation spectra at aqueous interfaces.* Chemical reviews, 2014. **114**(17): p. 8447-8470.
225. Gregory, K.P., et al., *A quantum chemical molecular dynamics repository of solvated ions.* Scientific Data, 2022. **9**(1).
226. Nightingale Jr, E., *Phenomenological theory of ion solvation. Effective radii of hydrated ions.* The Journal of Physical Chemistry, 1959. **63**(9): p. 1381-1387.
227. Kalayan, J. and R.H. Henchman, *Convergence behaviour of solvation shells in simulated liquids.* Physical Chemistry Chemical Physics, 2021. **23**(8): p. 4892-4900.
228. Canady, W.J., *Comparison of Effective Ionic Radii in Solution.* Canadian Journal of Chemistry, 1957. **35**(9): p. 1073-1075.
229. Bera, M.K., et al., *Erbium(III) Coordination at the Surface of an Aqueous Electrolyte.* The Journal of Physical Chemistry B, 2015. **119**(28): p. 8734-8745.
230. Tobias, D.J., et al., *Simulation and Theory of Ions at Atmospherically Relevant Aqueous Liquid-Air Interfaces.* Annual Review of Physical Chemistry, 2013. **64**(1): p. 339-359.
231. Jungwirth, P. and B. Winter, *Ions at aqueous interfaces: From water surface to hydrated proteins.* Annual Review of Physical Chemistry, 2008. **59**: p. 343-366.
232. Allen, H.C., et al., *Shedding light on water structure at air–aqueous interfaces: ions, lipids, and hydration.* Physical Chemistry Chemical Physics, 2009. **11**(27): p. 5538.
233. Cwiklik, L., et al., *Segregation of inorganic ions at surfaces of polar nonaqueous liquids.* ChemPhysChem, 2007. **8**(10): p. 1457-1463.
234. Saladino, R., et al., *Formamide and the origin of life.* Physics of Life Reviews, 2012. **9**(1): p. 84-104.
235. Barthel, J. and W. Kunz, *Vapor pressure data for non-aqueous electrolyte solutions. Part 5. Tetraalkylammonium salts in acetonitrile.* Journal of Solution Chemistry, 1988. **17**(5): p. 399-415.
236. Haghighi, H., A. Chapoy, and B. Tohidi, *Freezing Point Depression of Electrolyte Solutions: Experimental Measurements and Modeling Using the Cubic-Plus-Association Equation of State.* Industrial & Engineering Chemistry Research, 2008. **47**(11): p. 3983-3989.
237. Andersson, G., et al., *Anions of alkali halide salts at surfaces of formamide solutions: Concentration depth profiles and surface topography.* The Journal of Physical Chemistry C, 2007. **111**(11): p. 4379-4387.
238. Hua, W., et al., *Impact of Salt Purity on Interfacial Water Organization Revealed by Conventional and Heterodyne-Detected Vibrational Sum Frequency Generation Spectroscopy.* The Journal of Physical Chemistry C, 2013. **117**(38): p. 19577-19585.
239. Kumar, A., et al., *Ion specificity in the measured concentration depth profile of ions at the Vapor-Glycerol interface.* Journal of Colloid and Interface Science, 2022. **626**: p. 687-699.
240. Mayer, U., V. Gutmann, and W. Gerger, *The acceptor number ? A quantitative empirical parameter for the electrophilic properties of solvents.* Monatshefte für Chemie/Chemical Monthly, 1975. **106**(6): p. 1235-1257.
241. Gutmann, V., *Empirical parameters for donor and acceptor properties of solvents.* Electrochimica Acta, 1976. **21**(9): p. 661-670.
242. Fajans, K. and O. Johnson, *Ion-Solvent Interaction and Individual Properties of Electrolytes.* Transactions of the Electrochemical Society, 1942. **82**(1): p. 273.
243. Lees, A.J., B.P. Straughan, and D.J. Gardiner, *Electrolyte—formamide interactions studied by raman spectroscopy.* Journal of Molecular Structure, 1981. **71**: p. 61-70.
244. You, X., et al., *Interfaces of propylene carbonate.* The Journal of chemical physics, 2013. **138**(11): p. 114708.
245. Wang, L., et al., *Surface Structure of Organic Carbonate Liquids Investigated by Molecular Dynamics Simulation and Sum Frequency Generation Spectroscopy.* The Journal of Physical Chemistry C, 2016. **120**(28): p. 15185-15197.
246. Arslanargin, A., et al., *Models of Ion Solvation Thermodynamics in Ethylene Carbonate and Propylene Carbonate.* The Journal of Physical Chemistry B, 2016. **120**(8): p. 1497-1508.
247. Peruzzi, N., et al., *The Solvation of Anions in Propylene Carbonate.* Journal of Solution Chemistry, 2015. **44**(6): p. 1224-1239.
248. Yeager, H.L., J.D. Fedyk, and R.J. Parker, *Spectroscopic studies of ionic solvation in propylene carbonate.* The Journal of Physical Chemistry, 1973. **77**(20): p. 2407-2410.

249. Battisti, D., et al., *Vibrational studies of lithium perchlorate in propylene carbonate solutions.* The Journal of Physical Chemistry, 1993. **97**(22): p. 5826-5830.
250. Cvjetićanin, N.D. and S. Mentus, *Conductivity, viscosity and IR spectra of Li, Na and Mg perchlorate solutions in propylene carbonate/water mixed solvents.* Physical Chemistry Chemical Physics, 1999. **1**(22): p. 5157-5161.
251. Soloman, M., *The Thermodynamics of Ion Solvation in Water and Propylene Carbonate.* The Journal of Physical Chemistry, 1970. **74**(12): p. 2519.
252. Joseph, J. and E.D. Jemmis, *Red-, Blue-, or No-Shift in Hydrogen Bonds: A Unified Explanation.* Journal of the American Chemical Society, 2007. **129**(15): p. 4620-4632.
253. Adel, T., et al., *Insight into the Ionizing Surface Potential Method and Aqueous Sodium Halide Surfaces.* Langmuir, 2021. **37**(26): p. 7863-7874.
254. Narayanan Krishnamoorthy, A., C. Holm, and J. Smiatek, *Specific ion effects for polyelectrolytes in aqueous and non-aqueous media: the importance of the ion solvation behavior.* Soft Matter, 2018. **14**(30): p. 6243-6255.
255. Smiatek, J., A. Heuer, and M. Winter, *Properties of ion complexes and their impact on charge transport in organic solvent-based electrolyte solutions for lithium batteries: insights from a theoretical perspective.* Batteries, 2018. **4**(4): p. 62.
256. Gregory, K.P., et al., *Understanding specific ion effects and the Hofmeister series.* Physical Chemistry Chemical Physics, 2022. **24**(21): p. 12682-12718.
257. Finlayson-Pitts, B.J., *The Tropospheric Chemistry of Sea Salt: A Molecular-Level View of the Chemistry of NaCl and NaBr.* Chemical Reviews, 2003. **103**(12): p. 4801-4822.
258. Marcus, Y., *Ions in Solution and their Solvation - Chapter 5.* 2015.
259. Wick, C.D. and S.S. Xantheas, *Computational Investigation of the First Solvation Shell Structure of Interfacial and Bulk Aqueous Chloride and Iodide Ions.* The Journal of Physical Chemistry B, 2009. **113**(13): p. 4141-4146.
260. Kunz, W., et al., *Osmotic Coefficients and Surface Tensions of Aqueous Electrolyte Solutions: Role of Dispersion Forces.* Journal of Physical Chemistry B, 2004. **108**(7): p. 2398-2404.
261. Dos Santos, A.P., A. Diehl, and Y. Levin, *Surface Tensions, Surface Potentials, and the Hofmeister Series of Electrolyte Solutions.* Langmuir, 2010. **26**(13): p. 10778-10783.
262. Parsegian, V., *Van Der Waals Forces Cambridge University Press.* 2006.
263. Okan, S.E. and P. Salmon, *A neutron diffraction study on the structure of Cl-solutions in hydrogen-bonded molecular solvents.* Journal of Physics: Condensed Matter, 1994. **6**(21): p. 3839.
264. Baer, M.D., et al., *Electrochemical Surface Potential Due to Classical Point Charge Models Drives Anion Adsorption to the Air–Water Interface.* The Journal of Physical Chemistry Letters, 2012. **3**(11): p. 1565-1570.
265. Slavchov, R.I. and J.K. Novev, *Surface tension of concentrated electrolyte solutions.* Journal of Colloid and Interface Science, 2012. **387**(1): p. 234-243.
266. Caleman, C., et al., *Atomistic simulation of ion solvation in water explains surface preference of halides.* Proceedings of the National Academy of Sciences, 2011. **108**(17): p. 6838-6842.
267. Eggimann, B.L. and J.I. Siepmann, *Size Effects on the Solvation of Anions at the Aqueous Liquid−Vapor Interface.* The Journal of Physical Chemistry C, 2008. **112**(1): p. 210-218.
268. Son, C.Y. and Z.-G. Wang, *Image-charge effects on ion adsorption near aqueous interfaces.* Proceedings of the National Academy of Sciences, 2021. **118**(19): p. e2020615118.
269. Miranda-Quintana, R.A. and J. Smiatek, *Calculation of donor numbers: Computational estimates for the Lewis basicity of solvents.* Journal of Molecular Liquids, 2021. **322**: p. 114506.
270. Andersson, G., H. Morgner, and H. Pohl, *Energy-loss straggling of helium projectiles at low kinetic energies: deconvolution of concentration depth profiles of inorganic salt solutes in aqueous solutions.* Physical Review A, 2008. **78**(3): p. 032904.
271. Andersson, G., *Concentration Depth Profiles of Inorganic Ions at Liquid Surfaces.* Australian Journal of Chemistry, 2010. **63**(3): p. 434-437.
272. Ceme, T.A.W., *Invesitgation of Ion Specific Effects in Adsoprtion of Divalent Ions at Liquid Surfaces*, in *College of Science and Engineering* 2021, Flinders University: Adelaide, South Australia.
273. Irving, H. and R. Williams, *637. The stability of transition-metal complexes.* Journal of the Chemical Society (Resumed), 1953: p. 3192-3210.
274. Kasimir Gregory, G.E., Erica Wanless, Grant Webber, and Alister Page, *Ion Solvation Repository (IonSolvR) (http://dx.doi.org/10.25817/40r8-t633)* 2022.
275. Nosé, S., *A unified formulation of the constant temperature molecular dynamics methods.* The Journal of Chemical Physics, 1984. **81**(1): p. 511-519.
276. Hoover, W.G., *Canonical dynamics: Equilibrium phase-space distributions.* Physical Review A, 1985. **31**(3): p. 1695-1697.
277. Martyna, G.J., M.L. Klein, and M. Tuckerman, *Nosé–Hoover chains: The canonical ensemble via continuous dynamics.* The Journal of Chemical Physics, 1992. **97**(4): p. 2635-2643.

278. Martyna, G.J., et al., *Explicit reversible integrators for extended systems dynamics.* Molecular Physics, 1996. **87**(5): p. 1117-1157.
279. Gaus, M., Q. Cui, and M. Elstner, *DFTB3: Extension of the self-consistent-charge density-functional tight-binding method (SCC-DFTB).* Journal of Chemical Theory and Computation, 2012. **7**(4): p. 931-948.
280. Kubillus, M., et al., *Parameterization of the DFTB3 Method for Br, Ca, Cl, F, I, K, and Na in Organic and Biological Systems.* Journal of Chemical Theory and Computation, 2014. **11**(1): p. 332-342.
281. Lu, X., et al., *Parametrization of DFTB3/3OB for Magnesium and Zinc for Chemical and Biological Applications.* The Journal of Physical Chemistry B, 2014. **119**(3): p. 1062-1082.
282. Gaus, M., et al., *Parameterization of DFTB3/3OB for Sulfur and Phosphorus for Chemical and Biological Applications.* Journal of Chemical Theory and Computation, 2014. **10**(4): p. 1518-1537.
283. Grimme, S., et al., *A consistent and accurate ab initio parametrization of density functional dispersion correction (DFT-D) for the 94 elements H-Pu.* The Journal of Chemical Physics, 2010. **132**(15): p. 154104-154104.
284. Grimme, S., S. Ehrlich, and L. Goerigk, *Effect of the damping function in dispersion corrected density functional theory.* Journal of Computational Chemistry, 2011. **32**(7): p. 1456-1465.
285. Becke, A.D. and E.R. Johnson, *A density-functional model of the dispersion interaction.* The Journal of Chemical Physics, 2005. **123**(15): p. 154101-154101.
286. Johnson, E.R. and A.D. Becke, *A post-Hartree–Fock model of intermolecular interactions.* The Journal of Chemical Physics, 2005. **123**(2): p. 24101-24101.
287. Andersson, G. and H. Morgner, *Investigations on solutions of tetrabutylonium salts in formamide with NICISS and ICISS: concentration depth profiles and composition of the outermost layer.* Surface Science, 2000. **445**(1): p. 89-99.
288. Soszka, N., et al., *The impact of the length of alkyl chain on the behavior of benzyl alcohol homologues – the interplay between dispersive and hydrogen bond interactions.* Physical Chemistry Chemical Physics, 2021. **23**(41): p. 23796-23807.
289. Valyashko, V., M. Buback, and E. Franck, *Infrared absorption of concentrated aqueous LiCl solutions to high pressures and temperatures.* Zeitschrift für Naturforschung A, 1980. **35**(5): p. 549-555.
290. Hribar, B., et al., *How Ions Affect the Structure of Water.* Journal of the American Chemical Society, 2002. **124**(41): p. 12302-12311.
291. Wang, H., et al., *Infrared Signature of the Cation−π Interaction between Calcite and Aromatic Hydrocarbons.* Langmuir, 2015. **31**(21): p. 5820-5826.
292. Andersson, G., *Energy-loss straggling of helium projectiles at low kinetic energies.* Physical Review A, 2007. **75**(3): p. 032901.
293. Alan C. Hymes, H., Minn.,, *Physological salt solutions of ethyl ene oxde-poly propylene glycol con. Densation products as blood plasma substitutes*, U.s.p. office, Editor. 1971, Wyandotte Chemicals Corporation, Wyandotte, Mich.: United States of America. p. 2.
294. Thormann, E., *On understanding of the Hofmeister effect: how addition of salt alters the stability of temperature responsive polymers in aqueous solutions.* RSC Adv., 2012. **2**(22): p. 8297-8305.
295. Chen, C.-γ., et al., *Sum frequency generation vibrational Spectroscopy studies on molecular conformation of liquid polymers poly (ethylene glycol) and poly (propylene glycol) at different interfaces.* Macromolecules, 2002. **35**(24): p. 9130-9135.
296. Moghaddam, S.Z. and E. Thormann, *The Hofmeister series: Specific ion effects in aqueous polymer solutions.* Journal of Colloid And Interface Science, 2019. **555**: p. 615-635.